

Photocatalytic Applications of Layered Niobates and their Composites

Von der Naturwissenschaftlichen Fakultät der
Gottfried Wilhelm Leibniz Universität Hannover

zur Erlangung des Grades

Doktorin der Naturwissenschaften (Dr. rer. nat.)

genehmigte Dissertation

von

Barbara Nascimento Nunes, Mestre (Brasilien)

2022

Referent: apl. Prof. Dr. rer. nat. habil. Detlef W. Bahnemann

Korreferent: Prof. Antonio Otavio de Toledo Patrocinio, Ph.D.

Korreferent: apl. Prof. Dr. rer. nat. habil. Armin Feldhoff

Korreferent: Prof. Dr. rer. nat. Michael Wark

Tag der Promotion: 12.04.2022

*Ao meu marido, Mayron, por ter me
dado tanto incentivo e força, por ser meu
grande companheiro.*

*Aos meus pais, Maria Aparecida e
José Elias por todo amor e dedicação.*

Acknowledgments

The accomplishment of this work was only possible because of all the great and inspiring people that I had the opportunity to meet during this period. Therefore, I am very glad to express all my gratitude to those who had supported and guided me all this time in Germany.

First, I express my deepest gratitude to my supervisor in Germany Prof. Dr. Detlef Bahnemann for giving me this invaluable opportunity to be one of his mentees, for all his support and guidance always filled with patience, kindness, and enthusiasm. I am also grateful for the freedom he has provided to develop my research and his continuous support enriched with his immense knowledge.

I would also like to extend my sincere gratitude to my supervisor in Brazil Prof. Dr. Antonio Otavio Toledo Patrocinio who has been an inspiration since my first steps in research. Thank you for being my mentor ever since and for encouraging me to go for my PhD in Germany. I also have no words to thank you for all the insightful and impeccable guidance in each idea or step on my research during these years, even from distance. Apart the professional aspects, I also express my appreciation to all your friendship and personal support, especially when my husband and I arrived in Germany.

I am thankful to Prof. Dr. Sascha Beutel, Prof. Dr. Michael Wark, and Prof. Dr. Armin Feldhoff for their time and kind acceptance for being part of my examination committee.

I very much appreciate the Brazilian foundation Coordenação de Aperfeiçoamento de Pessoal de Nível Superior (CAPES) for the financial supports through a full scholarship, CAPES/CNPQ (15/2017) program, grant number 88887.161403/2017-00.

Many thanks to Dr. Ralph Dillert for all his support in the labs, stimulating discussions, and constructive comments in our group seminars. I have learned so much from you and your valuable knowledge.

I would like to acknowledge the staff at the Institute of Technical Chemistry (TCI) for the assistance and the friendly environment. I am also grateful to Prof. Dr. Armin Feldhoff at the Institut für Physikalische Chemie and his students for the training and support on XRD analysis, and Dr. Fritz Schulze-Wischeler of the Laboratorium für Nano- und Quantenengineering (LNQE) for the training and support on TEM measurements.

My respectful acknowledgments for the institutions Leibniz University Hannover (Gottfried Wilhelm Leibniz Universität Hannover, LUH) in Germany and Federal University of Uberlandia (Universidade Federal de Uberlândia, UFU) in Brazil for making this cotutelle PhD possible. I also thank the LUH International Office, in special Dr. Solenne Schwanemann for all her kindness and solicitude. A special thanks to Ms. Merle Feldt for her kind assistance in the doctoral examination process.

I gratefully acknowledge all my colleagues of Bahnemann's group (AK Bahnemann) for the friendship, assistance and for all the scientific and non-scientific conversations. Special thanks to Dr. Narmina Balayeva, Dr. Saher Hamid, Dr. Luis Granone and Dr. Carsten Günemann for helping me so much in my early days in the group; Dr. Osama Al-Madanat and Dr. Yamen Alsalka for all the experimental support, for teaching me so much, and for the infinite kindness; Maria Teresa Ayala Ayala and Haoran Wang for becoming lifelong friends.

I also wish to thank the group Laboratory of Photochemistry and Materials Science (LAFOT-CM) in Brazil, for all the support and scientific discussion in our seminars. Special thanks to Leandro Faustino and Dr. Juliane Zacour for being so nice and supportive friends.

Last but not the least, my warmest gratitude to my family and friends, who fill my life with love and encouragement. I express my appreciation to my close friends here in Hannover, which have become my family in Germany, in special Patricia Toledo, Eliana and Rafael Gallo, Aline and Kako. My acknowledgments to my dear friend Camille Leite for being by my side since our bachelor's degree in Uberlandia.

I have no words to express how much I have missed my parents, Maria Aparecida and Jose Elias. I thank you two for everything that I have accomplished in my life and for you being around and taking care of me even from far away. My deepest gratitude to my husband Mayron. How lucky I am to have you in my life! I cannot even imagine going through all these years in Germany without you. Thank you so much for being by my side all the time, in each happy or hard moment, for your endless encouragement, patience, and support. Thanks also for my loved brother Gabriel for all the affection, for making me laugh often even by phone calls and for the support. Thanks for all my loved family and friends in Brazil who always support me.

Zusammenfassung

Photokatalytische Anwendungen von zweidimensionalen (2D) Materialien haben aufgrund ihrer zahlreichen elektronischen und strukturellen Vorteile großes Interesse geweckt. Unter diesen Materialien sind Schichtniobate bekannte Photokatalysatoren für die H₂-Entwicklung mit einer reichen Oberflächenchemie. Unter Berücksichtigung der stark exponierten aktiven Zentren seiner 2D-Struktur und der morphologischen Flexibilität wurden die Eigenschaften des Hexaniobatschichten als heterogener Photokatalysator in dieser Arbeit untersucht, mit besonderem Augenmerk auf die elektronischen und Grenzflächenprozesse, die an der H₂-Entwicklung beteiligt sind. Zunächst wurden hocheffiziente photokatalytische Oberflächen durch die schichtweise (LbL) Abscheidung von Hexaniobat-Nanorollen auf leitfähigen Gläsern erhalten. Diese Filme wurden unter Verwendung von Poly(allylaminhydrochlorid) als Polyelektrolyt abgeschieden und eine weitere thermische Behandlung führte zu Filmen, die aus einer ungeordneten Anordnung von Hexaniobat-Nanorollen bestanden. Diese Konfiguration begünstigte die Diffusion von Wasser- und Methanolmolekülen und erleichterte eine effiziente H₂-Entwicklung. Darüber hinaus ermöglichte die Voradsorption von [Pt(NH₃)₄]²⁺-Kationen auf den Niobatschichten die Produktion von metallischen Pt-Nanoclustern in den Nanorollen. Die Pt-modifizierten Filme zeigten scheinbare Quantenausbeuten von (4,0 ± 0,5) % für die H₂-Entwicklung aus Wasser/Methanol-Gemischen unter UV-A-Bestrahlung. Um neuartige elektronische Prozesse zu induzieren, ohne die Volumeneigenschaften des Hexaniobats zu verändern, wurde anschließend eine Oberflächenmodifizierung durch *grafting* mit metallischen Nanoclustern durchgeführt. Exfoliierte Hexaniobat(K_{4-x}H_xNb₆O₁₇)-Komposite mit Metallionen wie Co²⁺, Fe³⁺ und Cu²⁺ wurden hergestellt und ihre photokatalytischen Eigenschaften wurden vollständig untersucht. Die morphologische Charakterisierung zeigte, dass *grafting* Modifizierungen an die Hexaniobatoberfläche angelagert sind und amorphe Cluster bilden. Diese Spezies induzieren eine zusätzliche Absorptionseigenschaft im UV-A-Bereich, die einem Ladungstransfer an der Grenzfläche vom Niobat-Valenzband zu den Metallionenzentren zugeschrieben wird. Im Fall von Co²⁺ und Fe³⁺ wurde bei mit 0,1 Gew.% gepfropften Proben eine verstärkte UV-getriebene Photoaktivität in reinem Wasser beobachtet, insbesondere bei den mit Co²⁺-Ionen modifizierten, während mit zunehmender Konzentration der *grafting* Ionen geringere H₂-Entwicklungsraten beobachtet werden. Wenn das Pt auf der Oberfläche des Photokatalysators abgeschieden wurde, war die H₂-Entwicklungsrate für die 0,1 Gew.%ige Co Probe in reinem Wasser 70% höher als die, die für das Pt-Hexaniobat vor dem *grafting* beobachtet wurde. Für Cu²⁺-Hexaniobate lieferten Cu²⁺-Cluster eine deutliche Verbesserung der photokatalytischen H₂-Entwicklung aus methanolischer wässriger Lösung unter UV-Vis-Bestrahlung und vielversprechende Ergebnisse für die partielle Wasserspaltung im Vergleich zum Hexaniobat mit photoabgeschiedenem Pt. Diese Spezies auf der Hexaniobatoberfläche weisen eine hohe Redoxreversibilität auf, und können leicht zu Cu¹⁺/Cu⁰ reduziert und zu Cu²⁺ reoxidiert werden. Cu²⁺-Ionen wirken nach der Bandlückenanregung als Elektronenfänger, und die resultierenden reduzierten Spezies wirken als aktives Zentrum um H₂ zu produzieren. Somit kann das Vorhandensein verschiedener Ionen in unterschiedlichen Konzentrationen das Schicksal der photogenerierten Träger direkt beeinflussen und die photokatalytische Aktivität auf unterschiedliche Weise auslösen. Die *grafting* Ionen tragen zu einer effizienteren Ladungstrennung und höheren photokatalytischen Leistungen bei.

Stichwörter: 2D-Materialien, Nioboxid, Niobate, dünne Filme, photoaktive Oberfläche, Photokatalyse, Wasserstoff, Wasserspaltung, Mechanismusstudien.

Abstract

Photocatalytic applications of two-dimensional (2D) materials have called great interest due to several electronic and structural advantages. Among these materials, layered niobates are well-known photocatalysts for H₂ evolution with a rich surface chemistry. Taking into account the highly exposed active sites of its 2D structure and the morphological flexibility, the properties of the exfoliated hexaniobate as a heterogeneous photocatalyst has been explored in this work, with particular attention to the electronic and interfacial processes involved in the H₂ evolution. Firstly, highly efficient photocatalytic surfaces were obtained through the layer-by-layer (LbL) deposition of hexaniobate nanoscrolls on conductive glasses. These films were deposited by using poly(allylamine hydrochloride) as a polyelectrolyte and further thermal treatment leading to films composed of a fuzzy assembly of hexaniobate nanoscrolls. This configuration favored the diffusion of water and methanol molecules thus facilitating an efficient H₂ evolution. Moreover, pre-adsorption of [Pt(NH₃)₄]²⁺ cations on the niobate layers allowed the production of metallic Pt nanoclusters within the nanoscrolls. The Pt-modified films exhibited apparent quantum yields of (4.0 ± 0.5) % for H₂ evolution from water/methanol mixtures under UV-A irradiation. Then, in order to induce novel electronic processes without changing the bulk properties of the hexaniobate, surface modification was performed by grafting with metallic nanoclusters. Exfoliated hexaniobate (K_{4-x}H_xNb₆O₁₇) composites with metal ions such as Co²⁺, Fe³⁺ and Cu²⁺ were prepared and their photocatalytic properties were fully investigated. Morphological characterization showed that the grafting ions are attached to the hexaniobate surface forming amorphous clusters. These species induce an additional absorption feature in the UV-A region, which is attributed to an interfacial charge transfer from the niobate valence band to the metal ion centers. In the case of Co²⁺ and Fe³⁺, enhanced UV-driven photoactivity in plain water was observed for 0.1 wt.% grafted samples, especially for those modified with Co²⁺ ions, while smaller H₂ evolution rates are observed as the concentration of the grafting ions increased. When Pt was added to the photocatalyst, the H₂ evolution rate for the 0.1% Co-grafted sample in plain water was 70% higher than that observed for the nongrafted Pt-hexaniobate. For Cu²⁺-grafted hexaniobates, Cu²⁺ clusters provided an expressive improvement in the photocatalytic H₂ evolution under UV-vis irradiation from methanolic aqueous solution and promising results for partial water splitting, in comparison to the hexaniobate with photodeposited Pt. These species on the hexaniobate surface present a high redox reversibility, being easily reduced to Cu¹⁺/Cu⁰ and reoxidized to Cu²⁺. Cu²⁺ ions work as electron scavenger following band gap excitation while the resulting reduced species act as active sites to produce H₂. Thus, the presence of different ions at different concentrations can directly affect the fate of the photogenerated carriers thus triggering the photocatalytic activity in different ways. Overall, the grafted ions contribute to a more efficient charge separation and to higher photocatalytic performances.

Keywords: 2D materials, niobium oxide, niobates, thin films, photoactive surface, photocatalysis, hydrogen, water splitting, mechanism studies.

Resumo

Aplicações fotocatalíticas de materiais bidimensionais (2D) têm despertado grande interesse devido às diversas vantagens eletrônicas e estruturais desses materiais. Dentre eles, os niobatos lamelares são fotocatalisadores bem conhecidos para a evolução de H₂ com uma rica química de superfície. Levando em consideração os sítios ativos altamente expostos de sua estrutura 2D e sua flexibilidade morfológica, as propriedades do hexaniobato esfoliado como fotocatalisador heterogêneo foram exploradas neste trabalho, com particular atenção aos processos eletrônicos e interfaciais envolvidos na evolução de H₂. Primeiramente, superfícies fotocatalíticas de alta eficiência foram obtidas através da deposição camada por camada (LbL) de nanoscrolls de hexaniobato em vidros condutores. Esses filmes foram depositados usando poli(cloridrato de alilamina) como polieletrólito, e o posterior tratamento térmico resultou em filmes compostos por uma montagem difusa de nanoscrolls de hexaniobato. Esta configuração favoreceu a difusão das moléculas de água e metanol, facilitando uma evolução eficiente de H₂. Além disso, a pré-adsorção de cátions [Pt(NH₃)₄]²⁺ nas camadas de niobato permitiu a produção de nanoaglomerados metálicos de Pt nos nanoscrolls. Os filmes modificados com Pt exibiram rendimentos quânticos aparentes de (4,0 ± 0,5)% para a evolução de H₂ a partir de misturas de água / metanol sob irradiação UV-A. Em sequência, a fim de induzir novos processos eletrônicos sem alterar as propriedades do hexaniobato, a modificação da superfície foi realizada por *grafting* com nanoclusters metálicos. Compósitos de hexaniobato esfoliado (K_{4-x}H_xNb₆O₁₇) com íons metálicos como Co²⁺, Fe³⁺ e Cu²⁺ foram preparados e suas propriedades fotocatalíticas foram extensivamente investigadas. A caracterização morfológica mostrou que os íons adicionados por *grafting* estão fixados na superfície do hexaniobato formando aglomerados amorfos. Essas espécies induzem uma de absorção adicional característica na região UV-A, que é atribuída a uma transferência de carga interfacial da banda de valência do niobato para os centros de íons metálicos. No caso de Co²⁺ e Fe³⁺, a melhor fotoatividade conduzida por UV em água pura foi observada para amostras modificadas a 0,1%, especialmente para aquelas com íons Co²⁺, enquanto menores taxas de evolução de H₂ são observadas conforme a concentração dos íons de *grafting* aumenta. Quando a Pt foi adicionada ao fotocatalisador, a taxa de evolução de H₂ para a amostra modificada a 0,1% em água pura foi 70% maior do que a observada para o Pt-hexaniobato não modificado por *grafting*. Para hexaniobatos com Cu²⁺, os clusters de Cu²⁺ proporcionaram expressiva melhora na evolução fotocatalítica de H₂ sob irradiação UV-vis de uma solução aquosa metanólica e resultados promissores para a quebra parcial da água, em comparação ao hexaniobato com Pt fotodepositada. Essas espécies na superfície do hexaniobato apresentam alta reversibilidade redox, que pode ser facilmente reduzida para Cu¹⁺/Cu⁰ e reoxidada para Cu²⁺. Os íons Cu²⁺ funcionam como eliminadores de elétrons após a excitação do *bandgap* e as espécies reduzidas resultantes atuam como sítio ativo para produzir H₂. Assim, a presença de diferentes íons em diferentes concentrações pode afetar diretamente o destino dos portadores fotogerados, desencadeando a atividade fotocatalítica de diferentes maneiras. Os íons adicionados por *grafting* contribuem para uma separação de carga mais eficiente e desempenhos fotocatalíticos mais elevados.

Palavras-chave: materiais 2D, óxido de nióbio, niobatos, filmes finos, superfície fotoativa, fotocatalise, hidrogênio, quebra da água, estudos de mecanismo.

Table of Contents

Dedication.....	I
Acknowledgments.....	II
Zusammenfassung.....	V
Abstract.....	VI
Resumo.....	VII
Chapter 1 – Introduction and Objectives.....	12
1.1. Introduction.....	12
1.2. Objectives.....	16
1.3. Structure of the Thesis.....	16
1.4. References.....	18
Chapter 2 - Recent Advances in Niobium-Based Materials for Photocatalytic Solar Fuel Production.....	25
2.1. Foreword.....	25
2.2. Abstract.....	25
2.3. Introduction.....	25
2.4. H ₂ Evolution and Water Splitting.....	27
2.4.1. Niobium Pentoxide (Nb ₂ O ₅).....	27
2.4.2. Niobium Layered Compounds.....	33
2.4.3. Nb-Doped Materials.....	50
2.5. Photoreduction of CO ₂	55
2.6. Concluding Remarks and Perspectives.....	65
2.7. References.....	66
Chapter 3 - Photocatalytic Properties of Layer-by-Layer Thin Films of Hexaniobate Nanoscrolls.....	78
3.1. Foreword.....	78
3.2. Abstract.....	78
3.3. Introduction.....	79
3.4. Materials and Methods.....	80
3.4.1. Preparation of lamellar K _{4-x} H _x Nb ₆ O ₁₇	80
3.4.2. Preparation of K _{4-x} H _x Nb ₆ O ₁₇ LbL films.....	80
3.4.3. Characterization techniques.....	81
3.4.4. Photocatalytic H ₂ evolution.....	82
3.5. Results and Discussion.....	83
3.5.1. Film assembly and characterization.....	83
3.5.2. Photocatalytic H ₂ evolution.....	88

3.5.3. Photoelectrochemical properties.....	90
3.6. Conclusions.....	94
3.7. Supporting Information.....	95
3.8. References.....	101
Chapter 4 - Photoinduced H₂ Evolution by Hexaniobate Sheets Grafted with Metal Ions: The Fate of Photogenerated Carriers.....	110
4.1. Foreword.....	110
4.2. Abstract.....	110
4.3. Introduction.....	111
4.4. Materials and Methods.....	113
4.4.1. Characterization techniques.....	113
4.4.2. Photocatalytic experiments.....	115
4.5. Results and Discussion.....	115
4.5.1. Optical and Morphological properties.....	115
4.5.2. Photocatalytic activity in plain water and methanolic solutions...	119
4.6. Conclusions.....	131
4.7. Supporting Information.....	133
4.8. References.....	144
Chapter 5 - Efficient Photocatalytic H₂ Evolution by Hexaniobate Nanosheets Grafted with Copper Nanoclusters	151
5.1. Foreword.....	151
5.2. Abstract.....	151
5.3. Introduction.....	151
5.4. Materials and Methods.....	153
5.4.1. Hexaniobate nanosheets.....	153
5.4.2. Cu ²⁺ grafting.....	154
5.4.3. Characterization.....	154
5.4.4. Photocatalytic H ₂ evolution.....	155
5.5. Results and Discussion.....	155
5.6. Conclusions.....	168
5.7. Supporting Information.....	169
5.8. References.....	175
Chapter 6 - Summarizing Discussion and Conclusions.....	181
Curriculum Vitae.....	196
Publications List.....	197

1. Introduction and Objectives

1.1. Introduction

Despite the impressive technological developments and the globalization during recent decades, environmental preservation is still a major world concern. Currently, along with great energy demand and population growth, fuel and electricity supplies are still strongly dependent on nonrenewable sources. Consequently, high quantities of carbon dioxide are emitted every day. In this scenario, application of molecular hydrogen as a fuel has been considered as an eminent solution due to its high energy content per unit weight and its clean combustion with water being the only product. Indeed, it is also noteworthy that H₂ is essential for the chemical industry either as raw material or as reducing agent, particularly for fertilizer production and oil refining¹. The annual demand for molecular hydrogen achieves values around 70 Mt². Nevertheless, fossil sources such as natural gas and coal are still the main feedstock for H₂ production and consequently, great amounts of CO₂ are emitted, achieving 830 million tons per year only in this sector³. In this context, to classify and facilitate the differentiation of methods of H₂ production according to their impacts to the environment, some colors are used to represent them³⁻⁵. The so-called “brown or black hydrogen” is produced by coal gasification yielding high amounts of CO₂ and CO. Alternatively, “gray hydrogen” can be produced by steam methane reforming of natural gas, which is currently the primary source of hydrogen being less hazardous than coal gasification but still non-renewable leading also to high amounts of CO₂. The “blue hydrogen” is also produced by the steam methane reforming, but in this case, the CO₂ gas is captured before reaching the atmosphere. In contrast, when a clean and renewable source, such as solar, hydro, and wind energy, is used, the H₂ is known as “green hydrogen”. Therefore, a clean and renewable method to produce green hydrogen has great significance not only in a clean energy perspective but also in terms of sustainability and environmental liability^{6,7}.

Heterogeneous photocatalysis has been found as an effective alternative to harness light energy in a renewable and environmental-friendly way. It has gained great importance due to its clean, safe, low-cost, and renewable characteristics for both H₂ evolution and environmental remediation⁸. Hereby, light energy can be transformed into chemical energy or fuels and then used as function of its demand. In addition, solar light as an energy resource stands out for its advantages in terms of wide spread availability

and accessibility in an inexhaustible and inexpensive way around the world. It also may cause less damage to the environment in relation to waste production, polluting gas emissions or impacts to different ecosystems. The total sum of renewable energy from all other sources accounts to only 1% of the solar energy supplied to the Earth surface by the sun, i.e., 173 000 TW. This amount of energy is more than 9000 times larger than the current total energy consumption of the world (17.91 TW in 2017)⁹. Hence, heterogeneous photocatalysis makes it possible to take advantage of this abundant source of energy in order to produce other products of interest. For instance, once a photocatalyst absorbs light, this energy can be converted to electric energy by photovoltaic cells¹⁰⁻¹², into fuels¹³⁻¹⁵, or even be used to degrade pollutants¹⁶⁻¹⁸. Thus, investigations regarding the properties of the photocatalyst are essential for the effectiveness of the desired reactions.

Typically, a heterogeneous photocatalyst is an inorganic semiconductor and its electronic structure can be described by a formation of two main energy bands. According to their energy level, the combination of atoms that compose the photocatalyst structure gives rise to a valence band consisting of bonding orbitals that are filled with electrons. Concomitantly, the antibonding orbitals form an empty level named conduction band, which is separated from the valence band by an energy barrier called bandgap¹⁹. Therefore, to start a photocatalytic reaction, the photocatalyst must absorb a photon with proper energy generating an electron-hole pair, which can either migrate to the surface and react with adsorbed species, or undergo recombination. Among the first investigations of metallic oxides as photocatalysts, Carl Renz reported in 1921 the behavior of the TiO₂, CeO₂, Nb₂O₅ and Ta₂O₅ when exposed to solar light in the presence of organic compounds²⁰. Then, in 1924, Baur and Perret described a photocatalytic deposition of metallic silver on ZnO and proposed a reaction mechanism with the generation of charges following photon absorption by ZnO²¹. Since then, photocatalytic studies have been mainly based on oxide materials such as ZnO and TiO₂²². A breakthrough in the heterogeneous photocatalysis field occurred after the work of Fujishima and Honda, who described the possibility to photo-oxidize water by exposing a TiO₂-based photoanode to UV light²³. In principle, this reaction not only dissociates water but also forms hydroxyl radicals, molecular oxygen and molecular hydrogen. Soon, it became noticeable that different semiconductors could promote these reactions.

In 1986, Domen and coworkers showed that layered niobates can act as efficient photocatalysts for H₂ production²⁴. These materials are formed by Nb⁵⁺ ions combined

with oxygen forming octahedral $[\text{NbO}_6]$ units connected through adjacent or opposite sharing edges or corners resulting in an extended two dimensional (2D) layered arrangement. The resulting layers are negatively charged and then stacked by cations in the interlayer space^{25,26}. This arrangement offers the possibility of various modifications, either by ion exchange or by intercalation. Moreover, these materials can be found as nanosheets or nanoscrolls through exfoliation with a bulky organic base such as tetrabutylammonium hydroxide (TBA(OH))^{25,27}. Besides, these materials provide interesting characteristics for photocatalytic applications such as a high surface area and the presence of acidic sites. In addition, the 2D configuration is of considerable interest due to the electronic and structural advantages which offer a superior electron mobility²⁸. Some of the most common structures of layered niobates are shown in Figure 1.

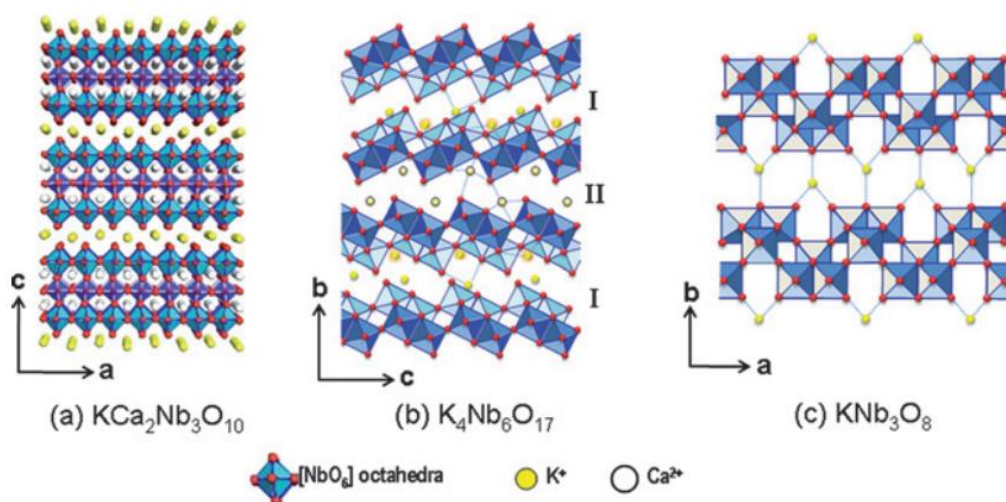


Figure 1 - Schematic representation of structures of (a) $\text{KCa}_2\text{Nb}_3\text{O}_{10}$, (b) $\text{K}_4\text{Nb}_6\text{O}_{17}$ and (c) KNb_3O_8 layered niobates. Reprinted with permission from [25].

In that report of Domen et al., the authors firstly investigated niobates of formula KNbO_3 , $\text{K}_2\text{Nb}_6\text{O}_{16}$ and $\text{K}_4\text{Nb}_6\text{O}_{17}$ for H_2 evolution using methanol (20% v/v) as a sacrificial electron donor²⁴. Potassium hexaniobate ($\text{K}_4\text{Nb}_6\text{O}_{17}$) showed the best performance, also when compared to TiO_2 and SrTiO_3 . In the following, it was applied for water splitting experiments where a stoichiometric photodecomposition to H_2 and O_2 was achieved by adding NiO (0.1 wt%) as co-catalyst. The highest water splitting efficiency was also observed for this same composite when comparing to $\text{K}_4\text{Nb}_6\text{O}_{17}$ loaded with other metallic oxides such as Cr_2O_3 , Mn_3O_4 , Fe_2O_3 , Co_3O_4 , CuO , PtO , RuO_2 and Rh_2O_3 ²⁹. Then, further studies with NiO (0.1 wt%)- $\text{K}_4\text{Nb}_6\text{O}_{17}$ were subsequently reported^{30,31}. Employing a heating and redox treatment, Ni ultrafine metallic centers were deposited inside the interspaces. It could be shown that these centers acted as active sites

for H₂ evolution being localized separately from the O₂ evolution sites. Using the same strategy, the group could later show the photocatalytic evolution of O₂ and H₂ from water by Pt-intercalated K₄Nb₆O₁₇ using [Pt(NH₃)₄]²⁺ as a precursor³², with quantum efficiencies of 20% for H₂ evolution³³.

Concomitantly, some studies with titanoniobate (KTiNbO₅) demonstrated the effective intercalation of more voluminous cations such as alkylammonium, which were able to widen the interlayer spaces^{34,35}. Later on, the effective niobate intercalation with large interlayer expansions was reported by Jacobson and coworkers by using HCa₂Nb₃O₁₀ with a series of alkylamines³⁶. The authors also described the total exfoliation of calcium niobate into thin sheets by monoamine surfactant molecules³⁷. One of the most well-known exfoliation agents, that is, TBAOH (tetrabutylammonium hydroxide), was then reported by Mallouk's group³⁸, which also investigated in detail the colloidal suspension of K₄Nb₆O₁₇ in TBA aqueous solution³⁹. Differently from the other investigated lamellar oxides, K_{4-x}H_xNb₆O₁₇ colloids resulted in both, sheets and high aspect ratio tubules. Thus, Domen's group was pioneer in applying the exfoliated niobate for highly efficient photocatalytic H₂ evolution from alcoholic solutions^{40,41}. They also noted an increase of the surface area of this photocatalyst from 4 m² g⁻¹ to 108 m² g⁻¹ achieved by H₄Nb₆O₁₇ after exfoliation. In their studies, using ethanol and n-propanol as electron donors, the restacked niobate with deposited Pt exhibited higher activity for H₂ evolution in comparison to the non-exfoliated one⁴⁰.

The investigations of Domen's group, within the vast niobates diversity, employed as one of the most studied structures for the photocatalytic H₂ production potassium hexaniobate (K₄Nb₆O₁₇)^{29,42-44}. Its layered structure formed by Nb₆O₁₇⁴⁻ units provides interlayer spaces which are accessible to both, hydronium ions and water¹⁴. It is a *n*-type semiconductor with the position of the conduction band being around -0.5 V (*vs.* SHE) and that of the valence band above +2.5 V (*vs.* SHE) which both are appropriate for water splitting⁴⁵. However, this material shows also limitations, related to the high band gap energy around 3.5 eV, the high propensity to produce H₂O₂ and the fact that it suffers from self-poisoning. Osterloh's group reported a noteworthy work where they describe the mechanism of partial water splitting on niobates⁴⁶. Concurrently with the photocatalytic H₂ evolution, they identified a close to 1:1 stoichiometric ratio for the production of H₂O₂ as oxidation product. Moreover, the photogenerated H₂O₂ is able to associate onto the surface of the photocatalyst and to provoke its full deactivation after long time irradiation. The H₂ evolution rates decayed from 1.59 μmol h⁻¹ to 0.31 μmol

h^{-1} after 48h under irradiation in a quartz flask with four 175 W low-pressure Hg lamps. Later, the same researchers measured a rate of about $250 \mu\text{mol h}^{-1}$ for H_2 formation on a platinized photocatalyst in a quartz round bottom flask equipped with a 300 W Xe arc lamp⁴². As expected, H_2O_2 was identified as main reaction product on post-irradiated platinated scrolls while the O_2 evolution was not effective even when applying AgNO_3 as electron acceptor. The authors clarified that due to the strong binding affinity to Nb^{5+} and fewer reactive intermediates and redox steps, H_2O_2 formation is energetically and kinetically favoured in relation to O_2 .

1.2. Objectives

Therefore, further improvements of the photocatalytic activity of exfoliated hexaniobates requires their surface modification to avoid self-poisoning and deactivation. Additionally, new strategies for a possible large-scale utilization, such as thin film deposition, are still poorly investigated. These topics will be explored in this cumulative thesis. Our main objectives comprehend the modification of the hexaniobate in a way to improve the photocatalytic performances of this material and to more deeply understand the photocatalytic surface processes that take place on hexaniobate-based composites. In this way, the surface modification of the hexaniobate and the combination with other species able to induce novel electronic processes without changing the bulk properties will be investigated. Moreover, photochemical and photophysical properties will be examined by different techniques, to better understand the electron transfer reactions and photocatalytic mechanisms.

1.3. Structure of the Thesis

For these purposes, the topics of this work are presented in the following chapters. At first, after giving a brief introduction on the necessity of green H_2 production and the context of layered niobate as photocatalysts (Chapter 1), Chapter 2 will introduce the scope of the last advances of niobium-based photocatalyst within a review entitled “*Recent Advances in Niobium-Based Materials for Photocatalytic Solar Fuel Production*” published in *Catalysts*¹³. In addition to niobates being photosensitive, stable and versatile in relation to morphology and composition, they can be exfoliated, resulting in stable suspensions of nanosheets that enable the arrangement of composites on a nanometric scale. Their charged layers offer the possibility to build films employing

electrostatic interactions with different components such as polymers, metallic nanoparticles, oxides, etc. In this sense, the assembly of thin films can favour the application as photocatalysts due to the ease of recovering, smaller losses and reduced material agglomeration. Taking this into account, bare niobate and the Pt-niobate films were assembled by the Layer-by-Layer (LbL) technique, which will be presented in Chapter 3 by the publication “*Photocatalytic properties of layer-by-layer thin films of hexaniobate nanoscrolls*” published in *Catalysis Today*⁴⁷. The LbL technique is one of the most versatile methods to assemble thin films because it is simple, of low cost, allows the application of different materials and substrates, and also the control of film thickness by the number of bilayers^{48,49}. Subsequently, in order to investigate and explore the surface properties of the hexaniobates nanosheets, surface grafting with metallic nanoclusters was employed (Chapters 4 and 5). Facing some limitations of the material, changes in the mechanisms of the photochemical reactions may be a strategic pathway to improve its photocatalytic performance for H₂ production. Surface grafting is a soft and simple method that has recently gained attention for inducing electronic process on the catalyst surface without changing the crystallinity and electronic structure in the bulk^{50–52}. Hashimoto’s group has, for example, reported many results regarding this methodology on TiO₂ for increasing the rate of photo-oxidation reactions for organic pollutants^{52–55}. The higher photocatalytic activity provided by metallic cations such as Fe³⁺, Cu²⁺ and Cr³⁺ is based on an interfacial charge transfer (IFCT) between the semiconductor and the metal oxide nanoclusters, which can extend the light absorption range of the materials into the visible light region and improve the charge separation efficiency. Thus, Chapter 4 includes the article “*Photoinduced H₂ Evolution by Hexaniobate Sheets Grafted with Metal Ions: The Fate of Photogenerated Carriers*” published in *ACS Applied Energy Materials*⁵⁶, in which hexaniobate nanosheets were modified by grafting with metal ions such as Co²⁺ and Fe³⁺. These metal ions could support the photocatalytic activity, particularly when using Co²⁺ and Pt as cocatalysts for the H₂ evolution by partial water splitting. The following, Chapter 5 presents the work “*Efficient photocatalytic H₂ evolution by hexaniobate nanosheets grafted with copper nanoclusters*” published in *ChemPhotoChem*. In this case, Cu²⁺ ions were added to the hexaniobate by grafting and a higher performance of H₂ production was observed in comparison to deposited Pt or Cu. Lastly, Chapter 6 includes a summarizing discussion comprising all the studies and a conclusion.

1.4. References

- (1) Armaroli, N.; Balzani, V. The Hydrogen Issue. *ChemSusChem* **2011**, *4* (1), 21–36. <https://doi.org/10.1002/cssc.201000182>.
- (2) Jose M Bermudez; Taku Hasegawa. Hydrogen <https://www.iea.org/reports/hydrogen>.
- (3) International Energy Agency. The Future of Hydrogen <https://www.iea.org/reports/the-future-of-hydrogen>.
- (4) Howarth, R. W.; Jacobson, M. Z. How Green Is Blue Hydrogen? *Energy Sci. Eng.* **2021**, *9* (10), 1676–1687. <https://doi.org/10.1002/ese3.956>.
- (5) Farmer, M. What Colour is Your Hydrogen? A Power Technology jargon-buster <https://www.power-technology.com/features/hydrogen-power-blue-green-grey-brown-extraction-production-colour-renewable-energy-storage/> (accessed Nov 1, 2021).
- (6) Clark, W. W.; Rifkin, J. A Green Hydrogen Economy. *Energy Policy* **2006**, *34* (17), 2630–2639. <https://doi.org/10.1016/j.enpol.2005.06.024>.
- (7) Oliveira, A. M.; Beswick, R. R.; Yan, Y. A Green Hydrogen Economy for a Renewable Energy Society. *Curr. Opin. Chem. Eng.* **2021**, *33*, 100701. <https://doi.org/10.1016/j.coche.2021.100701>.
- (8) Liu, C.; Zhang, Q.; Hou, W.; Zou, Z. 2D Titanium/Niobium Metal Oxide-Based Materials for Photocatalytic Application. *Sol. RRL* **2020**, *2000070*, 2000070. <https://doi.org/10.1002/solr.202000070>.
- (9) Kim, J. H.; Hansora, D.; Sharma, P.; Jang, J. W.; Lee, J. S. Toward Practical Solar Hydrogen Production-an Artificial Photosynthetic Leaf-to-Farm Challenge. *Chem. Soc. Rev.* **2019**, *48* (7), 1908–1971. <https://doi.org/10.1039/c8cs00699g>.
- (10) Paula, L. F.; Amaral, R. C.; Murakami Iha, N. Y.; Paniago, R. M.; Machado, A. E. H.; Patrocínio, A. O. T. New Layer-by-Layer Nb₂O₅–TiO₂ Film as an Effective Underlayer in Dye-Sensitised Solar Cells. *RSC Adv.* **2014**, *4* (20), 10310–10316. <https://doi.org/10.1039/C4RA00058G>.
- (11) Bjelajac, A.; Petrović, R.; Stan, G. E.; Socol, G.; Mihailescu, A.; Mihailescu, I.

- N.; Veltruska, K.; Matolin, V.; Siketić, Z.; Provatas, G.; Jakšić, M.; Janačković, D. C-Doped TiO₂ Nanotubes with Pulsed Laser Deposited Bi₂O₃ Films for Photovoltaic Application. *Ceram. Int.* **2021**.
<https://doi.org/10.1016/j.ceramint.2021.10.251>.
- (12) Hong, Y.; Li, J.; Wu, W.; Wu, Y.; Bai, H.; Shi, K.; Meng, Q.; Zhou, Z.; Jia, D. Structure, Electricity, and Bandgap Modulation in Fe₂O₃-Doped Potassium Sodium Niobate Ceramics. *Ceram. Int.* **2018**, *44* (13), 16069–16075.
<https://doi.org/10.1016/j.ceramint.2018.05.174>.
- (13) Nunes, B. N.; Lopes, O. F.; Patrocinio, A. O. T.; Bahnemann, D. W. Recent Advances in Niobium-Based Materials for Photocatalytic Solar Fuel Production. *Catalysts* **2020**, *10* (1), 126. <https://doi.org/10.3390/catal10010126>.
- (14) Osterloh, F. E. Inorganic Nanostructures for Photoelectrochemical and Photocatalytic Water Splitting. *Chem. Soc. Rev.* **2013**, *42* (6), 2294–2320.
<https://doi.org/10.1039/c2cs35266d>.
- (15) Jiao, X.; Zheng, K.; Chen, Q.; Li, X.; Li, Y.; Shao, W.; Xu, J.; Zhu, J.; Pan, Y.; Sun, Y.; Xie, Y. Photocatalytic Conversion of Waste Plastics into C₂ Fuels under Simulated Natural Environment Conditions. *Angew. Chemie - Int. Ed.* **2020**, *59* (36), 15497–15501. <https://doi.org/10.1002/anie.201915766>.
- (16) Garg, A.; Singhanian, T.; Singh, A.; Sharma, S.; Rani, S.; Neogy, A.; Yadav, S. R.; Sangal, V. K.; Garg, N. Photocatalytic Degradation of Bisphenol-A Using N, Co Codoped TiO₂ Catalyst under Solar Light. *Sci. Rep.* **2019**, *9* (1), 1–13.
<https://doi.org/10.1038/s41598-018-38358-w>.
- (17) Zhang, Y.; Nie, J.; Wang, Q.; Zhang, X.; Wang, Q.; Cong, Y. Synthesis of Co₃O₄/Ag/TiO₂ Nanotubes Arrays via Photo-Deposition of Ag and Modification of Co₃O₄ (311) for Enhancement of Visible-Light Photoelectrochemical Performance. *Appl. Surf. Sci.* **2018**, *427*, 1009–1018.
<https://doi.org/10.1016/j.apsusc.2017.09.008>.
- (18) Al-Madanat, O.; AlSalka, Y.; Curti, M.; Dillert, R.; Bahnemann, D. W. Mechanistic Insights into Hydrogen Evolution by Photocatalytic Reforming of Naphthalene. *ACS Catal.* **2020**, *10* (13), 7398–7412.
<https://doi.org/10.1021/acscatal.0c01713>.

- (19) Gaya, U. I. *Heterogeneous Photocatalysis Using Inorganic Semiconductor Solids*; Springer Netherlands: Dordrecht, 2014. <https://doi.org/10.1007/978-94-007-7775-0>.
- (20) Renz, C. Lichtreaktionen Der Oxyde Des Titans, Cers Und Der Erdsäuren. *Helv. Chim. Acta* **1921**, 4 (1), 961–968. <https://doi.org/10.1002/hlca.192100401101>.
- (21) Baur, E.; Perret, A. Über Die Einwirkung von Licht Auf Gelöste Silbersalze in Gegenwart von Zinkoxyd. *Helv. Chim. Acta* **1924**, 7 (1), 910–915. <https://doi.org/10.1002/hlca.192400701109>.
- (22) Lettieri, S.; Pavone, M.; Fioravanti, A.; Santamaria Amato, L.; Maddalena, P. Charge Carrier Processes and Optical Properties in TiO₂ and TiO₂-Based Heterojunction Photocatalysts: A Review. *Materials (Basel)*. **2021**, 14 (7), 1645. <https://doi.org/10.3390/ma14071645>.
- (23) Fujishima, A.; Honda, K. Electrochemical Photolysis of Water at a Semiconductor Electrode. *Nature* **1972**, 238, 38–40. <https://doi.org/10.1038/238038a0>.
- (24) Domen, K.; Kudo, A.; Shinozaki, A.; Tanaka, A.; Maruya, K. I.; Onishi, T. Photodecomposition of Water and Hydrogen Evolution from Aqueous Methanol Solution over Novel Niobate Photocatalysts. *J. Chem. Soc. Chem. Commun.* **1986**, No. 4, 356–357. <https://doi.org/10.1039/C39860000356>.
- (25) Bizeto, M. A.; Shiguihara, A. L.; Constantino, V. R. L. Layered Niobate Nanosheets: Building Blocks for Advanced Materials Assembly. *J. Mater. Chem.* **2009**, 19 (17), 2512–2525. <https://doi.org/10.1039/b821435b>.
- (26) Nunes, B. N.; Patrocínio, A. O. T.; Bahnemann, D. W. Influence of the Preparation Conditions on the Morphology and Photocatalytic Performance Pt-Modified Hexaniobate Composites. *J. Phys. Condens. Matter* **2019**, 31 (39), 394001. <https://doi.org/10.1088/1361-648x/ab2c5e>.
- (27) Souza, E. C. C. Thermal Stability and Spectroscopic Assessment of Brønsted Sites in Solid Acid-Layered Niobates. *J. Phys. Chem. C* **2019**, 123 (40), 24426–24435. <https://doi.org/10.1021/acs.jpcc.9b07087>.
- (28) Low, J.; Cao, S.; Yu, J.; Wageh, S. Two-Dimensional Layered Composite

- Photocatalysts. *Chem. Commun.* **2014**, 50 (74), 10768–10777.
<https://doi.org/10.1039/c4cc02553a>.
- (29) Kudo, A.; Tanaka, A.; Domen, K.; Maruya, K. Ichi; Aika, K. Ichi; Onishi, T. Photocatalytic Decomposition of Water over NiO-K₄Nb₆O₁₇ Catalyst. *J. Catal.* **1988**, 111 (1), 67–76. [https://doi.org/10.1016/0021-9517\(88\)90066-8](https://doi.org/10.1016/0021-9517(88)90066-8).
- (30) Kudo, A.; Sayama, K.; Tanaka, A.; Asakura, K.; Domen, K.; Maruya, K.; Onishi, T. Nickel-Loaded K₄Nb₆O₁₇ Photocatalyst in the Decomposition of H₂O into H₂ and O₂: Structure and Reaction Mechanism. *J. Catal.* **1989**, 120 (2), 337–352. [https://doi.org/10.1016/0021-9517\(89\)90274-1](https://doi.org/10.1016/0021-9517(89)90274-1).
- (31) Domen, K.; Kudo, A.; Tanaka, A.; Onishi, T. Overall Photodecomposition of Water on a Layered Niobate Catalyst. *Catal. Today* **1990**, 8 (1), 77–84. [https://doi.org/10.1016/0920-5861\(90\)87009-R](https://doi.org/10.1016/0920-5861(90)87009-R).
- (32) Sayama, K.; Tanaka, A.; Domen, K.; Maruya, K.; Onishi, T. Photocatalytic Decomposition of Water over Platinum-Intercalated K₄Nb₆O₁₇. *J. Phys. Chem.* **1991**, 95 (3), 1345–1348.
- (33) Tabata, S.; Ohnishi, H.; Yagasaki, E.; Ippommatsu, M.; Domen, K. Light-Intensity Dependence in Photocatalytic Decomposition of Water over K₄Nb₆O₁₇ Catalyst. *Catal. Letters* **1994**, 28 (2–4), 417–422. <https://doi.org/10.1007/BF00806072>.
- (34) Rebbah, H.; Borel, M. M.; Raveau, B. Intercalation of Alkylammonium Ions and Oxide Layers [TiNbO₅]-. *Mater. Res. Bull.* **1980**, 15, 317–321.
- (35) Kikkawa, S.; Koizumi, M. Organic Intercalation on Layered Compound KTiNbO₅. *Mater. Res. Bull.* **1980**, 15 (5), 533–539.
- (36) Jacobson, A. J.; Johnson, J. W.; Lewandowski, J. T. Intercalation of the Layered Solid Acid HCa₂Nb₃O₁₀ by Organic Amines. *Mater. Res. Bull.* **1987**, 22 (1), 45–51. [https://doi.org/10.1016/0025-5408\(87\)90148-6](https://doi.org/10.1016/0025-5408(87)90148-6).
- (37) Treacy, M. M. J.; Rice, S. B.; Jacobson, A. J.; Lewandowski, J. T. Electron Microscopy Study of Delamination in Dispersions of the Perovskite-Related Layered Phases K[Ca₂Na_{n-3}Nb_nO_{3n+1}]: Evidence for Single-Layer Formation. *Chem. Mater.* **1990**, 2 (3), 279–286. <https://doi.org/10.1021/cm00009a018>.

- (38) Keller, S. W.; Kim, H. N.; Mallouk, T. E. Layer-by-Layer Assembly of Intercalation Compounds and Heterostructures on Surfaces: Toward Molecular “Beaker” Epitaxy. *J. Am. Chem. Soc.* **1994**, *116* (19), 8817–8818.
<https://doi.org/10.1021/ja00098a055>.
- (39) Saupe, G. B.; Waraksa, C. C.; Kim, H. N.; Han, Y. J.; Kaschak, D. M.; Skinner, D. M.; Mallouk, T. E. Nanoscale Tubules Formed by Exfoliation of Potassium Hexaniobate. *Chem. Mater.* **2000**, *12* (6), 1556–1562.
<https://doi.org/10.1021/cm981136n>.
- (40) Domen, K.; Ebina, Y.; Ikeda, S.; Tanaka, A.; Kondo, J. N.; Maruya, K. Layered Niobium Oxides - Pillaring and Exfoliation. *Catal. Today* **1996**, *28*, 167–174.
[https://doi.org/10.1016/0920-5861\(95\)00223-5](https://doi.org/10.1016/0920-5861(95)00223-5).
- (41) Abe, R.; Shinohara, K.; Tanaka, A.; Hara, M.; Kondo, J. N.; Domen, K. Preparation of Porous Niobium Oxides by Soft-Chemical Process and Their Photocatalytic Activity. *Chem. Mater.* **1997**, *9* (10), 2179–2184.
<https://doi.org/10.1021/cm970284v>.
- (42) Townsend, T. K.; Sabio, E. M.; Browning, N. D.; Osterloh, F. E. Improved Niobate Nanoscroll Photocatalysts for Partial Water Splitting. *ChemSusChem* **2011**, *4* (2), 185–190. <https://doi.org/10.1002/cssc.201000377>.
- (43) Liu, C.; Feng, Y.; Han, Z.; Sun, Y.; Wang, X.; Zhang, Q.; Zou, Z. Z-Scheme N-Doped $K_4Nb_6O_{17}/g-C_3N_4$ Heterojunction with Superior Visible-Light-Driven Photocatalytic Activity for Organic Pollutant Removal and Hydrogen Production. *Chinese J. Catal.* **2021**, *42* (1), 164–174.
[https://doi.org/https://doi.org/10.1016/S1872-2067\(20\)63608-7](https://doi.org/https://doi.org/10.1016/S1872-2067(20)63608-7).
- (44) Sarahan, M. C.; Carroll, E. C.; Allen, M.; Larsen, D. S.; Browning, N. D.; Osterloh, F. E. $K_4Nb_6O_{17}$ -Derived Photocatalysts for Hydrogen Evolution from Water: Nanoscrolls versus Nanosheets. *J. Solid State Chem.* **2008**, *181* (7), 1678–1683. <https://doi.org/10.1016/j.jssc.2008.06.021>.
- (45) Islam, A.; Teo, S. H.; Taufiq-Yap, Y. H.; Vo, D.-V. N.; Awual, M. R. Towards the Robust Hydrogen (H_2) Fuel Production with Niobium Complexes-A Review. *J. Clean. Prod.* **2021**, *318* (April), 128439.
<https://doi.org/10.1016/j.jclepro.2021.128439>.

- (46) Compton, O. C.; Osterloh, F. E. Niobate Nanosheets as Catalysts for Photochemical Water Splitting into Hydrogen and Hydrogen Peroxide. *J. Phys. Chem. C* **2009**, *113* (1), 479–485. <https://doi.org/10.1021/jp807839b>.
- (47) Nunes, B. N.; Haisch, C.; Emeline, A. V.; Bahnemann, D. W.; Patrocínio, A. O. T. Photocatalytic Properties of Layer-by-Layer Thin Films of Hexaniobate Nanoscrolls. *Catal. Today* **2019**, *326* (June 2018), 60–67. <https://doi.org/10.1016/j.cattod.2018.06.029>.
- (48) Richardson, J. J.; Björnmalm, M.; Caruso, F. Technology-Driven Layer-by-Layer Assembly of Nanofilms. *Science* (80-.). **2015**, *348* (6233). <https://doi.org/10.1126/science.aaa2491>.
- (49) Nunes, B. N.; Paula, L. F.; Costa, Í. A.; Machado, A. E. H.; Paterno, L. G.; Patrocínio, A. O. T. Layer-by-Layer Assembled Photocatalysts for Environmental Remediation and Solar Energy Conversion. *J. Photochem. Photobiol. C Photochem. Rev.* **2017**, *32*. <https://doi.org/10.1016/j.jphotochemrev.2017.05.002>.
- (50) Balayeva, N. O.; Fleisch, M.; Bahnemann, D. W. Surface-Grafted WO₃/TiO₂ Photocatalysts: Enhanced Visible-Light Activity towards Indoor Air Purification. *Catal. Today* **2018**, *313*, 63–71. <https://doi.org/10.1016/j.cattod.2017.12.008>.
- (51) Khan, A.; Alam, U.; Ali, D.; Muneer, M. Visible-Light Induced Simultaneous Oxidation of Methyl Orange and Reduction of Cr(VI) with Fe(III)-Grafted K₂Ti₆O₁₃ Photocatalyst. *ChemistrySelect* **2018**, *3* (27), 7906–7912. <https://doi.org/10.1002/slct.201800982>.
- (52) Miyauchi, M.; Irie, H.; Liu, M.; Qiu, X.; Yu, H.; Sunada, K.; Hashimoto, K. Visible-Light-Sensitive Photocatalysts: Nanocluster-Grafted Titanium Dioxide for Indoor Environmental Remediation. *J. Phys. Chem. Lett.* **2016**, *7* (1), 75–84. <https://doi.org/10.1021/acs.jpcclett.5b02041>.
- (53) Irie, H.; Miura, S.; Nakamura, R.; Hashimoto, K. A Novel Visible-Light-Sensitive Efficient Photocatalyst, Cr(III)-Grafted TiO₂. *Chem. Lett.* **2008**, *37* (3), 252–253. <https://doi.org/10.1246/cl.2008.252>.
- (54) Irie, H.; Kamiya, K.; Shibayama, T.; Miura, S.; Tryk, D. A.; Yokoyama, T.; Hashimoto, K. Visible Light-Sensitive Cu(II)-Grafted TiO₂ Photocatalysts:

Activities and X-Ray Absorption Fine Structure Analyses. *J. Phys. Chem. C* **2009**, *113* (24), 10761–10766. <https://doi.org/10.1021/jp903063z>.

- (55) Liu, M.; Qiu, X.; Miyauchi, M.; Hashimoto, K. Energy-Level Matching of Fe(III) Ions Grafted at Surface and Doped in Bulk for Efficient Visible-Light Photocatalysts. *J. Am. Chem. Soc.* **2013**, *135* (27), 10064–10072. <https://doi.org/10.1021/ja401541k>.
- (56) Nunes, B. N.; Bahnemann, D. W.; Patrocinio, A. O. T. Photoinduced H₂ Evolution by Hexaniobate Sheets Grafted with Metal Ions: The Fate of Photogenerated Carriers. *ACS Appl. Energy Mater.* **2021**, *4* (4), 3681–3692. <https://doi.org/10.1021/acsaem.1c00128>.

2. Recent Advances in Niobium-Based Materials for Photocatalytic Solar Fuel Production

2.1. Foreword

This chapter includes the review “Recent Advances in Niobium-Based Materials for Photocatalytic Solar Fuel Production” by Barbara N. Nunes, Osmando F. Lopes, Antonio Otavio T. Patrocínio and Detlef W. Bahnemann published on Catalysts 2020, 10, 126 (open access) <https://doi.org/10.3390/catal10010126>.

2.2. Abstract

The search for renewable and clean energy sources is a key aspect for sustainable development as energy consumption has continuously increased over the years concomitantly with environmental concerns caused by the use of fossil fuels. Semiconductor materials have great potential for acting as photocatalysts for solar fuel production, a potential energy source able to solve both energy and environmental concerns. Among the studied semiconductor materials, those based on niobium pentacation are still shallowly explored, although the number of publications and patents on Nb⁵⁺-based photocatalysts has increased in the last years. A large variety of Nb⁵⁺-based materials exhibit suitable electronic/morphological properties for light-driving reactions. Not only the extensive group of Nb₂O₅ polymorphs is explored, but also many types of layered niobates, mixed oxides, and Nb⁵⁺-doped semiconductors. Therefore, the aim of this manuscript is to provide a review of the latest developments of niobium based photocatalysts for energy conversion into fuels, more specifically, CO₂ reduction to hydrocarbons or H₂ evolution from water. Additionally, the main strategies for improving the photocatalytic performance of niobium-based materials are discussed.

2.3. Introduction

Increasing energy demand concomitantly with global warming is a major world concern. Currently, fuels and electricity supplies are still strongly dependent on nonrenewable sources. For instance, in 2018 the worldwide consumption of fossil energy was almost 36.5 billion of barrels of oil, 3850 billion cubic meters of natural gas and 3800 million tons oil equivalent of coal per year. As a consequence, more than 33000 million

tons of carbon dioxide was emitted, which represents an annual increasing of 2.0%, the fastest growth for seven years ¹. This scenario can trigger serious problems for the current and next generations such as the insufficiency of fossil fuel resources, air pollution and also climates changes as a result of the greenhouse effect ².

In face to this issue, the development of methods to obtain energy in a clean and sustainable way becomes imperative. Therefore, solar light as primary energy resource stands out for its advantages in terms of spread availability and accessibility in an inexhaustible and inexpensive way around the world. In addition, obtaining energy from the sun may cause less damage to the environment in relation to waste production, polluting gases emission or impacts to different ecosystems. The possibility to convert light into valuable solar fuels from water or even CO₂ is a promising approach to provide clean energy and at the same time, contribute to diminishing the global warming effect ³. Additionally, the total sum of renewable energy from all the reserves is around 1% of the solar energy supplied to the earth surface by the sun, i.e. 173 000 TW. This amount of energy is more than 9000 times larger than current total energy consumption of the world (17.91 TW in 2017). The challenge lies on the development of economically viable technologies for solar energy harvesting, storage, and utilization ⁴.

Thus, since Fujishima and Honda ⁵ reported the possibility of promoting the photo-oxidation of water on the surface of TiO₂ photoanodes, semiconductor materials have been extensively investigated as photocatalysts to store solar energy in chemical bonds. Among different photocatalysts, it is worth pointing out Nb⁵⁺-based materials that have been investigated due to their suitable electronic and morphological properties for light-driving reactions. Nb⁵⁺ is characterized by its high affinity to oxygen and its oxides exhibit different properties depending on the preparation and desired application ^{6,7}. Niobium pentoxide is considered the most thermodynamically stable Nb-based compound with more than 15 different structural configurations. Depending on the crystalline phase, its band-gap energy can vary from 3.2 eV to larger values such as 5 eV ⁸⁻¹⁰.

Besides Nb₂O₅ polymorphs, Nb⁵⁺ can also combine with oxygen to form extended lamellar structures resulting in polyoxy anions, the niobates. They are basically constituted of stacked negative charged layers with intercalated cations ¹¹. This configuration provides a considerable surface area and allows easy modification either by intercalation, superficial modification or formation of nanosheets and nanoscrolls ¹²⁻¹⁴. Furthermore, Nb⁵⁺ is also frequently applied as a doping agent. It is commonly combined

to TiO₂ and considered one of the most promising dopants for modifying the matrix crystalline structure and minimize the electron-hole recombination^{15–18}.

In this paper, the recent developments of niobium based materials for photocatalytic solar fuel production, especially those in the last three years, are systematically reviewed. The main strategies for improving the photocatalytic performance for H₂ production from water splitting and CO₂ reduction to hydrocarbons, focused on niobium species will be presented. In section 2.5 application to H₂ evolution is discussed, followed by section 2.6 related to CO₂ reduction.

2.4. H₂ Evolution and Water Splitting

2.4.1. Niobium Pentoxide (Nb₂O₅)

Nb₂O₅ is a typical *n*-type semiconductor that, along with other oxides, has been widely studied as a photocatalyst due to its electronic properties such as excellent chemical and thermal stability, large abundance, rich morphologies and several polymorphs^{19–22}. It is a white solid powder, insoluble in water, and can be dissolved just by fusion with strong basic or acid fluxes. In general, its structure is formed by NbO₆ octahedral, which can result in an amorphous state or may crystallize in a wide range of polymorphs with different physical properties^{6,8}. Some of those polymorphs are pseudohexagonal (TT-Nb₂O₅), orthorhombic (T-Nb₂O₅) and monoclinic (B, H, R and N-Nb₂O₅)¹⁹. The most known nomenclature is based on Brauer' system in which the crystalline phases are identified by letters corresponding to the temperature at which they are obtained⁸.

Despite these properties, bulk Nb₂O₅ is not able to achieve a considerable photoactivity owing to its low specific surface area and fast recombination rate of the photogenerated charge carriers²¹. In this sense, several approaches have been applied to increase its photocatalytic performance. One of them is to control the shape and morphology of particles in order to tune the Nb₂O₅ properties. This can be possible, for instance, by selecting a suitable precursor to obtain the desired configuration of Nb₂O₅. Wen and coauthors firstly synthesized orthorhombic Nb₂O₅ (O-Nb₂O₅) by a hydrothermal reaction using K₄Nb₆O₁₇·4.5H₂O as a precursor. This sample exhibited rectangle nanosheets with dominantly exposed (010) plane (Figures 1 (a)-(d))²². After acid treatment of K₄Nb₆O₁₇·4.5H₂O to get H₄Nb₆O₁₇·3H₂O, the ion-exchanged material was

treated hydrothermally for 24 h at different conditions of temperature (195-215 °C) and pH (1.5-11.5) as shown in Figure 1 (e). At first, by changing the temperature at pH 3.5, X ray diffraction (XRD) results showed that the O-Nb₂O₅ phase began to be formed at 200 °C, and at 210 °C, the peaks of H₄Nb₆O₁₇·3H₂O disappeared completely and all observed peaks could be indexed as the O-Nb₂O₅ phase. From the Figure 1 (e), it can be also observed that the O-Nb₂O₅ was obtained in all selected pHs; however, the authors reported that, at pH 3.5, the material showed higher crystallinity and more regular morphology. A commercial O-Nb₂O₅ sample with spherical morphology was used for comparison and exhibited a band gap value of 3.2 eV, in contrast to 3.0 eV for the as synthesized O-Nb₂O₅ rectangle nanosheets. Then, the photoelectrochemical activity of both samples was evaluated by measuring the photocurrent resulted from H₂ evolution under 370 nm UV light irradiation (30 W·m⁻²). Both photoelectrodes show very low dark current, but under illumination, the O-Nb₂O₅ nanosheet-based photoelectrode exhibited photocurrents 4.3 times higher than the commercial sample. The authors could justify the improved performance to a larger number of charge carriers coming from the exposed (010) facet with lower band gap energy, fewer recombination centers and also faster charge transfer by the regular rectangle nanosheets with high crystallinity.

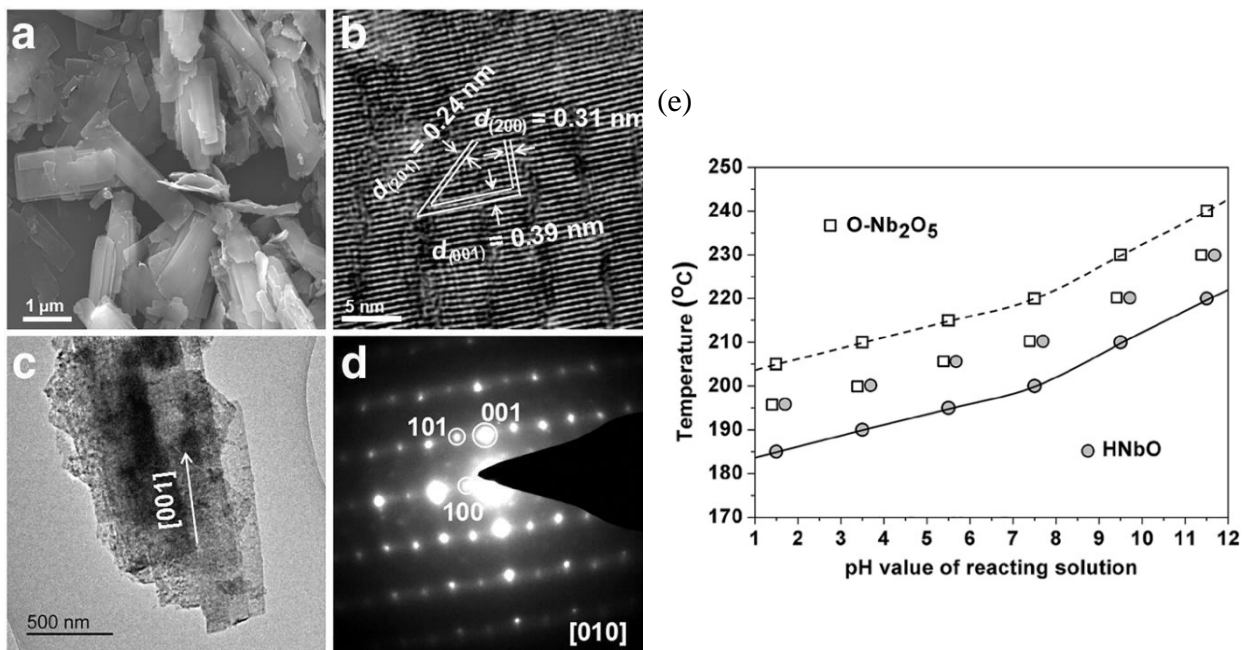


Figure 1 – O-Nb₂O₅ microscopies images of (a) field emission scanning electron microscopy (FE-SEM), (b) high-resolution transmission electron microscopy (HRTEM), (c) transmission electron microscopy (TEM), and (d) selected area electron diffraction (SAED) pattern and (e) diagram for the transformation of O-Nb₂O₅ nanosheets from

$\text{H}_4\text{Nb}_6\text{O}_{17} \cdot 3\text{H}_2\text{O}$ (HNbO) nanosheets under hydrothermal conditions. Reproduced with permission from 22. Copyright (2019), Elsevier, Amsterdam, Netherlands.

Later, the same strategy was employed by the same group to obtain crystalline hexagonal Nb_2O_5 (H- Nb_2O_5) nanobelt clusters with exposed (-110) plane²³. In this case, a fiber-like $\text{K}_2\text{Nb}_2\text{O}_6 \cdot \text{H}_2\text{O}$ material was used as precursor. In order to improve the photocatalytic performance of H- Nb_2O_5 under visible light, metallic Ag was deposited by in-situ photoreduction. UV-vis diffuse reflectance spectra showed that the absorption edges were 375 nm for the H- Nb_2O_5 nanobelt clusters and 423 nm for the Ag-modified sample. Then, both samples were evaluated photoelectrochemically under simulated sunlight illumination (100 W m^{-2}) at zero applied voltage. The Ag-modified sample achieved a photocurrent of $10.73 \mu\text{A}$, 535 times higher than that observed for bare H- Nb_2O_5 , which was attributed to the improved light-harvesting efficiency as well as the better charge transfer performance.

Zhou and coauthors reported monoclinic Nb_2O_5 nanorod superstructures by a similar route using $\text{Sn}_2\text{Nb}_2\text{O}_7$ nanoparticles as the precursor²⁴. SEM images showed that Nb_2O_5 nanorods were obtained with lengths around $2 \mu\text{m}$ and diameters of 200 nm. The light absorption properties of the Nb_2O_5 nanorods were compared to that for commercial Nb_2O_5 powders and a considerable blue shift was observed in the absorption edge, which could be related to the nanosized of the former. Photocatalytic H_2 production was also evaluated with 0.5 wt% Pt as co-catalyst in 25% methanol aqueous solution, employing a 500 W high-pressure mercury lamp as light source. The Nb_2O_5 nanorod superstructures sample showed a H_2 evolution rate of $91 \mu\text{mol h}^{-1}$, whereas the commercial one exhibited a rate of $0.6 \mu\text{mol h}^{-1}$, ca. 150 times lower than that for the Nb_2O_5 nanorod. Moreover, Nb_2O_5 nanorod superstructures maintained an almost constant photocatalytic H_2 production rate after 24 h. The higher performances were explained by the authors based on the superstructures of the material (Figure 2), in which photogenerated electrons could be transferred along the 1D nanorods direction and also transported to the neighboring nanorods, leading to a more efficient separation of photogenerated charge carriers.

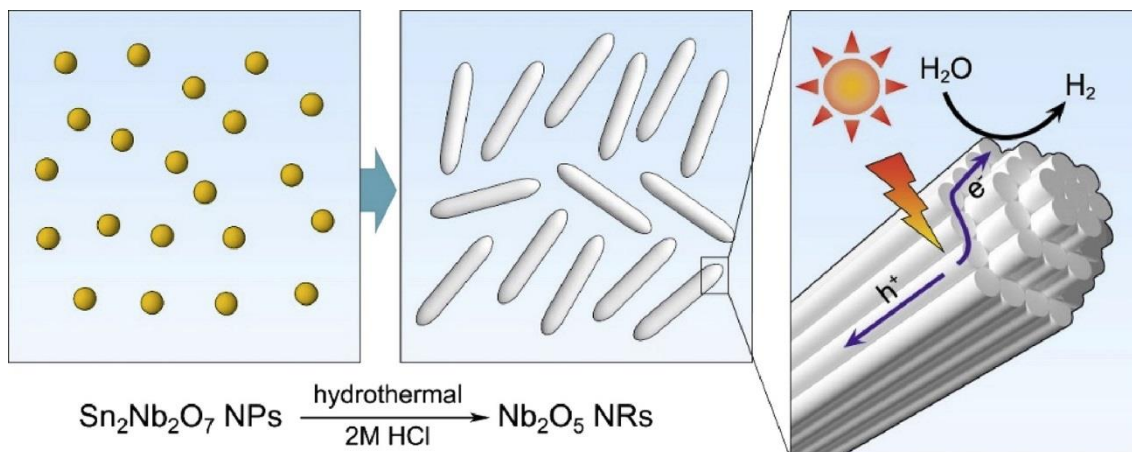


Figure 2 – Scheme of Nb_2O_5 nanorod superstructures synthesis and the improved photogenerated charge carries separation. Reproduced with permission from 24. Copyright (2019), Elsevier, Amsterdam, Netherlands.

Clearly, such morphological and structural transformations lead to changes in the optical and electronic properties of niobium oxide. In this sense, Zhang et al. reported an enclosed porous structure of pseudo-hexagonal tief-tief (TT) Nb_2O_5 nanowires, which showed a significant decrease in the band gap from 3.22 to 2.95 eV in relation to the nonporous Nb_2O_5 nanowires, and then, an enhancement of H_2 evolution under visible light irradiation ($\lambda > 420 \text{ nm}$)²⁵. The material was prepared by a solvothermal synthesis using ammonium niobate(V) oxalate hydrate and oleic acid mixed with trioctylamine. The sample was calcined at different temperatures. Thermal treatment at 600 °C and 700 °C causes the formation of orthorhombic phase, while at 580 °C pristine TT-phase was formed, so this last condition was selected for further analysis. In TEM images, it was observed that the porous nanowires were shorter than 1 μm and exhibited well separated pores inside the structure, whereas nonporous ones were longer than 5 μm and showed ripple-like contrast owing to bending-induced strain. The authors could explain the formation of such porosity to the replacement of oxalate anion by oleic acid and trioctylamine in the Nb center, resulting in a structure with hydrophobic core and surrounding Nb species. Then, the subsequent heating treatment induced the formation of pores from the cores and the Nb_2O_5 crystalline nanowires from the coordination structure. However, the samples were not characterized by isotherms of N_2 adsorption to be properly classified as porous material. The authors suggested that under-coordinated ions in the twisted lattice around the pores could generate mid-gap states, and hence lower band gap energies. As a result, the H_2 production rate of the porous sample was 243.8

$\mu\text{mol g}^{-1} \text{h}^{-1}$, considerable higher than the nonporous one, which exhibited H_2 evolution rate of $113.1 \mu\text{mol g}^{-1} \text{h}^{-1}$ under similar conditions, and even higher than that for P25 TiO_2 ($129.6 \mu\text{mol g}^{-1} \text{h}^{-1}$).

Besides the morphology, other strategies can be applied to increase the photocatalytic activity of Nb_2O_5 species. The introduction of defects into the crystal lattice could be used to engineer the electronic transport properties along the oxide structure or even to create new trap states inside the forbidden band gap region²⁶. Zhao and coauthors reported improved solar-light absorption via partial reduction of Nb_2O_5 nanorods with active exposed (001) surfaces, which result in the black niobium oxide²⁷. In summary, the previous prepared Nb_2O_5 was thermally treated in an aluminum reduction device, where the sample and aluminum powder were positioned independently in a two-zone tube oven, and then the Nb_2O_5 and aluminum powders were heated to 500°C and 800°C , respectively. This procedure led to the formation of Nb^{4+} centers and hence substantial oxygen vacancies that resulted in a black powder, and thus an enhancement in visible and infrared light absorption compared with the pristine Nb_2O_5 . The reduction of Nb_2O_5 could be confirmed by Raman and X ray photoelectron spectroscopies. The Nb^{4+} centers were also characterized by electron paramagnetic resonance. High resolution transmission electron microscopy indicated predominant (001) crystal plane exposed on the nanorod surfaces, suggesting good crystallinity of samples before and after reduction. The samples were evaluated as photoanode using dip-coated FTO glasses in a 1 M NaOH electrolyte under 100 mW cm^{-2} illumination with a 150 W Xe lamp. At 1.23 V, the reduced Nb_2O_5 sample showed a photocurrent density 138 times higher than that for Nb_2O_5 . The carrier density was calculated by Mott-Schottky plots and was 3×10^4 times higher for the reduced sample, evidencing an enhanced electrical conductivity, charge transport, and separation. Finally, the samples were evaluated to produce H_2 with 0.5 wt% Pt and 20% methanol solution under full-sunlight irradiation from 300 W Xe lamp, which, for the reduced Nb_2O_5 , resulted in 13 times higher production rate of $274.8 \mu\text{mol h}^{-1} \text{g}^{-1}$ in comparison to Nb_2O_5 nanorods ($21.1 \mu\text{mol h}^{-1} \text{g}^{-1}$).

An extended visible light activity of orthorhombic Nb_2O_5 was achieved by Kulkarni et al. as result of nitrogen doping using a solid state reaction of urea and niobium salt²⁰. At 500°C , ammonia is released and works as nitrogen source to be introduced into the Nb_2O_5 lattice, filling oxygen vacancies. Field emission scanning electron microscopy (FE-SEM) analysis showed that the urea concentration was crucial for the observed

morphologic changes. Concerning the optical properties, the modified samples were analyzed by UV-vis diffuse reflectance and compared to the pristine Nb₂O₅, which had band gap energy of 3.4 eV. In general, all the N-doped Nb₂O₅ samples showed significant absorption in the range of 400-600 nm and a higher red shift in the band gap absorption when the urea concentration was increased (2.6-2.4 eV). Density functional theory (DFT) calculations described that N 2p bands falls above the O 2p bands and so the top of the valence band giving rise to the reduction in the band gap. At the highest Nb/urea ratio investigated (1:15), this trend was not observed and higher band gap edge than the expected trend (2.5 eV) was obtained. This would have resulted from nitrogen saturation of the niobia matrix. Photoluminescence measurements indicate that the optimal Nb/urea ratio was 1:10. This sample exhibited the lowest luminescence intensity among the other samples, indicating the efficient electron/hole separation. These results were in agreement with the photocatalytic H₂ evolution experiments.

Another strategy to achieve higher photocatalytic performances is coupling to different Nb₂O₅ compounds with special attributes to create an efficient heterostructured photocatalyst. Owing to its flexibility in morphological, electronic, and structural properties, Nb₂O₅ is a promising candidate to design an effective heterojunction. Huang and coauthors reported a synergic combination of highly ordered mesoporous Nb₂O₅ (MNb) nanostructure to two-dimensional N-doped graphene (NGR) through a good interfacial connection (Figure 3)²⁸. UV-vis diffuse reflectance spectroscopy evidenced gradual shifts to longer wavelengths as the NGR quantity was increased, so the band gap energies were shift from 3.12 eV up to 2.67 eV. Photoluminescence analysis suggested that NGR supported an efficient separation of charge carriers due to the fast electron transfer from the conduction band (CB) of MNb to NGR sheets.

Huang and coauthors reported an in-situ growth of mesoporous Nb₂O₅ microspheres on the surface of g-C₃N₄²¹. In this case, assuming the photocatalytic activity of g-C₃N₄ under visible light, the enhanced photoactivity was mainly achieved due to the effective interfacial charge transfer between g-C₃N₄ and Nb₂O₅. Therefore, it is mandatory to ensure sufficient interfacial contact, and this condition was succeeded by the authors via a so-called in-situ self-assembly process of synthesis. The introduction of Nb₂O₅ microspheres on g-C₃N₄ caused an expressive enhancement on the specific surface area. UV-visible diffuse reflectance spectroscopy showed that g-C₃N₄ and the composites presented an absorption edge at ca. 450 nm, while pure Nb₂O₅ had slight a band edge of ca. 420 nm. The slightly visible light absorption of Nb₂O₅ was justified by traces of

carbonate species from the thermal decomposition of the triblock copolymer used in the synthesis. Photoluminescence spectroscopy evidenced that pure $g\text{-C}_3\text{N}_4$ exhibits stronger emission than the composites. Photocatalytic activities for H_2 evolution over the samples were evaluated and the composite with 38.1 wt% of Nb_2O_5 exhibited the highest H_2 evolution rate. With higher amounts of the Nb_2O_5 (69.6 wt%), the photocatalytic performance was still higher than pure $g\text{-C}_3\text{N}_4$, but slightly decreased in relation to the composite with 38.1 wt% of Nb_2O_5 . This fact could be related to a less effective interfacial contact between the two semiconductors and to a considerable reduction of light absorption by the composite. Other successful combinations between Nb_2O_5 and $g\text{-C}_3\text{N}_4$ are reported elsewhere^{29,30}

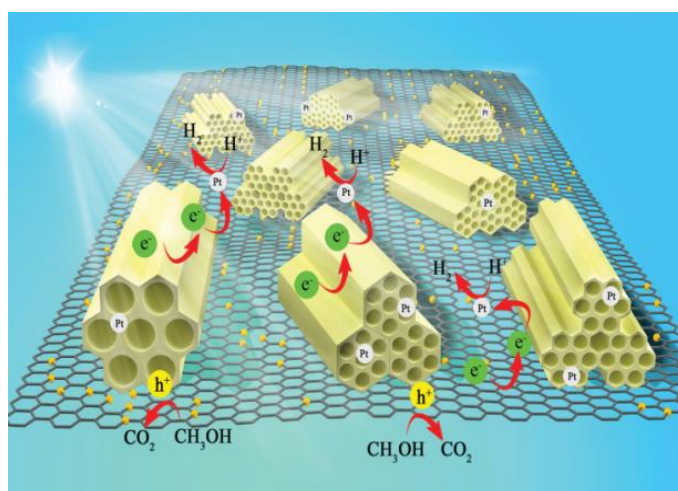


Figure 3 - Schematic illustration of the transfer of photoexcited electrons and production of H_2 photocatalyzed by MNb-N -doped graphene (NGR) under visible light. Reproduced with permission from 28. Copyright (2019), The Royal Society of Chemistry, London, United Kingdom.

Therefore, it can be observed that Nb_2O_5 pristine or modified has been employed successfully as photocatalyst for H_2 evolution. The role of crystalline phase, morphology/shape, defects/oxygen vacancies, and heterojunction formation were investigated and showed great contribution for H_2 evolution activity of Nb_2O_5 .

2.4.2. Niobium Layered Compounds

Layered niobates are composed by a repetition of $[\text{NbO}_6]$ octahedral units connected through adjacent or opposite sharing edges or corners, resulting in an extended 2D layered arrangement. This configuration is built by the stacking of negative charged

layers separated by cations in the interlayer space ^{11,31}. The first niobate phases were reported in 1955 by Reisman and Frederic ³². In this work, they could investigate the products K_3NbO_4 , $KNbO_3$, $K_4Nb_6O_{17}$, KNb_3O_8 , and “ $K_6Nb_{44}O_{113}$ ” from the reaction of K_2CO_3 and Nb_2O_5 by differential thermal analysis ^{32,33}. Then, in 1969, the $K_4Nb_6O_{17}$ and KNb_3O_8 crystals were further investigated by Nassau and coauthors ³³. In 1982, a new series of phases $MCa_2Nb_3O_{10}$ ($M = Li, Na, K, Rb, Cs, NH_4, Tl$) was reported by Dion et al. ³⁴. Similarly, some years later, Jacobson and coauthors were able to prepare and investigate the interlayer reactivity of the series of layered compounds $K[Ca_2Na_{n-3}Nb_nO_{3n+1}]$ ³⁵. Since then, a class of layered perovskite with general formula $A_x[B_{m-1}Nb_nO_{3n+1}]$ is known as Dion-Jacobson compounds (where A represents an alkaline monocation; B an alkaline earth ion; $m = 1, 2$ and $2 \leq n \leq 7$; n indicates the number of $[NbO_6]$ chains that form each perovskite-like slab) ¹¹. Moreover, plenty of different niobates are currently known such as alkali (M^+NbO_3), columbite ($M^{2+}Nb_2O_6$) and rare-earths orthoniobates ($YNbO_4$) ⁶.

These materials are known as promising photocatalysts not just due to their different structures and band gap energies, but also to their extended 2D layered arrangement, which provides a considerable surface area and allows easy modification either by intercalation, superficial modification, or formation of nanosheets and nanoscrolls through exfoliation with bulky n-alkylammonium salts ^{11,31,36}. Recently, our group investigated the influence of the medium, co-catalyst precursor, and the heat treatment in the photoactivity of Pt-modified hexaniobate ($K_{4-x}H_xNb_6O_{17}$) for H_2 evolution ³¹. The effect of Pt^0 precursor and the deposition method (absorption or impregnation) was also investigated. These different conditions of the samples preparation affected mainly their configuration and morphology. At the end, the H_2 evolution performance was dependent of those conditions, where a 'soft' photoreduction of platinum precursors was identified as the best method for preparation of those photocatalysts.

Suspended hexaniobate layers ($K_{4-x}H_xNb_6O_{17}$) in TBAOH showed a good performance to design photocatalytic film through the layer-by-layer (LbL) deposition technique ³⁶. Thin films were assembled by alternative immersions of FTO substrate into exfoliated hexaniobate with pre-adsorbed $[Pt(NH_3)_4]^{2+}$ suspension (pH = 8) and poly(allylamine hydrochloride) solution (pH = 4) up to 25 bilayers. Further thermal treatment at 500 °C removed the organic species leading to a fuzzy assembly of hexaniobate nanoscrolls with Pt evenly distributed in the surface as shown in the FE-SEM

image (Figure 4). In this case, it could be concluded that the scrolled morphology was favored in relation to the opened sheets. The Nb-based films were photoactive to produce H₂ from 20% (v/v) methanol/water solutions under UV-irradiation. The bare hexaniobate LbL films were able to photocatalyze the H₂ evolution, with the apparent quantum yield being proportional to the number of deposited bilayers. This behavior evidenced that no photocatalytic surface is lost due to material deposition. Moreover, when the Pt nanoclusters are added to the film composition, the observed H₂ evolution rates are approx. two times higher, reaching $4.0 \pm 0.5\%$.

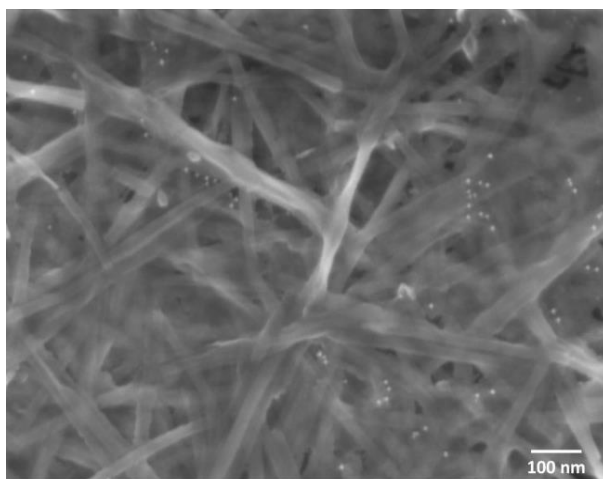


Figure 4 - FE-SEM image of the surface of Pt-modified hexaniobate layer-by-layer (LbL) films with 25 bilayers (the bright small spots are Pt nanoclusters). Reproduced with permission from 36. Copyright (2019), Elsevier, Amsterdam, Netherlands.

Oshima and coauthors reported the photocatalytic activity of Pt-deposited $\text{KCa}_2\text{Nb}_3\text{O}_{10}$ for water splitting³⁷. With an adsorption method, cationic precursor of Pt ($[\text{Pt}(\text{NH}_3)_4]\text{Cl}_2$) was attached on niobate surface (1.3 wt%) by the $\text{TBA}^+/\text{Ca}_2\text{Nb}_3\text{O}_{10}^-$ suspension, followed by restacking with KOH and reduction with H₂ gas in various temperatures. The authors noted that the deposition of Pt occurred in the interlayer spaces of the restacked nanosheets. Additionally, the increase in the annealing temperature up to 973 K, decrease the Pt content in the $\text{KCa}_2\text{Nb}_3\text{O}_{10}$ interlayer space. Diffuse reflectance and X-ray photoelectron spectroscopies suggested that the adsorbed Pt was reduced from an oxidized to the metallic state according to the applied temperature, and that interlayer Pt species were less susceptible to reduction. The samples were evaluated for water splitting in NaI 10 mmol L⁻¹ solution and using a 300 W xenon lamp ($\lambda \geq 300$ nm). The maximum rate of both H₂ and O₂ production was achieved with the sample treated at 473 K, and higher reduction temperatures led to a decline in the photoactivity. This fact could

be explained by an improved contact between Pt and the niobate and the formation of suitable active sites. At higher temperatures, the Pt species were located mostly at external surface. The authors also investigated the impact of Pt valence state on water splitting activity, comparing the performance of samples heated at the 573 K under H₂ and air atmosphere. By TEM, both methodologies led to the formation of Pt with same size. However, more electron-deficient Pt species were identified on the sample treated in air, which performed a better overall water splitting reaction than the sample treated at H₂.

Distinct species to form the layered Dion-Jacobson materials AB₂Nb₃O₁₀ plays also an essential role in the physical properties of the material and especially in their photocatalytic performance. From this point of view, Kulischow et al. investigated a family of layered Dion-Jacobson perovskite type materials AB₂Nb₃O₁₀ (A = K, Rb, Cs and B = Ca, Sr, Ba) and their photocatalytic activity for hydrogen production³⁸. Seven different niobate were prepared by molten salt method mixing BCO₃ or B(NO₃)₂, (B = Ca, Sr, Ba), Nb₂O₅, A₂CO₃ with ACl (A = K, Rb, Cs) and at specific reaction temperatures (750 – 1200 °C). UV-vis diffuse reflectance revealed that the band gap energies varied only with different B-cations seeming to be independent of A-cations. In the case of Ca²⁺ as B-cation, the band gap value was 3.6 eV, whereas it was 3.3 eV for Sr²⁺ and 3.0 eV for Ba²⁺. This trend suggested a dependence on the ionic radii of the B-cations that filled the spaces among NbO₆ octahedral units. With bigger B-cation, the overlap of the Nb 4d orbitals was greater, stabilizing the conduction band energy and, as a result the band was shifted negatively. The prepared niobates were evaluated for H₂ evolution in 10% methanol aqueous solution without a co-catalyst, and then Rh was in-situ photodeposited (0.05 wt% Rh loading) on the catalyst. Without co-catalyst, the KCa₂Nb₃O₁₀ sample exhibited the highest H₂ evolution rate, however, after the Rh addition, the highest overall hydrogen production was achieved by CsCa₂Nb₃O₁₀. In this case, photocatalytic behavior was influenced by the type of the A-cation at the interlayer, suggesting a dependence on the ionic radii in the order Cs > Rb > K, with the exception of RbSr₂Nb₃O₁₀. The B-cation influenced the hydrogen generation rates due to more cathodic conduction band edges in the order Ca > Sr > Ba.

Zhou and coauthors showed that the performance of KCa₂Nb₃O₁₀ for H₂ evolution could be enhanced through a nitrogen and tetravalent niobium doping to generate yellow and black [Ca₂Nb₃O₁₀]⁻ nanosheets³⁹. After the preparation of KCa₂Nb₃O₁₀ by solid state reaction, the material was treated at 800 °C for 5 h under NH₃ flow, resulting in the black niobate (N⁻/Nb⁴⁺-codoped). The previous addition of a certain stoichiometric excess of

K_2CO_3 prevented the formation of oxygen defect, and thus the reduction of Nb^{5+} ions, which resulted in the yellow niobate (N-doped). Then, the samples were acid-exchanged followed by the exfoliation reaction with tetrabutylammonium hydroxide (TBAOH). X-ray Absorption Fine Structure (XAFS) data on the Nb K-edge (18.986 keV) of all the samples indicate that doping did not change the perovskite-type crystal structure since all the three samples showed very similar overall profiles. However, an increase of the pre-edge peak (18.985 keV) of black niobate could be attributed to the partially reduction from Nb^{5+} to Nb^{4+} and the increased Nb–N bonding for yellow niobate, whereas the black one, showing a simultaneous decrease of both Nb–O and Nb–N, could point out the dominating generation of oxygen vacancies during the ammoniation process without K_2CO_3 additive. The samples were evaluated for photocatalytic H_2 production using 20 vol% methanol aqueous solution under full range irradiation with an Xe lamp. Undoped nanosheets show very low photocatalytic activity (11.4 mmol h^{-1}) comparing to the activity of yellow and black niobate nanosheets (42.9 and $154.7 \text{ mmol h}^{-1}$, respectively). In this sense, the self-doping with Nb^{4+} could significantly promote an enhanced separation efficiency of photogenerated carriers and also the light absorption beyond single N^{3-} doping. When Pt was loaded at 0.5 wt%, the H_2 evolution rates were three times higher, 190.1 and $429.5 \text{ mmol h}^{-1}$ for yellow and black niobate nanosheets, respectively. The last one could achieve energy conversion efficiency for solar hydrogen production of 2.7%.

Later, the same group could also investigate the combination of elemental doping, liquid exfoliation, and composition control for a series of typical Dion-Jacobson phases $\text{KCa}_2\text{Na}_{n-3}\text{Nb}_n\text{O}_{3n+1}$ photocatalysts⁴⁰. As the scheme presented at Figure 5, $\text{KCa}_2\text{Na}_{n-3}\text{Nb}_n\text{O}_{3n+1}$ were prepared with various values of n in order to tune the thickness of the perovskite layer. Theoretically, using $n = 3-6$ the desired thickness of the layer should increase from 2.4 to 4.0 nm. The materials were obtained from the molar ratio of $\text{K/Na/Ca/Nb}=1.05/2/1.05(n-3)/n$ through calcination at $1200 \text{ }^\circ\text{C}$, followed by the N/Nb^{4+} -doping via heat treatment under NH_3 flow. This method resulted in samples with different colors, varying from white to black. Samples before and after NH_3 treatment were analyzed by UV-vis diffuse reflectance where red-shifts of the absorption edge were observed in all N/Nb^{4+} doped samples. Even after liquid exfoliation of bulk doped samples to obtain nanosheets, their suspension in water kept the colors from the bulk materials. TEM and atomic force microscopy (AFM) images revealed ultrathin sheets with several micrometers in size and thicknesses of 2.4, 2.8, 3.3 and 4.0 nm for the $n = 3,$

4, 5, and 6 homologues, respectively. The photocatalytic performance of the doped nanosheets was evaluated towards hydrogen evolution from 20 vol% methanol solution under full arc irradiation (Xe lamp, 300 W). Considering all samples with and without 0.5 wt% Pt, the $n = 4$ product exhibited the highest H_2 production rate. This fact can be related to the migration length, which affects the electron-hole separation step. The higher photocurrent measurement was also found for $n = 4$ with a sequence of $n = 4 > 5 > 3 > 6$, which is consistent of H_2 evolution experiments.

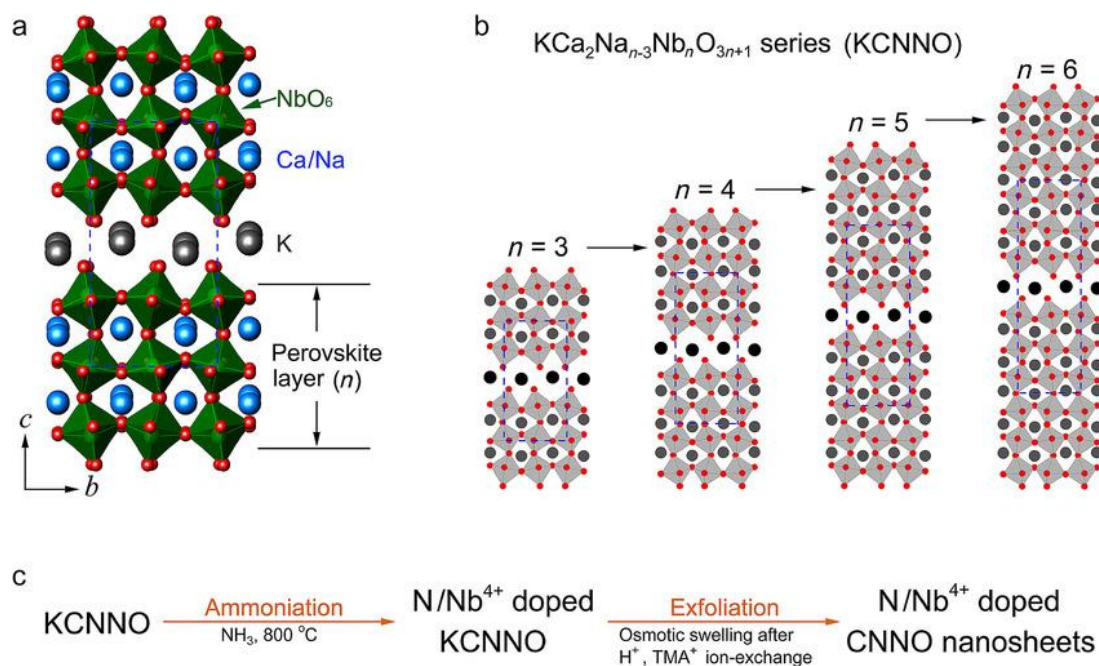


Figure 5 - Schematic representation of (a) general structure of $KCa_2Nb_3O_{10}$ (KCNNO), (b) $KCa_2NaN_{n-3}Nb_nO_{3n+1}$ with thickness control of the perovskite layer by varying the n value and (c) preparation of N/Nb^{4+} codoped nanosheets (CNNO). Reproduced with permission from 40. Copyright (2019), John Wiley & Sons, Inc., Hoboken, NJ, USA.

The photocatalytic activity of $HCa_2Nb_3O_{10}$ for hydrogen production was also extended for visible irradiation region by combination with CdS⁴¹. In this composite, after light excitation of CdS, the photo-generated electrons were transferred to the calcium niobate nanosheets due to their matched conduction band position of -1.32 eV for CdS and -1.18 eV for niobate (V vs. Ag/AgCl, pH = 7.0). So, the observed increase of the EPR signal after illumination is due to the efficient electron transfer that further induced the growth of oxygen vacancies. The samples were evaluated for photocatalytic H_2 evolution in (0.1 M) SO_3^{2-} / (0.15 M) S^{2-} solution under visible light in which the exfoliated niobate was not able to be excited. The best performance was achieved by samples containing 53.6 wt% of CdS with a H_2 production rate of $16.5 \mu\text{mol h}^{-1}$, about 4

times higher than pure CdS. Further increase of CdS resulted in lower activity, which was related to the aggregation of CdS nanoparticles. Later, a similar approach was applied by Hu and coauthors to design nanohybrid of CdS and $\text{HCa}_2\text{Nb}_3\text{O}_{10}$ and get photocatalytic H_2 production under visible light⁴². It has been shown that CdS has more negative conduction band energy than that of the employed niobate indicating the spontaneous transfer of photoinduced electrons from CdS to niobate nanosheets.

Xiong and coauthors could improve the photocatalytic hydrogen production activity of HNb_3O_8 nanosheets by loading Cu with a facile photodeposition method⁴³. Exfoliated HNb_3O_8 niobate was dispersed in Cu^{2+} solutions with corresponding loadings of 2%, 1%, 0.5%, and 0.25% which was photodeposited *in situ* in triethanolamine solution. Firstly, the authors evaluated the samples for H_2 evolution activity with 10 vol% of triethanolamine aqueous solution under the simulated solar light using a 300 W Xenon lamp. The photocatalytic performance increased after addition of Cu^{2+} up to 0.5% reaching the maximum rate of $59.1 \mu\text{mol h}^{-1}$. With higher amounts of Cu, the shielding effect was detrimental for the photoactivity. In addition, when methanol was used as the sacrificial agent, the photocatalytic hydrogen production activity achieved the value of $98.2 \mu\text{mol h}^{-1}$. The authors argued that *in situ* photodeposition induced selective deposition on the photocatalytic reduction sites of HNb_3O_8 nanosheets rather than arbitrary distribution.

The same type of niobate was recently applied to engineer a stable nanocomposite photocatalyst. Xia and coauthors reported a method to growth NiS in a highly dispersive way on HNb_3O_8 surface⁴⁴. In general, the random deposition and easy agglomeration in large particles of NiS are described as a problematic for the photocatalytic H_2 evolution. Therefore, an electrostatic adsorption/self-assembly methodology was developed to obtain NiS on HNb_3O_8 nanosheet as an efficient photocatalyst for the first time. The photocatalytic H_2 evolution was performed with a 300 W Xenon lamp in a 10% triethanolamine (TEOA) aqueous solution, where the bare NiS and layered KNb_3O_8 showed no or very low H_2 production. In this condition, for the composite with 1 wt% NiS, the H_2 evolution rate was $1519.4 \mu\text{mol g}^{-1} \text{h}^{-1}$, higher than the physical mixture of the components ($582.5 \mu\text{mol g}^{-1} \text{h}^{-1}$). Time-resolved fluorescence decay analysis was applied to calculate the lifetime of the photogenerated electrons and holes. The kinetic data showed a slower decay for the composite, which indicate that the applied methodology resulted in more efficient utilization of photogenerated electrons and holes.

The potential of niobates structures for water splitting also have been demonstrated by some theoretical works. The perovskite-type niobate NaNbO_3 was selected by Wang and coauthors to investigate the effect of anionic monodoping with N, C, P, and S dopants, as well as with (N + N), (C + S), and (N + P) codoping pairs by hybrid density functional theory calculations⁴⁵. At first, the direct band gap of pure cubic NaNbO_3 was predicted to be 3.30 eV, with conduction band mainly formed by Nb-4d orbitals and valence band by the O-2p orbitals, and almost no Na related states around the band edge were found, indicating that the Na atoms has negligible effects on the electronic structures near the Fermi level. In this sense, one of O atoms in the cell was firstly substitute by one of four different species (N, C, P, and S), corresponding to doping concentration of 2.5%. In case of N-doped NaNbO_3 , a hole would be generated as the N dopant has less valence electrons than O atom. The higher energy of N-2p states (around 2.0 eV) induced a localized unoccupied impurity state above the Fermi level and several occupied impurity states also around the valence band of NaNbO_3 . For C doping, the substitution would result in two holes in the system, however, no unoccupied localized impurity states was found above the Fermi level. As a result, the total magnetic moment was higher and there were several impurity states above the valence band which shifted up of about 1.58 eV. The doping with P resulted in a spin-polarized ground state as well, and, owing to the P-3p higher energy than the O-2p, several empty impurity states were found near the conductive band. When S was applied as a dopant, no empty states were found within the band gap, but several localized impurity states was localized below the Fermi level, right above the valence band of the niobate, which resulted in a narrowed band gap. This filled impurity states originated from the hybridization of S-3p and O-2p orbitals. Thus, the band gap values for N-, C-, P-, and S-doped NaNbO_3 were calculated to be 1.88, 1.61, 1.04, and 2.34 eV, respectively. Despite the narrower band gap energies, some disadvantages were observed as the undesirable empty gap states from N and P monodoping, which may act as trapping and recombination centers, and the elevated valence band of NaNbO_3 after C doping, precluding the oxygen evolution reaction. In this sense, the codoping possibility using pairs of (N + N), (C + S), and (N + P) was also investigated. It resulted in the band values as showed in Figure 6. In comparison to the pristine niobate, for (N + N) codoping, two fully filled states were generated within the band gap and its effective energy was 1.24 eV lower. The (C + S) doping led to mid-gap states above the valence band of host system, and then a narrow band gap of 1.42 eV. For both systems, the band edges matched properly with the redox potentials of water, indicating that the photocatalyst would be

suitable for overall photocatalytic water splitting. However, in the case of (C + S) codoping, the conductive band showed to be no longer good for a spontaneous water splitting process even with a band gap value about 1.33 eV. This study suggested that codoping can be a successful approach to improve the visible light photocatalytic performance of perovskite NaNbO_3 .

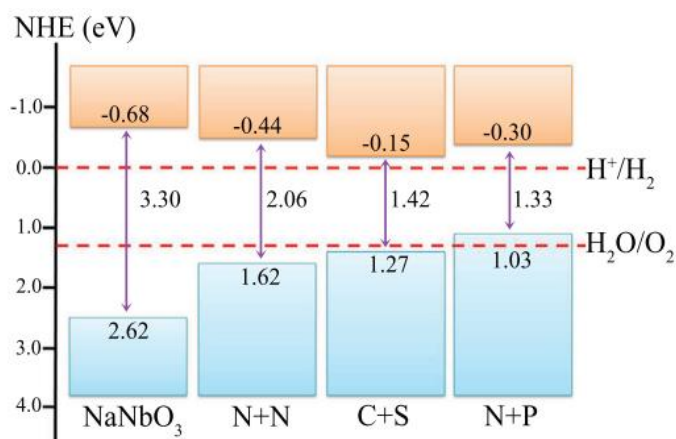


Figure 6 - Band edge positions of the pure and codoped NaNbO_3 . Reproduced with permission from 45. Copyright (2019), John Wiley & Sons, Inc., Hoboken, NJ, USA. NHE, normal hydrogen electrode.

Kaneko and coauthors deeply investigated the origin of the visible light absorption and the optical band gap of 1.9 eV in the d1 metallic strontium niobate (SrNbO_3)⁴⁶. By computational methods, firstly, they could verify which electronic states the photoexcitation takes place, from $\text{CB} \rightarrow \text{B}_1$ transition or $\text{B}_{-1} \rightarrow \text{CB}$ (B_{-1} denotes the band below the conductive band (CB), and B_1 , the band above the conductive band). By the band structures and projected density of states calculations, it was found that B_{-1} state lies at around -4 eV and consists of O(p). Thus, from the atomic orbitals constituting each band, it was inferred that the optical gap corresponds to the $\text{Nb(d)} \rightarrow \text{Sr(d)}/\text{Nb(d)}$ transition, and so the optical gap was attributed to the $\text{CB} \rightarrow \text{B}_1$ transition. The shifts of Fermi level and also the changes in the optical gap concerning the Sr defects and O vacancies were investigated. The authors could conclude that the optical gap hardly depends on the amount of Sr defects. Sr and O are divalent cation and divalent anion, respectively, and the valence of the Nb ion constituting CB did not change even if the Sr defect and the O vacancy were produced in the same amount. Thus, if the valence of the Nb ions constituting CB does not change, the Fermi level will not shift either. Consequently, the optical gap, which is mainly caused by the excitation from the Fermi

level to B_1 , does not change by $Sr_{1-x}NbO_{3-x}$. In addition, in the case of $Sr_{0.875}NbO_3$ and $Sr_{0.875}NbO_{2.875}$, it was found that the latter evidenced the dependence of the optical gap on the amount of Sr defects and its light absorption intensity was larger than that of the former.

Such doped niobates have been prepared and evaluated as photocatalysts. Yu et al. reported at first time the performance of carbon-doped $KNbO_3$ and also the effect of MoS_2 addition in the material for photocatalytic H_2 evolution⁴⁷. Both pristine and C-doped $KNbO_3$ presented the orthorhombic phase, however, the latter resulted in peaks of $30-32^\circ$ shifted to lower angle, indicating that carbon atom was doped into the lattice of $KNbO_3$. In addition, the C species were identified as C^{4+} by XPS analysis which meant that it did not replace the position of lattice oxygen. In addition, it was also confirmed that the substitution of Nb^{5+} by C^{4+} occurred and also generated some oxygen vacancies to compensate the charge balance. The pristine niobate showed only UV light absorption with band gap of 3.07 eV. C-doped niobate presented very similar behavior, however, it showed a difference in the peak tailing in the range of 400-600 nm. The samples after the addition of MoS_2 in 0.2 wt% also presented the peak tailing in the visible-light region. H_2 evolution was performed in methanol solution (20% v/v) under 300 W Xe lamp irradiation and *in situ* photodeposition of metallic Pt (0.37 wt%). The C doping of $KNbO_3$ could enhance the H_2 evolution from $5 \mu mol g^{-1} h^{-1}$ to $142 \mu mol g^{-1} h^{-1}$ in comparison to the pristine sample. The decoration of MoS_2 on C- $KNbO_3$ could further increase the rate of H_2 evolution to $1300 \mu mol g^{-1} h^{-1}$. The samples were also evaluated under visible light; where pure niobate did not show activity, while C- $KNbO_3$ and $MoS_2/C-KNbO_3$ resulted in rates of $4.2 \mu mol g^{-1} h^{-1}$ and $9.3 \mu mol g^{-1} h^{-1}$, respectively. These activities were much lower compared with values under UV-vis light, indicating that the composite is more suitable for working in the UV region of irradiation.

Columbites are also founded in the literature to further application in photocatalytic research. The effect of structural distortion of $SnNb_xO_y$ in comparison to the crystalline $SnNb_2O_6$ regarding the photocatalytic activity was investigated by Huang et al⁴⁸. The crystalline sample exhibits a band gap energy of 2.10 eV, while the band gap energies for disordered and amorphous samples were 2.33 eV and 2.43 eV, respectively. Furthermore, the electronic band gap could be tuned by the structural disorder engineering since an increase of structural lattice disorder led to an increase of band gap energies. By XPS and UV-vis absorption analysis, the valence band edge of crystalline $SnNb_2O_6$ was about 1.42 V and conduction band of -0.68 V, whereas for the disordered sample the values were

1.98 V and -0.35 V, respectively. As a consequence, the latter exhibited H₂ evolution rate 11 times and 1.7 times higher than that of crystalline and amorphous samples under visible light irradiation ($\lambda \geq 420$ nm). The photoinduced charge carrier behaviors under pulse laser at 532 nm were investigated by transient absorption spectroscopy (TAS). The three samples presented broad and continuous absorption in the visible range at a delay time of 100 ns, indicating the separation of charge carries at different trap states. This behavior was especially pronounced in disordered SbNb_xO_y, which indicated a better charge separation. The transient absorption decay kinetics also expressed the same, with effective lifetime for the amorphous, disordered and crystalline samples of 0.52 ms, 0.56 ms and 0.26 ms.

The influence of type of polymorph on the photocatalytic activity of CuNb₂O₆ columbite was further explored by Kamimura et al ⁴⁹. Two different polymorphs, monoclinic and orthorhombic, revealed that the local crystal structure of the CuO₆ octahedral was strongly correlated to the optical absorption property. Both samples exhibited the same band gap, 2.7 eV. However, two additional broad bands in the near-infrared (NIR) region were observed for the orthorhombic sample, being ascribed to Cu²⁺ d-d transitions in a distorted octahedral ligand field. In principle, this transition is forbidden by the Laporte selection rule owing to the symmetric CuO₆, but in case of orthorhombic phase, it was partially allowed because of Jahn-Teller effects of orthorhombic CuNb₂O₆. The photocatalytic H₂ evolution was performed using a 10 vol% methanol solution and an Air Mass (AM) 1.5G solar light irradiation. The two polymorphs of CuNb₂O₆ produced H₂ under these conditions, but the monoclinic sample was more active than the orthorhombic one. Thus, to elucidate if the d-d absorption affects the photocatalytic activity, the previous results were compared with that using a near-infrared (NIR) cutoff filter. When the monoclinic sample was tested, the rate of H₂ evolution rate did not change expressively when the NIR filter was applied. In this case, the loss of 20% of activity could be explained by the by low transmittance of the employed cutoff filter in the visible region. In contrast, the activity for orthorhombic CuNb₂O₆ decreased 90% in relation to that observed without NIR filter. On contrary to the monoclinic phase, which was insensitive to the excitation of the d-d transition in Cu²⁺ ions, for orthorhombic one, the electron 3d⁹ configuration of Cu²⁺ readily induces structural distortion by Jahn-Teller effects in an octahedral crystal field. The empty 3d orbitals of Cu²⁺ could work as deep traps for the photo-generated electrons and thus increase the recombination rate, resulting in a significant decrease in photocatalytic

activity in the presence of an NIR cut-off filter. With NIR photons, the photo-generated electrons filled 3d orbitals of Cu^{2+} via d-d absorption, a state that inhibited the recombination of photogenerated electrons in the conduction band. These distinct mechanisms were schematically represented on Figure 7. So, in the case of orthorhombic structure, the photocatalytic performance was dependent on fully filled Cu 3d-orbitals.

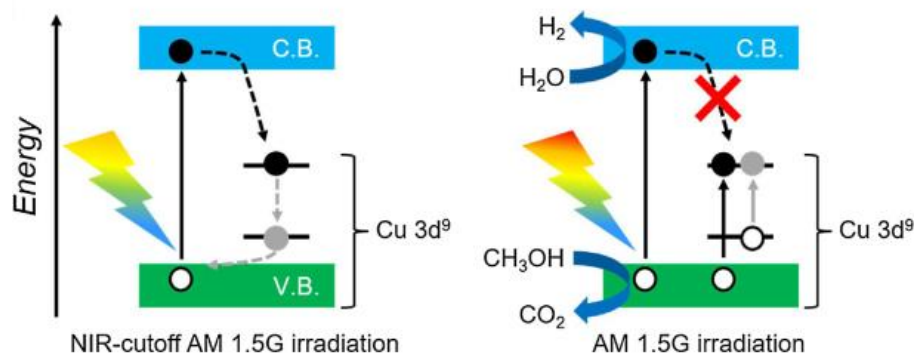


Figure 7 - Photocatalytic process over orthorhombic CuNb_2O_6 , comparing the presence and absence of (NIR)-cutoff filter. C.B. and V.B. correspond to conduction band and valence band, respectively. AM 1.5G defines the employed irradiation conditions following the ASTM G-173-03 Standard. Reproduced with permission from 49. Copyright (2019), Elsevier, Amsterdam, Netherlands.

Chun and coauthors employed a two-step hydrothermal process to form nanosized ZnNb_2O_6 columbite⁵⁰. The samples were applied to photocatalytic H_2 evolution in 20 vol% methanol under irradiation of 500 W high-pressure mercury lamp. The sample prepared by the new method produced an optimal activity of $23.6 \mu\text{mol H}_2 \text{ h}^{-1} \text{ g}^{-1}$; while a bulk ZnNb_2O_6 prepared by solid state exhibited a H_2 evolution rate of $9 \mu\text{mol h}^{-1} \text{ g}^{-1}$. This fact was attributed to its appropriate crystallinity and high specific surface area ($61 \text{ m}^2 \text{ g}^{-1}$). Further, the authors evaluated the effect co-catalyst deposition on nano- ZnNb_2O_6 . In this case, both pristine water and methanol aqueous solution media were applied. In pure water, the bare photocatalyst showed an undetectable amount of H_2 . The optimal co-catalyst was found to be Pt, as the H_2 generation rate achieved up to 680 and $3200 \mu\text{mol h}^{-1} \text{ g}^{-1}$ in pure water and methanol aqueous solution, respectively. Moreover, with the modified sample and at optimal conditions, a maximal AQY value of 4.54% was obtained in pure water. The value increase to 9.25% with the assistance of methanol as the sacrificial agent.

The manipulation of composition, morphological and surface properties of three-dimensional hierarchical $\text{Nb}_3\text{O}_7(\text{OH})$ superstructures was achieved through Ti^{4+}

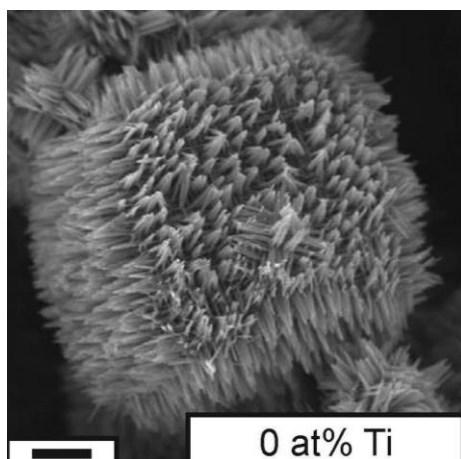
incorporation, as reported by Betzler and coauthors⁵¹. Firstly, the undoped Nb₃O₇(OH) consisted of blocks of corner-sharing NbO₆ octahedra, forming hollow cubic superstructures of nanowire networks (Figure 8(a)). When an average amount of 5.5% titanium was incorporated into the crystal lattice, it formed a spherical morphology, hollow and built up from nanowires as well (Figure 8(b)). With higher amount of Ti⁴⁺ (10.8-31.2%), a cubic morphology with smaller nanowires arranged to form the walls of hollow cubes was observed (Figure 8(c)). All the samples presented the same nanowire arrangement; however, it became smaller, shorter, and flatter as the quantity of Ti was increased. Both XRD and energy-dispersive X ray (EDX) measurements indicated a homogeneous distribution of titanium, however, with more than 12% Ti, the crystal lattice of Nb₃O₇(OH) was not able to accommodate it and then, the formation of niobium-doped anatase TiO₂ plates was favored for further titanium excess. The specific surface area was also affected and it changed from 79 m² g⁻¹ for Nb₃O₇(OH) (morphology a) to 132 m² g⁻¹ and 173 m² g⁻¹ for morphologies b and c, respectively. The three samples showed the same band gap energy of 3.2 eV, but an additional absorbance in the 550–850 nm region was observed, which came from oxygen vacancies in the TiO₂ plates. Further, the samples were evaluated to H₂ evolution under a Xe lamp irradiation (600 mW cm⁻²), with 10 vol% methanol and *in situ* photodeposited Pt at 8 wt%. The Nb₃O₇(OH) resulted a rate of 870 μmol g⁻¹ h⁻¹, and then, as the Ti concentration increase, the H₂ rates raised to 1773 μmol g⁻¹ h⁻¹ for morphology b and 1988 μmol g⁻¹ h⁻¹ for morphology c. The same trend was also expressed by transient absorption measurements, where the morphology a showed an averaged lifetime of 54 ± 2 ps, while the morphologies B and C presented lifetimes of 64 ± 2 ps and 73 ± 4 ps, respectively. The authors explained this behavior by the fewer amounts of hydroxyl groups required for charge neutrality with the replacement of Nb⁵⁺ by Ti⁴⁺, as they are known for acting as non-radiative recombination sites. The doubled H₂ production rate of morphology b, compared to morphology a, was most likely due to a combination of its fewer recombination sites and larger surface area. The further, but less pronounced increase of the H₂ production rate for morphology c came from the presence of TiO₂ plates, which did not have so strong effect on the photocatalytic reaction.

It is clearly noted that niobates offer the possibility to be combined with innumerable co-catalyst. Previous cited works and other examples from the literature are summarized on Table 1.

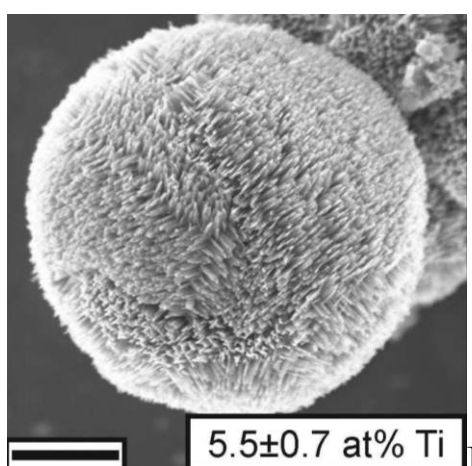
Table 1. Summary of the photocatalytic activity of niobates combined with distinct materials towards H₂ evolution from aqueous solution.

Niobate	Co-catalyst	Light source	Sacrificial reagent	H ₂ rate	Ref.
HCa ₂ Nb ₃ O ₁₀	CdS, Pt	300 W Xe, λ>400 nm	lactic acid	52.6 μmol h ⁻¹	41
HCa ₂ Nb ₃ O ₁₀	CdS	300 W Xe, λ>420 nm	methanol	450 μmol g ⁻¹ h ⁻¹	42
HNb ₃ O ₈	Cu ²⁺	300 W Xe	methanol	98.2 μmol h ⁻¹	43
HNb ₃ O ₈	NiS	300 W Xe	triethanolamine	1519.4 μmol g ⁻¹ h ⁻¹	44
C-doped KNbO ₃	MoS ₂ , Pt	300 W Xe	methanol	1300 μmol g ⁻¹ h ⁻¹	47
H _{1.78} Sr _{0.78} Bi _{0.2} 2Nb ₂ O ₇	Ni- CH ₃ CH ₂ NH ₂	300 W Xe	methanol	372.67 μmol h ⁻¹	52
KNb ₃ O ₈	g-C ₃ N ₄	1000 W Hg λ>400 nm	dimethylhydrazine	25.0 μmol g ⁻¹ h ⁻¹	53
K ₃ H ₃ Nb _{10.8} O ₃₀	g-C ₃ N ₄	1000 W Hg λ>400 nm	dimethylhydrazine	27.0 μmol g ⁻¹ h ⁻¹	53
HNb ₃ O ₈	g-C ₃ N ₄	1000 W Hg λ>400 nm	dimethylhydrazine	37.0 μmol g ⁻¹ h ⁻¹	53
Ca ₂ Nb ₂ TaO ₁₀	g-C ₃ N ₄ , Pt	300 W Xe, λ>400 nm	triethanolamine	43.54 μmol h ⁻¹	54
Ba ₅ Nb ₄ O ₁₅	g-C ₃ N ₄	3 W LEDs 420 nm	oxalic acid	2673 μmol g ⁻¹ h ⁻¹	55
AgNbO ₃	g-C ₃ N ₄ , Pt	300 W Xe, λ>420 nm	methanol	88.0 μmol g ⁻¹ h ⁻¹	56
KTa _{0.75} Nb _{0.25} O ₃	g-C ₃ N ₄ , Pt	300 W Xe λ>420 nm	methanol	86.2 μmol·g ⁻¹ ·h ⁻¹	57

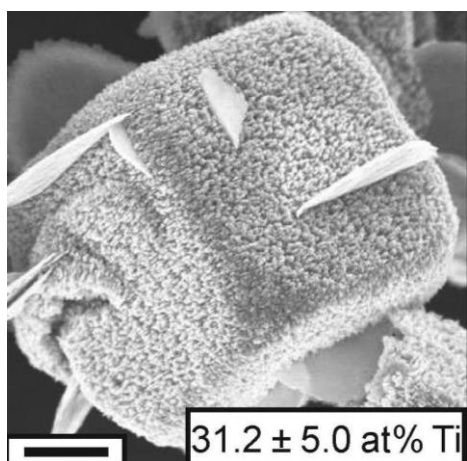
Besides the previous cited materials, niobium is also flexible in terms to design different layered compounds with distinct elements. Fujito and coauthors reported a visible light response of layered perovskite oxychloride $\text{Bi}_4\text{NbO}_8\text{Cl}$ for water splitting⁵⁸. This material consists of single-layer NbO_4 perovskite units separated by $(\text{Bi}_2\text{O}_2)_2\text{Cl}$ blocks. It presented a band gap of 2.39 eV with valence and conductive bands of 2.11 eV and -0.28 eV, respectively. Experimental and theoretical results suggested that the valence band was formed by highly dispersive O-2p orbitals coming from the interactions within and between Bi–O and Nb–O slabs. As expected from the conductive band value, $\text{Bi}_4\text{NbO}_8\text{Cl}$ showed activity for H_2 evolution from an aqueous methanol solution under UV irradiation (300 W Xe lamp) and Pt (0.5 wt%) loading. However, the obtained rate of $\sim 0.1 \mu\text{mol h}^{-1}$ was considered low and a higher performance for O_2 was found out. Apparent quantum efficiency for O_2 evolution was determined as $\sim 0.4\%$ with FeCl_3 as electron acceptor, under monochromatic light at 420 nm ($\sim 25\text{mW/cm}^2$). So, through a Z-scheme mechanism, the system was coupled to a H_2 -evolving photocatalyst of Rh-doped SrTiO_3 and $\text{Fe}^{3+}/\text{Fe}^{2+}$. In this way, as schematic shown in Figure 9, a simultaneous evolution of H_2 and O_2 under visible light was successfully observed.



(a)



(b)



(c)

Figure 8 - SEM images of (a) $\text{Nb}_3\text{O}_7(\text{OH})$ and (b), (c) Ti^{4+} modified samples with the titanium content averaged over the morphology indicated relative to niobium (scale bar of $1\ \mu\text{m}$). Reprinted with permission from 51. Copyright (2019) American Chemical Society, Washington, DC, USA.

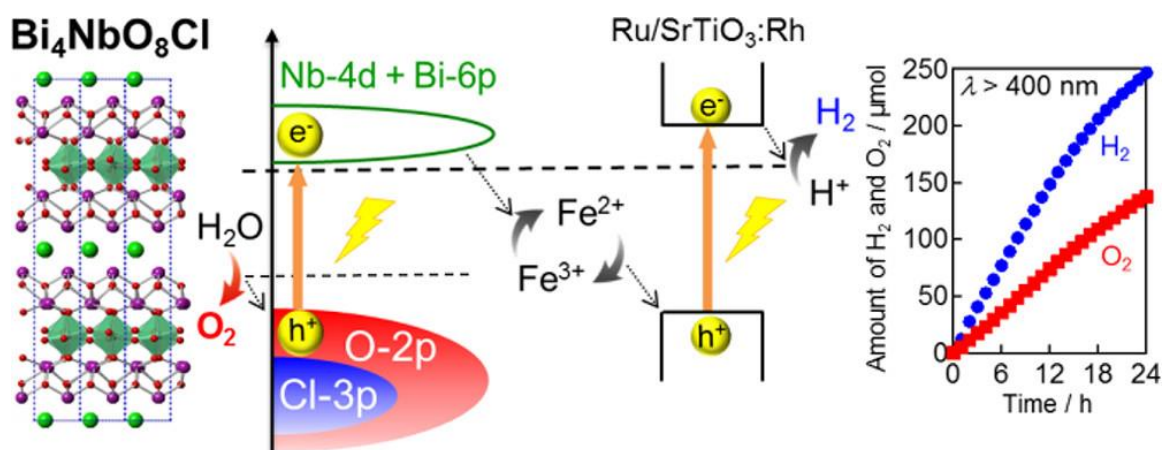


Figure 9 – Scheme of Z-scheme water splitting of $\text{Bi}_4\text{NbO}_8\text{Cl}$ coupled with $\text{Ru}/\text{SrTiO}_3:\text{Rh}$ photocatalyst via $\text{Fe}^{3+}/\text{Fe}^{2+}$ redox mediator. Reprinted with permission from 58. Copyright (2019) American Chemical Society, Washington, DC, USA.

Wakayama and coauthors reported a novel compound obtained from a mixture of layered $\text{RbNdNb}_2\text{O}_7$ and Rb_2CO_3 ⁵⁹. The new layered niobium oxynitride, $\text{Rb}_2\text{NdNb}_2\text{O}_6\text{N}$, resulted in a structure as $\text{Rb}_2\text{NdNb}_2\text{O}_6\text{N} \cdot \text{H}_2\text{O}$ composed of double-layer $[\text{NdNb}_2\text{O}_6\text{N}]^{2-}$ perovskite slabs separated by two Rb cations and one H_2O molecule. The material showed a band gap of 2.5 eV with visible light absorption whereas the precursor $\text{RbNdNb}_2\text{O}_7$ essentially absorbs UV light with band gap energy of 3.7 eV. In the former case, additional N 2p orbitals in the valence-band formation caused a valence-band maximum much more negative. In contrast, since the conduction band consist mainly of Nb 4d orbitals, its value remained basically unaffected. Thus, the H_2 evolution was evaluated in presence of TEOA as electron donor in dimethyl sulfoxide (DMSO) containing 1 mL of water. The sample was irradiated with visible light ($\lambda > 400$ nm) by 300 W xenon lamp, and Pt was previously deposited at 0.5 wt%. As shown in Figure 10, a stable H_2 evolution was observed for 20 h from $\text{Rb}_2\text{NdNb}_2\text{O}_6\text{N}$ sample, in contrast to the precursor, which did not show response under visible light irradiation.

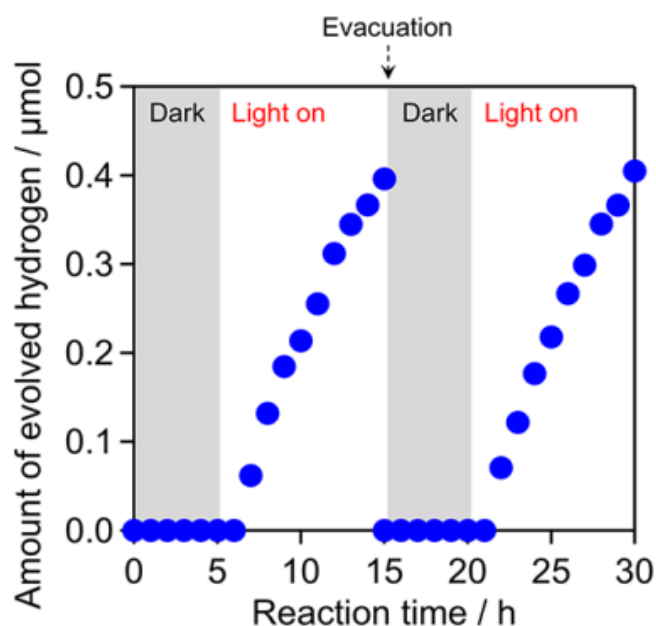


Figure 10 - H₂ evolution over Pt/Rb₂NdNb₂O₆N in DMSO/TEOA solution containing 1 mL of water. Reprinted with permission from 59. Copyright (2019) American Chemical Society, Washington, DC, USA.

Therefore, it can be observed that niobium layered compounds is a versatile Nb-based materials class that exhibit great activity for H₂ evolution reaction. Additionally, several procedures to tuning the photocatalytic performance niobium layered compounds were discussed, such as changes in the structural and morphology, doping and co-doping, combination with other semiconductors.

2.4.3. Nb-Doped Materials

Two of main drawbacks in the photocatalysis heterogeneous are the rapid recombination of electron/hole pair and semiconductor activation only under UV irradiation. A strategy to increase the photocatalytic performance of semiconductors by overcome these challenges is the introduction of impurities able to change the electronic behavior of the material, in one word, the doping. Niobium is well known in the literature as a dopant agent especially for titanium based semiconductors, since its higher charged ion can substitute Ti⁴⁺ site in the oxide structure and simultaneously act the role of donor, improving carrier concentration and conductivity⁶⁰. For TiO₂, the defect state provided by the doping is located upon the conduction band minimum and contributes electrons to the unoccupied Ti 3d orbital without introducing additional states in the bandgap. However, in order to satisfy the charge compensation, the substitution can be

accompanied by the incorporation of other defects as oxygen vacancies or even Ti^{3+} defects below the conductive band, which lead to a visible range absorption⁶¹. In Table 2, examples of Nb-doped semiconductors for H_2 evolution are listed.

Table 2. Summary of Nb-doped photocatalysts employed for H_2 evolution from aqueous solution.

Semiconductor	Co-catalyst	Light source	Sacrificial reagent	H_2 rate	Ref.
TiO_2	-	300 W Xe $\lambda > 420$ nm	ethanol	1146 $\mu\text{mol g}^{-1}$	15
TiO_2	Pd	500 W Hg-Xe 420–680 nm	methanol	~0.6 mmol $\text{g}^{-1} \text{h}^{-1}$	62
TiO_2	Pt	500 W Hg-Xe 420–680 nm	methanol	~0.1 mmol $\text{g}^{-1} \text{h}^{-1}$	62
TiS_3	-	200 W halogen	Na_2SO_3 (electrolyte)	2.2 $\mu\text{mol min}^{-1} \cdot \text{cm}^2$	63
$\text{Cu}_5\text{Ta}_{11}\text{O}_{30}$	Pt	1000 W Xe arc $\lambda > 420$ nm	methanol	6 $\mu\text{mol h}^{-1}$	64
Ta_3N_5	-	400-700 nm	water	41.4 $\mu\text{mol g}^{-1} \text{h}^{-1}$	65
KTaO_3	Pt	300 W Xe	methanol	728 $\mu\text{mol g}^{-1} \text{h}^{-1}$	66
BiVO_4		100 mW cm^{-2} Xe	NaHCO_3 (electrolyte)	0.18 mmol h^{-1}	67

The performance of Nb- TiO_2 photocatalyst was evaluated using various sacrificial agents as methanol, ethanol, and 2-propanol by Fontelles-Carceller⁶⁸. The photocatalyst was prepared with Nb/Ti ratio of 0.025:0.975, which was confirmed by XPS measurements. In principle, the presence of Nb does not change significantly the band gap (3.15 eV) or the specific surface area ($80.5 \text{ m}^2 \text{ g}^{-1}$) of the photocatalyst in comparison to pure TiO_2 (3.18 eV of band gap and $82.1 \text{ m}^2 \text{ g}^{-1}$ of surface area). The H_2 evolution was investigated by the photocatalysts loaded with 0.5 wt% of Pt in presence of 3:7 (v/v)

alcohol/water mixture under irradiation of Hg-Xe lamp (500 W). For both TiO₂ and Nb-TiO₂, the maximum rates were observed for methanol, followed by ethanol and 2-propanol. In all tested conditions, as shown in Figure 11, the doped sample showed a significant better result than the non-doped sample. Both samples presented maximum rates for methanol, followed by ethanol and 2-propanol. In addition, the products formed during the photocatalytic reaction were investigated and, for methanol and ethanol, basically the same compounds were identified. Both samples generated formic acid and methyl formate by methanol oxidation with the addition of formaldehyde for Nb doped sample under UV illumination. When ethanol was applied, in all condition of irradiation and applied samples, acetaldehyde and ethyl acetate were founded. Nevertheless, when 2-propanol was applied as sacrificial reagent, the Nb-doped sample generated acetone and propanone-diisopropyl-acetal, whereas bare TiO₂ produced only acetone. So, it was possible to affirm that the presence of Niobium at the surface even in small proportion was able to generate a new compound not observed for the pristine sample. In this sense, in-situ infrared studies were also carried out under dark and illumination conditions and in presence of the alcohol in water vapor. In principle, under the dark, it was possible to verify the adsorption of the alcohols on the surface of both samples. Under UV irradiation, the infrared spectra showed that alcohol and alkoxy species were consumed and/or desorbed from the surface of the samples. For methanol and ethanol, carboxylate/carbonate species were found as the main surface product. This could indicate the attack from hole to the alcohol to form oxidized species related to the corresponding alcohol/alkoxy adsorbed species. In case of 2-propanol, carboxylate species were less present at the surface due to the low coverage of products from the relatively easy desorption of acetone. Regarding the H₂ evolution, the authors suggested that the differences in activity are correlated quantitatively with the average oxidation potential of the alcohol. When comparing methanol with ethanol using infrared spectroscopy, they showed essentially the same behavior of the titania surfaces against the alcohol and evolving molecules coming from the hole-attack.

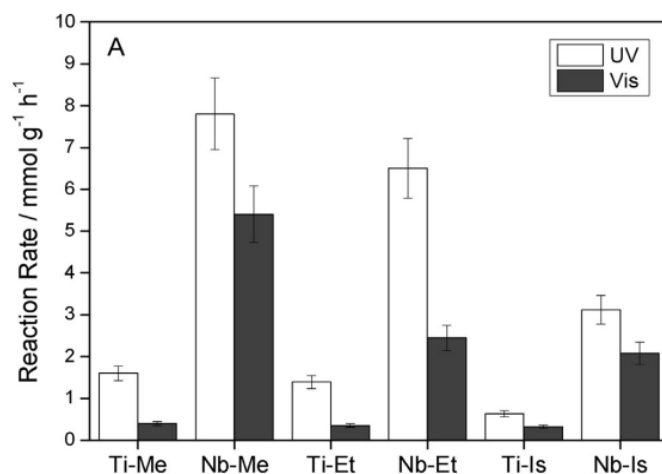


Figure 11 - Reaction rate of the H₂ photoproduction using different alcohols. Me, Et and Is stand for methanol, ethanol and 2-propanol (isopropanol), respectively. Reproduced with permission from 68. Copyright (2019), Elsevier, Amsterdam, Netherlands.

Different materials that were doped by niobium ions to make them able to split water have been reported in literature. The improvement of WO₃ for water splitting by photoelectrochemical process was achieved by Nb-doping⁶⁹. The morphology of the material turned from nanorod to nanotriangle, which also increased the porosity of the WO₃ films. Also, the band gap increased to 2.74 eV by Nb-doping in comparison to WO₃ (2.63 eV) and additional oxygen vacancies were induced. Besides that, the carrier densities significantly increased from $\sim 3.44 \times 10^{19} \text{ cm}^{-3}$ to $1.27 \times 10^{22} \text{ cm}^{-3}$, indicating that Nb⁵⁺ ions act as donor dopants in WO₃ lattice. It could improve the charge separation, electron transport, and then, the doped sample exhibited higher photocurrent, IPCE (39% to 52% at 300 nm and 1.23 V vs. RHE) and photoconversion efficiencies.

Also, with the objective to promote photoelectrochemical water splitting, niobium could support the activity of BiVO₄ films⁶⁷. In this case, the authors concluded that Nb⁵⁺ ions were not placed in the crystalline structure of BiVO₄, rather as niobium oxide or oxochloride. Firstly, the addition of 10% of Nb⁵⁺ resulted a higher IPCE, which reached 75% in comparison to pristine BiVO₄ of 55% at 2.08 V vs. RHE (380–550 nm). The H₂ evolution experiments were run by an H-shaped cell with pristine or modified BiVO₄ film as photoanode coupled with a cathode of Pt and carbon paste. After 16 h of irradiation at 2.08 V, pristine sample reached a maximum H₂ evolution rate of 0.09 mmol h⁻¹, whereas Nb-modified BiVO₄ increased about 2 times to 0.18 mmol h⁻¹. The authors argued that the higher performance of the modified sample would be related to the modification of

the nanostructure of the film, but also due to other effects not obvious by the obtained data. A high efficiency for photoelectrochemical water splitting reaction was achieved by doping of SnO₂ nanotubes (NTs) with Nb and N co-doping⁷⁰. Niobium could be ascribed as an effective dopant due to its abundant electronic states and lower ionic radii of Nb⁴⁺ (69 pm) compared to Sn⁴⁺ (71 pm), resulting in minimum lattice strain. As shown in Figure 12 (a), the addition of Nb could improve the absorption of light at lower wavelengths, suggesting a decrease in the band gap of the doped samples, with increase in Nb content. Then, a further doping with N could result in a significant decrease of band gap to 1.99 eV from 3.1 eV of (Sn_{0.95}Nb_{0.05})O₂. The lowering of the optical band gap for this sample could provide an IPCE of 10% at 500 nm and potential of ~0 V (vs RHE), which was described by the author as the highest IPCE value obtained for semiconductor materials explored so far for PEC water splitting. The generated H₂ and O₂ gases at the cathode (Pt wire) and the photoanode are shown in Figure 12 (b). The theoretical concentration of H₂ from Faraday's Law was also calculated, which was very similar to the experimental one, suggesting a Faradaic efficiency close to 100%. Besides that, the ratio of produced gases was around 2, showing a stoichiometric decomposition of water into H₂ and O₂. From these and also theoretical results, it was possible to conclude that the Nb and N co-doping in SnO₂ afford better light absorption properties, increased carrier density, and facile electrochemical charge transfer.

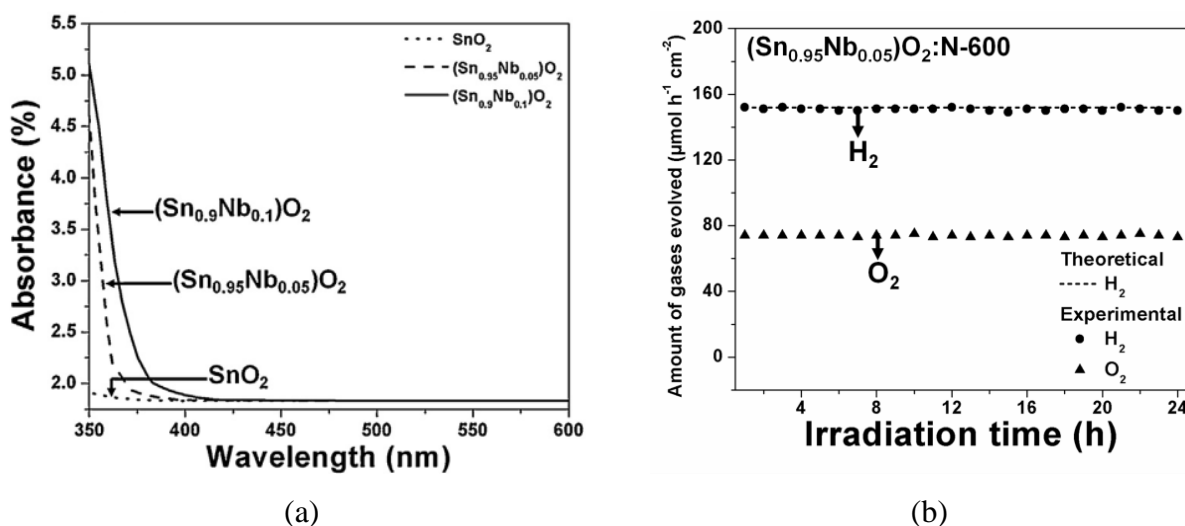


Figure 12 – (a) UV–vis absorption spectra of SnO₂ NTs and (Sn_{1-x}Nb_x)O₂ NTs (x = 0.05, 0.1) and (b) theoretical H₂ gas and measured H₂ and O₂ gases, during 24 h chronoamperometry test of (Sn_{0.95}Nb_{0.05})O₂:N performed in 0.5 M H₂SO₄ solution at 0.75 V (vs RHE) and 26 °C. Reproduced with permission from 70. Copyright (2019), Elsevier, Amsterdam, Netherlands.

2.5. Photoreduction of CO₂

Artificial Photosynthesis

Carbon dioxide (CO₂) emission from fossil fuels is the main concern when discussing global warming and related climate changes. Because the global energy demand will continue to increase, the consumption fossil fuels will continue high for the next few decades, which undoubtedly brings the necessity of large scale CO₂ mitigation from the atmosphere ⁷¹. The observation of natural photosynthesis in green plants motivated the development of photocatalytic CO₂ reduction (artificial photosynthesis), which is one promising solution to transform the current fossil fuel-based economy into a CO₂-neutral energy systems using sustainable “photon” economy and mitigate the greenhouse gas effect ^{3,72–74}. Another advantage of the photocatalytic CO₂ reduction is the indirect solar energy storage on carbon-based molecules. Therefore, the artificial photosynthesis acts as killing two birds with one stone in view of protecting the environment and simultaneously supplying renewable energy. However, CO₂ is very stable/inertness regarding chemical reactions, meaning that CO₂ conversion demands a considerable amount of energy; therefore, it is quite difficult converting it to reusable chemicals ⁷⁵.

In the beginning of 1900s Giacomo Ciamician published a seminal paper with the first idea about the artificial photosynthesis with the suggestion that society should shift from consuming fossil fuels to generating sustainable energy from the sun ⁷⁶. Later, Inoue et al. report the photoelectrocatalytic reduction of CO₂ to form organic compounds such as formic acid, formaldehyde, methyl alcohol and methane, in the presence of various semiconductors, it was demonstrated the dependence between the formed products and the semiconductor conduction band energy ⁷⁷.

The CO₂ photoreduction process is a multielectron process (2, 4, 6 or 8 electrons) that can yield diverse products and occurs through of different steps that involve adsorption, activation, and dissociation of C=O bond. The adsorption and activation step is especially challenging because CO₂ highly stable and inert ⁷⁸. In Table 3, some of the possible CO₂ reduction reactions are summarized along with their respective redox potentials. Selected potentials are compared with Nb-based photocatalysts at Figure 13. The formation of first intermediate (CO₂^{•-}) state imposes a significant energy to the reaction and is frequently identified as the rate determining step. Once CO₂^{•-} is formed,

it may be subsequently reduced via the protonation of its oxygen atom, resulting in the formation of $\cdot\text{COOH}$. This intermediate can be reduced to CO and released from the semiconductor surface. Alternatively, $\text{CO}_2^{\cdot-}$ may also be reduced via the protonation of its carbon atom to form HCOO^{\cdot} , which is further reduced to formate (HCOO^-)^{79–81}. Therefore, the CO_2 reduction mechanism is very complex and imposes kinetic and thermodynamic limitations.

Table 3. Common products from CO_2 reduction, their simplified half reaction and redox potential at $\text{pH} = 7$.

Reactions	E° (V vs RHE)
$\text{CO}_2 + 2e^- + 2\text{H}^+ \rightarrow \text{CO} + \text{H}_2\text{O}$	-0.53
$\text{CO}_2 + 2e^- + 2\text{H}^+ \rightarrow \text{HCOOH}$	-0.61
$\text{CO}_2 + 4e^- + 4\text{H}^+ \rightarrow \text{HCOH} + \text{H}_2\text{O}$	-0.48
$\text{CO}_2 + 6e^- + 6\text{H}^+ \rightarrow \text{CH}_3\text{OH} + \text{H}_2\text{O}$	-0.38
$\text{CO}_2 + 8e^- + 8\text{H}^+ \rightarrow \text{CH}_4 + 2\text{H}_2\text{O}$	-0.24

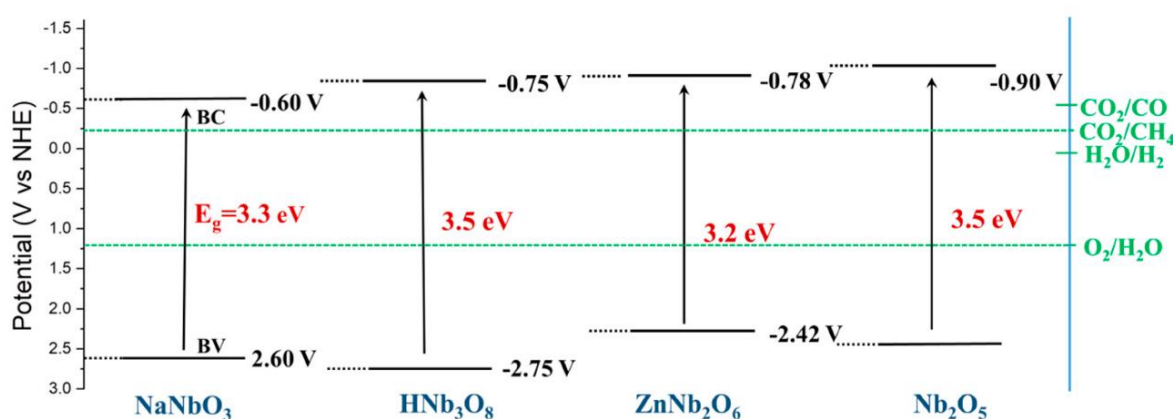


Figure 13 - Band gap (E_g) and band positions of Nb-based semiconductors vs. normal hydrogen electrode (NHE). On the right side, the standard potentials of several redox couples are presented for comparison.

The semiconductors that have been investigated for CO_2 conversion present low activity, selectivity, stability, and high band gap values, therefore challenges remain on how to make this process feasible. The CO_2 reduction reaction competes with H_2 evolution in protic media, thus efficient catalysts must exhibit high activity for CO_2 conversion with low or negligible activity for H_2 evolution. This requires a very high

activation energy barrier for H₂ evolution or a change in the reaction pathway to slow down the kinetics of H₂ formation ⁸².

Few semiconductors have been identified with high surface affinity to CO₂ and, simultaneously, with suitable electronic properties for CO₂ reduction via a photo-activated mechanism. In this sense, Nb-based materials are promising for application in the CO₂ photoreduction due to their properties, such as high acidity, excellent textural properties, and interesting electronic properties. Additionally, it is well-known that the product selectivity is significantly affected by the nanostructure design and the architecture of the photoactive components ⁸³.

Efficient CO₂ reduction involves the optimization of synthetic procedures and the development of different architectures in order to achieve the structural, electronic, morphological and surface properties required for this application. Despite that the application of Nb-based semiconductors for CO₂ photocatalytic reduction has been only recently explored, some reports have revealed the potential of these structures for artificial photosynthesis. It can be highlighted some materials, such as: alkali niobates (NaNbO₃ and KNbO₃), columbite niobates (CuNb₂O₆ and ZnNb₂O₆), niobium oxide (Nb₂O₅), niobic acid (HNb₃O₈). Additionally, Nb-based materials have been involved in some strategies were to improve the CO₂ photocatalytic reduction activity and selectivity, such as doping and formation of composites

Shi et al. ⁸⁴ evaluated the CO₂ photocatalytic performance of NaNbO₃ with different morphologies for the first time. NaNbO₃ in orthorhombic phase were prepared by a conventional solid-state reaction and hydrothermal method, with micron-sized particles and homogeneous nanowires, respectively. It was observed that NaNbO₃ decorated with Pt was efficient to convert CO₂ in CH₄, while there was almost no CH₄ to be detected over pristine NaNbO₃. Additionally, the CO₂ reduction performance of Pt-NaNbO₃ nanowires was higher than the micron-sized particles, due to higher specific surface area of Pt-NaNbO₃ nanowires.

It is well-known that the photocatalytic reaction (oxidative or reductive processes) are particularly affected by the semiconductor crystal structure ⁸⁵. Therefore, it was evaluated the CO₂ photocatalytic reduction performance of the cubic and orthorhombic NaNbO₃. The samples were obtained using inorganic and organic Nb-precursors by a furfural alcohol-derived polymerization–oxidation ⁸⁵. Both samples exhibited the same morphology features, i.e. cuboids particles with size between 30 and 50 nm, likely due to the use of poloxamers with surfactant behavior (Figure 14). The cubic Pt-NaNbO₃

presented lower band gap energy than the orthorhombic Pt-NaNbO₃. Cubic NaNbO₃ exhibited a better photocatalytic performance for H₂ evolution and CO₂ reduction for CH₄ than orthorhombic NaNbO₃, the authors attributed this behavior to its unique electronic structure which benefits the generation and migration of photo-generated electrons and holes. This behavior was confirmed for the same group in another publication⁸⁶. The authors also investigated the effect of annealing temperature in the CO₂ reduction performance, it was observed a deleterious effect with the increasing in the temperature.

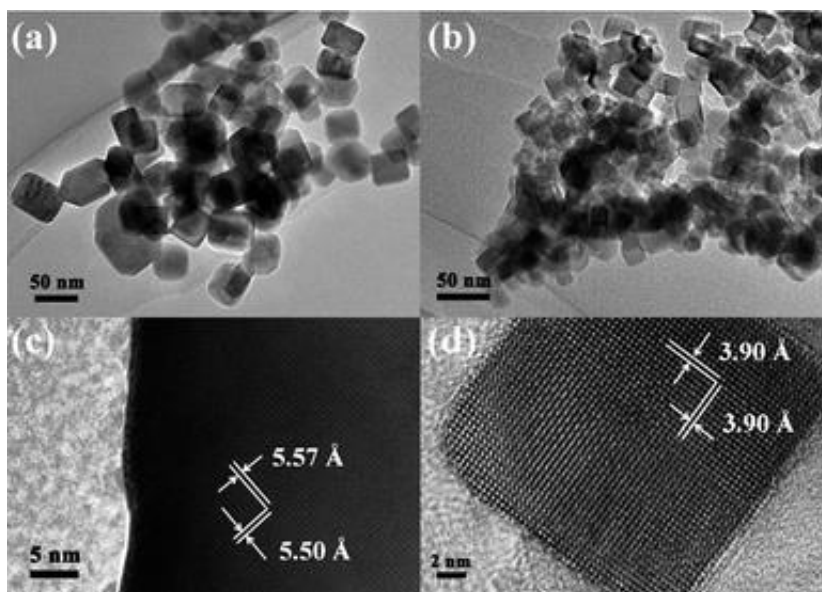


Figure 14 - TEM images of (a) NaNbO₃–cubic and (b) NaNbO₃–orthorhombic. HR-TEM of (c) NaNbO₃–orthorhombic and (d) NaNbO₃–cubic. Reproduced with permission from 85. Copyright (2019), Royal Society of Chemistry, London, United Kingdom.

On the basis of previous reports, Fresno et. al. evaluated the CO₂ photoreduction performance of NaNbO₃ obtained by solid state reaction at 900 °C and compared it with NaTaO₃ photoactivity⁸⁷. Owing to high annealing temperature, orthorhombic NaNbO₃ with low surface area was obtained (~ 1 m²g⁻¹). The main CO₂ reduction products were CO, CH₄ and CH₃OH, together with H₂ coming from the concomitant reduction of water competing with that of CO₂. It was observed that NaNbO₃ and NaTaO₃ give rise to similar conversions in the CO₂ reduction reaction. Additionally, they demonstrated that NaNbO₃ was photoactive even without co-catalyst, although the main product was CO, the authors attributed this difference in the selectivity for absence of co-catalyst (Pt)⁸⁷.

Inspired in the Degussa P25, which consists of anatase and rutile TiO₂ (*i.e.* heterostructure) and shows higher activities than either pure anatase or rutile in water splitting and gaseous pollutant photodegradation⁸⁸, Ye's group proposed the

investigation of heterojunction formation between NaNbO₃ in cubic and orthorhombic phases for CO₂ photocatalytic reduction⁸⁹. The NaNbO₃ samples were synthesized at 400 °C to 600 °C based on the polymerized complex method. Pure cubic and orthorhombic NaNbO₃ were respectively obtained at 400 and 600 °C, respectively, while the NaNbO₃ samples with mixed phases were formed at the temperature ranging from 400 to 600 °C (Figure 15 (b), (c)). Along with the phase transition from the cubic phase to the orthorhombic phase, the absorption edge of NaNbO₃ shows a slight and gradual blue shift, which is consistent with the previous report that cubic NaNbO₃ has a narrower band gap than orthorhombic NaNbO₃ (Figure 15(c)). Additionally, the presence of heterojunctions between the two phases was verified; the smaller ones less than 10 nm (cubic phase) and the bigger ones about 30 nm (orthorhombic). For CO₂ photocatalytic reduction experiment, Pt was used as co-catalyst and CH₄ was the main product. All the mixed-phase samples were more efficient in CH₄ formation than the pure phases. The authors state that the photo-excited electrons migrate from the conduction band of the orthorhombic phase to the trapping sites on the cubic surface, thus avoiding the electron–hole recombination in orthorhombic NaNbO₃ and improving the charge separation efficiency in the mixed-phase NaNbO₃ samples.

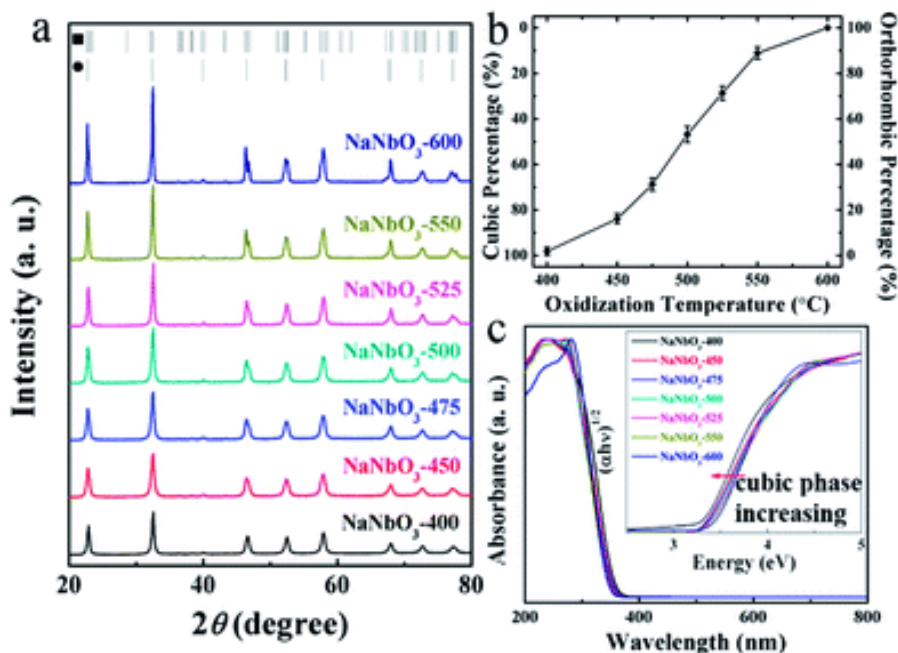


Figure 15. (a) XRD patterns of the as-prepared NaNbO₃ samples. (b) Dependence of cubic and orthorhombic NaNbO₃ contents on the annealing temperature. (c) UV-vis absorption spectra of the as-prepared NaNbO₃ samples and the inset in the figure is the corresponding $(\alpha h\nu)^{1/2} - h\nu$ curves. Reproduced with permission from 89. Copyright (2019), Royal Society of Chemistry, London, United Kingdom.

Niobates materials are also efficient photocatalysts for CO₂ photoreduction, because layered materials configuration is favorable for the separation and transportation of photo-excited carriers (*i.e.*, electrons and holes)^{90,91}. In this sense, niobic acid (HNb₃O₈) is a promising material, since exhibited the valence band and the conduction band edges at desirable potential levels. The layered structure facilitates electron transfer, and the protonic acidity is favorable for water adsorption through hydrogen bonding⁹¹. It is expected that these properties should exert certain positive impact on CO₂ photoreduction by water⁹¹.

Therefore, Li et. al.⁹² evaluated the photocatalytic CO₂ reduction performance of HNb₃O₈ obtained through two different methods, hydrothermal (HT) and solid state reaction (SSR), and compared with that of KNb₃O₈. HNb₃O₈ is isostructural with KNb₃O₈, and both samples were crystallized in an orthorhombic symmetry. The samples obtained through HT method exhibited thin nanobelts with several micrometers in length, while the samples obtained by SSR method showed containing irregular particles in micron size. The surface area value increased from 2.7 m² g⁻¹ of KNb₃O₈ (SSR) to 28.8 m² g⁻¹ of KNb₃O₈ (HT), and from 6.5 m² g⁻¹ of HNb₃O₈ (SSR) to 39.4 m² g⁻¹ of HNb₃O₈ (HT). CH₄ was the only one hydrocarbon product detected in the gas phase during CO₂ photoreduction for all samples. The rate of CH₄ formation over KNb₃O₈ (HT) was seventeen times higher than that over KNb₃O₈ (SSR), and the rate of CH₄ formation over HNb₃O₈ (HT) is about twenty times higher than that over HNb₃O₈ (SSR). Additionally, the solid acid sample (HNb₃O₈) exhibited higher activity than the corresponding potassium salt (KNb₃O₈). Also, both samples exhibited higher activity than degussa TiO₂-P25. Therefore the sample morphology, specific surface area and the protonic acidity of HNb₃O₈ play important roles in the photocatalytic reduction of CO₂ to CH₄.

In order to improve the CO₂ photocatalytic reduction performance of HNb₃O₈, the intercalation of guest components into the interlayer space was evaluated, and lamellar HNb₃O₈ was purposely pillared with silica⁹³. The pillarization of HNb₃O₈ with SiO₂ was verified by interlayer distance expanded, from 1.13 nm to 2.85 nm. Owing to the notably expanded interlayer distance, the surface area value of SiO₂-HNb₃O₈ was as large as 197.3 m² g⁻¹, in contrast to 6.5 m² g⁻¹ of the nonpillared HNb₃O₈. All of the samples were loaded with 0.4 wt% Pt by photodeposition to evaluate the CO₂ photoreduction. The yield of CH₄ over the HNb₃O₈ sample was almost three times higher than that achieved over Nb₂O₅. The improved activity for the solid acid material might be ascribed to its layered structure and the stronger adsorption ability to H₂O through hydrogen bonding. The rate

of CH₄ formation was further enhanced with SiO₂-HNb₃O₈ sample. Additionally, the activity of the current SiO₂-HNb₃O₈ photocatalyst was higher than that of previously reported HNb₃O₈ nanobelts⁹². Compared to nonpillared HNb₃O₈, the SiO₂ pillared HNb₃O₈ sample has notably expanded interlayer distance and much greater surface area. Thus, the reactive active sites at the interlayer space of SiO₂-HNb₃O₈ should be more accessible to the substrate. To investigate the role of protonic acidity for CO₂ reduction, it was compared the activity of SiO₂-HNb₃O₈, with SiO₂-KNb₃O₈ and anatase TiO₂ in different molar ratio of H₂O/CO₂ (0.06 or 0.25). The SiO₂-HNb₃O₈ sample showed higher activity than SiO₂-KNb₃O₈ and anatase TiO₂, it is noteworthy that the activity of the SiO₂-HNb₃O₈ sample enhanced more significantly than the other two samples at elevated water content. This confirms that water molecules could react easily with the protons at the interlayer space of lamellar solid acids through hydrogen bonding.

Despite columbite niobates exhibited interesting electronic properties and suitable conduction and valence band energies for CO₂ photoreduction⁶, this class of material have been few explored. Kormányos et. al. evaluated the CO₂ photoelectrochemical reduction activity of monoclinic type-p CuNb₂O₆ and orthorhombic type-n ZnNb₂O₆ semiconductors⁹⁴. The CuNb₂O₆ and ZnNb₂O₆ samples showed an indirect bandgap of 1.77 eV and 3.55 eV, respectively. The photoelectrochemical (PEC) performance of the p-CuNb₂O₆ sample was tested in CO₂- and N₂-saturated 0.1 M NaHCO₃ solution. The photocurrents are two times higher (at E = -0.4 V) when the solution was saturated with CO₂. According to the authors, the dramatic increase in the presence of CO₂ is clearly attributable to the ability of CuNb₂O₆ to photoelectrochemically reduce CO₂. However, the CuNb₂O₆ sample's efficiency and selectivity was not evaluated, since the products formed from CO₂ photoelectrochemical reduction were not monitored.

Recently, da Silva et al. investigated the role of Nb₂O₅ surface acidity for CO₂ reduction performance⁹⁵. Nb₂O₅ catalysts were prepared through a modified peroxide sol-gel method using different annealing temperatures, and it was verified that the increase in the annealing temperature decreases the surface acidity. The authors related the activity and selectivity of the Nb₂O₅ samples to their surface acidity; high surface acidity prompted the conversion of CO₂ to CO, HCOOH, and CH₃COOH, whereas low surface acidity led to the conversion of CO₂ to CH₄. It was verified that CO is the main intermediary during the CO₂ photoreduction in all conditions. This work once unveiling the importance of surface acidity for CO₂ photoreduction.

Despite the remarkable properties of NaNbO_3 and interesting performance for CO_2 photocatalytic reduction, the relative wide band gap (3.4 eV) limits its photocatalytic activity only to be active in the ultraviolet light region (4% of the solar spectrum). Therefore, there is a growing necessity to develop photocatalysts with an efficient response under visible-light irradiation. In this sense, Shi et. al. design a heterostructure between NaNbO_3 and C_3N_4 in order to extend the absorption spectral range for visible region⁹⁶. The NaNbO_3 sample was obtained through hydrothermal synthesis, the heterostructure was tailored by annealing NaNbO_3 with melamine (C_3N_4 precursor) at 520 °C for 4h. The XRD patterns of $\text{g-C}_3\text{N}_4/\text{NaNbO}_3$ revealed coexistence crystalline phase of NaNbO_3 and $\text{g-C}_3\text{N}_4$ in the composite. NaNbO_3 nanowires are found to randomly deposit and distribute on the surface of $\text{g-C}_3\text{N}_4$ sheets, which results in forming a heterostructured $\text{g-C}_3\text{N}_4/\text{NaNbO}_3$ material. The CO_2 photoreduction under visible irradiation showed that $\text{g-C}_3\text{N}_4/\text{NaNbO}_3$ improved over eight-fold the activity than that of bare C_3N_4 in the CH_4 formation. Such a remarkable enhancement of photocatalytic activity was mainly attributed to the improved separation and transfer of photogenerated electron–hole pairs at the intimate interface of $\text{g-C}_3\text{N}_4/\text{NaNbO}_3$ heterojunctions. The same group evaluated the CO_2 photoreduction performance of $\text{g-C}_3\text{N}_4/\text{KNbO}_3$, and the photocatalytic activity of $\text{g-C}_3\text{N}_4/\text{KNbO}_3$ for CO_2 reduction was almost four times higher than that of individual $\text{g-C}_3\text{N}_4$ under visible light irradiation⁹⁷.

Another Nb-based material that worth mentioning is $\text{Sr}_2\text{Bi}_2\text{Nb}_2\text{TiO}_{12}$, an Aurivillius-type perovskite. Yu et al. investigated for the first time the $\text{Sr}_2\text{Bi}_2\text{Nb}_2\text{TiO}_{12}$ as photocatalyst for CO_2 photoreduction⁹⁸. The introduction of oxygen vacancies on the surface of $\text{Sr}_2\text{Bi}_2\text{Nb}_2\text{TiO}_{12}$ extends photoresponse to cover the whole visible region and also tremendously promotes separation of photoinduced charge carriers. Compared with the bulk material prepared by traditional solid-state reaction, the $\text{Sr}_2\text{Bi}_2\text{Nb}_2\text{TiO}_{12}$ nanosheets with the optimal oxygen vacancies concentration yields a substantially high CO evolution rate of $17.11 \mu\text{mol g}^{-1} \text{h}^{-1}$.

Niobium has been used also as dopant, since it can improve the photocatalytic activities of anatase TiO_2 ^{61,99–101}, by changing the crystal structure, electrical properties, and absorption characteristics of TiO_2 . It was proposed that Nb would dope into TiO_2 lattice and decrease the band gap energy of the photocatalyst and thereby, Nb substitution on the Ti site creates a Nb^{5+} defect state located upon the conduction band minimum. Therefore, Nb doped TiO_2 would work as a visible light-driven photocatalyst^{61,100,101}.

Nogueira et. al. investigated the role of Nb-doped TiO₂ for CO₂ photocatalytic reduction to methanol¹⁰². The samples were obtained through Pechini method that promoted the substitution of Ti⁴⁺ for Nb⁴⁺ at different concentrations. It was observed that the surface area tends to increase with the concentration of Nb. The concentration of formed methanol was directly proportional to the Nb concentration in the TiO₂, the authors attributed the formation of methanol to the presence of Nb in the lattice of TiO₂.

The evaluation of CO₂ photoreduction performance of Z-scheme formed between Nb-TiO₂ and g-C₃N₄ was also evaluated¹⁰³. It was confirmed that the band gap energy of the Nb-TiO₂ (2.91 eV) was lower than that of the TiO₂ (3.2 eV). The formation of Z-scheme Nb-TiO₂/g-C₃N₄ was evidenced through XRD and TEM analysis. CO, CH₄ and O₂ were formed from CO₂ photoreduction when used the Nb-TiO₂ sample. Nb-TiO₂/g-C₃N₄ not only converted CO₂ to CO, CH₄ and O₂ but also generated HCOOH. Additionally, 50Nb-TiO₂/50g-C₃N₄ was the best material for the CO₂ reduction.

It is well-known, while metals and semiconductors usually exhibit great stability but poor selectivity for CO₂ reduction, while enzymes and metal complexes can selectively convert CO₂ into CO, but they lack long-term stability. Therefore, Faustino et. al. evaluated the role of hexaniobate nanoscrolls (K_xH_(4-x)Nb₆O₁₇) as suitable substrates for the immobilization of two kind of Re(I)-based molecular catalyst (namely I and II) for CO₂ photoreduction¹⁰⁴. Hexaniobate nanoscrolls were obtained through solid state reaction with subsequent proton exchange and exfoliation with *tert*-butylammonium hydroxide. The Re(I) complexes were immobilized by an adsorption process that was verified for UV-Vis absorption and FTIR spectroscopies. As a result of the hexaniobate exfoliation, the specific surface area was increased from 2 m² g⁻¹ to 110 m² g⁻¹. The sensitized oxides were employed as visible-light photocatalysts for CO₂ reduction in 5:1 DMF/TEOA exposed to a 300W Xe lamp ($\lambda=420$ nm). The possible gaseous products were analyzed by mass spectrometry with CO being the only detected photoproduct. The complexes immobilized on the surfaces of the oxides exhibited much higher turnover number (TON_{CO}) than in solution. For comparative purposes, the complexes were immobilized on TiO₂ as well. While for complex I the immobilization on the niobate nanoscrolls led to 20% higher TON_{CO} in comparison with that observed on TiO₂, for complex II, the opposite behavior was observed; that is, the immobilization on TiO₂ leads to better photoactivities. Such behavior was rationalized based on the recombination kinetics of each composite and on the reductive potential of the injected electrons on the

niobate or TiO₂ conduction bands. For comparison, a summary of the photoactivity of Nb-based photocatalysts towards CO₂ reduction is presented in Table 4.

Table 4 - Summary of the photocatalytic activity of Nb-based compounds combined with distinct materials towards CO₂ reduction.

Nb-Based Material	Co-Catalyst	Light Source	Main Products	Observed Rate	Ref
NaNbO ₃	Pt	300 W Xe	CH ₄	653 ppm h ⁻¹ g ⁻¹	84
NaNbO ₃	Pt	300 W Xe λ > 300 nm	CH ₄	10.4 μmol h ⁻¹ m ⁻²	85
NaNbO ₃	None	300 W Xe λ > 420 nm	CO, CH ₄ , CH ₃ OH, H ₂	NA	87
NaNbO ₃ heterojunction	Pt	300 W Xe λ > 300 nm	CH ₄	~10 μmol h ⁻¹ m ⁻²	89
HNb ₃ O ₈	None	350 W Xe	CH ₄	3.5 μmol g ⁻¹ h ⁻¹	92
SiO ₂ -Pillared HNb ₃ O ₈	Pt	350 W Xe	CH ₄	2.90 μmol g ⁻¹ h ⁻¹	93
Nb ₂ O ₅	None	UVC lamp, 0.167 mW cm ⁻²	CO, CH ₄ , CH ₃ COOH, HCOOH	~10 μmol L ⁻¹ g ⁻¹	95
C ₃ N ₄ /NaNbO ₃	None	300 W Xe λ > 420 nm	CH ₄	~6 μmol h ⁻¹ g ⁻¹	96
C ₃ N ₄ /KNbO ₃	Pt	300 W Xe λ > 420 nm	CH ₄	0.25 μmol h ⁻¹	97
Re(I) polypyridyl complexes/ K _x H _{4-x} Nb ₆ O ₁₇	None	300 W Xe λ > 420 nm	CO	2.9 *	104

* Turnover frequency (TOF), h⁻¹

2.6. Concluding Remarks and Perspectives

Over the past few years, great efforts have been spent by the scientific community to develop clean renewable energy sources. Photocatalysis can be described as an efficient method to produce solar fuels from available sources as H₂O and CO₂. Nevertheless, it is always a challenge to develop efficient materials able to promote solar-to-fuel conversion. In this sense, niobium-based materials offer diverse possibilities to engineer compounds showing important characteristics for photocatalytic processes such as efficient light absorption, charge separation, and charge transfer reaction. Herein, we could provide a glimpse from the last years on the extensive flexibility offered by niobium-based compounds for CO₂ reduction and notably for H₂ evolution. Niobium oxides as Nb₂O₅ and the wide range of niobates offer untold possibilities of structure, morphologies, and electronic configuration, which can supply desired properties for photocatalytic reactions. Moreover, niobium cations as a dopant have provided the opportunity to tune band energy positions and increase the efficiency of other materials. Thus, niobium-based compounds are promising materials that still offer opportunities of new investigations and insights regarding photocatalytic applications.

2.7. References

- (1) *BP Statistical Review of World Energy Statistical Review of World*; 2019.
- (2) Christoforidis, K. C.; Fornasiero, P. Photocatalysis for Hydrogen Production and CO₂ Reduction: The Case of Copper-Catalysts. *ChemCatChem* **2019**, *11* (1), 368–382. <https://doi.org/10.1002/cctc.201801198>.
- (3) Li, K.; Peng, B.; Peng, T. Recent Advances in Heterogeneous Photocatalytic CO₂ Conversion to Solar Fuels. *ACS Catal.* **2016**, *6* (11), 7485–7527. <https://doi.org/10.1021/acscatal.6b02089>.
- (4) Kim, J. H.; Hansora, D.; Sharma, P.; Jang, J. W.; Lee, J. S. Toward Practical Solar Hydrogen Production-an Artificial Photosynthetic Leaf-to-Farm Challenge. *Chem. Soc. Rev.* **2019**, *48* (7), 1908–1971. <https://doi.org/10.1039/c8cs00699g>.
- (5) Fujishima, A.; Honda, K. Electrochemical Photolysis of Water at a Semiconductor Electrode. *Nature* **1972**, *238*, 38–40. <https://doi.org/10.1038/238038a0>.
- (6) Nico, C.; Monteiro, T.; Graça, M. P. F. Niobium Oxides and Niobates Physical Properties: Review and Prospects. *Prog. Mater. Sci.* **2016**, *80*, 1–37. <https://doi.org/10.1016/j.pmatsci.2016.02.001>.
- (7) Lopes, O. F.; Mendonça, V. R. de; Silva, F. B. F.; Paris, E. C.; Ribeiro, C. Niobium Oxides: An Overview of the Synthesis of Nb₂O₅ and Its Application in Heterogeneous Photocatalysis. *Quim. Nova* **2014**, *38* (1), 106–117. <https://doi.org/10.5935/0100-4042.20140280>.
- (8) Nunes, B. N.; Faustino, L. A.; Muller, A. V.; Polo, A. S.; Patrocínio, A. O. T. Nb₂O₅ Dye-Sensitized Solar Cells. In *Nanomaterials for Solar Cell Application*; Thomas, S., Sakho, E.H.M., Kalarikkal, N., Oluwafemi, S.O. Wu, J., Ed.; Elsevier: Oxford, UK, 2019; pp 287–322. <https://doi.org/10.1192/bjp.111.479.1009-a>.
- (9) Nowak, I.; Ziolk, M. Niobium Compounds: Preparation, Characterization, and Application in Heterogeneous Catalysis. *Chem. Rev.* **1999**, *99* (12), 3603–3624. <https://doi.org/10.1021/cr9800208>.
- (10) Ziolk, M. Niobium-Containing Catalysts - The State of the Art. *Catal. Today* **2003**, *78* (1-4 SPEC.), 47–64. [https://doi.org/10.1016/S0920-5861\(02\)00340-1](https://doi.org/10.1016/S0920-5861(02)00340-1).
- (11) Bizeto, M. A.; Shiguihara, A. L.; Constantino, V. R. L. Layered Niobate Nanosheets: Building Blocks for Advanced Materials Assembly. *J. Mater. Chem.*

- 2009**, *19* (17), 2512–2525. <https://doi.org/10.1039/b821435b>.
- (12) Sarahan, M. C.; Carroll, E. C.; Allen, M.; Larsen, D. S.; Browning, N. D.; Osterloh, F. E. $K_4Nb_6O_{17}$ -Derived Photocatalysts for Hydrogen Evolution from Water: Nanoscrolls versus Nanosheets. *J. Solid State Chem.* **2008**, *181* (7), 1678–1683. <https://doi.org/10.1016/j.jssc.2008.06.021>.
- (13) Ebina, Y.; Sasaki, T.; Watanabe, M. Study on Exfoliation of Layered Perovskite-Type Niobates. *Solid State Ionics* **2002**, *151* (1–4), 177–182. [https://doi.org/10.1016/S0167-2738\(02\)00707-5](https://doi.org/10.1016/S0167-2738(02)00707-5).
- (14) Shiguihara, A. L.; Bizeto, M. A.; Constantino, V. R. L. Exfoliation of Layered Hexaniobate in Tetra(n-Butyl)Ammonium Hydroxide Aqueous Solution. *Colloids Surfaces A Physicochem. Eng. Asp.* **2007**, *295* (1–3), 123–129. <https://doi.org/10.1016/j.colsurfa.2006.08.040>.
- (15) Ravishankar, T. N. N.; de O. Vaz, M.; Ramakrishnappa, T.; Teixeira, S. R. R.; Dupont, J.; de, M.; Ramakrishnappa, T.; Teixeira, S. R. R.; Dupont, J.; de O. Vaz, M.; Ramakrishnappa, T.; Teixeira, S. R. R.; Dupont, J.; de, M.; Ramakrishnappa, T.; Teixeira, S. R. R.; Dupont, J. Ionic Liquid-Assisted Hydrothermal Synthesis of Nb/TiO₂ Nanocomposites for Efficient Photocatalytic Hydrogen Production and Photodecolorization of Rhodamine B under UV-Visible and Visible Light Illuminations. *Mater. Today Chem.* **2019**, *12*, 373–385. <https://doi.org/10.1016/j.mtchem.2019.04.001>.
- (16) Yang, M.; Kim, D.; Jha, H.; Lee, K.; Paul, J.; Schmuki, P. Nb Doping of TiO₂nanotubes for an Enhanced Efficiency of Dye-Sensitized Solar Cells. *Chem. Commun.* **2011**, *47* (7), 2032–2034. <https://doi.org/10.1039/c0cc04993j>.
- (17) Emeline, A. V.; Furubayashi, Y.; Zhang, X.; Jin, M.; Murakami, T.; Fujishima, A. Photoelectrochemical Behavior of Nb-Doped TiO₂ Electrodes. *J. Phys. Chem. B* **2005**, *109* (51), 24441–24444. <https://doi.org/10.1021/jp055090e>.
- (18) Singh, R.; Ryu, I.; Yadav, H.; Park, J.; Jo, J. W.; Yim, S.; Lee, J. J. Non-Hydrolytic Sol-Gel Route to Synthesize TiO₂ Nanoparticles under Ambient Condition for Highly Efficient and Stable Perovskite Solar Cells. *Sol. Energy* **2019**, *185* (May), 307–314. <https://doi.org/10.1016/j.solener.2019.04.066>.
- (19) El-Shazly, T. S.; Hassan, W. M. I.; Abdel Rahim, S. T.; Allam, N. K. Unravelling the Interplay of Dopant Concentration and Band Structure Engineering of Monoclinic Niobium Pentoxide: A Model Photoanode for Water Splitting. *Int. J. Hydrogen Energy* **2015**, *40* (40), 13867–13875.

- <https://doi.org/10.1016/j.ijhydene.2015.08.056>.
- (20) Kulkarni, A. K.; Praveen, C. S.; Sethi, Y. A.; Panmand, R. P.; Arbuj, S. S.; Naik, S. D.; Ghule, A. V.; Kale, B. B. Nanostructured N-Doped Orthorhombic Nb₂O₅ as an Efficient Stable Photocatalyst for Hydrogen Generation under Visible Light. *Dalt. Trans.* **2017**, *46* (43), 14859–14868.
<https://doi.org/10.1039/c7dt02611k>.
- (21) Huang, Q. Z.; Wang, J. C.; Wang, P. P.; Yao, H. C.; Li, Z. J. In-Situ Growth of Mesoporous Nb₂O₅ Microspheres on g-C₃N₄ Nanosheets for Enhanced Photocatalytic H₂ Evolution under Visible Light Irradiation. *Int. J. Hydrogen Energy* **2017**, *42* (10), 6683–6694.
<https://doi.org/10.1016/j.ijhydene.2017.02.052>.
- (22) Wen, P.; Ai, L.; Liu, T.; Hu, D.; Yao, F. Hydrothermal Topological Synthesis and Photocatalyst Performance of Orthorhombic Nb₂O₅ Rectangle Nanosheet Crystals with Dominantly Exposed (010) Facet. *Mater. Des.* **2017**, *117*, 346–352.
<https://doi.org/10.1016/j.matdes.2017.01.004>.
- (23) Wen, P.; Ai, L.; Wei, F.; Hu, D.; Guo, J.; Yao, F.; Liu, T. In-Situ Synthesis of Crystalline Ag-Nb₂O₅ Nanobelt Clusters with Enhanced Solar Photo-Electrochemical Performance for Splitting Water. *Mater. Des.* **2017**, *131* (March), 219–225. <https://doi.org/10.1016/j.matdes.2017.06.034>.
- (24) Zhou, C.; Shi, R.; Yang, G.; Meng, X.; Wu, L. Z.; Tung, C. H.; Zhang, T. Spatial Separation of Charge Carriers in Nb₂O₅ Nanorod Superstructures for Enhanced Photocatalytic H₂ Production Activity. *Mater. Today Chem.* **2018**, *10*, 259–263.
<https://doi.org/10.1016/j.mtchem.2018.09.005>.
- (25) Zhang, Y.; Zhao, H.; Zhao, X.; Lin, J.; Li, N.; Huo, Z.; Yan, Z.; Zhang, M.; Hu, S. Narrow-Bandgap Nb₂O₅ Nanowires with Enclosed Pores as High-Performance Photocatalyst. *Sci. China Mater.* **2019**, *62* (2), 203–210.
<https://doi.org/10.1007/s40843-018-9308-7>.
- (26) Kumar, A.; Islam, R.; Pramanik, D.; Saraswat, K. On the Limit of Defect Doping in Transition Metal Oxides. *J. Vac. Sci. Technol. A* **2019**, *37* (2), 021505.
<https://doi.org/10.1116/1.5055563>.
- (27) Zhao, W.; Zhao, W.; Zhu, G.; Lin, T.; Xu, F.; Huang, F. Black Nb₂O₅ Nanorods with Improved Solar Absorption and Enhanced Photocatalytic Activity. *Dalt. Trans.* **2016**, *45* (9), 3888–3894. <https://doi.org/10.1039/c5dt04578a>.
- (28) Huang, H.; Zhou, J.; Zhou, J.; Zhu, M. Structure-Retentive Synthesis of a Highly

- Ordered Mesoporous Nb₂O₅/N-Doped Graphene Nanocomposite with Superior Interfacial Contacts and Improved Visible-Light Photocatalysis. *Catal. Sci. Technol.* **2019**, *9* (13), 3373–3379. <https://doi.org/10.1039/c9cy00555b>.
- (29) Khan, I.; Baig, N.; Qurashi, A. Graphitic Carbon Nitride Impregnated Niobium Oxide (g-C₃N₄/Nb₂O₅) Type (II) Heterojunctions and Its Synergetic Solar-Driven Hydrogen Generation. *ACS Appl. Energy Mater.* **2019**, *2* (1), 607–615. <https://doi.org/10.1021/acsaem.8b01633>.
- (30) Idrees, F.; Dillert, R.; Bahnemann, D.; Butt, F.; Tahir, M. In-Situ Synthesis of Nb₂O₅/g-C₃N₄ Heterostructures as Highly Efficient Photocatalysts for Molecular H₂ Evolution under Solar Illumination. *Catalysts* **2019**, *9* (2), 169. <https://doi.org/10.3390/catal9020169>.
- (31) Nunes, B. N.; Patrocinio, A. O. T.; Bahnemann, D. W. Influence of the Preparation Conditions on the Morphology and Photocatalytic Performance Pt-Modified Hexaniobate Composites. *J. Phys. Condens. Matter* **2019**, *31* (39), 394001. <https://doi.org/10.1088/1361-648x/ab2c5e>.
- (32) Reisman, A.; Holtzberg, F. Phase Equilibria in the System K₂CO₃-Nb₂O₅ by the Method of Differential Thermal Analysis. *J. Am. Chem. Soc.* **1955**, *77* (8), 2115–2119. <https://doi.org/10.1021/ja01613a025>.
- (33) Nassau K; Shiever JW; Berstein JL. Crystal Growth and Properties of Nica-Like Potassium Niobates. *J. Electrochem. Soc.* **1969**, *116* (3), 348–353.
- (34) Dion, M.; Ganne, M.; Tournoux, M. Nouvelles Familles de Phases M^IM^{II}₂Nb₃O₁₀ a Feuillettes “Perovskites.” *Mater. Res. Bull.* **1981**, *16* (11), 1429–1435. [https://doi.org/10.1016/0025-5408\(81\)90063-5](https://doi.org/10.1016/0025-5408(81)90063-5).
- (35) Jacobson, A. J.; Johnson, J. W.; Lewandowski, J. T. Interlayer Chemistry between Thick Transition-Metal Oxide Layers: Synthesis and Intercalation Reactions of K[C₂Na_{n-3}Nb_nO₃₊₁] (3 ≤ n ≤ 7). *Inorg. Chem.* **1985**, *24* (23), 3727–3729. <https://doi.org/10.1021/ic00217a006>.
- (36) Nunes, B. N.; Haisch, C.; Emeline, A. V.; Bahnemann, D. W.; Patrocinio, A. O. T. Photocatalytic Properties of Layer-by-Layer Thin Films of Hexaniobate Nanoscrolls. *Catal. Today* **2019**, *326* (June 2018), 60–67. <https://doi.org/10.1016/j.cattod.2018.06.029>.
- (37) Oshima, T.; Lu, D.; Maeda, K. Preparation of Pt-Intercalated KCa₂Nb₃O₁₀ Nanosheets and Their Photocatalytic Activity for Overall Water Splitting. *ChemNanoMat* **2016**, *2* (7), 748–755. <https://doi.org/10.1002/cnma.201600072>.

- (38) Kulischow, N.; Ladasiu, C.; Marschall, R. Layered Dion-Jacobson Type Niobium Oxides for Photocatalytic Hydrogen Production Prepared via Molten Salt Synthesis. *Catal. Today* **2017**, *287*, 65–69.
<https://doi.org/10.1016/j.cattod.2016.10.009>.
- (39) Zhou, Y.; Wen, T.; Guo, Y.; Yang, B.; Wang, Y. Controllable Doping of Nitrogen and Tetravalent Niobium Affords Yellow and Black Calcium Niobate Nanosheets for Enhanced Photocatalytic Hydrogen Evolution. *RSC Adv.* **2016**, *6* (69), 64930–64936. <https://doi.org/10.1039/c6ra11407e>.
- (40) Zhou, Y.; Wen, T.; Zhang, X.; Chang, B.; Kong, W.; Guo, Y.; Yang, B.; Wang, Y. A Multiple Structure-Design Strategy towards Ultrathin Niobate Perovskite Nanosheets with Thickness-Dependent Photocatalytic Hydrogen-Evolution Performance. *Chem. - An Asian J.* **2017**, *12* (20), 2727–2733.
<https://doi.org/10.1002/asia.201701001>.
- (41) Xiong, J.; Jing, K.; Zou, J.; Liang, S.; Wu, L. A Hybrid of CdS/HCa₂Nb₃O₁₀ Ultrathin Nanosheets for Promoting Photocatalytic Hydrogen Evolution. *Dalt. Trans.* **2017**, *46* (40), 13935–13942. <https://doi.org/10.1039/c7dt03027d>.
- (42) Hu, Y.; Li, G.; Zong, S.; Shi, J.; Guo, L. Self-Assembled Nanohybrid of Cadmium Sulfide and Calcium Niobate: Photocatalyst with Enhanced Charge Separation for Efficient Visible Light Induced Hydrogen Generation. *Catal. Today* **2018**, *315* (March), 117–125. <https://doi.org/10.1016/j.cattod.2018.03.037>.
- (43) Xiong, J.; Liu, Y.; Liang, S.; Zhang, S.; Li, Y.; Wu, L. Insights into the Role of Cu in Promoting Photocatalytic Hydrogen Production over Ultrathin HNb₃O₈ Nanosheets. *J. Catal.* **2016**, *342*, 98–104.
<https://doi.org/10.1016/j.jcat.2016.07.016>.
- (44) Xia, Y.; Liang, S.; Wu, L.; Wang, X. Ultrasmall NiS Decorated HNb₃O₈ Nanosheets as Highly Efficient Photocatalyst for H₂ Evolution Reaction. *Catal. Today* **2019**, *330*, 195–202. <https://doi.org/10.1016/j.cattod.2018.03.061>.
- (45) Wang, J.; Teng, J.; Pu, L.; Huang, J.; Wang, Y.; Li, Q. Double-Hole-Mediated Coupling of Anionic Dopants in Perovskite NaNbO₃ for Efficient Solar Water Splitting. *Int. J. Quantum Chem.* **2019**, *119* (14), 1–11.
<https://doi.org/10.1002/qua.25930>.
- (46) Kaneko, M.; Mishima, K.; Yamashita, K. First-Principles Study on Visible Light Absorption of Defected SrNbO₃. *J. Photochem. Photobiol. A Chem.* **2019**, *375*, 175–180. <https://doi.org/10.1016/j.jphotochem.2019.02.018>.

- (47) Yu, J.; Chen, Z.; Chen, Q.; Wang, Y.; Lin, H.; Hu, X.; Zhao, L.; He, Y. Giant Enhancement of Photocatalytic H₂ Production over KNbO₃ Photocatalyst Obtained via Carbon Doping and MoS₂ Decoration. *Int. J. Hydrogen Energy* **2018**, *43* (9), 4347–4354. <https://doi.org/10.1016/j.ijhydene.2018.01.055>.
- (48) Huang, S.; Lang, J.; Du, C.; Bian, F.; Su, Y.; Wang, X. Enhanced Driving Force and Charge Separation Efficiency in Disordered SnNb_xO_y: Boosting Photocatalytic Activity toward Water Reduction. *Chem. Eng. J.* **2017**, *309*, 313–320. <https://doi.org/10.1016/j.cej.2016.10.061>.
- (49) Kamimura, S.; Abe, S.; Tsubota, T.; Ohno, T. Solar-Driven H₂ Evolution over CuNb₂O₆: Effect of Two Polymorphs (Monoclinic and Orthorhombic) on Optical Property and Photocatalytic Activity. *J. Photochem. Photobiol. A Chem.* **2018**, *356*, 263–271. <https://doi.org/10.1016/j.jphotochem.2017.12.039>.
- (50) Chun, Y.; Yue, M.; Jiang, P.; Chen, S.; Gao, W.; Cong, R.; Yang, T. Optimizing the Performance of Photocatalytic H₂ Generation for ZnNb₂O₆ Synthesized by a Two-Step Hydrothermal Method. *RSC Adv.* **2018**, *8* (25), 13857–13864. <https://doi.org/10.1039/c8ra01624k>.
- (51) Betzler, S. B.; Podjaski, F.; Beetz, M.; Handloser, K.; Wisnet, A.; Handloser, M.; Hartschuh, A.; Lotsch, B. V.; Scheu, C. Titanium Doping and Its Effect on the Morphology of Three-Dimensional Hierarchical Nb₃O₇(OH) Nanostructures for Enhanced Light-Induced Water Splitting. *Chem. Mater.* **2016**, *28* (21), 7666–7672. <https://doi.org/10.1021/acs.chemmater.6b02470>.
- (52) Zhang, B.; Hui, D.; Li, Y.; Zhao, H.; Wang, C. Synthesis and Photocatalytic Hydrogen Production Activity of the Ni-CH₃CH₂NH₂/H_{1.78}Sr_{0.78}Bi_{0.22}Nb₂O₇ Hybrid Layered Perovskite. *Cuihua Xuebao/Chinese J. Catal.* **2017**, *38* (12), 2039–2047. [https://doi.org/10.1016/S1872-2067\(17\)62953-X](https://doi.org/10.1016/S1872-2067(17)62953-X).
- (53) Grodziuk, G. Y.; Shcherban, N. D.; Shvalagin, V. V.; Korzhak, A. V.; Andryushina, N. S.; Skoryk, M. A.; Kuchmiy, S. Y. Photocatalytic Activity of Nanostructured Composites Based on Layered Niobates and C₃N₄ in the Hydrogen Evolution Reaction from Electron Donor Solutions under Visible Light. *Int. J. Hydrogen Energy* **2017**, *42* (38), 24108–24116. <https://doi.org/10.1016/j.ijhydene.2017.07.238>.
- (54) Thaweesak, S.; Lyu, M.; Peerakiathajohn, P.; Butburee, T.; Luo, B.; Chen, H.; Wang, L. Applied Catalysis B : Environmental Two-Dimensional g-C₃N₄/Ca₂Nb₂TaO₁₀ Nanosheet Composites for Efficient Visible Light Photocatalytic

- Hydrogen Evolution. **2017**, *202*, 184–190.
- (55) Wang, K.; Li, Y.; Li, J.; Zhang, G. Boosting Interfacial Charge Separation of Ba₅Nb₄O₁₅/g-C₃N₄ Photocatalysts by 2D/2D Nanojunction towards Efficient Visible-Light Driven H₂ Generation. *Appl. Catal. B Environ.* **2019**, 117730. <https://doi.org/10.1016/j.apcatb.2019.05.032>.
- (56) Chen, P.; Xing, P.; Chen, Z.; Hu, X.; Lin, H.; Zhao, L.; He, Y. In-Situ Synthesis of AgNbO₃/g-C₃N₄ Photocatalyst via Microwave Heating Method for Efficiently Photocatalytic H₂ Generation. *J. Colloid Interface Sci.* **2019**, *534*, 163–171. <https://doi.org/10.1016/j.jcis.2018.09.025>.
- (57) Chen, Z.; Chen, P.; Xing, P.; Hu, X.; Lin, H.; Wu, Y.; Zhao, L. Rapid Fabrication of KTa_{0.75}Nb_{0.25}/g-C₃N₄ Composite via Microwave Heating for Efficient Photocatalytic H₂ Evolution. **2019**, *241*, 1–11. <https://doi.org/10.1016/j.fuel.2018.12.011>.
- (58) Fujito, H.; Kunioku, H.; Kato, D.; Suzuki, H.; Higashi, M.; Kageyama, H.; Abe, R. Layered Perovskite Oxochloride Bi₄NbO₈Cl: A Stable Visible Light Responsive Photocatalyst for Water Splitting. *J. Am. Chem. Soc.* **2016**, *138* (7), 2082–2085. <https://doi.org/10.1021/jacs.5b11191>.
- (59) Wakayama, H.; Hibino, K.; Fujii, K.; Oshima, T.; Yanagisawa, K.; Kobayashi, Y.; Kimoto, K.; Yashima, M.; Maeda, K. Synthesis of a Layered Niobium Oxynitride, Rb₂NdNb₂O₆N·H₂O, Showing Visible-Light Photocatalytic Activity for H₂ Evolution. *Inorg. Chem.* **2019**, *58* (9), 6161–6166. <https://doi.org/10.1021/acs.inorgchem.9b00414>.
- (60) Tian, Z.; Cui, H.; Xu, J.; Zhu, G.; Shao, F.; He, J.; Huang, F. Efficient Charge Separation of In-Situ Nb-Doped TiO₂ Nanowires for Photoelectrochemical Water-Splitting. *ChemistrySelect* **2017**, *2* (9), 2822–2827. <https://doi.org/10.1002/slct.201700319>.
- (61) Kong, L.; Wang, C.; Zheng, H.; Zhang, X.; Liu, Y. Defect-Induced Yellow Color in Nb-Doped TiO₂ and Its Impact on Visible-Light Photocatalysis. *J. Phys. Chem. C* **2015**, *119* (29), 16623–16632. <https://doi.org/10.1021/acs.jpcc.5b03448>.
- (62) Caudillo-Flores, U.; Muñoz-Batista, M. J.; Cortés, J. A.; Fernández-García, M.; Kubacka, A. UV and Visible Light Driven H₂ Photo-Production Using Nb-Doped TiO₂: Comparing Pt and Pd Co-Catalysts. *Mol. Catal.* **2017**, *437*, 1–10. <https://doi.org/10.1016/j.mcat.2017.04.035>.

- (63) Flores, E.; Ares, J. R.; Sánchez, C.; Ferrer, I. J. Ternary Transition Titanium-Niobium Trisulfide as Photoanode for Assisted Water Splitting. *Catal. Today* **2019**, 321–322, 107–112. <https://doi.org/10.1016/j.cattod.2018.01.024>.
- (64) Zoellner, B.; O'Donnell, S.; Wu, Z.; Itanze, D.; Carbone, A.; Osterloh, F. E.; Geyer, S.; Maggard, P. A. Impact of Nb(V) Substitution on the Structure and Optical and Photoelectrochemical Properties of the $\text{Cu}_5(\text{Ta}_{1-x}\text{Nb}_x)_{11}\text{O}_{30}$ Solid Solution. *Inorg. Chem.* **2019**, 58 (10), 6845–6857. <https://doi.org/10.1021/acs.inorgchem.9b00304>.
- (65) Thanh Truc, N. T.; Tran, D. T.; Hanh, N. T.; Pham, T. D. Novel Visible Light-Driven Nb-Doped Ta_3N_5 Sensitized/Protected by PPy for Efficient Overall Water Splitting. *Int. J. Hydrogen Energy* **2018**, 43 (33), 15898–15906. <https://doi.org/10.1016/j.ijhydene.2018.06.128>.
- (66) Chen, Z.; Chen, P.; Xing, P.; Hu, X.; Lin, H.; Wu, Y.; Zhao, L. Novel Carbon Modified $\text{KTa}_{0.75}\text{Nb}_{0.25}\text{O}_3$ Nanocubes with Excellent Efficiency In. **2018**, 233, 486–496. <https://doi.org/10.1016/j.fuel.2018.06.090>.
- (67) Monfort, O.; Sfaelou, S.; Satrapinsky, L.; Plecenik, T.; Roch, T.; Plesch, G.; Lianos, P. Comparative Study between Pristine and Nb-Modified BiVO_4 Films Employed for Photoelectrocatalytic Production of H_2 by Water Splitting and for Photocatalytic Degradation of Organic Pollutants under Simulated Solar Light. *Catal. Today* **2017**, 280, 51–57. <https://doi.org/10.1016/j.cattod.2016.07.006>.
- (68) Fontelles-Carceller, O.; Muñoz-Batista, M. J.; Conesa, J. C.; Kubacka, A.; Fernández-García, M. H_2 Photo-Production from Methanol, Ethanol and 2-Propanol: Pt-(Nb)TiO₂ Performance under UV and Visible Light. *Mol. Catal.* **2018**, 446, 88–97. <https://doi.org/10.1016/j.mcat.2017.12.023>.
- (69) Kalanur, S. S.; Yoo, I. H.; Cho, I. S.; Seo, H. Niobium Incorporated WO_3 Nanotriangles: Band Edge Insights and Improved Photoelectrochemical Water Splitting Activity. *Ceram. Int.* **2019**, 45 (7), 8157–8165. <https://doi.org/10.1016/j.ceramint.2019.01.117>.
- (70) Patel, P. P.; Hanumantha, P. J.; Velikokhatnyi, O. I.; Datta, M. K.; Gattu, B.; Poston, J. A.; Manivannan, A.; Kumta, P. N. Vertically Aligned Nitrogen Doped (Sn,Nb)O₂ Nanotubes - Robust Photoanodes for Hydrogen Generation by Photoelectrochemical Water Splitting. *Mater. Sci. Eng. B Solid-State Mater. Adv. Technol.* **2016**, 208, 1–14. <https://doi.org/10.1016/j.mseb.2016.02.001>.
- (71) IPCC The Intergovernmental Panel on Climate Change <http://www.ipcc.ch/>

(accessed Nov 20, 2019).

- (72) Lim, C. H.; Holder, A. M.; Hynes, J. T.; Musgrave, C. B. Catalytic Reduction of CO₂ by Renewable Organohydrides. *J. Phys. Chem. Lett.* **2015**, *6* (24), 5078–5092. <https://doi.org/10.1021/acs.jpcclett.5b01827>.
- (73) Mondal, B.; Song, J.; Neese, F.; Ye, S. Bio-Inspired Mechanistic Insights into CO₂ Reduction. *Curr. Opin. Chem. Biol.* **2015**, *25*, 103–109. <https://doi.org/10.1016/j.cbpa.2014.12.022>.
- (74) Mao, Z.; Chen, J.; Yang, Y.; Wang, D.; Bie, L.; Fahlman, B. D. Novel G-C₃N₄/CoO Nanocomposites with Significantly Enhanced Visible-Light Photocatalytic Activity for H₂ Evolution. *ACS Appl. Mater. Interfaces* **2017**, *9* (14), 12427–12435. <https://doi.org/10.1021/acsami.7b00370>.
- (75) Gutierrez-Guerra, N.; Moreno-Lopez, L.; Serrano-Ruiz, J. C.; Valverde, J. L.; de Lucas-Consuegra, A. Gas Phase Electrocatalytic Conversion of CO₂ to Syn-Fuels on Cu Based Catalysts-Electrodes. *Appl. Catal. B Environ.* **2016**, *188*, 272–282. <https://doi.org/10.1016/j.apcatb.2016.02.010>.
- (76) Ciamician, G. The Photochemistry of the Future. *Science (80-.)*. **1912**, *36* (926), 385–394. <https://doi.org/10.1126/science.36.926.385>.
- (77) Inoue, T.; Fujishima, A.; Konishi, S.; Honda, K. Photoelectrocatalytic Reduction of Carbon Dioxide in Aqueous Suspensions of Semiconductor Powders [3]. *Nature* **1979**, *277* (5698), 637–638. <https://doi.org/10.1038/277637a0>.
- (78) D'Alessandro, D. M.; Smit, B.; Long, J. R. Carbon Dioxide Capture: Prospects for New Materials. *Angew. Chemie - Int. Ed.* **2010**, *49* (35), 6058–6082. <https://doi.org/10.1002/anie.201000431>.
- (79) Kauffman, D. R.; Thakkar, J.; Siva, R.; Matranga, C.; Ohodnicki, P. R.; Zeng, C.; Jin, R. Efficient Electrochemical CO₂ Conversion Powered by Renewable Energy. *ACS Appl. Mater. Interfaces* **2015**, *7* (28), 15626–15632. <https://doi.org/10.1021/acsami.5b04393>.
- (80) Hsieh, Y.-C.; Senanayake, S. D.; Zhang, Y.; Xu, W.; Polyansky, D. E. Effect of Chloride Anions on the Synthesis and Enhanced Catalytic Activity of Silver Nanocoral Electrodes for CO₂ Electroreduction. *ACS Catal.* **2015**, 5349–5356. <https://doi.org/10.1021/acscatal.5b01235>.
- (81) Kortlever, R.; Shen, J.; Schouten, K. J. P.; Calle-Vallejo, F.; Koper, M. T. M. Catalysts and Reaction Pathways for the Electrochemical Reduction of Carbon Dioxide. *J. Phys. Chem. Lett.* **2015**, *6* (20), 4073–4082.

- <https://doi.org/10.1021/acs.jpcclett.5b01559>.
- (82) Ma, Y.; Wang, X.; Jia, Y.; Chen, X.; Han, H.; Li, C. Titanium Dioxide-Based Nanomaterials for Photocatalytic Fuel Generations. *Chem. Rev.* **2014**, *114* (19), 9987–10043. <https://doi.org/10.1021/cr500008u>.
- (83) Ong, W.-J.; Tan, L.-L.; Ng, Y. H.; Yong, S.-T.; Chai, S.-P. Graphitic Carbon Nitride (g-C₃N₄)-Based Photocatalysts for Artificial Photosynthesis and Environmental Remediation: Are We a Step Closer To Achieving Sustainability? *Chem. Rev.* **2016**, *acs.chemrev.6b00075*.
<https://doi.org/10.1021/acs.chemrev.6b00075>.
- (84) Shi, H.; Wang, T.; Chen, J.; Zhu, C.; Ye, J.; Zou, Z. Photoreduction of Carbon Dioxide over NaNbO₃ Nanostructured Photocatalysts. *Catal. Letters* **2011**, *141* (4), 525–530. <https://doi.org/10.1007/s10562-010-0482-1>.
- (85) Li, P.; Ouyang, S.; Zhang, Y.; Kako, T.; Ye, J. Surface-Coordination-Induced Selective Synthesis of Cubic and Orthorhombic NaNbO₃ and Their Photocatalytic Properties. *J. Mater. Chem. A* **2013**, *1* (4), 1185–1191.
<https://doi.org/10.1039/c2ta00260d>.
- (86) Li, P.; Ouyang, S.; Xi, G.; Kako, T.; Ye, J. The Effects of Crystal Structure and Electronic Structure on Photocatalytic H₂ Evolution and CO₂ Reduction over Two Phases of Perovskite-Structured NaNbO₃. **2012**, *3*.
- (87) Fresno, F.; Jana, P.; Reñones, P.; Coronado, J. M.; Serrano, D. P.; De La Peña O’Shea, V. A. CO₂ Reduction over NaNbO₃ and NaTaO₃ Perovskite Photocatalysts. *Photochem. Photobiol. Sci.* **2017**, *16* (1), 17–23.
<https://doi.org/10.1039/c6pp00235h>.
- (88) Ohno, T.; Sarukawa, K.; Tokieda, K.; Matsumura, M. Morphology of a TiO₂ Photocatalyst (Degussa, P-25) Consisting of Anatase and Rutile Crystalline Phases. **2001**, *86*, 82–86. <https://doi.org/10.1006/jcat.2001.3316>.
- (89) Li, P.; Xu, H.; Liu, L.; Kako, T.; Umezawa, N.; Abe, H.; Ye, J. Constructing Cubic-Orthorhombic Surface-Phase Junctions of NaNbO₃ towards Significant Enhancement of CO₂ Photoreduction. *J. Mater. Chem. A* **2014**, *2* (16), 5606–5609. <https://doi.org/10.1039/c4ta00105b>.
- (90) Low, J.; Cao, S.; Yu, J.; Wageh, S. Two-Dimensional Layered Composite Photocatalysts. *Chem. Commun.* **2014**, *50* (74), 10768–10777.
<https://doi.org/10.1039/c4cc02553a>.
- (91) Li, X.; Kikugawa, N.; Ye, J. Nitrogen-Doped Lamellar Niobic Acid with Visible

- Light-Responsive Photocatalytic Activity. *Adv. Mater.* **2008**, *20* (20), 3816–3819. <https://doi.org/10.1002/adma.200702975>.
- (92) Li, X.; Pan, H.; Li, W.; Zhuang, Z. Photocatalytic Reduction of CO₂ to Methane over HNb₃O₈ Nanobelts. *Appl. Catal. A Gen.* **2012**, *413–414* (301), 103–108. <https://doi.org/10.1016/j.apcata.2011.10.044>.
- (93) Li, X.; Li, W.; Zhuang, Z.; Zhong, Y.; Li, Q.; Wang, L. Photocatalytic Reduction of Carbon Dioxide to Methane over SiO₂-Pillared HNb₃O₈. *J. Phys. Chem. C* **2012**, *116*, 16047–16053.
- (94) Kormányos, A.; Thomas, A.; Huda, M. N.; Sarker, P.; Liu, J. P.; Poudyal, N.; Janáky, C.; Rajeshwar, K. Solution Combustion Synthesis, Characterization, and Photoelectrochemistry of CuNb₂O₆ and ZnNb₂O₆ Nanoparticles. *J. Phys. Chem. C* **2016**, *120*, 16024–16034. <https://doi.org/10.1021/acs.jpcc.5b12738>.
- (95) da Silva, G. T. S. T.; Nogueira, A. E.; Oliveira, J. A.; Torres, J. A.; Lopes, O. F.; Ribeiro, C. Acidic Surface Niobium Pentoxide Is Catalytic Active for CO₂ Photoreduction. *Appl. Catal. B Environ.* **2019**, *242* (July 2018), 349–357. <https://doi.org/10.1016/j.apcatb.2018.10.017>.
- (96) Shi, H.; Chen, G.; Zhang, C.; Zou, Z. Polymeric G-C₃N₄ Coupled with NaNbO₃ Nanowires toward Enhanced Photocatalytic Reduction of CO₂ into Renewable Fuel. *ACS Catal.* **2014**, *4* (10), 3637–3643. <https://doi.org/10.1021/cs500848f>.
- (97) Shi, H.; Zhang, C.; Zhou, C.; Chen, G. Conversion of CO₂ into Renewable Fuel over Pt-g-C₃N₄/KNbO₃ Composite Photocatalyst. *RSC Adv.* **2015**, *5* (113), 93615–93622. <https://doi.org/10.1039/c5ra16870h>.
- (98) Yu, H.; Li, J.; Zhang, Y.; Yang, S.; Han, K.; Dong, F.; Ma, T.; Huang, H. Three-in-One Oxygen Vacancies: Whole Visible-Spectrum Absorption, Efficient Charge Separation, and Surface Site Activation for Robust CO₂ Photoreduction. *Angew. Chemie - Int. Ed.* **2019**, *58* (12), 3880–3884. <https://doi.org/10.1002/anie.201813967>.
- (99) Yang, X.; Min, Y.; Li, S.; Wang, D.; Mei, Z.; Liang, J.; Pan, F. Conductive Nb-Doped TiO₂ Thin Films with Whole Visible Absorption to Degrade Pollutants. *Catal. Sci. Technol.* **2018**, *8* (5), 1357–1365. <https://doi.org/10.1039/c7cy02614e>.
- (100) Mattsson, A.; Leideborg, M.; Larsson, K.; Westing, G.; Österlund, L. Adsorption and Solar Light Decomposition of Acetone on Anatase TiO₂ and Niobium Doped TiO₂ Thin Films. *J. Phys. Chem. B* **2006**, *110* (3), 1210–1220. <https://doi.org/10.1021/jp055656z>.

- (101) Yang, J.; Zhang, X.; Wang, C.; Sun, P.; Wang, L.; Xia, B.; Liu, Y. Solar Photocatalytic Activities of Porous Nb-Doped TiO₂ Microspheres Prepared by Ultrasonic Spray Pyrolysis. *Solid State Sci.* **2012**, *14* (1), 139–144.
<https://doi.org/10.1016/j.solidstatesciences.2011.11.010>.
- (102) Nogueira, M. V.; Lustosa, G. M. M. M.; Kobayakawa, Y.; Kogler, W.; Ruiz, M.; Monteiro Filho, E. S.; Zaghete, M. A.; Perazolli, L. A. Nb-Doped TiO₂ Photocatalysts Used to Reduction of CO₂ to Methanol. *Adv. Mater. Sci. Eng.* **2018**, *2018*. <https://doi.org/10.1155/2018/7326240>.
- (103) Thanh Truc, N. T.; Giang Bach, L.; Thi Hanh, N.; Pham, T. D.; Thi Phuong Le Chi, N.; Tran, D. T.; Nguyen, M. V.; Nguyen, V. N. The Superior Photocatalytic Activity of Nb Doped TiO₂ /g-C₃N₄ Direct Z-Scheme System for Efficient Conversion of CO₂ into Valuable Fuels. *J. Colloid Interface Sci.* **2019**, *540*, 1–8.
<https://doi.org/10.1016/j.jcis.2019.01.005>.
- (104) Faustino, L. A.; Souza, B. L.; Nunes, B. N.; Duong, A.-T.; Sieland, F.; Bahnemann, D. W.; Patrocínio, A. O. T. Photocatalytic CO₂ Reduction by Re(I) Polypyridyl Complexes Immobilized on Niobates Nanoscrolls. *ACS Sustain. Chem. Eng.* **2018**, *6* (5), 6073–6083.
<https://doi.org/10.1021/acssuschemeng.7b04713>.

3. Photocatalytic Properties of Layer-by-Layer Thin Films of Hexaniobate Nanoscrolls

3.1. Foreword

This chapter contains the article “Photocatalytic Properties of Layer-by-Layer Thin Films of Hexaniobate Nanoscrolls” by Barbara N. Nunes, Christoph Haisch, Alexei V. Emeline, Detlef W. Bahnemann and Antonio Otavio T. Patrocinio published on *Catalysis Today* 2019, 326, 60. doi.org/10.1016/j.cattod.2018.06.029. The figures and tables identified through this chapter with the letter “A” are reproduced in Appendix A. Reprinted with permission. Copyright 2019 Elsevier.

3.2. Abstract

High efficient photocatalytic surfaces were obtained through the layer-by-layer (LbL) deposition of hexaniobate nanoscrolls on conductive glasses. These films were deposited by alternative immersions of the substrate into exfoliated hexaniobate suspensions (pH = 8) and poly(allylamine hydrochloride) solutions (pH = 4). The organic species were further removed by thermal treatment leading to a fuzzy assembly of hexaniobate nanoscrolls. Pre-adsorption of $[\text{Pt}(\text{NH}_3)_4]^{2+}$ cations on the niobate layers allows the production of metallic Pt nanoclusters on the film layers. The Pt-modified films exhibited apparent quantum yields of $(4.0 \pm 0.5) \%$ for H_2 evolution from water/methanol mixtures under UV-A irradiation. The H_2 evolution rates varied linearly with the number of deposited bilayers, indicating that no active sites are lost as the film is grown. The photoelectrochemical properties of the films reveal that the small size of the hole scavenger and its easy diffusion into the hexaniobate layers are key aspects for the photocatalytic activity. In the absence of alcohols as hole scavengers, irradiation of the hexaniobate LbL films in aqueous solutions leads to the production of surface-bound peroxides that limit the photocatalytic water splitting ability of these materials. The results presented here provide evidence for the effectiveness of the LbL technique to deposit thin films of layered materials retaining their interesting adsorption chemistry. This methodology can be further employed for the development of highly active photocatalytic surfaces.

3.3. Introduction

Photocatalysis currently attracts great interest due to its potential to harvest and convert solar energy into fuels¹⁻³ or to be used in environmental remediation⁴⁻⁶. A key step in this field is the development of new materials able to act as photocatalysts. Among them, layered niobates offer diversity and flexibility in terms of preparation and application. They are semiconductor oxides formed from octahedral [NbO₆] units. Some common structures reported in the literature include potassium hexaniobate (K₄Nb₆O₁₇)⁷⁻⁹ and calcium niobates¹⁰⁻¹⁴.

The high charge density of Nb⁵⁺ ions leads to a very strong affinity to oxygen, thus the niobates tend to form extended lamellar structures^{2,15}. This configuration provides a considerable surface area and allows easy modification by intercalation, superficial modification or formation of nanosheets and nanoscrolls through exfoliation with bulky n-alkylammonium salts^{16,17}.

The exfoliated niobates form stable suspensions, which can be used to produce thin films by the Layer-by-Layer (LbL) technique. Some advantages of the LbL method are easy thickness control, simplicity, low cost and possibility of using different materials and substrates¹⁸⁻²⁰. In the LbL methodology the nanostructures are typically assembled on the substrate surface by electrostatic interactions between the particles and a supporting polyelectrolyte. Its application in photocatalysis has been continuously growing during recent years²¹⁻³¹. Specifically, LbL films based on niobate nanosheets were reported by Mallouk's group^{32,33} and also by other groups aiming at different applications³⁴⁻³⁹. The role of the number of deposited bilayers on the photocatalytic properties, however, as well as aspects concerning the electronic properties and interfacial processes in these surfaces has still not been investigated.

Aiming at a deeper understanding of the photocatalytic processes on hexaniobate-based LbL films, this work describes the use of exfoliated (Nb₆O₁₇)⁴⁻ sheets to design photocatalytic films with unique morphology. The photochemical H₂ evolution by these films as well as their photoelectrochemical properties are investigated in different electrolytes.

3.4. Material and Methods

All chemicals were of analytical or HPLC grade and were used as received. Nb₂O₅ was provided by CBMM (“Companhia Brasileira de Metalurgia e Mineração”). Potassium carbonate, potassium sulphate, tert-butylamine hydroxide and poly(allylamine hydrochloride) (PAH) MW = 50,000 were acquired from Aldrich. Fluorine-doped thin oxide (FTO) glassy substrates (15 Ω/ square) were acquired from Pilkington Co. [Pt(NH₃)₄]Cl₂ was synthesized as previously reported [40] and its purity was confirmed by elemental analysis, ¹H NMR and ¹⁹⁵Pt NMR (Figure A1, Table A1 of Appendix A).

3.4.1. Preparation of lamellar K_{4-x}H_xNb₆O₁₇

Bulk K₄Nb₆O₁₇·3H₂O was prepared by a solid state method^{40,41}. Nb₂O₅ and K₂CO₃ in a molar proportion of 2:3 were grinded and heated at 1100 °C for 10 h. The final product was washed with deionized water and then dried at 80 °C. The bulk material was then submitted to an acid treatment to partially exchange K⁺ cations by protons. 3.0 g of K₄Nb₆O₁₇·3H₂O were stirred in 150 ml of 0.2 mol L⁻¹ H₂SO₄ solution during 3 days. The solid was subsequently separated by filtration, washed with water and dried at 80 °C. The hexaniobate nanoscrolls were obtained by exfoliation of bulk K_{4-x}H_xNb₆O₁₇ (0.5 g) with 100 ml of 8 × 10⁻³ mol L⁻¹ tert-butylammonium hydroxide during seven days^{17,34}. When the stirring is suspended the non-exfoliated material tends to precipitate, while the exfoliated layers remain as a stable suspension. The suspension was collected and used for the LbL deposition.

3.4.2. Preparation of K_{4-x}H_xNb₆O₁₇ LbL films

The LbL hexaniobate films were deposited onto FTO conductive surfaces using PAH as supporting counter-ion. The concentration and pH of the Nb₆O₁₇⁴⁻ suspension were adjusted to 6 mg mL⁻¹ and 8, respectively. Prior the deposition, FTO conductive glasses were washed with detergent, rinsed with water and sonicated first in isopropanol and then in deionized water for 10 min each. Finally, they were dried at 80 °C. Afterwards, cleaned FTO glasses were alternatively immersed in the hexaniobate suspension and in a pH 4 aqueous solution of PAH (6 mg mL⁻¹) for three minutes. After each immersion, the substrate was rinsed with reagent-grade water (60 s, under magnetic stirring) and dried with compressed air. The film growth was followed by UV-vis spectroscopy. The films with different number of deposited bilayers were then sintered at

500 °C for 30 min for removal of the organic content. Pt-modified hexaniobate LbL films were obtained by previous adsorption of $[\text{Pt}(\text{NH}_3)_4]\text{Cl}_2$ on the layered niobate, as reported elsewhere⁴². The amount of Pt-precursor was determined, so the final ratio could be 1% (m/m) Pt in relation to the hexaniobate mass. After the addition of the precursor, the suspension was stirred for 30 min and then used for the film deposition as described above.

3.4.3. Characterization techniques

Electronic absorption spectra were recorded on a double beam Shimadzu UV-1650 spectrophotometer. The films were placed in a quartz cuvette, kept parallel to the wall and perpendicular to the light beam. Attenuated total reflectance infrared (ATR-FTIR) spectra were recorded using a Perkin-Elmer Frontier spectrometer. The measurements were performed in a diamond crystal plate, using 32 scans at a resolution of 2 cm^{-1} . The spectrum of a bare FTO was taken under same conditions and used as background. X ray diffractograms of the powders were obtained using a Shimadzu XRD-6000 diffractometer, with a $\text{CuK}\alpha$ ($\lambda = 1.54148\text{ nm}$) monochromatic source. Specific surface area measurements were determined from N_2 adsorption/desorption isotherms using the BET methodology⁴³ and a Quantachrome NOVAtouch LX1 surface analyser. X ray photoelectron spectroscopy (XPS) was carried out employing a Leybold Heraeus analyser equipped with an Al non monochromatic X ray source and a hemispherical electron energy analyser. The beam energy was 1484 eV and the residual C1s peak at 284.6 eV was used as internal standard. Thermogravimetric analysis was carried out under air in a Shimadzu DTG-60H analyser. Field emission scanning electron microscopy (FESEM) images were obtained in a Jeol JSM 6700 F microscopy at 2.0 kV acceleration voltage. Raman spectra were collected at a LabRAM HR Evolution. Samples were excited at 532 nm. Spectra were obtained by the accumulation of 8 scans in the range of 70 to 2000 cm^{-1} . Atomic force microscopy (AFM) images were obtained using a SPM-9600 scanning probe microscope (Shimadzu). AFM images were registered under contact mode at a scan rate of 1 Hz. The software Gwyddion (v. 2.45) was used to estimate the film thickness, taking the difference in the Z values related to the film and the FTO surfaces. Photoelectrochemical characterization of the films was carried out in a Zennium potentiostat and a PECC-2 photoelectrochemical cell (Zahner-Elektrik GmbH & Co. KG). A Pt wire was used as counter electrode along with an Ag/AgCl , NaCl 3 mol L^{-1} reference electrode. A $\text{pH} = 6.0$ K_2SO_4 0.1 mol L^{-1} solution was employed as electrolyte.

10% (v/v) of methanol or isopropanol was also added to the electrolyte in some experiments. The electrolyte was purged with argon prior each experiment. Samples were illuminated by a Hamamatsu LC8 light source (model L9566-01 A) equipped with a 200 W Xe lamp and a light guide. The light guide output was placed at ~60 mm from the sample surface, providing $\sim 0.2 \text{ W cm}^{-2}$ at 365 nm. All reported potentials are against NHE ($-0.209 \text{ mV vs Ag/AgCl, NaCl } 3 \text{ mol L}^{-1}$). Electrochemical Impedance spectroscopy (EIS) was carried out under illumination in the frequency range of 1 MHz-100 mHz and at +1 V vs NHE.

3.4.4. Photocatalytic H₂ evolution

For the photocatalytic tests, $0.5 \times 2.5 \text{ cm}^2$ films were immersed in a quartz cuvette containing 20% (v/v) methanol/water solutions. The films were retained parallel to the cuvette wall during the entire irradiation time. The samples were kept in the dark for 60 min and then irradiated with a 450 W Xe lamp equipped with a water filter and a WG320 filter to block UV-B and UV-C light. The spectral irradiance was measured by a SpectraRad (BWTEK) irradiance meter. The irradiance spectrum is shown in appendix A (Figure A2, appendix A). The photon flux density (J) between 300 and 400 nm was $2200 \mu\text{mol cm}^{-2} \text{ h}^{-1}$. The system was closed and argon was bubbled to remove O₂ and N₂. Periodically, 0.500 ml of the overhead atmosphere were collected and analyzed by gas chromatography (Shimadzu GC-8 A; TCD detector). The photonic efficiency⁴⁴⁻⁴⁶ for the H₂ evolution (ξ) was calculated using Equation 1, with the rate of the H₂ evolution being given in $\mu\text{mol cm}^{-2} \text{ h}^{-1}$.

$$\xi = \frac{2 \times \text{rate}}{J}$$

Qualitative detection of the gases produced during the photolysis and photoelectrochemical experiments was also obtained by connecting the photoelectrochemical cell direct to a quadrupole mass spectrometer for gas analysis (Hiden HPR-20)^{47,48}. Argon (5 ml min^{-1}) was used as carrier gas.

3.5. Results and discussion

3.5.1. Film assembly and characterization

Lamellar $\text{K}_4\text{Nb}_6\text{O}_{17}$ was successfully synthesized by the solid state methodology previously reported^{40,41}. Its structure was confirmed by XRD and corresponds to $\text{K}_4\text{Nb}_6\text{O}_{17}\cdot 3\text{H}_2\text{O}$ (JCPDS 21-1297). After exfoliation with TBA(OH), the lamellar structure is lost as observed by XRD analysis of the powder precipitated as $\text{K}_{4-x}\text{H}_x\text{Nb}_6\text{O}_{17}$. Additionally, the diffractogram confirms that the in-plane crystalline order within the individual layers persisted after the exfoliation⁴⁹⁻⁵¹. The X ray diffractograms of both, the stacked and the exfoliated hexaniobates can be found in Appendix A (Figure A3). The exfoliated $\text{K}_{4-x}\text{H}_x\text{Nb}_6\text{O}_{17}$ exhibits an indirect band gap of 3.7 eV (Figure A4, appendix A), similar to the values reported before¹⁶, but an absorption tail up to 390 nm can be observed, probably due to the presence of defects that lead to the appearance of intraband gap states. The Urbach tail plot (Figure A5) exhibits a linear behaviour between 3.0–3.5 eV and thus corroborates with this conclusion.

The exfoliated $\text{Nb}_6\text{O}_{17}^{4-}$ sheets remain as a stable suspension at pH = 8 or above. They can also curl depending on the ionic strength of the medium to form scrolls. The free energy related to the curling/uncurling of the niobate nanosheets is relatively small⁵¹ and, thus we expect that both morphologies are present in suspensions at pH = 8. As the FTO substrate is alternatively immersed in the hexaniobate suspension and in the PAH (pH = 4) solution, the LbL films start to be deposited through electrostatic interactions between the $\text{Nb}_6\text{O}_{17}^{4-}$ layers and the polycation. The film growth can be followed by UV–vis absorption spectroscopy as shown in Fig. 1. As the number of deposited bilayers increases, the attenuation (absorbance plus losses due to scattering) between 320–380 nm increases as well as the light scattering in the visible range of the spectrum. If the attenuation at 380 nm is plotted as a function of the number of bilayers, a linear behavior can be observed (Fig. 1, inset), indicating that the same amount of material is deposited after each deposition cycle up to 25 bilayers. Further evidence for this conclusion is given by the linear variation of the photonic efficiency for H_2 evolution as function of the number of bilayer (section 3.5.2). LbL films do not have well defined interfaces, each individual layer cannot be identified separately and it is expected that the polyelectrolytes' segments can interpenetrate along the film stacking axis for 3–4 superior layers^{52,53}. The deposition of each layer is controlled by electrostatic interactions with

the film surface and ends spontaneously when the charge of the substrate is reversed. By controlling the deposition conditions, this process can be repeated several times with the same amount of material being deposited after each cycle ⁵⁴.

Similar behavior was observed for other nanoparticulate metal oxide LbL films ^{55,56} and, more recently by Xu et al ⁵⁷, for films assembled with metal oxide nanosheets and poly(diallyldimethylammonium chloride), PDDA, as polycation. When $[\text{Pt}(\text{NH}_3)_4]^{2+}$ is adsorbed to the hexaniobate sheets prior the film deposition, no significant changes are observed in the LbL assembly (Fig. 1, inset). This can most likely be explained by the fact that the amount of $[\text{Pt}(\text{NH}_3)_4]^{2+}$ was determined to ensure that the final film could have approximately 1% Pt⁰ (m/m) in relation to the hexaniobate. Consequently, only approx. 4% of the surface charges of the hexaniobate sheets could be neutralized by the cationic $[\text{Pt}(\text{NH}_3)_4]^{2+}$ precursor.

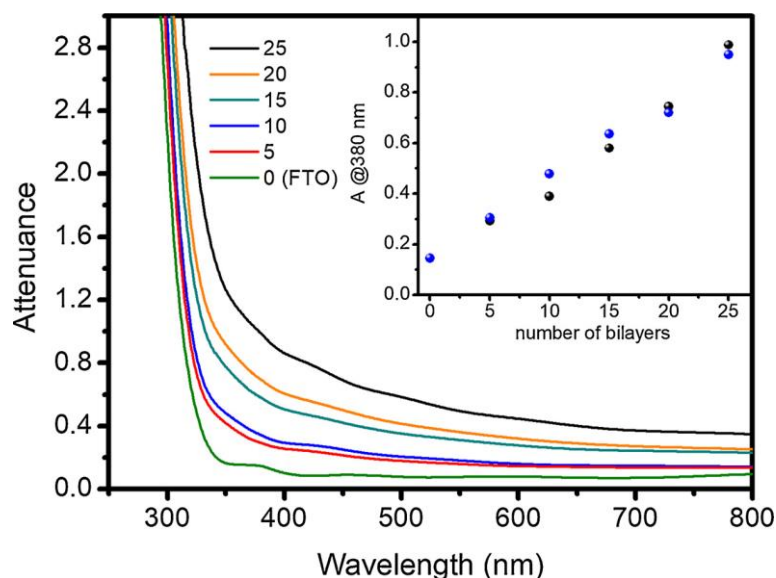


Fig. 1. UV-vis absorption spectra of $\text{Nb}_6\text{O}_{17}^{4-}/\text{PAH}$ bilayers deposited on FTO glass substrates. Inset: Plot of the attenuance at 380 nm as a function of the number of $\text{Nb}_6\text{O}_{17}^{4-}/\text{PAH}$ (●) or $(\text{Nb}_6\text{O}_{17}^{4-}[\text{Pt}(\text{NH}_3)_4]^{2+})/\text{PAH}$ (●) deposited bilayers.

The resulting films were treated at 500 °C for 30 min to ensure mechanical stability and also to remove most of the organic content, namely the PAH chains and possibly TBA^+ cations adsorbed on the film surface. Thermogravimetric analysis of PAH evidences that the polymer is decomposed after 450 °C (Figure A6, appendix A). The FTIR spectrum of non-sintered film, Fig. 2a, clearly shows a broad band between 3500 and 2500 cm^{-1} in which, besides the O–H stretching vibrations from adsorbed water, the N–H stretching can be identified at 3400 cm^{-1} and the C–H symmetric and asymmetric

stretching vibrations at 2920 and 2850 cm^{-1} , respectively. These bands confirm the presence of the polymeric chains on the FTO surface. Additionally, the peaks at 1630 and 1420 cm^{-1} correspond, respectively, to the asymmetric angular deformation of N–H bonds and the angular C–H deformation⁵⁸. After sintering, Fig. 2b, the intensity of these peaks is strongly decreased, while peaks at 900 cm^{-1} and in the 700-400 cm^{-1} region are still observed. These peaks are associated, respectively, to the Nb=O and the O-Nb-O stretching in the $[\text{NbO}_6]$ octahedron¹⁶. Raman spectrum of the sintered hexaniobate films, Fig. 2b inset, corroborates with the findings observed by FTIR. The characteristic $[\text{NbO}_6]$ peaks at 242 cm^{-1} (Nb-O-Nb angular deformation) and at 680 cm^{-1} (Nb-O stretching vibration)⁵⁹ are clearly observed. Additionally, the Nb=O stretching vibration at 945 cm^{-1} can also be observed.

XPS analysis of the sintered films does not reveal any signal in the expected N-1 s peak region, which further corroborate with the fact that the as prepared LbL hexaniobate film has none or less than 5% wt. carbon content after being thermally treated at 500 °C. Despite the presence of O^{2-} and Nb^{5+} ions, XPS data also reveal the presence some K^+ cations that along with protons ensure the electroneutrality of the films (Figure A7, appendix A). Thus, the LbL technique followed by the thermal treatment allowed to successfully deposit $\text{K}_{4-x}\text{H}_x\text{Nb}_6\text{O}_{17}$ nanostructures on FTO surfaces using a polymeric cation that can be further removed by thermal treatment at 500 °C.

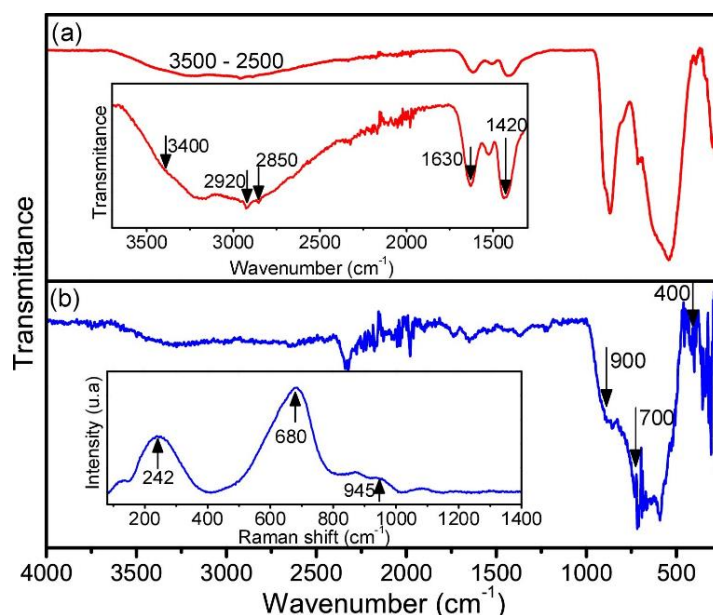


Fig. 2. FTIR spectra of the non-sintered (a) and 500 °C sintered (b) hexaniobate/PAH LbL film. The inset in (a) shows the N–H and C–H stretching vibrations in detail. In (b) the inset refers to the Raman spectrum of the sintered film.

The morphology of the hexaniobate LbL films was evaluated by FESEM and AFM, Fig. 3a. Additional images were added to the appendix (Figure A8). The FE-SEM images show that the film is constituted by relatively long hexaniobate nanoscrolls randomly distributed over the FTO surface. As the electrostatic interactions between the hexaniobate anions and the polycation occur, it seems that the scrolled morphology is favored in relation to the opened sheets. The nanoscrolls exhibit diameters of around 50 nm. In comparison with the results found by Xu et al. employing different niobates and PDDA as polycation⁵⁷, a completely different morphology was observed, which then allows us to conclude that the deposition conditions as well as the choice of the polycation plays a crucial role for the final film morphology. While the molecular structure of the polyelectrolyte determines the charge distribution along the polymer chain, the deposition conditions (pH, concentration, ionic strength) define the morphology of the niobate (scrolled or opened sheets). The thickness of the LbL hexaniobate films were estimated by AFM taking the difference in the Z values between the film and the FTO surfaces. The estimated values after 5, 15, and 25 bilayers were 0.7 ± 0.2 , 1.5 ± 0.4 , and 1.8 ± 0.5 μm , respectively. As the hexaniobate scrolls are not orderly arranged, the film thickness does not vary linearly with the number of bilayers. For films containing platinum species the measured thicknesses were 0.4 ± 0.1 , 1.0 ± 0.5 , and 1.5 ± 0.4 μm , experimentally similar to those found for the bare hexaniobate films. Moreover, bright spots can be observed spreading around the surface of the hexaniobate nanoscrolls which are associated to the formation of Pt^0 nanoclusters of less than 1–2 nm, Fig. 3(b). Oshima et al. reported the use of the adsorption properties of 2D hexaniobate nanosheets to produce photocatalysts with highly dispersed metallic nanoclusters⁴². The results presented here evidence that such properties can be conveniently combined with the layer-by-layer technique to obtain photocatalytic surfaces based on such composites.

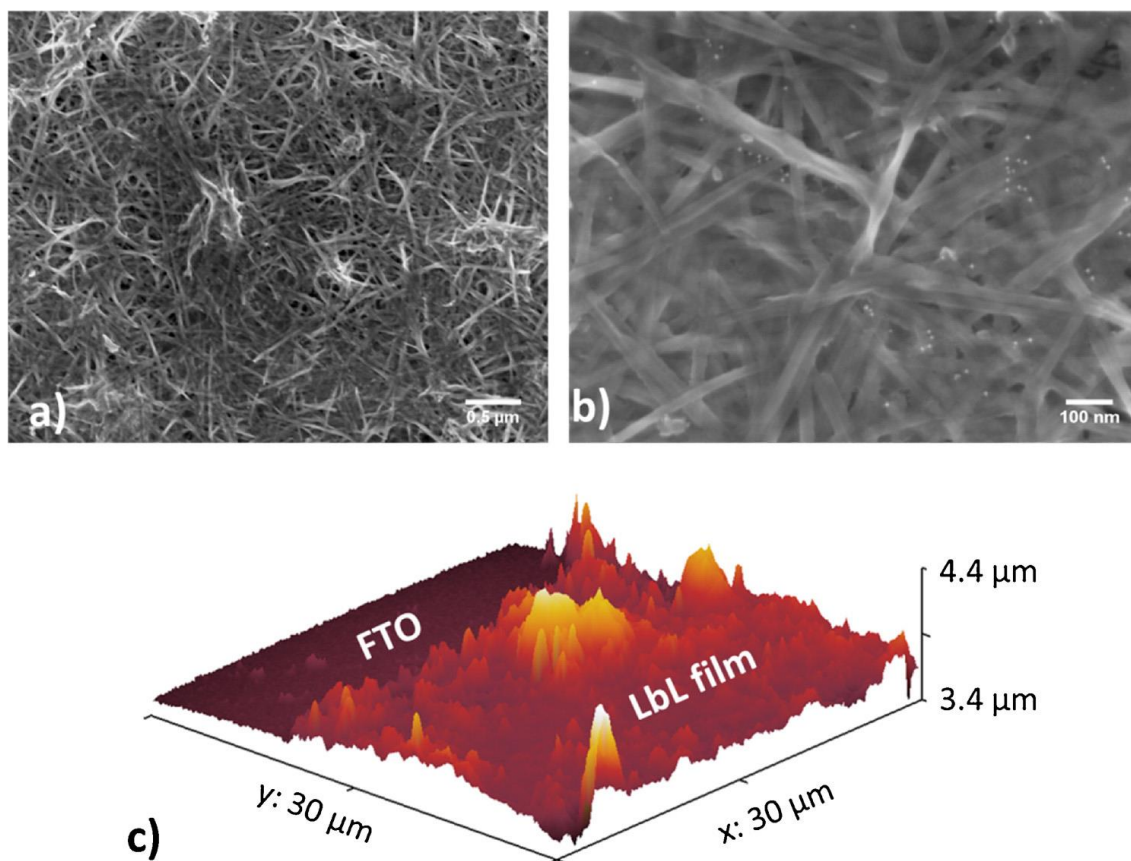


Fig. 3. (a) FE-SEM image of the surface of bare hexaniobate LbL films with 25 bilayers; (b) Pt-modified hexaniobate LbL films with 25 bilayers (the bright small spots are Pt nanoclusters); (c) AFM image showing the topology of bare hexaniobate LbL films with 15 bilayers.

Despite the fact that previous thermochemical data for the precursor $[\text{Pt}(\text{NH}_3)_4]\text{Cl}_2$ show that Pt^0 is its main decomposition product above $320\text{ }^\circ\text{C}$ ⁶⁰, XPS analysis of the Pt-modified hexaniobate LbL films reveals that after sintering the films at 500° in air, only 34% of the platinum species are converted into Pt^0 , with the remaining fraction staying as Pt^{2+} species, see Fig. 4(a). This difference is likely associated to the interaction between the Pt(II)tetraammine complex and the hexaniobate anions. Thus, an additional step is necessary to fully convert the Pt^{2+} species into Pt^0 . This was achieved by UV-A illumination of the films immersed in water/methanol mixtures (8:2 v/v). As shown in Fig. 4(b), continuous irradiation of the film leads to the reduction of Pt^{2+} species to Pt^0 .

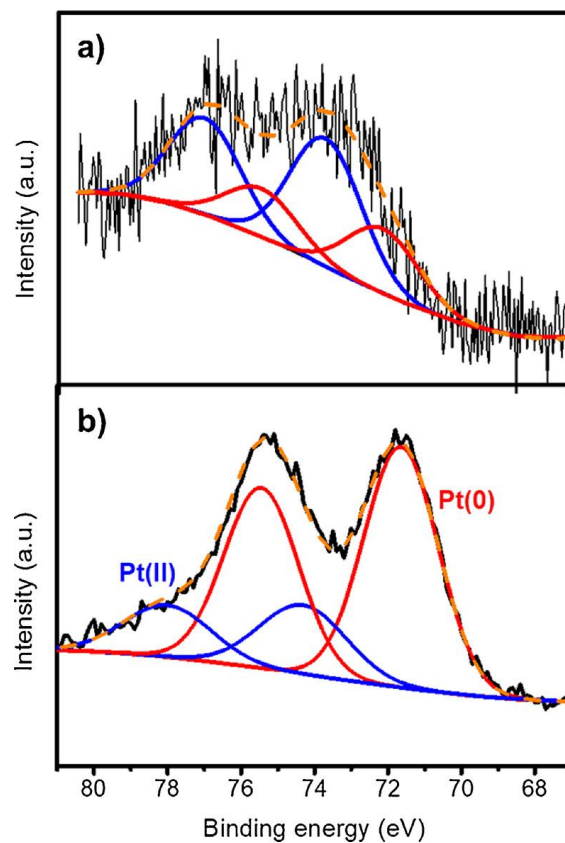


Fig. 4. XPS spectra (—) in the Pt 4f peak region of the Pt-modified hexaniobate LbL films before (a) and after (b) UV-A irradiation. The curves were fitted as a sum (- - -) of duplets related to Pt(II) (—) and Pt(0) (—) species.

3.5.2. Photocatalytic H₂ evolution

The photocatalytic activity of the hexaniobate LbL films was evaluated in water/methanol mixtures under UV-A irradiation. Under these conditions methanol acts as hole scavenger and electrons are transferred to water to produce molecular hydrogen. The rate for H₂ evolution was evaluated during up to 8 h of irradiation for LbL films with different amounts of deposited layers. A typical measurement is shown in Fig. 5a.

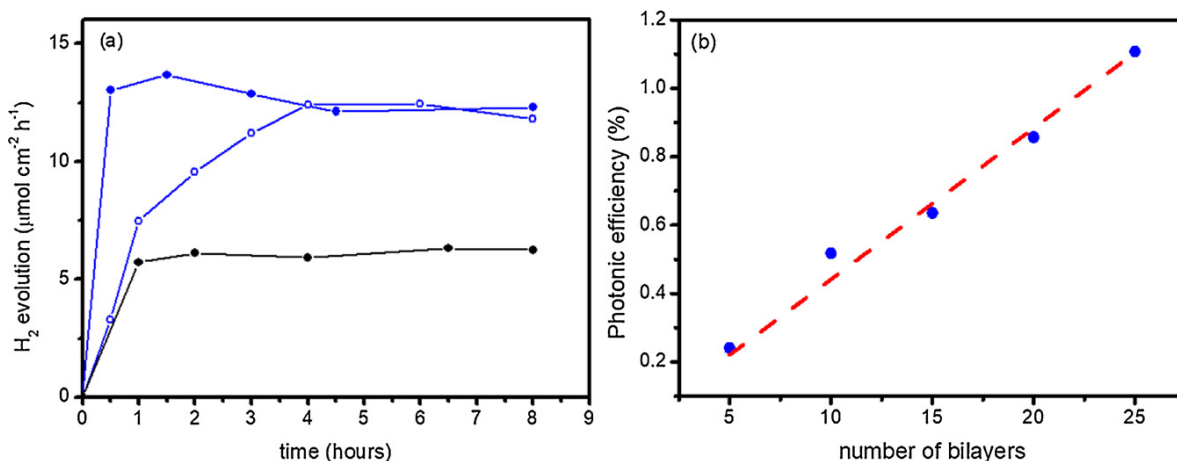


Fig. 5. (a) H₂ evolution rates in water/methanol mixtures using hexaniobate LbL films with 25 bilayers as photocatalysts: (●) bare films, (○) as prepared Pt-modified films and (●) previously irradiated Pt-modified films. (b) Photonic efficiency for the photochemical H₂ evolution in Pt-modified hexaniobate LbL films as a function of the number of deposited bilayers.

Even bare hexaniobate LbL films are able to catalyze the H₂ evolution from water/methanol mixtures without the presence of a cocatalyst. On thermodynamic grounds this is expected as the conduction band of K_{4-x}H_xNb₆O₁₇ has more negative reduction potentials than the H⁺/H₂ redox couple ($E^{\circ}_{CB} \approx -0.75$ V *vs* NHE^{61,62}). As the Pt nanoclusters are added to the film composition, the observed rates are approx. two times higher than those for the bare hexaniobate LbL films. In Fig. 5a, it is also possible to note the effect of the pre-irradiation of the Pt-modified films on the photocatalytic behavior. In the as-prepared films a significant fraction (66%) of the platinum species are still oxidized. Thus, during the first three hours, part of the photogenerated electrons are used to reduce these species to Pt⁰ hence reducing the H₂ evolution rate. As Pt⁰ is produced the gas evolution rate steadily increases up to the values observed for the pre-irradiated films. For the later, maximum H₂ evolution rates are observed promptly, that is after only 30 min of irradiation. The influence of the number of deposited layers on the H₂ evolution photonic efficiency is shown in Fig. 5b for Pt modified films. It can be clearly seen that the photonic efficiency increases linearly with the number of deposited layers, which corroborates with the spectrophotometric measurements (Fig. 1) and indicate that the same amount of material is deposited after each deposition cycle. As the light harvesting efficiency (LHE) of the films increases due to the greater amount of deposited material, the photonic efficiency also increases. This means that all

photocatalytic sites in the LbL film remains active, even those located in the inner layers. If only the absorbed fraction of light is considered ⁴⁴⁻⁴⁶, the apparent quantum yield determined for the Pt-hexaniobate LbL films is $4.0 \pm 0.5\%$, which is in the same order that the values reported for suspensions using the same photocatalyst ^{16,63}.

Therefore, along with the cost-effectiveness, the layer-by-layer technique allows the immobilization of the lamellar photocatalyst films with different thicknesses in a wide range of substrates without losses in the photoactivity. It seems that the methanol molecules can diffuse into the film and effectively act as hole scavenger, which is followed by the reduction of protons to hydrogen by the photogenerated electrons. The effective penetration of methanol in the interspace of the stacked $K_4Nb_6O_{17}$ was shown before by Ebina et al. ⁶⁴. This behavior was also corroborated by Sarahan and coworkers who did not observe great improvement in the photocatalytic H_2 evolution using different $K_4Nb_6O_{17}$ morphologies (stacked, nanosheets or nanoscrolls) ¹⁶. For the LbL films assembled with PAH as polycation, the mobility of the methanol molecules through the layers is maintained. Moreover, the adsorption of the cationic Pt^0 precursors leads to the creation of very small metallic nanoclusters which the role as co-catalysts is not hidden due to the deposition of multiple layers.

3.5.3. Photoelectrochemical properties

In order to better understand the charge mobility in the LbL hexaniobate films, photoelectrochemical measurements were carried out under UV-A irradiation employing the bare hexaniobate LbL films as working electrodes, Ag/AgCl (3 M NaCl) as reference electrode and a Pt-wire as counterelectrode. $0.1 \text{ mol L}^{-1} K_2SO_4$ aqueous solutions (pH = 6.0) were employed as supporting electrolyte. As expected for a *n*-type semiconductor, the hexaniobate LbL films exhibit anodic photocurrents, Fig. 6(a). As shown in Fig. 6(b), distinct behaviors are observed as a function of the number of deposited bilayers when the photocurrents are measured in K_2SO_4 aqueous solution or in the presence of alcohols such as methanol and isopropanol.

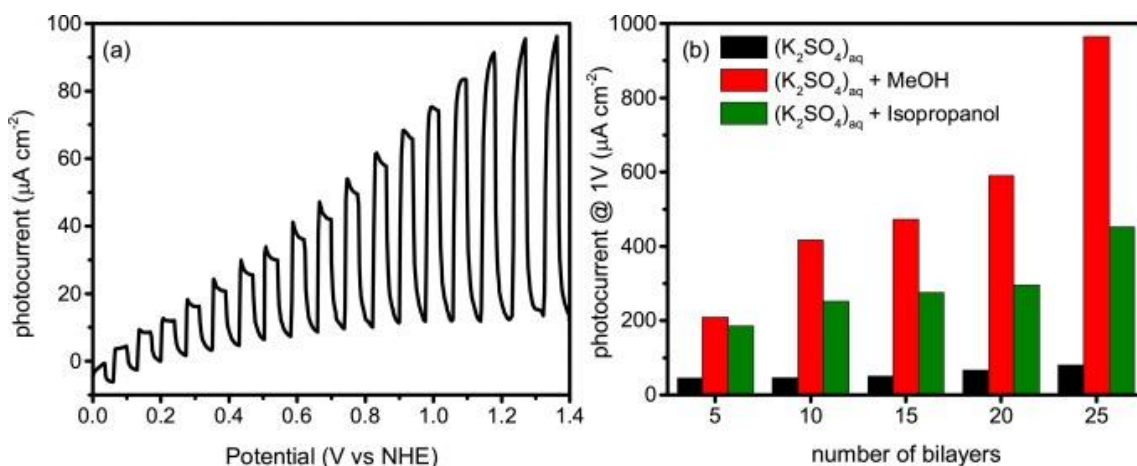


Fig. 6. (a) First sweep cyclic voltammogram (20 mV s^{-1}) of a hexaniobate LbL film (25 bilayers) in $0.1 \text{ mol L}^{-1} \text{ K}_2\text{SO}_4$ aqueous solution. (b) Variation of the photocurrent at 1 V vs NHE when different electrolyte compositions are used.

In aqueous K_2SO_4 solution in the absence of any alcohol, only a 2-fold enhancement in the photocurrent is observed as the number of deposited layers increases from 5 to 25. When 10% v/v methanol is added to the electrolyte, higher photocurrents are observed as a result of the alcohol oxidation and also the occurrence of the so-called current doubling effect⁶⁵. The photocurrents for the LbL films with 25 bilayers are approximately five times higher than those observed for films with 5 bilayers, but no linear enhancements could be observed as a function of the number of bilayers probably due to experimental variations. The increase in the photocurrent with the number of deposited layers is different than that reported by Izawa et al.³⁸ who investigated LbL films of different oxide-based nanosheets, assembled with La^{3+} as counter-ion. They observed that the photocurrent in the presence of methanol was independent from the number of bilayers (varied between 1 and 4).

In a photoelectrochemical cell, the photocurrent (I_{photo}) is proportional to the product of the light harvesting efficiency (LHE) and the quantum yields of charge transport (Φ_{CT}) and charge separation (Φ_{CS}), i.e. $I_{\text{photo}} \propto \text{LHE} \times \Phi_{\text{CT}} \times \Phi_{\text{CS}}$ ⁶⁶. Thus, a possible explanation for the different behaviors described above can be found by analyzing these three parameters. The photochemical H_2 evolution measurements indicate that the LHE depends linearly with the number of the deposited layers, hence changes in Φ_{CT} or in Φ_{CS} should be occurring as a function of the electrolyte composition.

The charge transport properties of the films can be evaluated by electrochemical impedance spectroscopy (EIS). In Figure A9 (appendix A), the Nyquist plots for EIS

measurements carried out in plain K_2SO_4 aqueous solution under illumination and upon 1 V applied potential are shown. The impedance of the system is dominated by the charge transfer between the photoanode and the electrolyte and is characterized by the incomplete semicircle observed in the Nyquist plots (Figure A9). The experimental plots can be successfully fitted to the equivalent circuit described by Xu et al.⁵⁷ (Figure A9 inset) and the fit parameters are listed in Table A2. The analysis of the EIS data reveals that the overall impedance of the photoanode does not vary significantly with the number of bilayers. The charge transfer resistance (R_{ct}) and the respective capacitance related to the photoanode/electrolyte interface do not vary greatly as the number of bilayers increases. This fact indicates that the films have good electron transport properties between the layers. As evidenced by the electron microscopy images, the LbL films are not composed of individual layers. Thus, the electron transport properties are mainly controlled by the intrinsic properties of the hexaniobate and not by the number of bilayers deposited.

Therefore, if the charge transport properties within the film are nearly independent upon the number of bilayers, the distinct behavior observed in the plain aqueous electrolyte and in the presence of methanol can only be explained by differences in the charge separation processes at the photoanode/electrolyte interface. It is well-known that photooxidation of methanol on oxide surfaces is a one electron process that occurs within hundreds of fs after photoexcitation⁵. As the small methanol molecule can have access to all active sites in the film, a linear increase in the photocurrent is observed as a function of the number of deposited bilayers. If a more bulky alcohol, such as isopropanol, is used as sacrificial reagent, Fig. 6(b), improvements in the photocurrent can still be observed in relation to those measured in the plain electrolyte, however the linearity with the number of bilayers is lost. Even being easily oxidized, the size of the isopropanol molecules avoid their access to all active sites in the films with higher number of deposited layers.

On the other hand, in the absence of alcohols the photoexcitation of the hexaniobate films should promote the oxidation of water. Compton and Osterloh⁶⁷ have shown that the photochemical water splitting in niobate nanosheets leads to production of hydrogen peroxide ($2\text{H}_2\text{O} \rightarrow \text{H}_2 + \text{H}_2\text{O}_2$). The authors have shown that hydrogen peroxide can be formed by two distinct pathways: one involving one electron reduction of O_2 and a second one involving the two electron oxidation of water (in the absence of O_2), i.e., $2\text{H}_2\text{O} + 2h_{\text{VB}}^+ \rightarrow \text{H}_2\text{O}_2 + 2\text{H}^+$, where h_{VB}^+ is the photogenerated hole at the photocatalyst. In fact, long term photolysis experiments in deaerated water allowed us to accumulate peroxide

species in the film surface. The peroxides could be detected by Raman spectroscopy, Figure A10(a), where a small intensity band at 875 cm^{-1} appeared after irradiation corresponding to the O–O stretching vibration of peroxy groups, generally found between $850\text{--}910\text{ cm}^{-1}$ when bound to metal centers⁶⁸. Additionally, a broadening of the Nb–O stretching band at 680 cm^{-1} can be observed, which is correlated to changes in the coordination environment of the Nb^{+5} ions due to the peroxide formation.

Further evidence for the peroxide formation was found by exposing the film to o-tolidine solutions, a well-known redox indicator for peroxide detection⁶⁹. The appearance of an absorption peak at 438 nm indicates the two electron oxidation of o-tolidine by the peroxides to form a diimine, Figure A10(b). The possible gaseous products produced during a photoelectrochemical assay carried out at 1 V vs NHE during UV-A illumination were also analyzed by mass spectrometry. For that, the photoelectrochemical cell was connected to the mass spectrometer and argon was used as carrier gas, Fig. 7. Only H_2 was produced during the photoelectrolysis, thus ruling out the possible O_2 evolution.

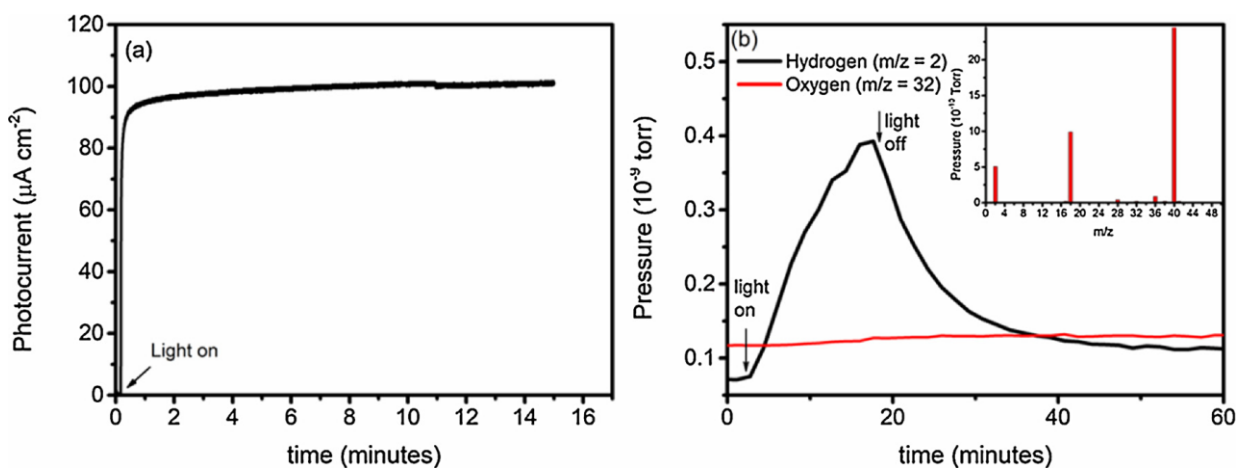


Fig. 7. (a) Chronoamperometry of an LbL hexaniobate film (25 bilayers) in 0.1 mol L^{-1} K_2SO_4 solution upon 1 V vs NHE. (b) Gases detected during the chronoamperometric measurements. In the inset an example of a mass spectrum in a given elapsed time is shown.

The formation of the surface bound peroxides is evidently slower than the one electron oxidation of methanol or isopropanol and therefore cannot compete efficiently with the electron hole recombination, limiting the observed photocurrent. As discussed by Compton and Osterloh⁶⁷, the reaction involves specific sites in the niobate layers, which cannot be directly correlated with the number of deposited bilayers in the hexaniobate LbL films. Thus, the photoactivity of the LbL hexaniobate films for the water

splitting process is apparently limited by the formation of surface-bound peroxides. Nevertheless, the films exhibit excellent photoactivity for the oxidation of small molecules, such as methanol, leading to efficient H₂ evolution.

3.6. Conclusions

In the present work, the deposition of layer-by-layer (LbL) thin films based on K₄H_{4-x}Nb₆O₁₇ is described. The films are composed of fuzzy assembled hexaniobate nanoscrolls, which can be conveniently used for the deposition of metallic Pt nanoclusters. UV-A irradiation of such films in water/methanol mixtures leads to the evolution of H₂ with apparent quantum yields of 4%, which is comparable with values obtained for suspensions of the same photocatalyst. These findings evidence the effectiveness of the LbL technique as a low-cost, up scalable technique to produce photoactive surfaces. Electrochemical Impedance measurements of the films reveal that the overall capacitance of the films is dominated by intrinsic properties of the niobate, rather than by the film thickness. Moreover, irradiation of the films in plain water leads to the formation of stable surface peroxides that limit the application for water splitting. The possibility to use the excellent adsorption properties of the layered materials for the production of LbL films can be effectively employed to tune the reactivity of these materials for photocatalytic processes.

3.7. Supporting Information

Figure A1. (a) ^1H NMR spectrum of $[\text{Pt}(\text{NH}_3)_4]\text{Cl}_2$ in D_2O ; (b) (a) ^{195}Pt NMR spectrum of $[\text{Pt}(\text{NH}_3)_4]\text{Cl}_2$ in D_2O

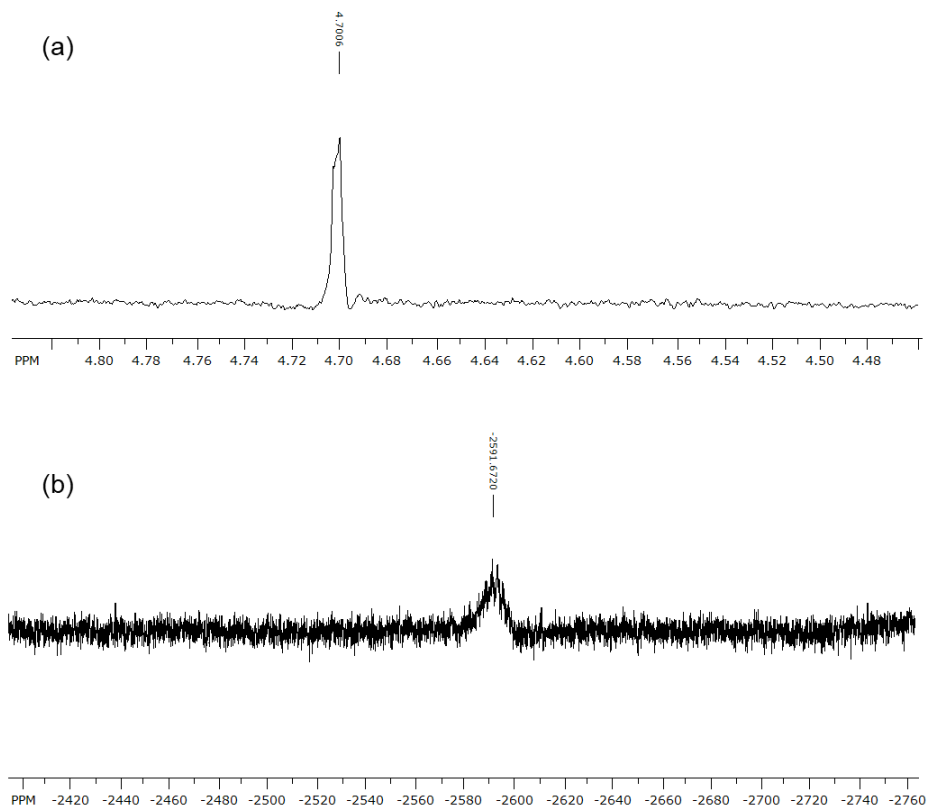


Table A1. Elemental analysis for $[\text{Pt}(\text{NH}_3)_4]\text{Cl}_2 \cdot \text{H}_2\text{O}$

	%C	%H	%N
Calculated	-	4.01	15.91
Obtained	0.09	3.98	15.95

Figure A2. Irradiance spectrum of the Xe lamp employed in the H₂ evolution measurements (a WG 320 filter, along with a water filter was also used in the experiments).

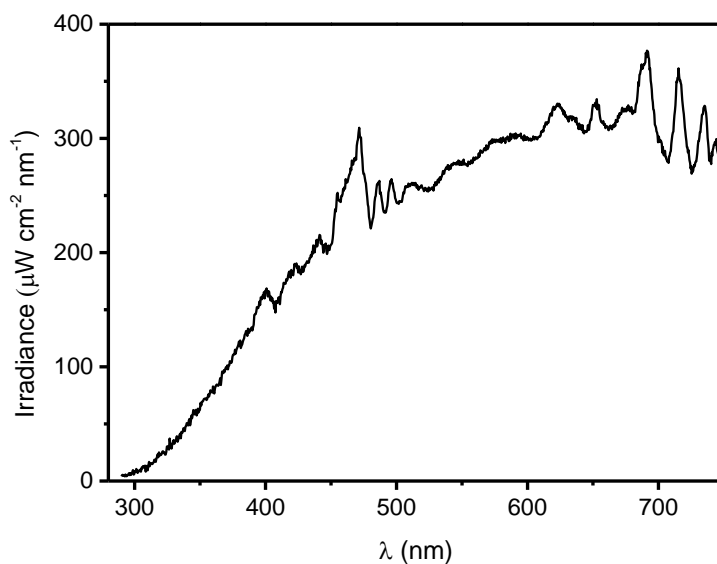


Figure A3. X ray diffractograms of the stacked and exfoliated hexaniobates

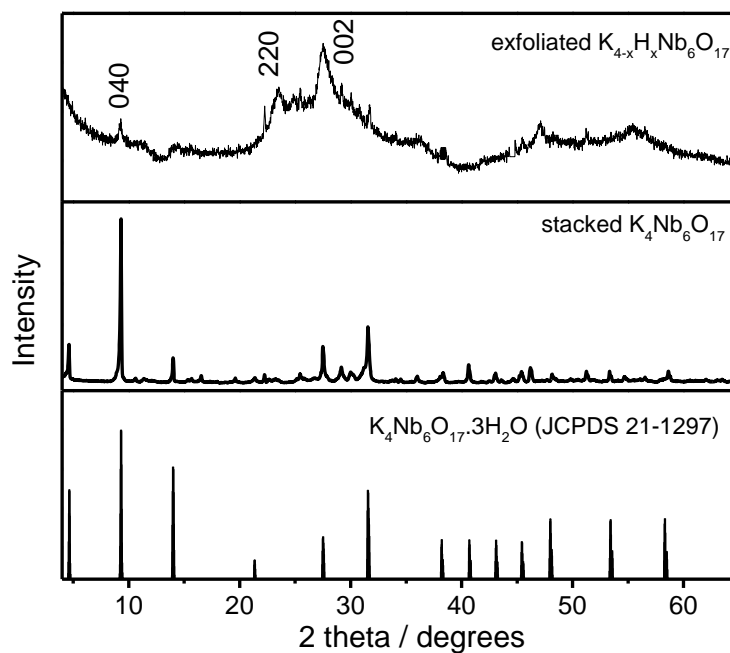


Figure A4. Reflectance spectrum of the exfoliated hexaniobate precipitated as $K_{4-x}H_x(Nb_6O_{17})$. *Inset:* Tauc plot for the band gap determination.

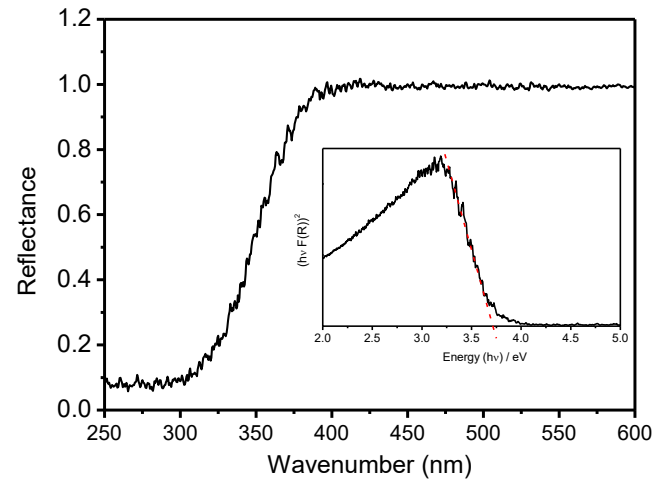


Figure A5. Urbach tail plot of the exfoliated hexaniobate precipitated as $K_{4-x}H_x(Nb_6O_{17})$.

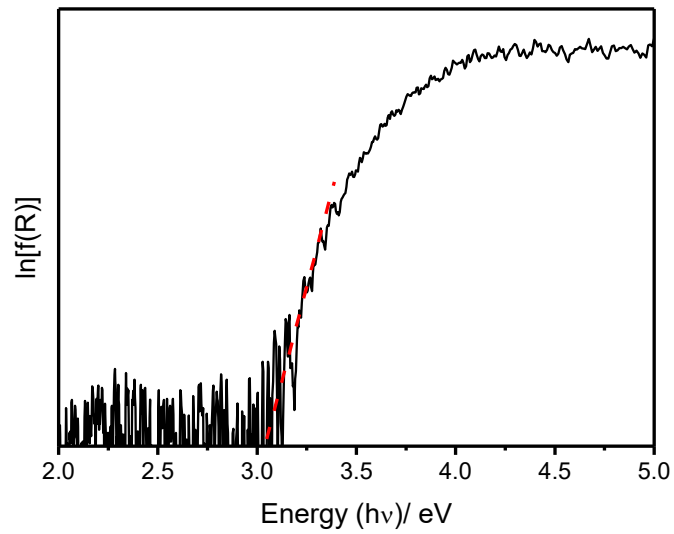


Figure A6. Thermogravimetric analysis of PAH in air (heating rate: $10\text{ }^{\circ}\text{C min}^{-1}$).

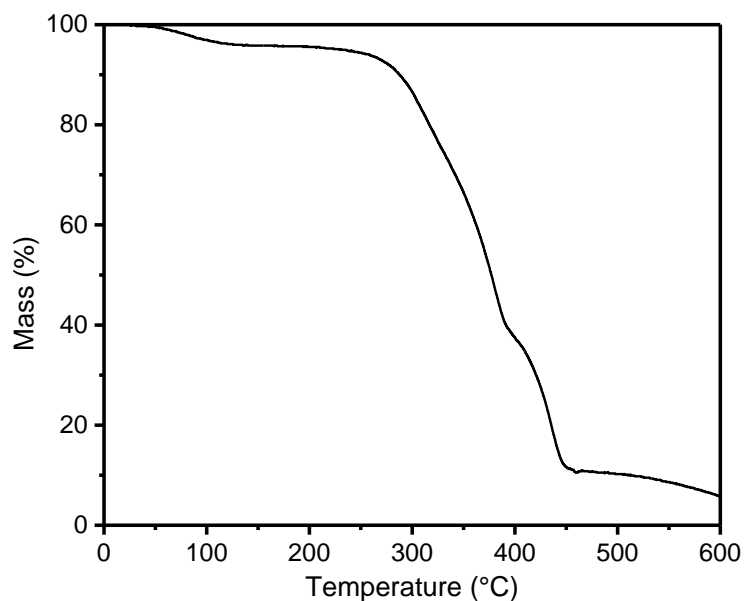


Figure A7. XPS spectra of the hexaniobate LbL film after sintering at 500°C . Survey spectrum (a) and high resolution spectrum at O 1s (b), Nb 3d (c) and K 1s (d) regions.

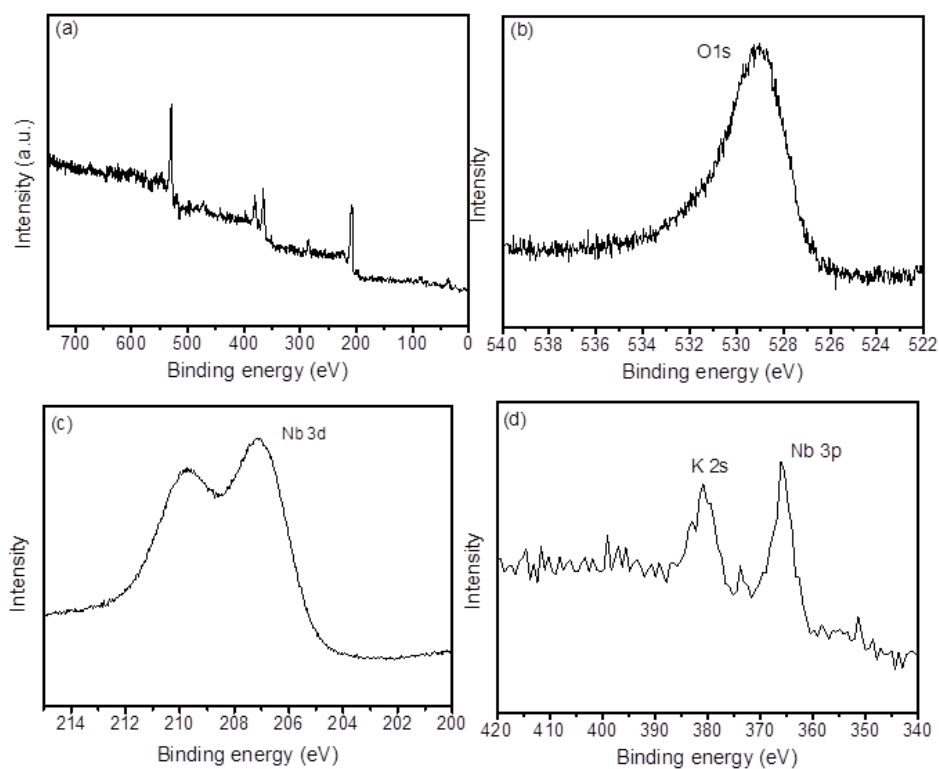


Figure A8. AFM images of the surface of the bare Nb₆O₁₇/PAH LbL films with 5 (a) or 25 (b) deposited bilayers and of the Pt-modified films with 15 (c) and 25 (d) deposited bilayers

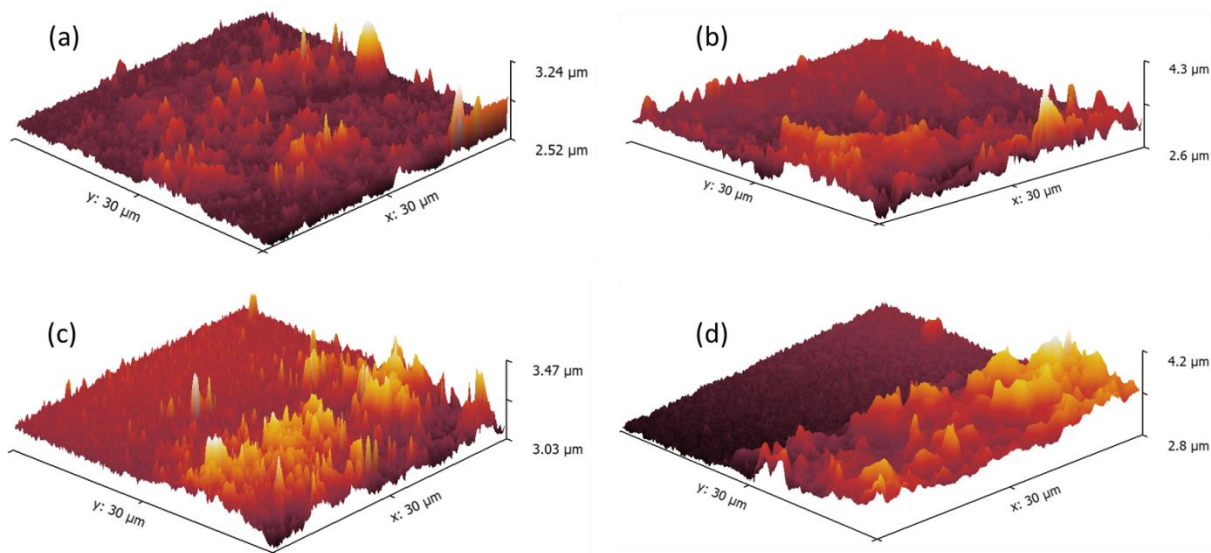
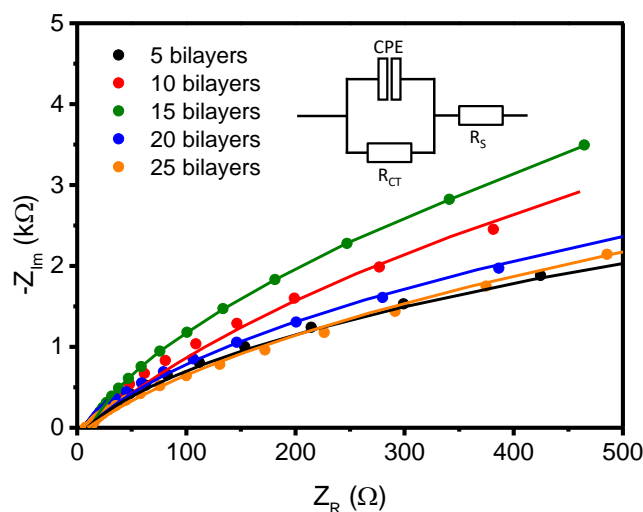


Figure A9. EIS measurements (Nyquist plots) under UV-A illumination and 1 V applied potential of hexaniobate LbL films as a function of the number of deposited bilayers. The lines correspond to the fit of the experimental points to the equivalent circuit shown as inset.



In the equivalent circuit, R_S represents the series resistance of the experimental setup, R_{CT} accounts for the charge transfer at the electrolyte/electrode interface and a CPE (constant phase element) was employed to describe the capacitance in this interface. The effective

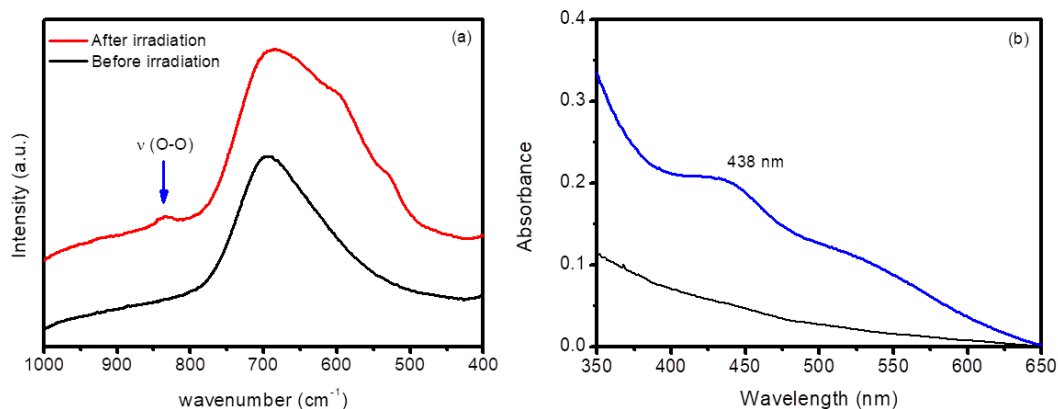
capacitance of the CPE was calculated using the model proposed by Brug et al.⁷⁰, Equation A1, where T and n are frequency-independent parameters. The fitting parameters are listed in the Table A2 (appendix A).

$$C_{CPE} = T^{1/n} \left(\frac{R_S R_{CT}}{R_S + R_{CT}} \right)^{(1-n)/n} \quad (A1)$$

Table A2. Fit parameters employed for fitting EIS data as a function of the number of bilayers

Bilayers	R_s (Ω)	R_{ct} ($k\Omega$)	T	n	C (μF)
5	9.35	13	3.00E-05	0.95	19.5
10	10.46	21	3.00E-05	0.95	19.6
15	10.21	23	2.50E-05	0.96	18.0
20	9.9	18	2.90E-05	0.95	19.0
25	9.8	19	3.40E-05	0.93	18.6

Figure A10. (a) Raman spectra of the hexaniobate LbL film (20 bilayers) before and after UV-A irradiation in plain water; (b) electronic absorption spectra of a *o*-toluidine solution before (black) and after (blue) being exposed to the irradiated hexaniobate LbL film (20 bilayers) having surface-bound peroxides.



3.8. References

- (1) Song, W.; Chen, Z.; Brennaman, M. K.; Concepcion, J. J.; Patrocinio, A. O. T.; Murakami Iha, N. Y.; Meyer, T. J. Making Solar Fuels by Artificial Photosynthesis. *Pure Appl. Chem.* **2011**, *83* (4), 749–768. <https://doi.org/10.1351/PAC-CON-10-11-09>.
- (2) Osterloh, F. E. Inorganic Materials as Catalysts for Photochemical Splitting of Water. *Chem. Mater.* **2008**, *20* (1), 35–54. <https://doi.org/10.1021/cm7024203>.
- (3) Acar, C.; Dincer, I.; Zamfirescu, C. A Review on Selected Heterogeneous Photocatalysts for Hydrogen Production. *Int. J. Energy Res.* **2014**, *38* (15), 1903–1920. <https://doi.org/10.1002/er.3211>.
- (4) Patrocinio, A. O. T.; Schneider, J.; Franca, M. D.; Santos, L. M.; Caixeta, B. P.; Machado, A. E. H.; Bahnemann, D. W. Charge Carrier Dynamics and Photocatalytic Behavior of TiO₂ Nanopowders Submitted to Hydrothermal or Conventional Heat Treatment. *RSC Adv.* **2015**, *5* (86), 70536–70545. <https://doi.org/10.1039/c5ra13291f>.
- (5) Schneider, J.; Matsuoka, M.; Takeuchi, M.; Zhang, J.; Horiuchi, Y.; Anpo, M.; Bahnemann, D. W. Understanding TiO₂ Photocatalysis: Mechanisms and Materials. *Chem. Rev.* **2014**, *114* (19), 9919–9986. <https://doi.org/10.1021/cr5001892>.
- (6) Nosaka, Y.; Nosaka, A. Y. Generation and Detection of Reactive Oxygen Species in Photocatalysis. *Chem. Rev.* **2017**, *117* (17), 11302–11336. <https://doi.org/10.1021/acs.chemrev.7b00161>.
- (7) Domen, K.; Kudo, A.; Tanaka, A.; Onishi, T. Overall Photodecomposition of Water on a Layered Niobate Catalyst. *Catal. Today* **1990**, *8* (1), 77–84. [https://doi.org/10.1016/0920-5861\(90\)87009-R](https://doi.org/10.1016/0920-5861(90)87009-R).
- (8) Domen, K.; Kudo, A.; Shinozaki, A.; Tanaka, A.; Maruya, K. I.; Onishi, T. Photodecomposition of Water and Hydrogen Evolution from Aqueous Methanol Solution over Novel Niobate Photocatalysts. *J. Chem. Soc. Chem. Commun.* **1986**, No. 4, 356–357. <https://doi.org/10.1039/C39860000356>.
- (9) Domen, K.; Kudo, A.; Shibata, M.; Tanaka, A.; Maruya, K.-I.; Onishi, T. Novel

- Photocatalysts, Ion-Exchanged $\text{K}_4\text{Nb}_6\text{O}_{17}$, with a Layer Structure. *J. Chem. Soc. Chem. Commun.* **1986**, No. 23, 1706. <https://doi.org/10.1039/c39860001706>.
- (10) Maeda, K.; Eguchi, M.; Oshima, T. Perovskite Oxide Nanosheets with Tunable Band-Edge Potentials and High Photocatalytic Hydrogen-Evolution Activity. *Angew. Chemie Int. Ed.* **2014**, *53* (48), 13164–13168. <https://doi.org/10.1002/anie.201408441>.
- (11) Maeda, K.; Eguchi, M.; Youngblood, W. J.; Mallouk, T. E. Calcium Niobate Nanosheets Prepared by the Polymerized Complex Method as Catalytic Materials for Photochemical Hydrogen Evolution. *Chem. Mater.* **2009**, *21* (15), 3611–3617. <https://doi.org/10.1021/cm9007766>.
- (12) Maeda, K.; Eguchi, M.; Lee, S.-H. A.; Youngblood, W. J.; Hata, H.; Mallouk, T. E. Photocatalytic Hydrogen Evolution from Hexaniobate Nanoscrolls and Calcium Niobate Nanosheets Sensitized by Ruthenium(II) Bipyridyl Complexes. *J. Phys. Chem. C* **2009**, *113* (18), 7962–7969. <https://doi.org/10.1021/jp900842e>.
- (13) Yin, G.; Nishikawa, M.; Nosaka, Y.; Srinivasan, N.; Atarashi, D.; Sakai, E.; Miyauchi, M. Photocatalytic Carbon Dioxide Reduction by Copper Oxide Nanocluster-Grafted Niobate Nanosheets. *ACS Nano* **2015**, *9* (2), 2111–2119. <https://doi.org/10.1021/nm507429e>.
- (14) Sabio, E. M.; Chamousis, R. L.; Browning, N. D.; Osterloh, F. E. Photocatalytic Water Splitting with Suspended Calcium Niobium Oxides: Why Nanoscale Is Better than Bulk – A Kinetic Analysis. *J. Phys. Chem. C* **2012**, *116* (4), 3161–3170. <https://doi.org/10.1021/jp209006n>.
- (15) Bizeto, M. A.; Shiguihara, A. L.; Constantino, V. R. L. Layered Niobate Nanosheets: Building Blocks for Advanced Materials Assembly. *J. Mater. Chem.* **2009**, *19* (17), 2512–2525. <https://doi.org/10.1039/b821435b>.
- (16) Sarahan, M. C.; Carroll, E. C.; Allen, M.; Larsen, D. S.; Browning, N. D.; Osterloh, F. E. $\text{K}_4\text{Nb}_6\text{O}_{17}$ -Derived Photocatalysts for Hydrogen Evolution from Water: Nanoscrolls versus Nanosheets. *J. Solid State Chem.* **2008**, *181* (7), 1678–1683. <https://doi.org/10.1016/j.jssc.2008.06.021>.
- (17) Shiguihara, A. L.; Bizeto, M. A.; Constantino, V. R. L. Exfoliation of Layered Hexaniobate in Tetra(n-Butyl)Ammonium Hydroxide Aqueous Solution.

- Colloids Surfaces A Physicochem. Eng. Asp.* **2007**, 295 (1–3), 123–129.
<https://doi.org/10.1016/j.colsurfa.2006.08.040>.
- (18) Nunes, B. N.; Paula, L. F.; Costa, Í. A.; Machado, A. E. H.; Paterno, L. G.; Patrocínio, A. O. T. Layer-by-Layer Assembled Photocatalysts for Environmental Remediation and Solar Energy Conversion. *J. Photochem. Photobiol. C Photochem. Rev.* **2017**, 32.
<https://doi.org/10.1016/j.jphotochemrev.2017.05.002>.
- (19) Decher, G.; Hong, J.-D. Buildup of Ultrathin Multilayer Films by a Self-Assembly Process, 1 Consecutive Adsorption of Anionic and Cationic Bipolar Amphiphiles on Charged Surfaces. *Makromol. Chemie. Macromol. Symp.* **1991**, 46 (1), 321–327. <https://doi.org/10.1002/masy.19910460145>.
- (20) Richardson, J. J.; Björnmalm, M.; Caruso, F. Technology-Driven Layer-by-Layer Assembly of Nanofilms. *Science (80-.)*. **2015**, 348 (6233).
<https://doi.org/10.1126/science.aaa2491>.
- (21) Jeon, D.; Kim, H.; Lee, C.; Han, Y.; Gu, M.; Kim, B.-S.; Ryu, J. Layer-by-Layer Assembly of Polyoxometalates for Photoelectrochemical (PEC) Water Splitting: Toward Modular PEC Devices. *ACS Appl. Mater. Interfaces* **2017**, 9 (46), 40151–40161. <https://doi.org/10.1021/acsami.7b09416>.
- (22) Faria, A. C. R.; Vebber, M. C.; Dal’Acqua, N.; Giovanela, M.; Aguzzoli, C.; Pereira, M. B.; Machado, G.; Crespo, J. S. Characterization and Application of Self-Assembled Thin Films of Polyelectrolytes/TiO₂/CdSe for Hydrogen Production. *Int. J. Hydrogen Energy* **2017**, 42 (26), 16568–16578.
<https://doi.org/10.1016/j.ijhydene.2017.05.080>.
- (23) Grandcolas, M.; Louvet, A.; Keller, N.; Keller, V. Layer-by-Layer Deposited Titanate-Based Nanotubes for Solar Photocatalytic Removal of Chemical Warfare Agents from Textiles. *Angew. Chemie Int. Ed.* **2009**, 48 (1), 161–164.
<https://doi.org/10.1002/anie.200802932>.
- (24) Teh, S. J.; Lai, C. W.; Hamid, S. B. A. Novel Layer-by-Layer Assembly of RGO-Hybridised ZnO Sandwich Thin Films for the Improvement of Photo-Catalysed Hydrogen Production. *J. Energy Chem.* **2016**, 25 (2), 336–344.
<https://doi.org/10.1016/j.jechem.2016.01.009>.

- (25) Truong-Phuoc, L.; Christoforidis, K. C.; Vigneron, F.; Papaefthimiou, V.; Decher, G.; Keller, N.; Keller, V. Layer-by-Layer Photocatalytic Assembly for Solar Light-Activated Self-Decontaminating Textiles. *ACS Appl. Mater. Interfaces* **2016**, *8* (50), 34438–34445. <https://doi.org/10.1021/acsami.6b12585>.
- (26) Sun, M.-C.; Liang, J.-B.; Peng, W.-Q.; Wang, Z.-M.; Negishi, N.; Koike, K.; Chu, Y.-H.; Yin, H.-Q. Photocatalytic Properties of Fresh and Pyrolyzed Transparent Nanocomposite Films Layer-by-Layer Fabricated from Alternative Layers of Graphene and Titanate Nanotube. *Mater. Sci. Semicond. Process.* **2015**, *40*, 954–963. <https://doi.org/10.1016/j.mssp.2015.07.092>.
- (27) Rongé, J.; Bets, J.; Pattanaik, S.; Bosserez, T.; Borellini, S.; Pulinthanathu Sree, S.; Decher, G.; Martens, J. A. Tailoring Preparation, Structure and Photocatalytic Activity of Layer-by-Layer Films for Degradation of Different Target Molecules. *Catal. Today* **2015**, *246*, 28–34. <https://doi.org/10.1016/j.cattod.2014.07.051>.
- (28) Chai, N.-N.; Wang, H.-X.; Hu, C.-X.; Wang, Q.; Zhang, H.-L. Well-Controlled Layer-by-Layer Assembly of Carbon Dot/CdS Heterojunctions for Efficient Visible-Light-Driven Photocatalysis. *J. Mater. Chem. A* **2015**, *3* (32), 16613–16620. <https://doi.org/10.1039/C5TA03649F>.
- (29) Carré, G.; Garnier, L.; Moeller-Siebert, J.; Gies, J.-P.; Keller, V.; André, P.; Keller, N. Antibacterial Textiles Functionalized by Layer-by-Layer Assembly of Polyelectrolytes and TiO₂ Photocatalyst. *RSC Adv.* **2015**, *5* (49), 38859–38867. <https://doi.org/10.1039/C5RA05541E>.
- (30) Patrocínio, A. O. T.; Paula, L. F.; Paniago, R. M.; Freitag, J.; Bahnemann, D. W. Layer-by-Layer TiO₂/WO₃ Thin Films As Efficient Photocatalytic Self-Cleaning Surfaces. *ACS Appl. Mater. Interfaces* **2014**, *6* (19), 16859–16866. <https://doi.org/10.1021/am504269a>.
- (31) Grandcolas, M.; Sinault, L.; Mosset, F.; Louvet, A.; Keller, N.; Keller, V. Self-Decontaminating Layer-by-Layer Functionalized Textiles Based on WO₃-Modified Titanate Nanotubes. Application to the Solar Photocatalytic Removal of Chemical Warfare Agents. *Appl. Catal. A Gen.* **2011**, *391* (1–2), 455–467. <https://doi.org/10.1016/j.apcata.2010.05.028>.
- (32) Keller, S. W.; Kim, H. N.; Mallouk, T. E. Layer-by-Layer Assembly of

- Intercalation Compounds and Heterostructures on Surfaces: Toward Molecular “Beaker” Epitaxy. *J. Am. Chem. Soc.* **1994**, *116* (19), 8817–8818.
<https://doi.org/10.1021/ja00098a055>.
- (33) Fang, M.; Kim, C. H.; Saupe, G. B.; Kim, H.-N.; Waraksa, C. C.; Miwa, T.; Fujishima, A.; Mallouk, T. E. Layer-by-Layer Growth and Condensation Reactions of Niobate and Titanoniobate Thin Films. *Chem. Mater.* **1999**, *11* (6), 1526–1532. <https://doi.org/10.1021/cm981066k>.
- (34) Silva, C. H. B.; Galiote, N. A.; Huguenin, F.; Teixeira-Neto, É.; Constantino, V. R. L.; Temperini, M. L. A. Spectroscopic, Morphological and Electrochromic Characterization of Layer-by-Layer Hybrid Films of Polyaniline and Hexaniobate Nanoscrolls. *J. Mater. Chem.* **2012**, *22* (28), 14052.
<https://doi.org/10.1039/c2jm31531a>.
- (35) Zhu, K.; Hong, Z.; Kang, S.-Z.; Qin, L.; Li, G.; Li, X. Assembly of Potassium Niobate Nanosheets/Silver Oxide Composite Films with Good SERS Performance towards Crystal Violet Detection. *J. Phys. Chem. Solids* **2018**, *115*, 69–74. <https://doi.org/10.1016/j.jpcs.2017.12.010>.
- (36) Ganter, P.; Lotsch, B. V. Photocatalytic Nanosheet Lithography: Photolithography Based on Organically Modified Photoactive 2D Nanosheets. *Angew. Chemie Int. Ed.* **2017**, *56* (29), 8389–8392.
<https://doi.org/10.1002/anie.201703149>.
- (37) Zhou, H.; Sabio, E. M.; Townsend, T. K.; Fan, T.; Zhang, D.; Osterloh, F. E. Assembly of Core–Shell Structures for Photocatalytic Hydrogen Evolution from Aqueous Methanol. *Chem. Mater.* **2010**, *22* (11), 3362–3368.
<https://doi.org/10.1021/cm903839t>.
- (38) Izawa, K.; Yamada, T.; Unal, U.; Ida, S.; Altuntasoglu, O.; Koinuma, M.; Matsumoto, Y. Photoelectrochemical Oxidation of Methanol on Oxide Nanosheets. *J. Phys. Chem. B* **2006**, *110* (10), 4645–4650.
<https://doi.org/10.1021/jp056210l>.
- (39) Saruwatari, K.; Sato, H.; Idei, T.; Kameda, J.; Yamagishi, A.; Takagaki, A.; Domen, K. Photoconductive Properties of Organic–Inorganic Hybrid Films of Layered Perovskite-Type Niobate. *J. Phys. Chem. B* **2005**, *109* (25), 12410–

12416. <https://doi.org/10.1021/jp0505476>.

- (40) Nakato, T.; Kuroda, K.; Kato, C. Syntheses of Intercalation Compounds of Layered Niobates with Methylviologen and Their Photochemical Behavior. *Chem. Mater.* **1992**, *4* (1), 128–132. <https://doi.org/10.1021/cm00019a027>.
- (41) Bizeto, M. A.; Constantino, V. R. L. Structural Aspects and Thermal Behavior of the Proton-Exchanged Layered Niobate $K_4Nb_6O_{17}$. *Mater. Res. Bull.* **2004**, *39* (11), 1729–1736. <https://doi.org/10.1016/j.materresbull.2004.05.001>.
- (42) Oshima, T.; Lu, D.; Ishitani, O.; Maeda, K. Intercalation of Highly Dispersed Metal Nanoclusters into a Layered Metal Oxide for Photocatalytic Overall Water Splitting. *Angew. Chemie - Int. Ed.* **2015**, *54* (9), 2698–2702. <https://doi.org/10.1002/anie.201411494>.
- (43) Barrett, E. P.; Joyner, L. G.; Halenda, P. P. The Determination of Pore Volume and Area Distributions in Porous Substances. I. Computations from Nitrogen Isotherms. *J. Am. Chem. Soc.* **1951**, *73* (1), 373–380. <https://doi.org/10.1021/ja01145a126>.
- (44) Serpone, N.; Terzian, R.; Lawless, D.; Kennepohl, P.; Sauvé, G. On the Usage of Turnover Numbers and Quantum Yields in Heterogeneous Photocatalysis. *J. Photochem. Photobiol. A Chem.* **1993**, *73* (1), 11–16. [https://doi.org/10.1016/1010-6030\(93\)80027-7](https://doi.org/10.1016/1010-6030(93)80027-7).
- (45) Serpone, N. Relative Photonic Efficiencies and Quantum Yields in Heterogeneous Photocatalysis. *J. Photochem. Photobiol. A Chem.* **1997**, *104* (1–3), 1–12. [https://doi.org/10.1016/S1010-6030\(96\)04538-8](https://doi.org/10.1016/S1010-6030(96)04538-8).
- (46) Kisch, H.; Bahnemann, D. Best Practice in Photocatalysis: Comparing Rates or Apparent Quantum Yields? *J. Phys. Chem. Lett.* **2015**, *6* (10), 1907–1910. <https://doi.org/10.1021/acs.jpcclett.5b00521>.
- (47) Belhadj, H.; Hamid, S.; Robertson, P. K. J.; Bahnemann, D. W. Mechanisms of Simultaneous Hydrogen Production and Formaldehyde Oxidation in H_2O and D_2O over Platinized TiO_2 . *ACS Catal.* **2017**, *7* (7), 4753–4758. <https://doi.org/10.1021/acscatal.7b01312>.
- (48) Kandiel, T. A.; Ivanova, I.; Bahnemann, D. W. Long-Term Investigation of the

- Photocatalytic Hydrogen Production on Platinized TiO₂: An Isotopic Study. *Energy Environ. Sci.* **2014**, 7 (4), 1420–1425.
<https://doi.org/10.1039/c3ee41511b>.
- (49) Maeda, K.; Eguchi, M.; Youngblood, W. J.; Mallouk, T. E. Niobium Oxide Nanoscrolls as Building Blocks for Dye-Sensitized Hydrogen Production from Water under Visible Light Irradiation. *Chem. Mater.* **2008**, 20 (21), 6770–6778.
<https://doi.org/10.1021/cm801807b>.
- (50) Kobayashi, Y.; Hata, H.; Salama, M.; Mallouk, T. E. Scrolled Sheet Precursor Route to Niobium and Tantalum Oxide Nanotubes. *Nano Lett.* **2007**, 7 (7), 2142–2145. <https://doi.org/10.1021/nl0708260>.
- (51) Saupe, G. B.; Waraksa, C. C.; Kim, H. N.; Han, Y. J.; Kaschak, D. M.; Skinner, D. M.; Mallouk, T. E. Nanoscale Tubules Formed by Exfoliation of Potassium Hexaniobate. *Chem. Mater.* **2000**, 12 (6), 1556–1562.
<https://doi.org/10.1021/cm981136n>.
- (52) Schmitt, J.; Gruenewald, T.; Decher, G.; Pershan, P. S.; Kjaer, K.; Loesche, M. Internal Structure of Layer-by-Layer Adsorbed Polyelectrolyte Films: A Neutron and x-Ray Reflectivity Study. *Macromolecules* **1993**, 26 (25), 7058–7063.
<https://doi.org/10.1021/ma00077a052>.
- (53) Yuri Lvov, Heinrich Haas, Cero Decher, H. M. Assembly of Polyelectrolyte Molecular Films onto Plasma-Treated Glass. *J. Phys. Chem.* **1993**, No. 97, 12835–12841.
- (54) Sasaki, T.; Ebina, Y.; Tanaka, T.; Harada, M.; Watanabe, M.; Decher, G. Layer-by-Layer Assembly of Titania Nanosheet/Polycation Composite Films. *Chem. Mater.* **2001**, 13 (12), 4661–4667. <https://doi.org/10.1021/cm010478h>.
- (55) Patrocínio, A. O. T.; Paterno, L. G.; Iha, N. Y. M. Role of Polyelectrolyte for Layer-by-Layer Compact TiO₂ Films in Efficiency Enhanced Dye-Sensitized Solar Cells. *J. Phys. Chem. C* **2010**, 114 (41), 17954–17959.
<https://doi.org/10.1021/jp104751g>.
- (56) Patrocínio, A. O. T.; Paterno, L. G.; Murakami Iha, N. Y. Layer-by-Layer TiO₂ Films as Efficient Blocking Layers in Dye-Sensitized Solar Cells. *J. Photochem. Photobiol. A Chem.* **2009**, 205 (1), 23–27.

- <https://doi.org/10.1016/j.jphotochem.2009.04.008>.
- (57) Xu, P.; Milstein, T. J.; Mallouk, T. E. Flat-Band Potentials of Molecularly Thin Metal Oxide Nanosheets. *ACS Appl. Mater. Interfaces* **2016**, *8* (18), 11539–11547. <https://doi.org/10.1021/acsami.6b02901>.
- (58) Mathapa, B. G.; Paunov, V. N. Fabrication of Novel Cyclodextrin-Polyallylamine Hydrochloride Co-Polymeric Microcapsules by Templating Oil-in-Water Emulsions. *Soft Matter* **2013**, *9* (19), 4780. <https://doi.org/10.1039/c3sm27935a>.
- (59) Jehng, J. M.; Wachs, I. E. Structural Chemistry and Raman Spectra of Niobium Oxides. *Chem. Mater.* **1991**, *3* (1), 100–107. <https://doi.org/10.1021/cm00013a025>.
- (60) Kinoshita, K.; Routsis, K.; Bett, J. A. S. The Thermal Decomposition of Platinum(II) and (IV) Complexes. *Thermochim. Acta* **1974**, *10* (1), 109–117. [https://doi.org/10.1016/0040-6031\(74\)85029-X](https://doi.org/10.1016/0040-6031(74)85029-X).
- (61) Townsend, T. K.; Sabio, E. M.; Browning, N. D.; Osterloh, F. E. Improved Niobate Nanoscroll Photocatalysts for Partial Water Splitting. *ChemSusChem* **2011**, *4* (2), 185–190. <https://doi.org/10.1002/cssc.201000377>.
- (62) Kim, Y. Il; Atherton, S. J.; Brigham, E. S.; Mallouk, T. E. Sensitized Layered Metal Oxide Semiconductor Particles for Photochemical Hydrogen Evolution from Nonsacrificial Electron Donors. *J. Phys. Chem.* **1993**, *97* (45), 11802–11810. <https://doi.org/10.1021/j100147a038>.
- (63) Sayama, K.; Tanaka, A.; Domen, K.; Maruya, K.; Onishi, T. Photocatalytic Decomposition of Water over Platinum-Intercalated $K_4Nb_6O_{17}$. *J. Phys. Chem.* **1991**, *95* (3), 1345–1348.
- (64) Ebina, Y.; Tanaka, A.; Kondo, J. N.; Domen, K. Preparation of Silica Pillared $Ca_2Nb_3O_{10}$ and Its Photocatalytic Activity. *Chem. Mater.* **1996**, *8* (10), 2534–2538. <https://doi.org/10.1021/cm960232q>.
- (65) Kandiel, T. A.; Dillert, R.; Robben, L.; Bahnemann, D. W. Photonic Efficiency and Mechanism of Photocatalytic Molecular Hydrogen Production over Platinized Titanium Dioxide from Aqueous Methanol Solutions. *Catal. Today*

- 2011**, *161* (1), 196–201. <https://doi.org/10.1016/j.cattod.2010.08.012>.
- (66) Mesa, C. A.; Kafizas, A.; Francàs, L.; Pendlebury, S. R.; Pastor, E.; Ma, Y.; Le Formal, F.; Mayer, M. T.; Grätzel, M.; Durrant, J. R. Kinetics of Photoelectrochemical Oxidation of Methanol on Hematite Photoanodes. *J. Am. Chem. Soc.* **2017**, *139* (33), 11537–11543. <https://doi.org/10.1021/jacs.7b05184>.
- (67) Compton, O. C.; Osterloh, F. E. Niobate Nanosheets as Catalysts for Photochemical Water Splitting into Hydrogen and Hydrogen Peroxide. *J. Phys. Chem. C* **2009**, *113* (1), 479–485. <https://doi.org/10.1021/jp807839b>.
- (68) Bayot, D.; Tinant, B.; Devillers, M. Water-Soluble Niobium Peroxo Complexes as Precursors for the Preparation of Nb-Based Oxide Catalysts. *Catal. Today* **2003**, *78* (1–4), 439–447. [https://doi.org/10.1016/S0920-5861\(02\)00325-5](https://doi.org/10.1016/S0920-5861(02)00325-5).
- (69) Kiwi, J.; Graetzel, M. Specific Analysis of Surface-Bound Peroxides Formed during Photoinduced Water Cleavage in Titanium Dioxide-Based Microheterogeneous Systems. *J. Mol. Catal.* **1987**, *39* (1), 63–70. [https://doi.org/10.1016/0304-5102\(87\)80047-0](https://doi.org/10.1016/0304-5102(87)80047-0).
- (70) Brug, G. J.; van den Eeden, A. L. G.; Sluyters-Rehbach, M.; Sluyters, J. H. The Analysis of Electrode Impedances Complicated by the Presence of a Constant Phase Element. *J. Electroanal. Chem. Interfacial Electrochem.* **1984**, *176* (1–2), 275–295. [https://doi.org/10.1016/S0022-0728\(84\)80324-1](https://doi.org/10.1016/S0022-0728(84)80324-1).

4. Photoinduced H₂ Evolution by Hexaniobate Sheets Grafted with Metal Ions: The Fate of Photogenerated Carriers

4.1. Foreword

This chapter contains the article “Photoinduced H₂ Evolution by Hexaniobate Sheets Grafted with Metal Ions: The Fate of Photogenerated Carriers” by Barbara N. Nunes, Detlef W. Bahnemann and Antonio Otavio T. Patrocínio published on ACS Applied Energy Materials 2021, 4, 3681. doi.org/10.1021/acsaem.1c00128. The figures and tables identified through this chapter with the letter “B” are reproduced in Appendix B. Reprinted with permission. Copyright 2021 American Chemical Society.

4.2. Abstract

Layered niobates are well-known photocatalysts for H₂ evolution with a rich surface chemistry. Their photoactivity, however, is limited by their wide band gap energy (~3.5 eV) and partial deactivation due to surface poisoning by photogenerated H₂O₂. In this way, a surface modification method able to induce novel electronic processes without changing the bulk properties can improve their performance. In this work, the surface of exfoliated hexaniobate (K_{4-x}H_xNb₆O₁₇) layers was modified by grafting with metal ions such as Co²⁺ and Fe³⁺ and their photocatalytic properties were fully investigated. Morphological characterization showed that grafting ions are attached to the niobate surface forming amorphous clusters. These species induce an additional absorption feature in the UV-A region, which is attributed to an interfacial charge transfer from the niobate valence band to the metal ion centers. Enhanced UV-driven photoactivity was observed for 0.1% grafted samples, especially for those modified with Co²⁺ ions, while smaller H₂ evolution rates are observed as the concentration of the grafting ions increases. When Pt was added to the photocatalyst, the H₂ evolution rate for the 0.1% Co-grafted sample in plain water was 70% higher than that observed for the nongrafted Pt-hexaniobate. Full characterization by electron paramagnetic resonance, transient absorption spectroscopy, and photoelectrochemical measurements reveals that grafted ions can work as both electron and hole acceptors. In the presence of Pt as a preferential electron acceptor, Co²⁺ ions act as hole acceptors forming Co³⁺ centers, favoring the formation of OH• radicals from water and avoiding surface poisoning. At higher Co²⁺ concentrations and in the absence of Pt clusters, electrons are trapped at the Co centers,

decreasing the H₂ evolution rate. Thus, grafted Co²⁺ ions act as active redox shuttles in the hexaniobate sheets, contributing to more efficient charge separation.

4.3. Introduction

Realization of the so-called H₂ economy requires, among other factors, the development of green H₂ production methods able to at least partially replace natural gas steam reforming. Photocatalytic water splitting is an attractive alternative to reach this goal, since it is a renewable method, and sunlight and water are available worldwide. Among a countless number of photocatalysts already reported for water splitting, layered niobates are well-known for H₂ evolution essentially due to their electronic and structural advantages, as recently reviewed ^{1,2}. Niobate layers are formed by [NbO₆] octahedral units connected through adjacent or opposite sharing edges or corners. They stack with one another due to their negatively charged slabs and the cations in the interlayer space ³. The high affinity of Nb⁵⁺ for O²⁻ gives rise to extended 2D layered arrangements, providing large surface area and allowing easy modification either by intercalation or superficial modification. Despite a bandgap energy close to 3.5 eV that limits the photoactivity to the ultraviolet region (<390 nm), these materials feature appropriate potentials for water splitting with conduction and valence bands lower than -0.5 V and higher than +2.5 V vs SHE, respectively ^{4,5}.

Niobates as photocatalysts for water splitting were firstly reported in 1986 by Domen and co-workers ⁶. K₄Nb₆O₁₇ exhibited the best result for H₂ evolution among the investigated niobates, however stoichiometric water photodecomposition into H₂ and O₂ was only achieved by employing a co-catalyst, such as NiO or RuO₂ ^{7,8}. Later, intercalated Pt clusters into K₄Nb₆O₁₇, by using [Pt(NH₃)₄]²⁺ as a precursor, resulted in stoichiometric water splitting which was explained by the inhibition of the reversal reaction as the produced O₂ and H₂ could not access the Pt surface at the interlayer space ⁹. Other strategies include dye-sensitization ¹⁰ and formation of heterostructures ¹¹. Further, other Pt-decorated niobate materials were reported as water splitting photocatalysts ¹².

Improved rates for H₂ evolution from alcoholic solutions could be further achieved by exfoliated niobate samples ¹³. Exfoliation of stacked niobates has been successfully employed to yield 2D nanostructures with enhanced surface area in relation to the as-synthesized oxides ¹⁴⁻¹⁶. The exfoliating agent role, generally a bulky ammonium cation, as well as that of individual niobate layers shape (nanosheets or nanoscrolls) on H₂

evolution has been investigated by Osterloh's group^{17,18}. In all cases, no O₂ could be detected upon water photolysis even when platinum was used as co-catalyst, a behavior also observed by us for niobate thin films assembled by the *layer-by-layer* technique⁴. The same group later reported that UV-driven water photolysis in the presence of exfoliated niobates actually yields H₂ and H₂O₂ in 1:1 molar ratio¹⁹. Moreover, the photogenerated H₂O₂ remains strongly adsorbed onto the niobate surface, thus leading to its total deactivation after long irradiation times⁵. Thus, further mechanistic investigations are required to unveil redox processes at exfoliated niobates and improve their efficiency and stability as H₂ evolution photocatalysts from water. Better light-harvesting properties towards the spectrum visible range is also desirable.

In this work, we have prepared hexaniobate nanosheets grafted with Co²⁺ and Fe³⁺ ions aiming at improving optical and surface properties in relation to the bare material. Surface grafting is a soft and simple method and has gained attention for inducing new electronic processes on catalysts surface without changing bulk crystallinity^{20,21}. The metal cations Co²⁺ and Fe³⁺ were grafted onto the hexaniobate surface in different concentrations, as represented on Figure 1, and the resulting materials were applied for photocatalytic reactions under different irradiation conditions. The fate of the photogenerated charge carriers was investigated in detail by in-situ EPR and transient absorption spectroscopies, which were then combined with H₂ evolution measurements and photoelectrochemical data to provide new insights on the behavior of 2D-niobate photocatalysts.

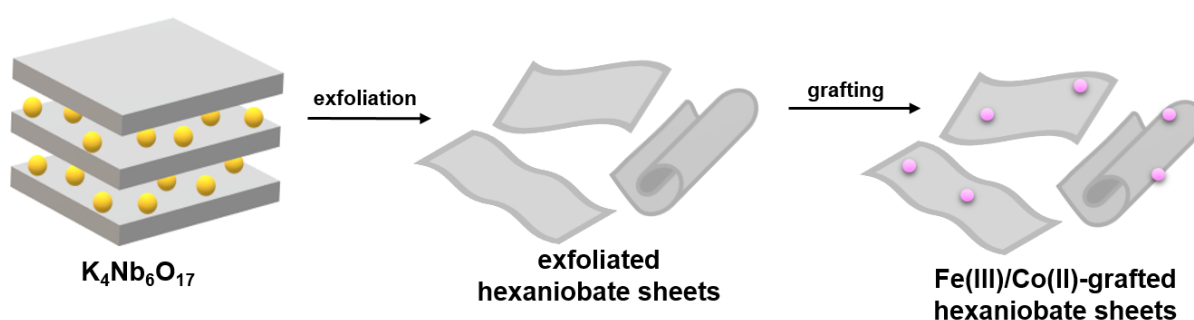


Figure 1 – Schematic representation of grafted hexaniobate following exfoliation of layered $K_4Nb_6O_{17}$.

4.4. Materials and Methods

All chemicals were used as received. Potassium carbonate, tert-butylamine hydroxide, cobalt acetate and iron nitrate were acquired from Aldrich. Nb₂O₅ optical grade was gently provided by CBMM (*Companhia Brasileira de Metalurgia e Mineração*). Deionized water with a resistivity of 18.2 MΩ cm at 25 °C was produced by a Millipore Milli-Q system.

Bulk K₄Nb₆O₁₇·3H₂O was prepared by the solid reaction method^{22,23}. Appropriated amounts of Nb₂O₅ and K₂CO₃ (molar ratio 2:3) were mixed and heated at 1100 °C for two cycles of 5h. Partial cation exchange from K⁺ to protons was performed by suspending 3.0 g of the as synthesized K₄Nb₆O₁₇·3H₂O into 150 ml of 0.2 mol L⁻¹ H₂SO₄ solution during 3 days²⁴. The solid was filtrated, washed with deionized water, and dried at 70 °C. Subsequently, the resulted K_{4-x}H_xNb₆O₁₇ (0.5 g) was submitted to exfoliation by stirring in 100 ml of 8×10⁻³ mol L⁻¹ tert-butylammonium hydroxide solution for seven days²⁵. When the stirring is suspended, the non-exfoliated material tends to precipitate, while the exfoliated layers remain as a stable suspension. Thus, the supernatant was separated from the solid and some drops of HNO₃ were added into the suspension in order to obtain the restacked hexaniobate nanosheets. The white powder was centrifuged and washed with deionized water until the supernatant achieved a pH > 6 and then, the final solid was dried at 70 °C.

Grafting of Fe³⁺ and Co²⁺ ions on the exfoliated hexaniobate surface was performed by the impregnation method^{20,26}. Appropriate metal salts (cobalt(II) acetate tetrahydrate or iron(III) nitrate nonahydrate) were added to an aqueous hexaniobate suspension and stirred at 90 °C for 1 h. Different ratios were investigated, 1, 0.5 and 0.1 wt % relative to the hexaniobate mass. Afterwards, the suspension was centrifuged and washed with deionized water. The final powder was dried at 70 °C.

4.4.1. Characterization techniques

X-ray diffraction patterns were obtained in a D8 Advance diffractometer (Bruker AXS GmbH) using Cu Kα radiation (λ = 1.54060 Å). Diffractograms were collected at 0.01° step. Raman spectra were measured in a confocal Bruker Senterra micro-Raman spectrometer equipped with an Olympus BX51 microscope. As excitation source, a 532 nm laser with a power of 2 mW was employed. Specific surface area was determined by a single-point standard Micromeritics FlowSorb II 2300 instrument fitted with a

Micromeritics AutoMate 23. Diffuse reflectance UV-Vis spectra were recorded in a spectrophotometer Varian Cary-100 Bio, Agilent technologies. Barium sulfate was used as standard. Optical bandgap energies were calculated following the Tauc method ²⁷. Transmission electron microscopy (TEM) was performed in Tecnai G2 F20 TMP (FEI Company) microscope with field emission gun (FEG) at 200 kV, objective lenses TWIN and point resolution of 0.27 nm. Electron Paramagnetic Resonance (EPR) measurements were performed in a MiniScope X-band EPR spectrometer (MS400 Magnostech GmbH) operating at about 9.42–9.44 GHz field frequency as described before ²⁰. For samples in suspension, 0.5 ml of 1 g L⁻¹ of photocatalyst in water was purged with argon or oxygen and 2 μL of DMPO was added. The center field was 335 mT and sweep time 15 s. For powder samples, liquid N₂ was used to maintain the temperature at 77 K, with center field at 335 mT and sweep time 60 s. Samples irradiation during EPR measurements was provided by a built-in optical fiber connected to a Hamamatsu LC8 light source (200 W Hg-Xe lamp). XPS analyses were carried out in a Phi5000 VersaProbeII, ULVAC-Phi Inc. spectrometer using monochromatic Al K-alpha X ray excitation. Survey spectra were collected with 187.5 eV pass energy and 0.8 eV step, while high resolution spectra were collected with 23.5 eV pass energy and 0.1 eV step.

Electrochemical measurements were performed in a Zennium potentiostat (Fa. Zahner-Elektrik GmbH & Co. KG, Germany) with three electrode cell type PECC-2 (Zahner-Elektrik GmbH & Co. KG, Germany) using 0.1 M Na₂SO₄ as electrolyte, a Pt wire as counter electrode and Ag/AgCl (3 M NaCl) as a reference electrode. The working electrodes were thin films of each sample deposited on fluoride-doped tin oxide (FTO) coated glasses (Sigma Aldrich, 8 Ω/sq) by the doctor blade technique. The coating paste was prepared by gridding 50 mg of the sample, 1 drop of Triton X-100 (Sigma-Aldrich, laboratory-grade), 25 mg of polyethylene glycol M_w= 10000 (Merck), 100 μl of deionized water, and ethanol. After homogenous dispersion on the conductive substrate, the films were treated at 400 °C for 2 h in air to remove organic materials.

For transient absorption spectroscopy, TAS, powder samples were placed in a 1 mm quartz cell and then, purged with pure N₂ or a mixture of nitrogen and methanol vapour for 30 min. The measurements were performed in a Applied Photophysics LKS 80 laser flash photolysis spectrometer equipped with a diffuse reflectance accessory and pumped by Nd:YAG laser (Quantel, Brilliant B) ²⁸. The third harmonic of the laser (355 nm, 6 ns pulses) was applied with an average energy of 6 mJ·cm⁻². A Xenon lamp Osram XBO 150 W provided the probe pulse. The signals between 400 and 660 nm were

detected by a R928 Hamamatsu PMT connected a 1 GHz oscilloscope, Agilent. Changes in the reflected light intensity (ΔJ) at each probed wavelength were calculated from the reflected light before (J_0) and after (J) the laser excitation, Equation 1.

$$\Delta J = 1 - 10^{-Abs} = \frac{J_0 - J}{J_0} \quad (1)$$

4.4.2. Photocatalytic experiments

H₂ evolution experiments were carried out in septum sealed 10 mL borosilicated glass reactors. The photocatalyst (6 mg) was suspended in 6 mL of deionized water. The system was purged with argon for 5 min and then irradiated with a 1000 W xenon lamp (Hönle UV Technology, Sol 1200)²⁹ under constant stirring. The temperature was maintained at 25 ± 1 °C using a water bath. When necessary, 2% wt. of Pt was deposited *in situ* by addition of the required amount of H₂PtCl₆. Evolved gases were quantified by gas chromatography using a Shimadzu GC-8A (TCD) or Shimadzu GC-2014 (FID) system. Isotope labeled experiments were propped with a Hiden HPR-20 QIC gas analyzer equipped with a quadrupole mass spectrometer (QMS)²⁹. For methanol photo-oxidation, 0.03 mol L⁻¹ MeOH solution was used with 0.50 g L⁻¹ of photocatalyst. The glass reactor was irradiated by 120 min in total and 0.3 ml aliquots were collected periodically. The amount of formaldehyde produced at different time intervals was determined by the Nash method³⁰.

4.5. Results and Discussion

4.5.1. Optical and Morphological properties

As described in our previous works²³ and shown in Figure B1, the structure of the K₄Nb₆O₁₇ synthesized by the solid state methodology corresponds to that for K₄Nb₆O₁₇.3H₂O (JCPDS 21-1297). As an effect of exfoliation with TBA(OH) with further precipitation with acid, the layered structure is lost yielding a broad diffraction pattern with few remaining peaks indexed to the 220 and 002 diffraction planes and attributed to remaining stacked layers²⁴, Figure 2(a). Concomitantly, enlargement of the specific surface area is observed, from 2–3 to 150 m² g⁻¹. The XRD behavior for the modified sample with the highest amount of Co²⁺ (1 wt.%) is quite similar to that for the bare hexaniobate, however small shifts for higher degrees were observed for both diffraction peaks (Figure 2(a) inset), which may indicate the presence of Co²⁺ ions also

in interlayer spaces of remaining stacked layers. The same trend was observed for Fe^{3+} -grafted samples, Figure B2(a). The relative concentrations of Co^{2+} in the samples were confirmed by inductively coupled plasma-optical emission spectrometry (ICP-OES). Experimental values were $(0.097 \pm 0.002)\%$, $(0.509 \pm 0.006)\%$ and $(1.080 \pm 0.004)\%$, which are quite similar to the respective nominal percentages of 0.1%, 0.5% and 1%. Additional XPS analysis of the sample having 1 wt% Co^{2+} , Figure B3, confirms the relative concentration of the grafted ion on the oxide surface. Also, high resolution spectrum clearly shows a peak at 281.3 eV correspondent to the Co^{2+} $2p_{3/2}$ peak^{31,32}.

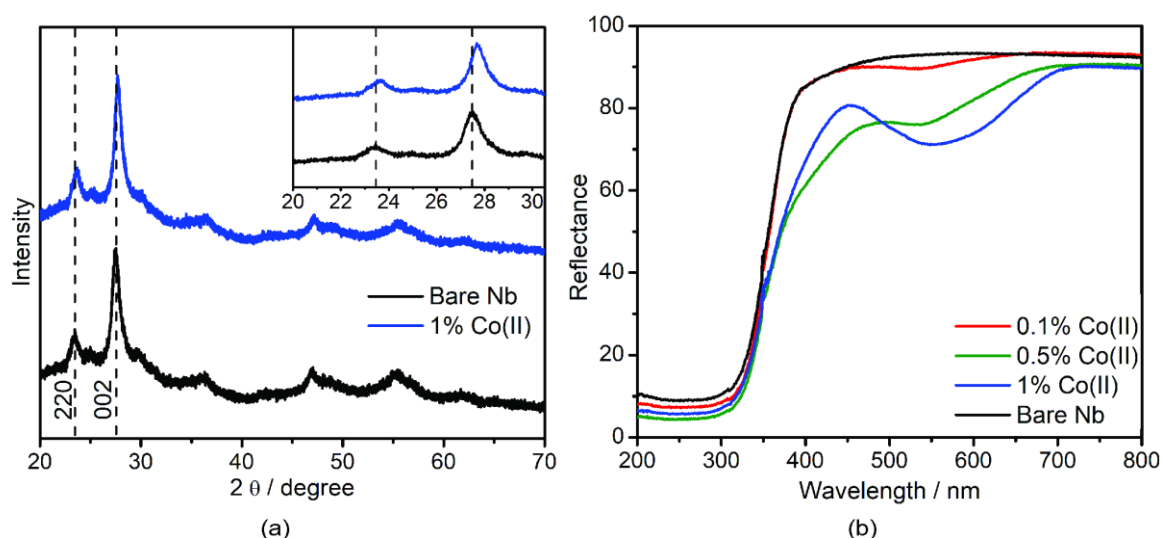


Figure 2 – XRD patterns (a) and diffuse reflectance UV–Vis spectra (b) of bare and Co^{2+} -grafted hexaniobate layers.

UV–Vis diffuse reflectance spectra of the samples are shown in Figure 2(b). All samples exhibit an intense absorption between 290 and 365 nm attributed to hexaniobate band gap excitation, which is estimated to be around 3.7 eV for all tested samples, in agreement with previous reports¹⁸. For the Co^{2+} -grafted samples, an additional absorption band appears in 450–650 nm region, with maximum at 535 nm, very similar to that reported for $[\text{Co}(\text{OH}_2)_6]^{2+}$ ions in water ($\lambda_{\text{max}} = 530 \text{ nm}$)³³, and it is therefore attributed to d-d transitions of Co^{2+} species on the hexaniobate surface. A shoulder between 350–400 nm can also be observed, especially for those with higher Co^{2+} concentrations (0.5% and 1%). This absorption shoulder could have originated from band gap excitation of CoO species estimated at $\sim 3.4 \text{ eV}$ ³⁴ or more likely to an interfacial charge transfer (IFCT) from the hexaniobate valence band to Co^{2+} centered orbitals due to the strong interaction of the metal ions with the hexaniobate surface, which will be discussed below through

vibrational spectroscopic data. IFCT bands have been previously reported for grafted TiO_2 with several metals ^{21,26,35}.

Fe^{3+} -grafted hexaniobate samples also exhibit an extended absorption toward the visible region in relation to the bare hexaniobate. A broad absorption band ranging from 350 to 600 nm is observed and attributed to an overlap between d-d and IFCT transitions, Figure B2(b), a very similar behavior to that reported by Yu and coworkers for Fe^{3+} -grafted TiO_2 ³⁵. In our case, despite the same band shape as observed for TiO_2 , the transition is shifted to lower wavelengths probably due to the more positive potential of hexaniobate valence band in relation to TiO_2 .

Raman and infrared spectra of bare Nb and 1 wt.% Co^{2+} -grafted samples are shown on Figure 3(a) and (b), respectively. In Raman spectra, typical bands related to octahedral units of niobium and oxygen [NbO_6] are observed and ascribed as follows: the band at 878 cm^{-1} corresponds to the stretching of Nb–O terminal groups with shorter bonds, and the stretching of longer Nb–O bonds leads to bands in $500\text{--}700\text{ cm}^{-1}$ region. Lattice vibrations appear below 150 cm^{-1} , and internal bending modes of O–Nb–O groups are responsible for bands in the range of $150\text{--}480\text{ cm}^{-1}$ ^{36,37}. For the Co^{2+} -grafted sample, three new bands appear at 809, 842, and 878 cm^{-1} , Figure 3(a) inset. The band at 809 cm^{-1} is assigned to the stretching modes of cobalt oxyhydroxide species, $\text{CoO}(\text{OH})$ ^{38,39}. The bands at 878 cm^{-1} and 842 cm^{-1} are related to distortions in the [NbO_6] octahedral units as a result of new Nb–O–Co surface bonds ⁴⁰. In this sense, small bands are also observed at 973 cm^{-1} and 998 cm^{-1} and attributed to more drastic distortions in the [NbO_6] octahedra. Between 100 and 200 cm^{-1} , slight changes are observed after grafting and may be ascribed to the translation of Co^{2+} species and their influence on the lattice vibration⁴⁰. Second-order Raman scattering from optical modes in CoO is reported at 1046 cm^{-1} in the literature ⁴¹, and similarly, an additional band at 1047 cm^{-1} for the grafted sample was also observed.

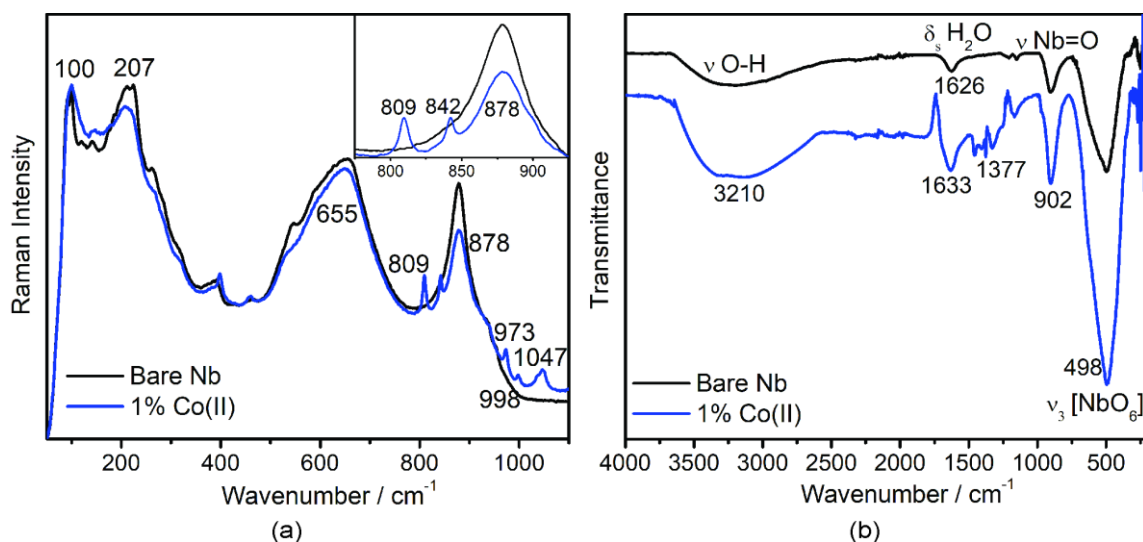


Figure 3 – Raman (a) and infrared (b) spectra of bare and 1 wt.% Co^{2+} grafted hexaniobate.

Infrared spectra analyses corroborate with the attributions made for the Raman data. Characteristic bands for hexaniobate are observed at 500 and 902 cm^{-1} , being assigned to O–Nb–O bonds from $[\text{NbO}_6]$ units and Nb=O stretching mode, respectively ^{19,23}. Bands at 3210 cm^{-1} and 1626 cm^{-1} are related to O–H stretching and symmetrical deformation of H–O–H from adsorbed water molecules, respectively ⁴². For the grafted sample, further bands are found in the region around 1200–1400 cm^{-1} similarly to those reported to cobalt oxyhydroxide species ⁴³. Particularly, the band at 1633 cm^{-1} is related to the Co–O bond ⁴⁴. Both Raman and FTIR data allow us to conclude that the Co^{2+} ions strongly interact with the hexaniobate surface through terminal oxygen atoms and are surrounded by H_2O molecules or OH^- ions, yielding amorphous clusters. In fact, high resolution XPS spectra of the 1 wt% Co^{2+} -grafted sample in the regions correspondent to O 1s and Nb 3d states, Figure B4, show additional peaks at lower binding energies than those observed for the bare hexaniobate, providing additional evidence of the strong interaction between Co^{2+} cations and the atoms of the nanosheets surface.

Raman and infrared spectra of 1% Fe^{3+} grafted hexaniobate also resemble those of the bare niobate (Figure B5), i.e. the majority of the bands are related to hexaniobate octahedral units $[\text{NbO}_6]$. In the Raman spectrum, similarly to the observed for Co^{2+} grafted sample, the appearance of a band at 842 cm^{-1} as well as the shift and lower relative intensity observed for the band at 848 cm^{-1} indicate the formation of Nb–O–Fe bonds. A small additional band is found at 809 cm^{-1} which can be correlated with bands reported

for hematite ⁴⁵. In the infrared spectrum, additional bands in the region of 1340–1250 cm^{-1} are assigned to chemisorbed O_2 on Fe^{3+} surface species ⁴⁶.

TEM images of the Co^{2+} -grafted samples are shown in Figure 4. As shown in Figure 4(a), the cobalt species appear as amorphous clusters on the hexaniobate surface with sizes around 2–3 nm. Furthermore, Figure 4(b) and 4(c) evidences that the hexaniobate substrate are formed by a mixture of open and some semi-scrolled sheets, forming tubes with length of 60 up to 120 nm. As previous reported ^{16,18}, both morphologies are expected after exfoliation with TBAOH. They ensure a high surface area for effective modification through grafting and coexist in aqueous solutions since the free energy difference between them is relatively small. Previous investigations also evidence that bare niobate sheets and scrolls have similar photocatalytic properties towards H_2 evolution. ¹⁸.

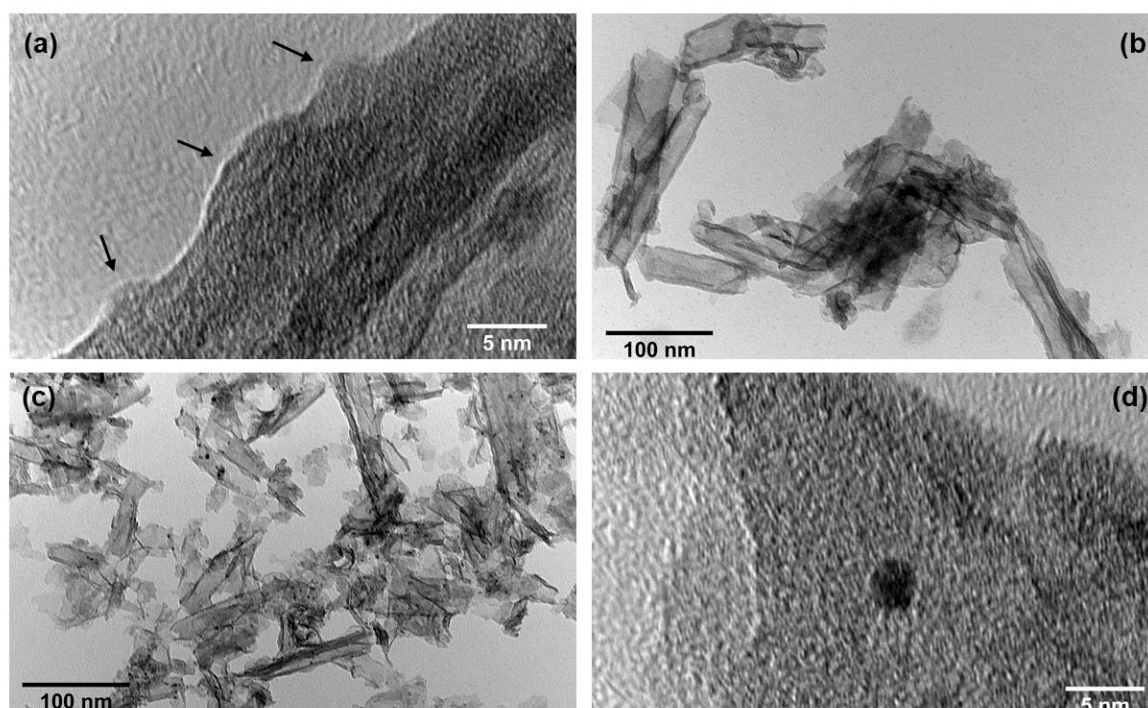


Figure 4 – TEM images of the 0.1 wt.% Co^{2+} -grafted hexaniobate before (a, b) and after (c, d) 2 wt% Pt photodeposition. The arrows in (a) indicate the Co^{2+} clusters on the hexaniobate layers surface.

4.5.2. Photocatalytic activity in plain water and in methanolic solutions

Photocatalytic activity for the grafted hexaniobate samples was initially screened in two different irradiation conditions, that is, under full UV-Vis excitation and only under visible light ($\lambda > 400$ nm). No H_2 evolution was observed under visible light even in presence of sacrificial agents, such as methanol, which is a clear indication that excitation

of d-d electronic transitions in the grafted metal ions are unable to promote redox reactions, likely due to kinetic reasons. We then focus our attention to UV-Vis irradiation where direct band gap and IFCT transitions are promoted.

Firstly, the samples were evaluated for H₂ evolution using 10% methanol aqueous solution. In this case, as shown in Figure 5(a), better performances for the samples with low amount of metal ions (0.1%) were observed in comparison to that for the bare hexaniobate. In contrast, higher amounts of metal ions on the hexaniobate surface as 0.5 and 1% lead to a decrease in the photocatalytic activity. In sequence, the samples were evaluated for H₂ evolution using pure water. In this case, for all the samples, no significant amounts of H₂ were detected without the presence of a co-catalyst. Therefore, Pt clusters were photodeposited over the hexaniobate layers to improve the H₂ evolution rate. Deposited Pt clusters are clearly distinguished as black spots in TEM images as shown in Figure 4(c), due to the difference in electron density between platinum and the hexaniobate²⁴. The platinum clusters exhibit spherical shape with diameters around 3–4 nm, as observed in Figure 4(d).

In plain water, 0.1% Co²⁺ grafted samples also exhibited the best photoactivity in relation to the bare hexaniobate and Fe³⁺ grafted samples, Figure 5(b). The observed H₂ evolution rate for the 0.1% Co²⁺ grafted sample in plain water is 86 μmol g⁻¹ h⁻¹, 70% higher than that observed for the unmodified hexaniobate, Table 1. The amount of Co²⁺ in the sample was also evaluated by ICP-OES after the photocatalytic experiment and the found values are exactly the same than those determined for fresh samples (0.097% ±0.002), confirming no lixiviation under irradiation conditions. In fact, recycling studies shown that the photocatalytic activity remains constant, considering the experimental deviation (Figure B6). XRD and XPS analyses of the 1 wt% Co²⁺-grafted sample after long term irradiation, Figure B7, also confirm the morphological and compositional stability of the system. Moreover, photocatalytic assays in the presence of 0.1% Co²⁺ grafted hexaniobate were carried out in D₂O and the evolved gasses analyzed by mass spectrometry (Figure B8). The results confirm that water is the proton source for H₂ evolution. No oxygen evolution was observed in the course of the irradiation.

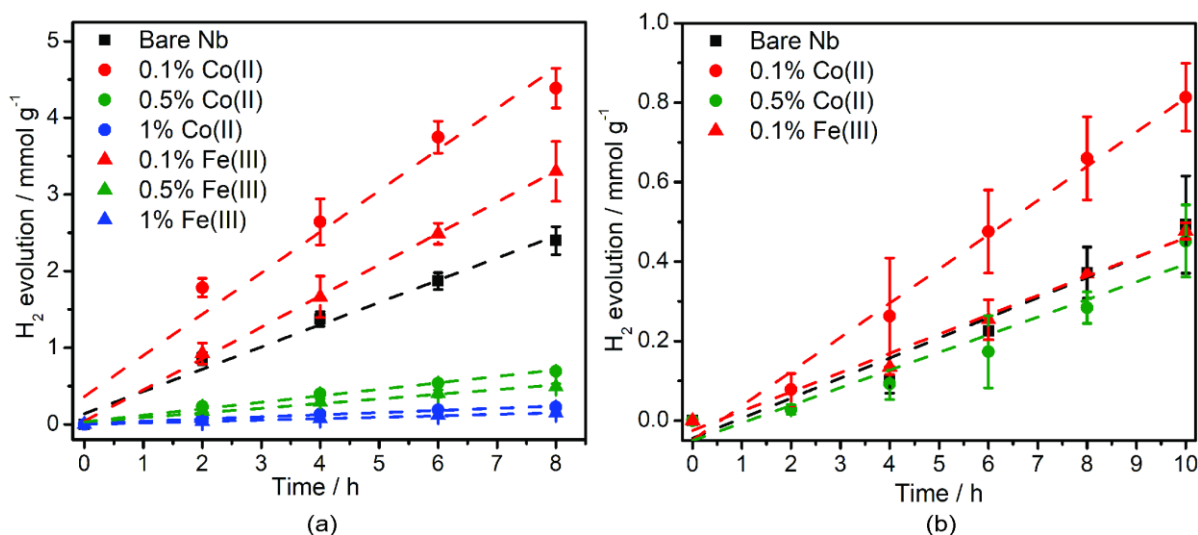


Figure 5 – H₂ evolution promoted by bare and grafted hexaniobate samples under UV-Vis irradiation from 10% methanol aqueous solution (a) and plain water after loading with 2 wt.% Pt (b).

When 0.1% grafted and bare hexaniobate samples were tested using 2 wt.% Pt and 10% methanol aqueous solution, they resulted in similar rates, Figure B9(a), with values of $1.1 \pm 0.1 \text{ mmol g}^{-1} \text{ h}^{-1}$, $1.3 \pm 0.1 \text{ mmol g}^{-1} \text{ h}^{-1}$ and $1.4 \pm 0.1 \text{ mmol g}^{-1} \text{ h}^{-1}$ for the bare, 0.1% Co²⁺ and 0.1% Fe³⁺ hexaniobate, respectively. These results indicate that the grafted ions on hexaniobate surface do not play a major role on the H₂ evolution rate when MeOH is used as hole scavenger, concomitantly with deposited Pt. Methanal formation rates from MeOH oxidation were also determined under solar simulator irradiation and confirm the behavior observed for H₂ evolution (Figure B9(b)). However, when methanol oxidation is carried out in the absence of platinum, it can be clearly seen that samples grafted with 0.1% Co²⁺ or Fe³⁺ exhibit improved photocatalytic performances for methanal formation in comparison to the bare hexaniobate or samples with higher concentrations of grafted ions (Table 1, Figure B10).

Table 1 – H₂ evolution rates for bare and grafted hexaniobates in pure water and in 10% MeOH aqueous solution. For MeOH photooxidation, the observed rates for methanal formation are also presented.

Sample	H ₂ evolution rate (10% MeOH) / μmol g ⁻¹ h ⁻¹	CH ₂ O formation rate / μmol L ⁻¹ h ⁻¹	H ₂ evolution rate (2% Pt, plain water) / μmol g ⁻¹ h ⁻¹
Bare Nb	290 ±20	140 ±1	50 ±6
0.1% Co ²⁺	540 ±60	300 ±1	86 ±5
0.5% Co ²⁺	0.080 ±10	110 ±1	44 ±6
1% Co ²⁺	30 ±2	80 ±1	-
0.1% Fe ³⁺	410 ±10	180 ±1	48 ±4
0.5% Fe ³⁺	60 ±4	70 ±1	-
1% Fe ³⁺	20 ±1	40 ±1	-

The photocatalytic behavior can be summarized as following: (i) no visible light activity is observed for the grafted samples; (ii) enhanced performances are observed for the 0.1% grafted samples, especially those modified with Co²⁺ ions, which exhibited considerable improvements both in plain water and in methanolic solutions. However, as the amount of Co²⁺ or Fe³⁺ increases, the H₂ evolution rate decreases, indicating an optimum surface concentration and a complex behavior under excitation. In order to unveil the grafted cations role on the photocatalytic hexaniobates behavior, detailed EPR and TAS studies were carried out as well as photoelectrochemical measurements.

EPR spectra of bare and Co²⁺-grafted hexaniobate suspensions in the presence of a radical scavenger (DMPO) at 298 K with and without atmospheric oxygen are shown in Figure 6. EPR spectra of the powder samples at 77 K in air without any radical scavenger are presented in Figure 7.

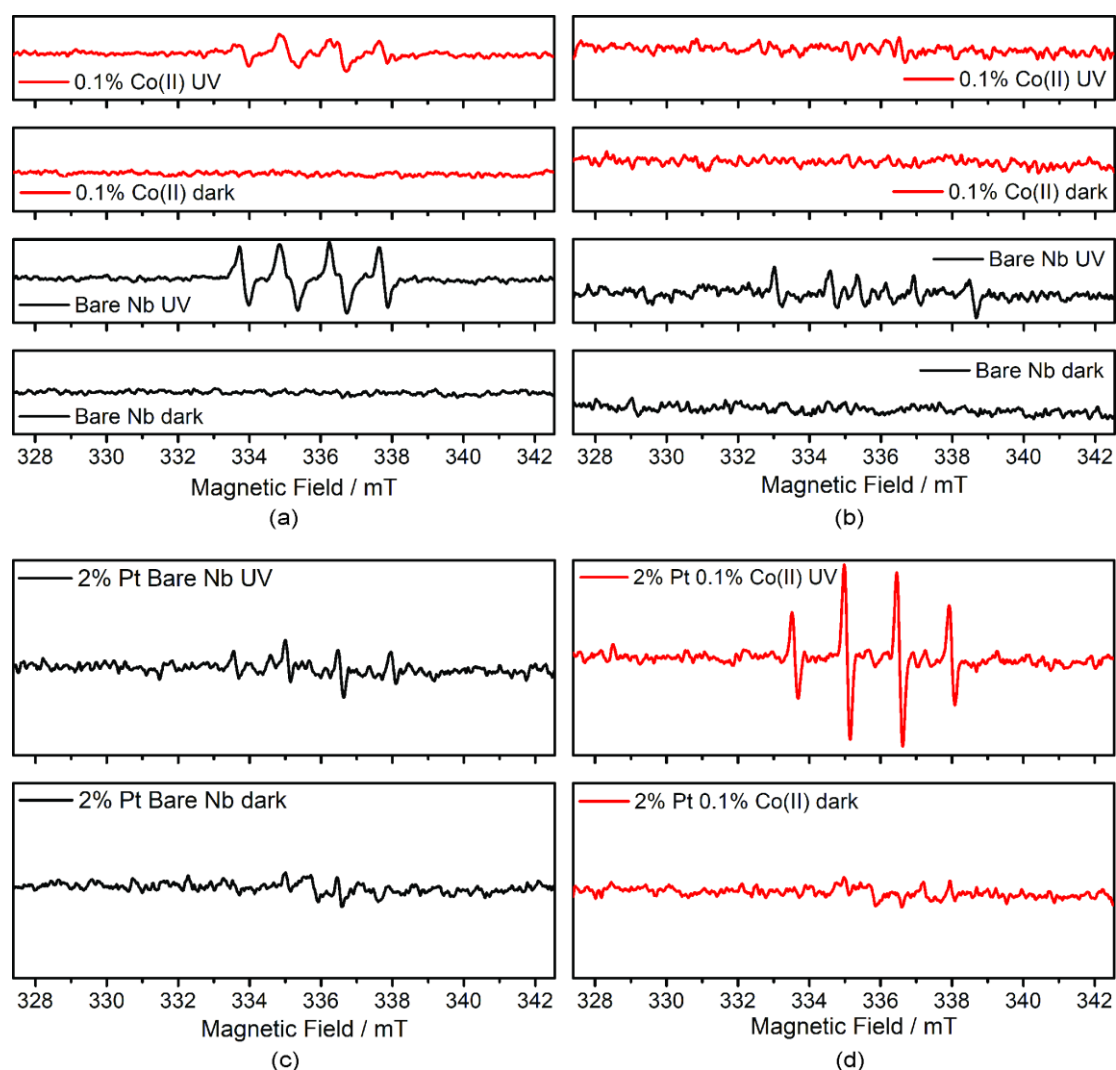


Figure 6 – EPR spectra at 298 K of aqueous suspensions of hexaniobate samples with DMPO in oxygen (a) and argon (b) atmospheres before and under irradiation. In (c) and (d), the spectra for Pt-decorated samples in argon atmosphere are shown.

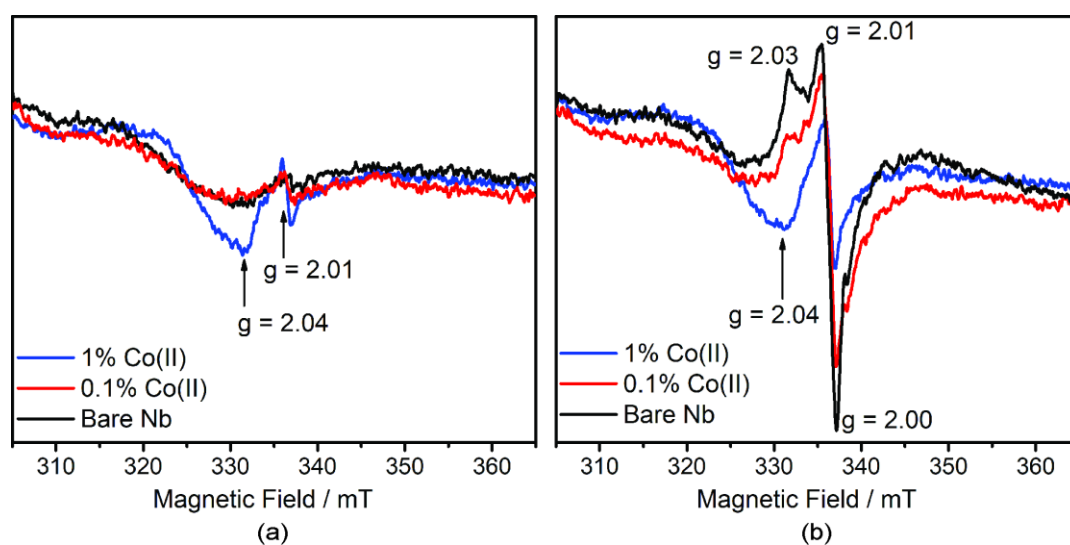


Figure 7 – EPR spectra of solid samples in air at 77 K before (a) and under UV irradiation (b).

EPR spin-trapping measurements carried out using DMPO in aqueous suspensions of bare and grafted hexaniobates and bubbled with oxygen, Figure 6(a), evidence that O_2 radical species are produced under irradiation. Four main peaks at 333.7, 334.8, 336.2 and 337.6 mT ($g = 2.02, 2.01, 2.00$ and 1.99) can be observed, which are associated to $\cdot\text{O}_2$ formation from gaseous O_2 ⁴⁷. Interestingly, the peaks magnitude for bare hexaniobate is higher than that for the grafted sample, showing that a fraction of photogenerated electrons are not been transferred to O_2 to form superoxide radicals but rather to Co^{2+} centers. Regarding the samples in argon, Figure 6(b), UV irradiation on bare hexaniobate results in a spectrum with 6 main peaks at 333, 334, 335.3, 336, 337 and 338.5 mT ($g = 2.02, 2.01, 2.00, 2.00, 1.99$ and 1.99). This profile is associated to $\cdot\text{CH}_3$ species produced from partial DMPO degradation in presence of oxidative species such as H_2O_2 ⁴⁸. On contrary, the 0.1% Co^{2+} -grafted sample under UV irradiation does not produce any significant signal. Therefore, this evidences the prompt H_2O_2 production by the bare hexaniobate under irradiation, whereas the Co^{2+} grafted sample does not produce H_2O_2 or other radical during the analysis. However, when Pt is deposited onto the grafted photocatalyst surface, Figure 6(c) and (d), the characteristic signal composed by four peaks (335.5, 334.9, 336.4 and 337.9 mT – $g = 2.02, 2.01, 2.00$ and 1.99) with intensity ratio of 1:2:2:1 related to $\text{DMPO}-\cdot\text{OH}$ adducts is clearly identified⁴⁸. Such signal is much more intense for the grafted sample than that observed for the bare hexaniobate under same conditions. In this sense, it seems 0.1% Co^{2+} grafted hexaniobate is more efficient on oxidation of water to yield hydroxyl radicals.

EPR spectra of powder samples in air and at 77K were also obtained and the data in the dark, Figure 7(a), was compared with those under UV irradiation, Figure 7(b). Here, to better evaluate the role of Co^{2+} on photocatalyst surface, the sample with 1% is also analyzed. Similar to the spectra for an aqueous suspension, under dark conditions, there is no signal for the bare hexaniobate spectrum, but a small one of $g = 2.01$ is found for the grafted samples, which can be related to free unpaired electrons trapped on oxygen-vacancy sites⁴⁹. Additionally, for the 1% Co^{2+} grafted hexaniobate, the signal at $g = 2.04$ is related to the Co^{2+} clusters, providing also experimental evidence of the ion oxidation state⁵⁰, in agreement with XPS data. Under UV irradiation, the bare hexaniobate exhibits a very similar spectrum to the one reported by Furukawa and coauthors for Nb_2O_5 ⁵¹. The three peaks with g around 2.03, 2.01 and 2.00 correspond to one set of rhombic g values, attributed to $\cdot\text{O}_2^{\bullet-}$ formation by a transfer of excited electrons to adsorbed O_2 molecules. Comparing the powder samples under UV irradiation, the spectrum of bare hexaniobate

exhibits more intense and defined peaks. As observed on EPR analyses for aqueous suspensions, this indicates that a fraction of electrons is transferred to Co^{2+} centers rather than to O_2 . This is even more evident for 1% Co^{2+} sample, in which the spectrum under UV irradiation is very similar to that in the dark and does not show the three characteristic peaks of $\text{O}_2^{\bullet-}$ as observed for the bare hexaniobate.

Further photoelectrochemical analyses were carried out employing bare and grafted hexaniobate photoanodes, Figure 8 and Figure B11.

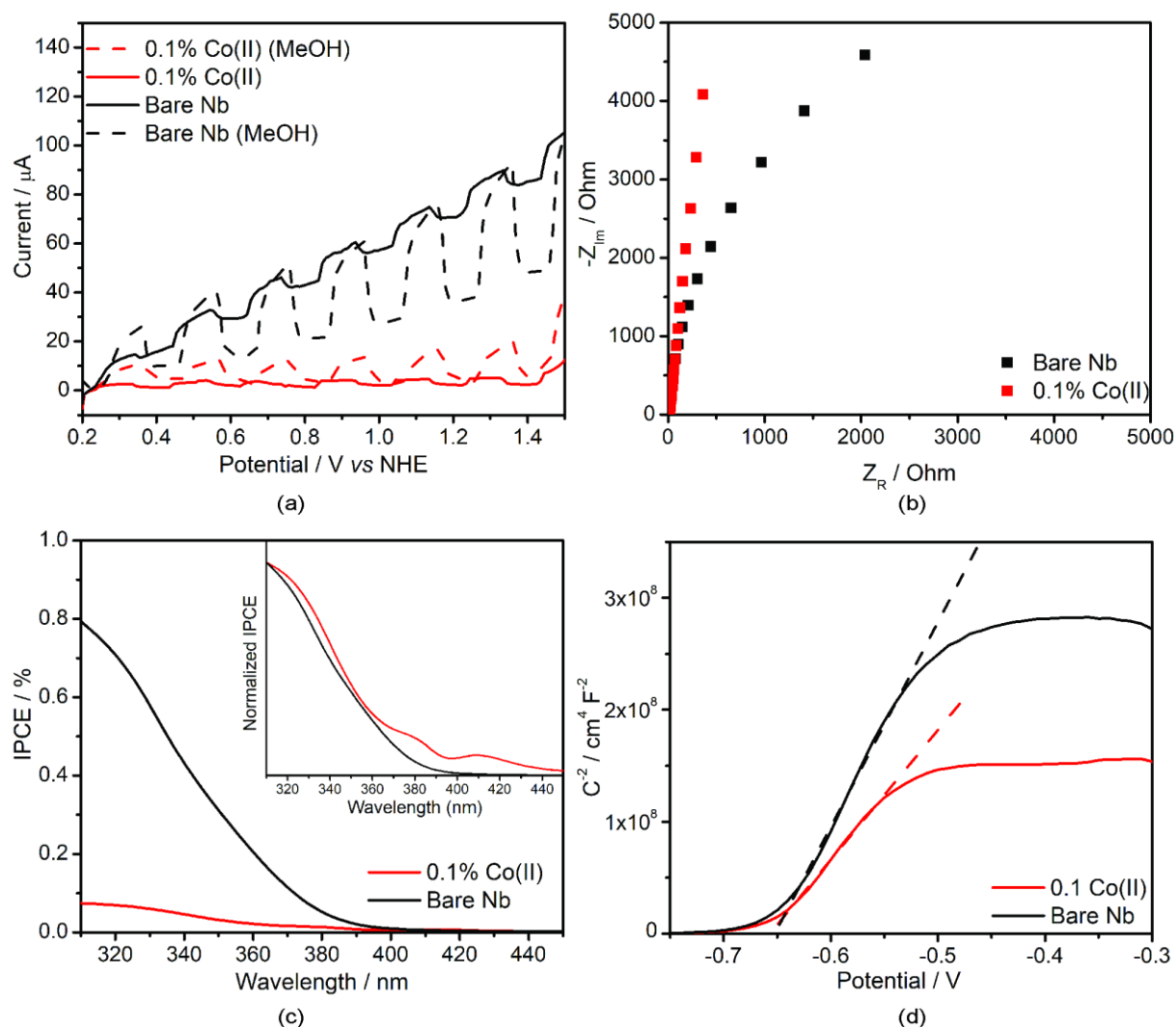


Figure 8 – Current–voltage curves under chopped UV-Vis irradiation (a), Nyquist plots at 1 V vs SHE (b), IPCE spectra (10% MeOH, 1 Hz, 1 V vs SHE) *inset*: normalized data (c), and Mott-Schottky plot (100 Hz) (d) of bare and 0.1% Co^{2+} grafted hexaniobate photoanodes in 0.1 M Na_2SO_4 electrolyte.

Linear-sweep voltammograms using a 365 nm LED coupled to a chopper were measured in the presence and absence of methanol in the electrolyte, Figure 8(a). Anodic

photocurrents are produced as consequence of photoelectrodes excitation. Photogenerated electrons are transferred to the circuit, while holes in the valence band are involved in oxidation reactions between the photoelectrode and the electrolyte. In the case of bare hexaniobate, only small improvements are observed under excitation, particularly in the absence of methanol. With 10% methanol in the electrolyte, the contribution of photogenerated current is greater. In addition, for both bare and grafted samples in methanol solutions, the photocurrent does not reach a plateau during the short period of constant light irradiation, which is related to the faster kinetics of methanol oxidation and quick electron transfer from the photocatalyst to FTO substrate. Other photoelectrochemical systems described in the literature also presented the same behavior^{52,53}. A comparison between bare and grafted photoresponses reveals that the Co^{2+} -grafted photoanodes yield smaller photocurrents, hence, charge transport within hexaniobate layers is partially inhibited due to the presence of Co^{2+} cations.

The electrochemical impedance spectroscopy spectrum of the grafted sample corroborates with the voltametric measurements as a more capacitive behavior is observed in the Nyquist plots when compared with that obtained for the bare hexaniobate, Figure 8(b). Moreover, incident photon-to-electron conversion efficiency (IPCE) spectra for both films confirm that the materials are only UV photoactive, with smaller conversion efficiencies for the Co^{2+} -grafted sample, in agreement with the voltammetric data. Looking more carefully on the normalized data, Figure 8(c) inset, in the action spectrum of the grafted sample, there are two small bands centered at 380 and 410 nm that do not appear for the bare hexaniobate and can be associated with the IFCT transitions.

Flat-band potentials of the photoanodes were calculated from the resulting Mott–Schottky plots (C^{-2} vs. applied potential) as shown in Figure 8(d). For both samples, positive slopes confirmed the fact that they are n-type semiconductors, with flat-band potentials of about -0.7 V vs. NHE in accordance with the literature⁵⁴. Comparing the two samples curves, the slope for the Co^{2+} grafted hexaniobate is smaller than that for bare hexaniobate. Considering the Mott–Schottky equation, this behavior suggests lower carrier density and faster charge transfer for the grafted sample⁵⁵. The exact carrier densities (N_D) were not calculated since the dielectric constant for hexaniobate is not available. Nevertheless, it indicates that electrons are being quickly transferred from hexaniobate conduction band to Co^{2+} . This fact is also supported by considering the $\text{Co}^{2+}/\text{Co}^0$ redox potential of -0.28 V versus SHE or also -0.73 V versus SHE for

$\text{Co}(\text{OH})_2/\text{Co}^0$, which are lower or close to the hexaniobate conduction band potential (-0.7 V)⁵⁶.

Further information concerning charge carrier kinetics was obtained by TAS measurements. Representative transient spectra of the bare and Co^{2+} grafted hexaniobates in N_2 atmosphere at 200 ns after laser excitation are shown in Figure 9(a). The spectra at different delay times and Fe^{3+} -grafted samples data are reported in Supporting Information (Figure B12, B13 and B14). In the TAS spectra, the change in reflectance (ΔJ) is directly proportional to the number of photogenerated charge carriers⁵⁷. All samples exhibit a broad profile in the visible range following 355 nm excitation, being quite similar to that observed for other semiconductors^{28,58}. Such profile is ascribed to an overlap between signals from trapped electrons and trapped holes. The latter species are expected to contribute more for absorption at higher energies or lower wavelengths ($\lambda < 500\text{ nm}$)⁵⁹. In fact, when samples are exposed to MeOH vapour, which acts as hole scavenger, Figure B13, the intensities at $\lambda > 500\text{ nm}$ are higher for all samples, confirming the attribution made. A transient feature that could be exclusively attributed to the grafting ions was not identified, even at different time delays.

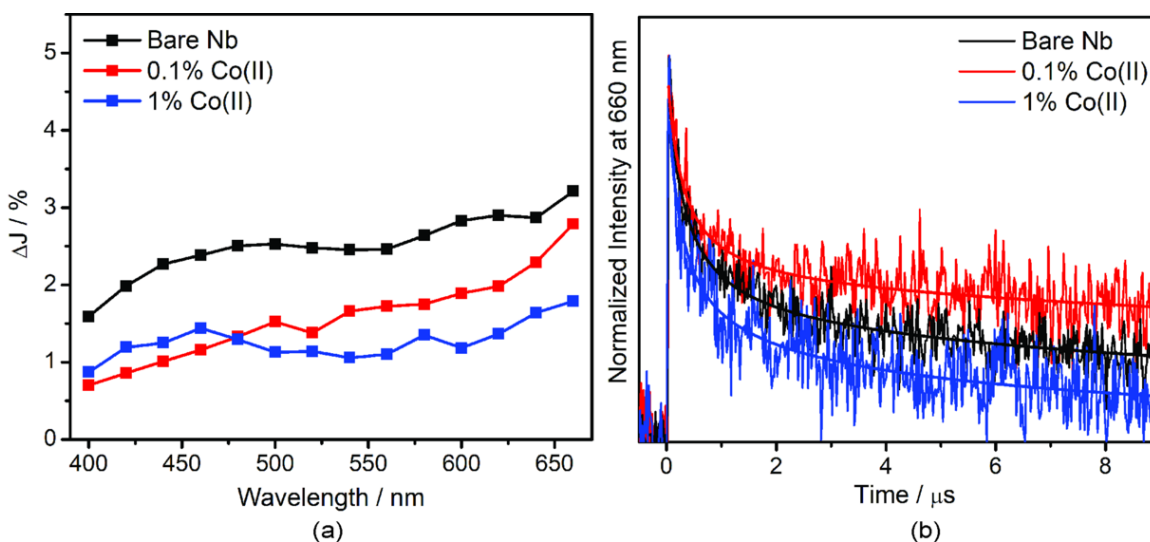


Figure 9 –Transient absorption spectra of the samples in N_2 200 ns after the laser pulse (a) and transient decays at 660 nm (b). $\lambda_{\text{exc}} = 355\text{ nm}$ (6 mJ cm^{-2} per pulse).

In Figure 9(a), transient spectrum of 0.1% Co^{2+} sample exhibits lower intensity in the region of 400–450 nm in relation to the bare hexaniobate. In fact, it resembles those expected for free electrons in a semiconductor⁶⁰ and is quite similar to those observed for all samples in the presence of MeOH vapor, Figure B13 and B14(b). In contrast, the bare hexaniobate in N_2 atmosphere exhibits a broad signal between 400 and 550 nm likely

related to different hole trapping states. In the hexaniobate sheets, electrons and holes can either undergo geminated recombination or migrate along the hexaniobate layer and be trapped in surface sites with different energies, giving rise to broad transient signals at short wavelengths.

When Co^{2+} centers are on the surface, two distinct behaviors are observed in the transient spectra as a function of Co^{2+} concentration. For the 0.1% Co^{2+} sample, transient signals in spectral regions where a major contribution from trapped holes is expected are partially suppressed in relation to the bare hexaniobate. As the Co^{2+} ions concentration is increased to 1%, the relative intensity at 450–500 nm is enhanced, but the main change occurs at higher wavelengths, where a major contribution from trapped electrons is found. The transient signal is relatively smaller than those observed for both bare hexaniobate and 0.1% Co^{2+} grafted samples. Changes in the transient spectra of the hexaniobate due to introduction of grafted Co^{2+} and Fe^{3+} ions evidence that the fate of both photogenerated electrons and holes are affected by the surface ions.

Looking at the charge recombination dynamics in N_2 atmosphere, Figure 9(b), small amounts of grafted Co^{2+} ions increase the charge carrier lifetimes, while samples having 1% Co^{2+} exhibit faster recombination rates than the bare hexaniobate. Transient decays for the samples in N_2/MeOH mixture can be found in Figure B15 and data for Fe^{3+} -grafted samples can be found in Figure B16. For all samples, decay kinetics at 660 nm exhibit non-exponential behavior and could be satisfactorily fitted by two second order components, Equation 2, following the model described elsewhere⁶¹ in which trapped electrons and holes are treated as independent equal concentration species. In Equation 2, t is the time elapsed after the laser pulse, k_1 and k_2 are the corresponding to the second order rate constants, ΔJ_0 is the initial amplitude of the signal at the probe wavelength directly after laser excitation, and ΔJ_2 corresponds to the initial amplitude of the slower component associated with k_2 . The fit parameters are shown in Table 2.

$$\Delta J = \frac{\Delta J_0 - \Delta J_2}{1 + \Delta J_0 k_1 t} + \frac{\Delta J_2}{1 + \Delta J_0 k_2 t} \quad (2)$$

Table 2. Second order fit parameters for bare and grafted hexaniobate samples following 355 nm excitation (298 K).

Sample	k_1 (10^6 s^{-1})	k_2 (10^4 s^{-1})	ΔJ_2 (%)
Bare Nb	5.0 ± 0.7	6.7 ± 0.8	25 ± 1
0.1% Co^{2+}	6.0 ± 0.8	2.2 ± 0.5	39 ± 1
1% Co^{2+}	6.5 ± 0.4	19 ± 1	24 ± 1
0.1% Fe^{3+}	4.7 ± 0.7	8.3 ± 0.3	29 ± 1

In the 0.1% Co^{2+} hexaniobate, the fast kinetics component (k_1) associated with geminated charge carrier recombination is slightly higher than that in the bare Nb sample, however a large fraction of charge carriers is trapped and undergoes slow recombination (k_2). Additionally, k_2 for 0.1% Co-grafted sample is half than that for bare hexaniobate and therefore, a large fraction of charge carriers is available milliseconds after light excitation to carry out chemical reactions. A similar behavior is observed for the hexaniobate sheets grafted with 0.1% Fe^{3+} .

As Co^{2+} surface concentration increases, k_1 does not change substantially but its contribution to the decay dynamics increases, which may be related to additional surface defects on the hexaniobate layers that act as recombination centers. Notably, k_2 value increases one order of magnitude as the Co^{2+} concentration is enhanced. TAS data agree quite well with the photoelectrochemical measurements, that is, grafted ions on hexaniobate sheets work as electron trapping sites, decreasing the charge mobility within the 2D structure, leading to smaller photocurrents but longer charge carrier lifetimes.

Based on the photoelectrochemical and spectroscopic characterizations, the photocatalytic behavior of the grafted hexaniobate layers can be rationalized. The structural, optical, and morphological characterizations clearly show that grafting ions are attached on niobate surface mainly by terminal oxygen groups forming amorphous clusters. Those species induced two additional absorption features in the UV-A and visible ranges in comparison to bare hexaniobate. The former can be related to an IFCT from the hexaniobate valence band to Co^{2+} or Fe^{3+} centered orbitals. The latter is related to d-d transitions of Co^{2+} and Fe^{3+} centers and is unable to promote redox reactions.

In relation to the photocatalytic activity, lower amounts of the loaded cation are more effective in all the evaluated conditions and for both tested metals. When using 10% MeOH for H_2 evolution without any additional co-catalyst, the observed reaction rate

increases 85% and 40% in relation to the bare hexaniobate for 0.1% Co^{2+} and 0.1% Fe^{3+} , respectively. This is in good agreement with the higher charge carrier lifetime, as the slow recombination rate (k_2) contribution for the electron-hole dynamics increases due to the electron transfer from the hexaniobate conduction band to the grafted ions. In plain water, however, the samples are unable to produce H_2 as photoexcited electrons are trapped as Co^{1+} or Fe^{2+} species. When the samples were tested for methanol oxidation in air atmosphere, 0.1% Co^{2+} was able to increase the methanol formation rate in 50% while 0.1% Fe^{3+} did not significantly change the rate when comparing to the bare hexaniobate, which reveals the role of the reductive pathway to yield peroxide radicals on the methanol oxidation. Apparently, electrons trapped on Fe^{3+} ions are not efficiently transferred to molecular oxygen.

In the absence of Pt clusters, Co^{2+} and Fe^{3+} ions act as electron acceptors either through IFTC transitions but also following direct bandgap excitation of the hexaniobate sheets, Figure 10(a). The electron transfer to the grafted ions, confirmed by EPR data, leads to enhanced charge carrier lifetimes, but the electron mobility is reduced as confirmed by photoelectrochemistry studies. In fact, redox potential for $\text{Co}^{2+}/\text{Co}^0$ of -0.28 V vs SHE is closer to the hexaniobate conduction band (-0.7 V) and should lead to more efficient electron transfer in comparison to the $\text{Fe}^{3+}/\text{Fe}^{2+}$ of $+0.77\text{ V vs SHE}$. The more positive redox potential of $\text{Fe}^{3+}/\text{Fe}^{2+}$ pair also justifies the inability of Fe^{3+} grafted hexaniobates to reduce O_2 molecules.

Once Pt clusters are deposited over the grafted hexaniobate surface, partial water splitting is finally achieved with sustainable H_2 production. In this case as well, the 0.1% Co^{2+} grafted sample shows the best reaction rates in comparison to both bare and 0.1% Fe^{3+} grafted hexaniobates. In Pt-modified samples, photoexcited electrons are expected to be trapped by the Pt metallic clusters. This is experimentally clear when Pt and MeOH are used for the photocatalytic evaluations and after the grafting with 0.1% of metal ions, the hexaniobate did not show better performances, Figure 10(b). This result can also be related to the ease in which methanol can be oxidized compared to pure H_2O , so the enhanced charge carrier lifetime does not play a significant role on the photocatalytic behavior. In plain water however, the improved performance of the 0.1% Co^{2+} grafted sample reveals that grafted Co^{2+} ions do affect the hole transfer to water. Small amounts of Co^{2+} on hexaniobate surface change the oxidative pathway and favor the formation of OH^\bullet radicals from water as could be confirmed by EPR. As previously reported^{5,19}, holes on hexaniobate sheets tend to oxidize water molecules to H_2O_2 , which remains strongly

adsorbed on the hexaniobate surface and leads to its fully deactivation after long irradiation times. It seems that Co^{2+} ions on the surface can act as hole acceptors to form Co^{3+} centers ($\text{Co}^{3+}/\text{Co}^{2+}$ 1.9 V vs SHE) which further react with water to yield OH^\bullet radicals. Alternatively, Co^{2+} ions can react with adsorbed H_2O_2 , “cleaning” the surface and avoiding the deactivation of the photocatalyst, Figure 10(c). Therefore, grafted Co^{2+} ions act as active redox shuttles in the hexaniobate sheets, contributing for more efficient charge separation. The higher stability of Fe^{3+} ions toward further oxidation makes it not suitable to behave in the same way. The dependence of the H_2 evolution on the ion surface concentration can be explained by a competition between Co^{2+} and Pt centers to act as electron acceptors. Hexaniobate surface grafting with Co^{2+} ions can be then employed to develop ternary systems, involving metallic centers responsible for the reductive reactions, while the Co^{2+} -grafted ions will carry out the oxidative reactions.

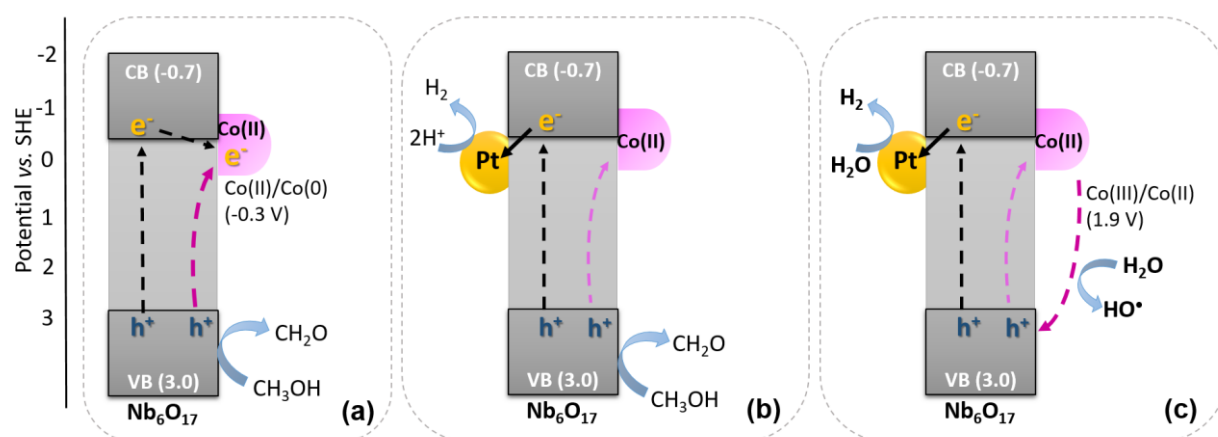


Figure 10 – Charge transfer steps following UV excitation of 0.1% Co^{2+} grafted hexaniobate in 10% methanol aqueous solution without (a) and with (b) Pt as co-catalyst and (c) in plain water with deposited Pt.

4.6. Conclusions

For the first time in the literature, exfoliated hexaniobate ($\text{H}_x\text{K}_{4-x}\text{Nb}_6\text{O}_{17}$) layers are modified by the surface grafting methodology. Through soft conditions, exfoliated hexaniobate was superficially modified by Co^{2+} or Fe^{3+} ions. The metal amorphous centers on hexaniobate surface were able to induce an extended UV-A absorption as a result of an IFCT transition. Photocatalytic studies show that 0.1 wt.% grafted samples can improve the performance for MeOH oxidation; however, they do not influence on

that mechanism in presence of an electron scavenger such as Pt. Interestingly, in pure water, the surface grafting leads to partial water splitting. The sample with 0.1 wt.% Co^{2+} reached the best performance with a H_2 evolution rate of $86 \mu\text{mol h}^{-1} \text{g}^{-1}$. As demonstrated by EPR, photoelectrochemical, and TAS studies, Co^{2+} clusters on the hexaniobate surface act as electron trap states but also promote the water oxidation to $\cdot\text{OH}$ radicals, playing an important role on the oxidative pathway, that is, on the fate of photogenerated holes, especially when an electron scavenger such as Pt is present. This effect is less pronounced in Fe^{3+} -grafted sample due to the more negative oxidation potential. Therefore, grafted Co^{2+} ions act as active redox shuttles in the hexaniobate sheets, contributing for more efficient charge separation and supporting the H_2 production. The results discussed here can support further developments on more efficient niobate-based photocatalysts.

4.7. Supporting Information

Figure B1. X ray diffractograms of the as prepared exfoliated hexaniobate, the stacked layered potassium hexaniobate obtained by the solid state synthesis and the reference $K_4Nb_6O_{17} \cdot 3H_2O$ (JCPDS 21-1297).

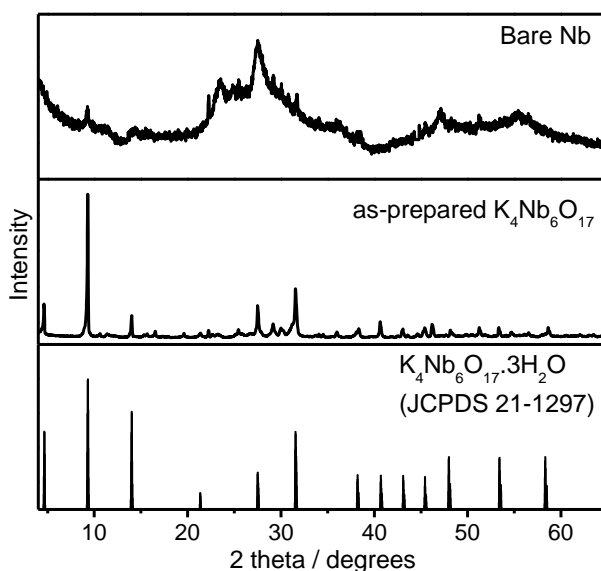


Figure B2. XRD patterns (a) and diffuse reflectance UV–Vis spectra (b) of Fe^{3+} -grafted hexaniobate compared to the bare sample.

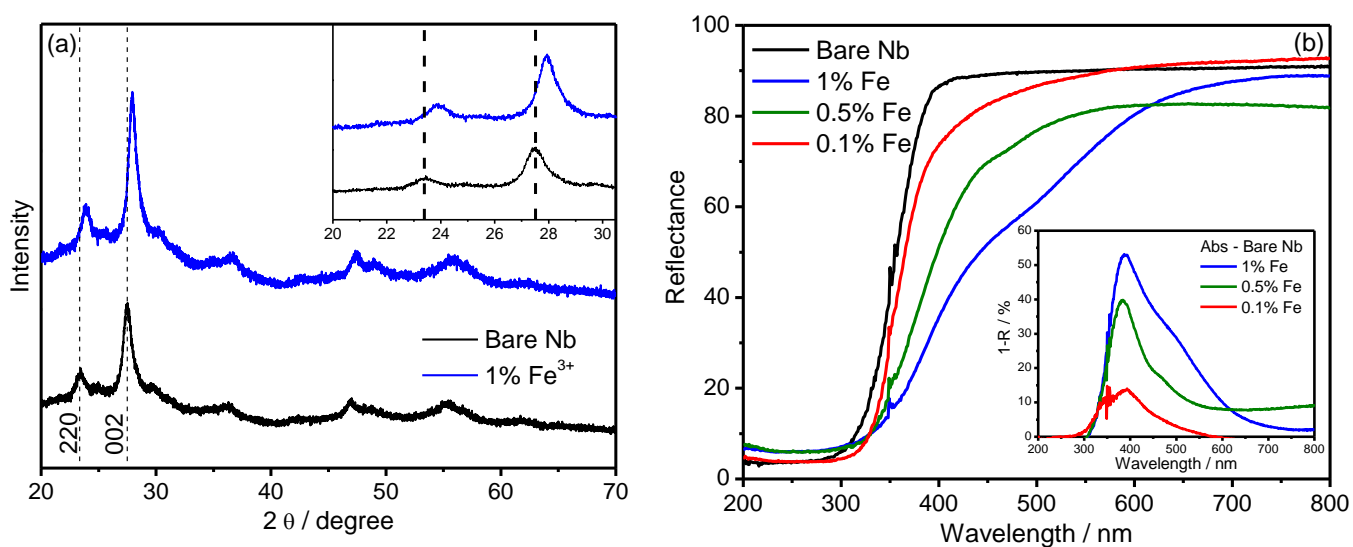


Figure B3. Survey XPS spectra of the bare niobate (a) and 1 wt% Co-grafted sample (b). In (c) is shown a high-resolution spectrum of Co $2p_{3/2}$ peak in 1 wt% Co-grafted sample.

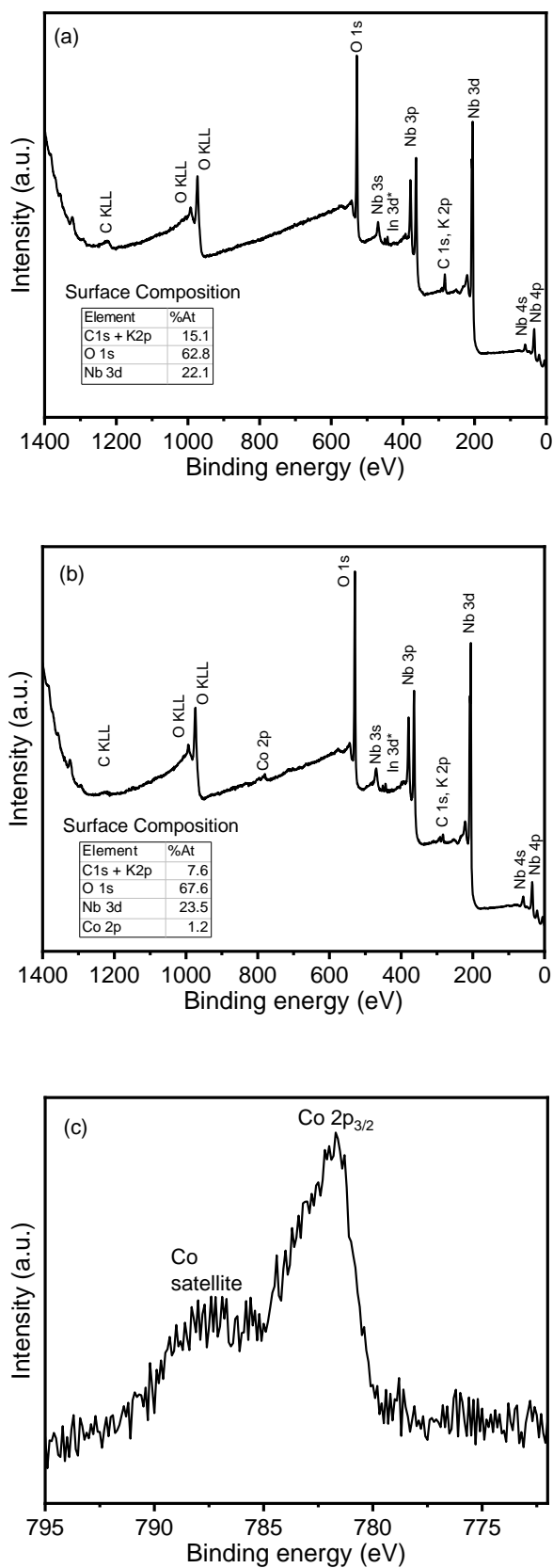


Figure B4. High resolution XPS spectra in the Nb 3d and O 1s regions of the bare and 1 wt% Co-grafted hexaniobate. New signals due to surface grafting are highlighted in orange.

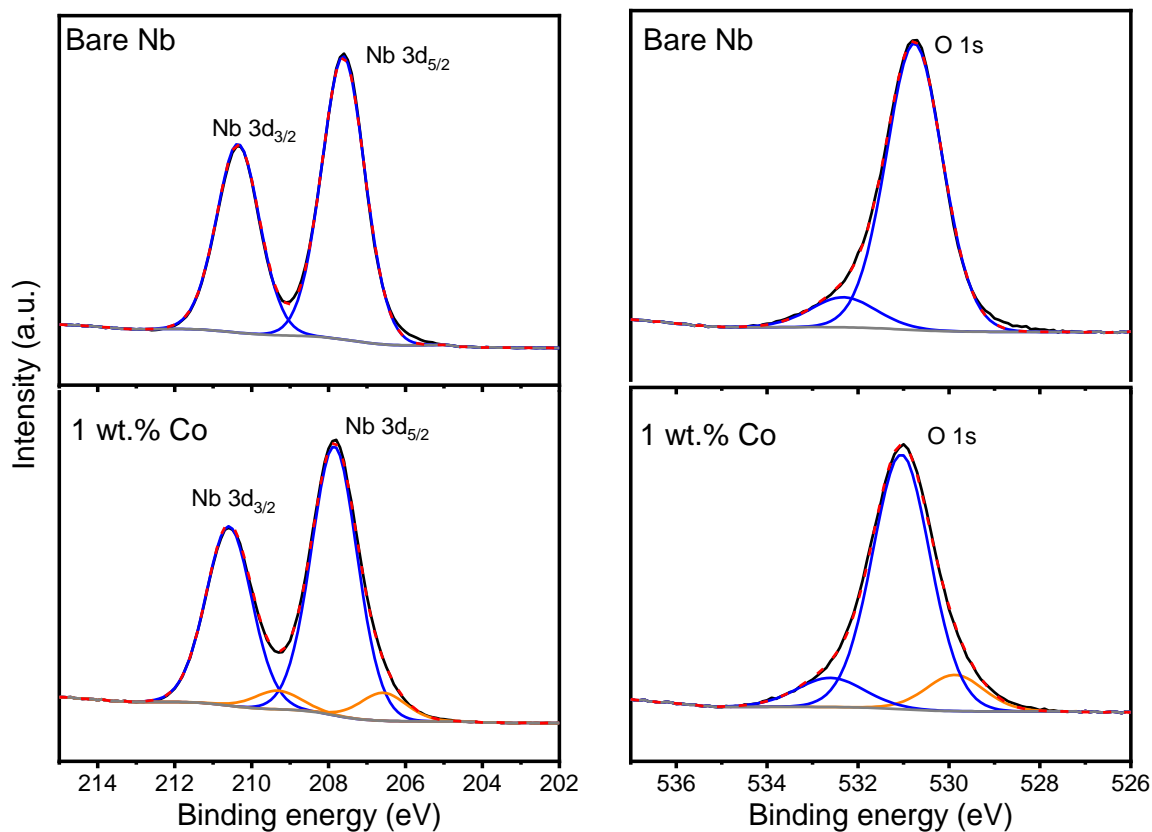


Figure B5. Raman (a) and infrared (b) spectra of bare and 1 wt.% Fe³⁺ grafted hexaniobate.

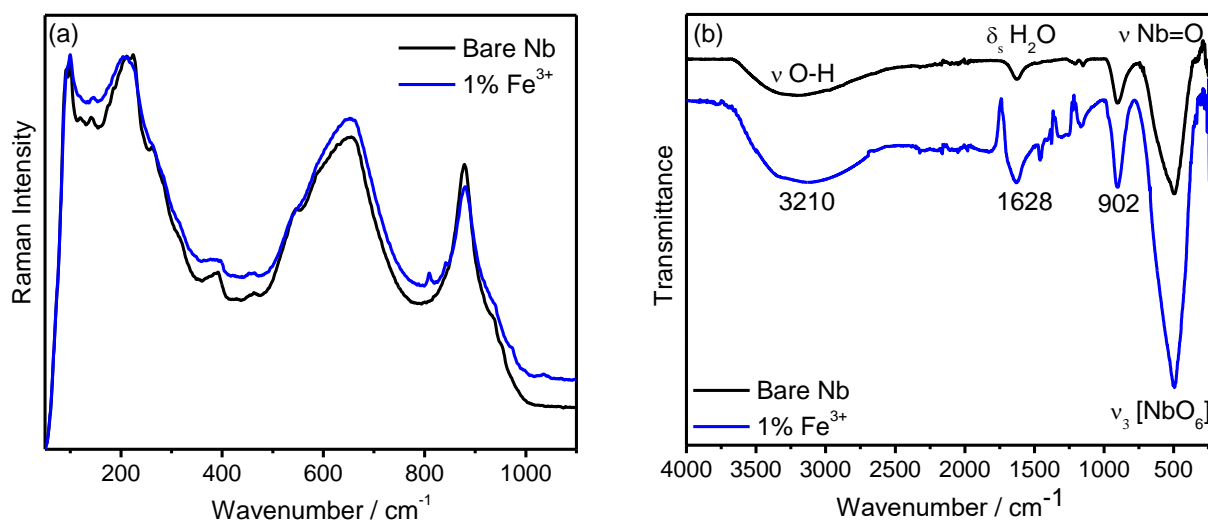


Figure B6. H₂ evolution profiles followed two consecutive UV-Vis irradiation tests employing aqueous suspensions of 0.1% Co²⁺-grafted hexaniobate loaded with 2 wt% Pt.

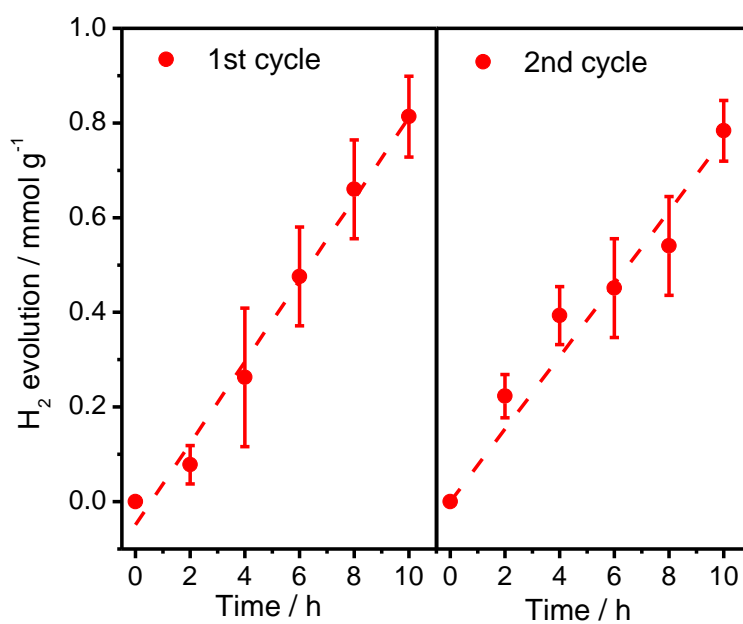


Figure B7. XRD pattern (a) and XPS survey spectrum (b) of 1 wt% Co^{2+} -grafted hexaniobate layers following long term UV-irradiation in argon atmosphere. *Inset* in (b) shows the high resolution spectrum at Co 2p region.

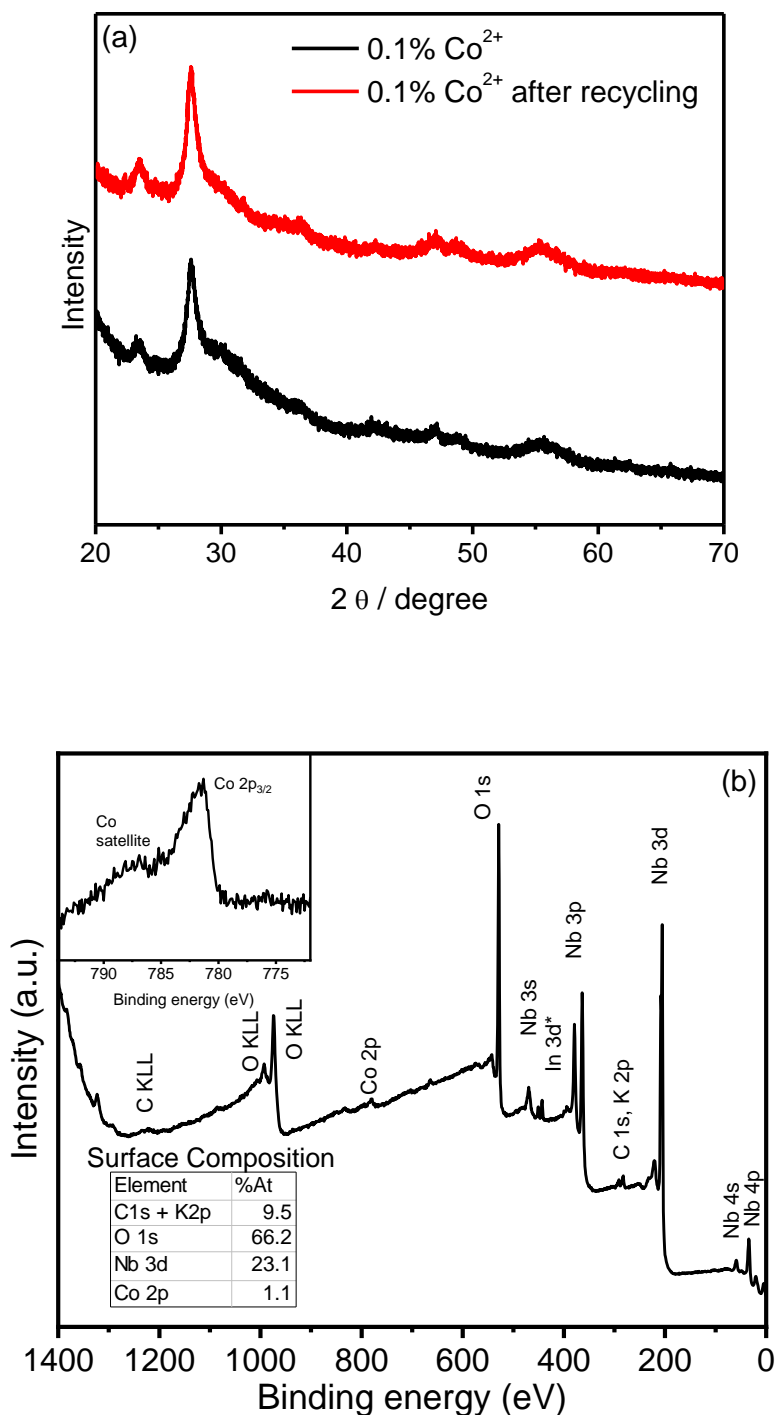


Figure B8. Mass spectrometry detection of H₂ (m = 2.014), D₂ (m = 4.028) and HD (m = 3.021) gasses at different time as aliquots of the reactor headspace with the photocatalyst (0.1% Co²⁺ grafted hexaniobate with 2 wt.% Pt) suspended in D₂O and submitted to UV-Vis irradiation (1000 W Xenon lamp).

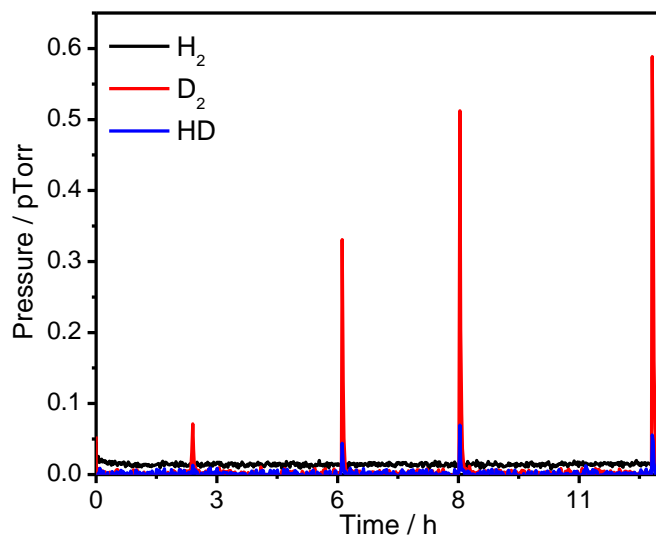


Figure B9. H₂ evolution from 10% methanol aqueous solution promoted by samples loaded with 2 wt.% Pt (a) and methanal production as a result of photocatalytic oxidation of 0.03 mol L⁻¹ methanol aqueous solutions (b) under UV-Vis irradiation.

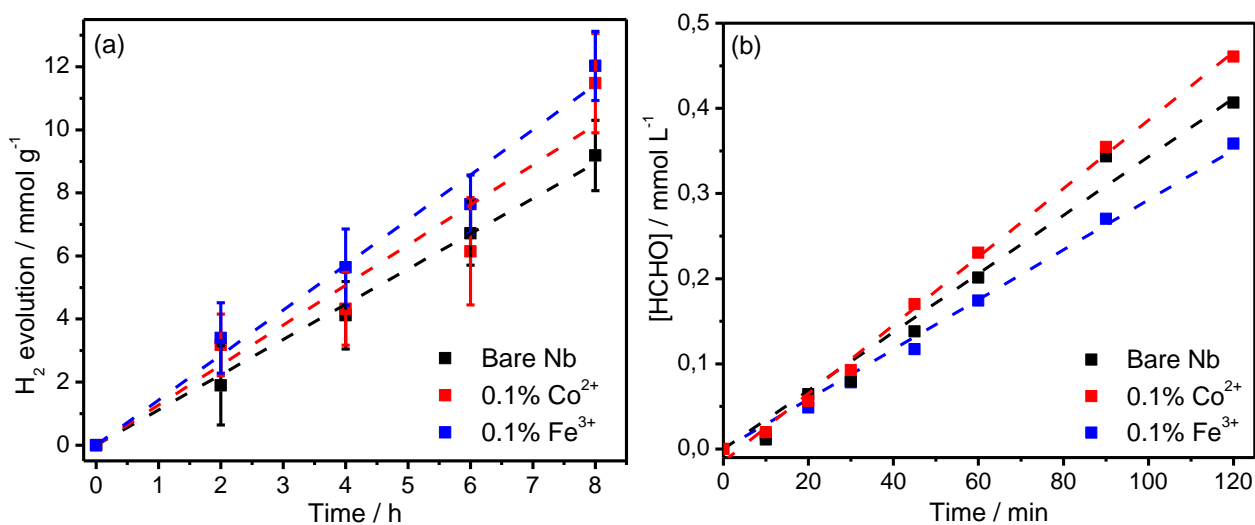


Figure B10. UV-induced methanal production from photocatalytic methanol oxidation (0.03 mol L^{-1}) in the presence of Co^{2+} (a) or Fe^{3+} (b) grafted or bare hexaniobate photocatalysts without Pt loading.

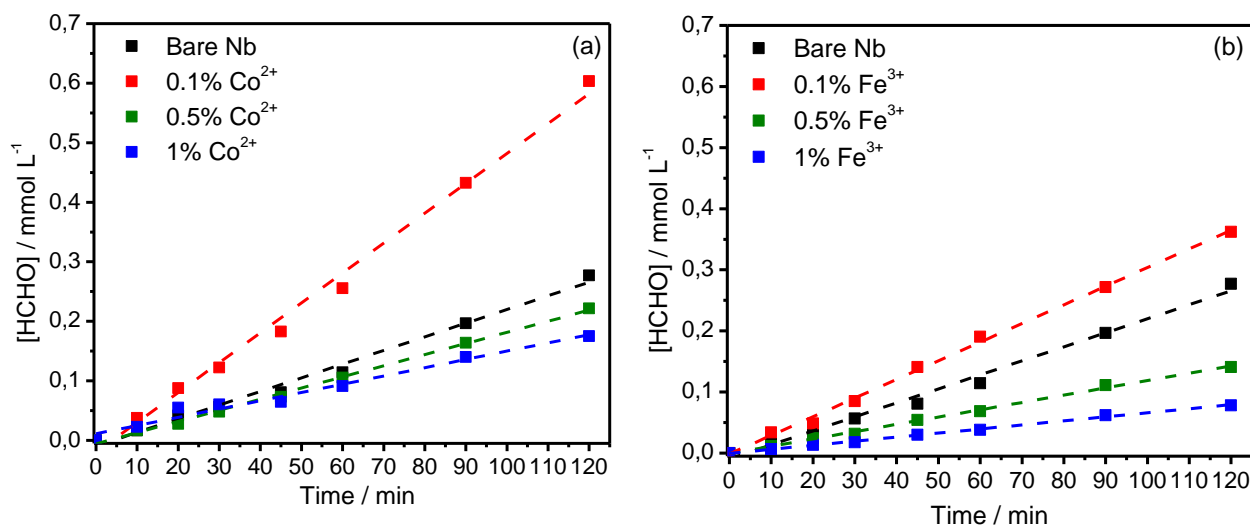


Figure B11. Current–voltage curves under chopped UV-Vis irradiation (a) and Nyquist plots at 1 V vs SHE (b) for the bare and 0.1% Fe^{3+} -grafted hexaniobate photoanodes in 0.1 M Na_2SO_4 electrolyte with and without methanol.

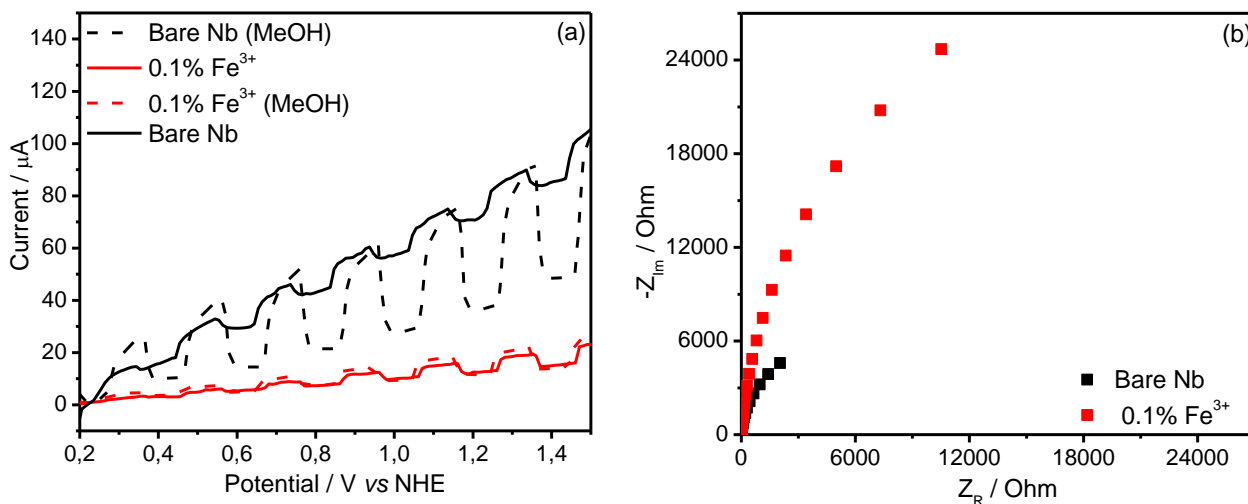


Figure B12. Transient absorption spectra of bare (a), 0.1% (b), and 1% Co^{2+} (c) grafted hexaniobate in N_2 atmosphere at different times after the laser pulse. $\lambda_{\text{exc}} = 355 \text{ nm}$ (6 mJ cm^{-2} per pulse).

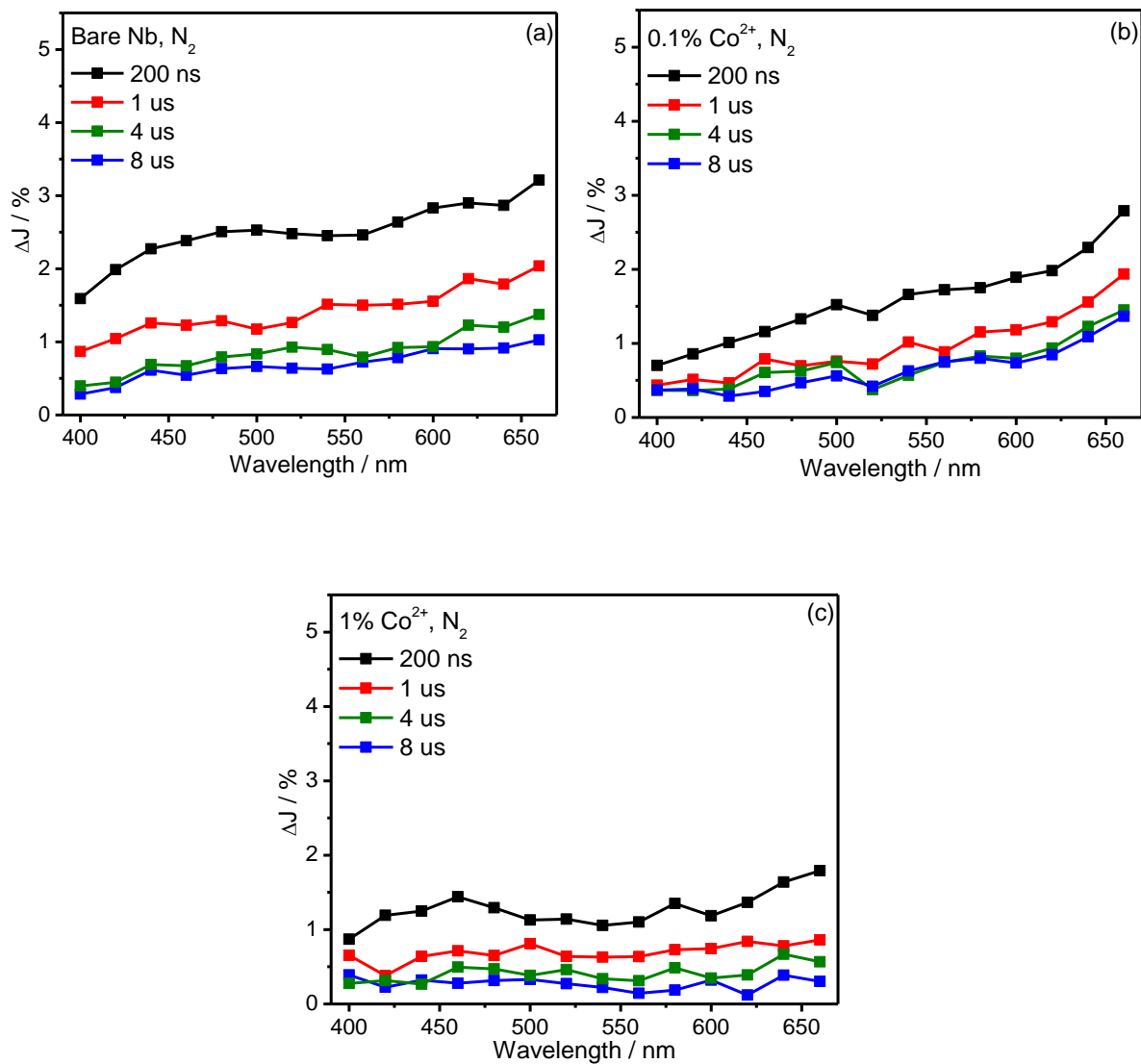


Figure B13. Transient absorption spectra of bare (a), 0.1% (b), and 1% Co^{2+} (c) grafted hexaniobate in N_2/MeOH atmosphere at different times after the laser pulse. $\lambda_{\text{exc}} = 355$ nm (6 mJ cm^{-2} per pulse).

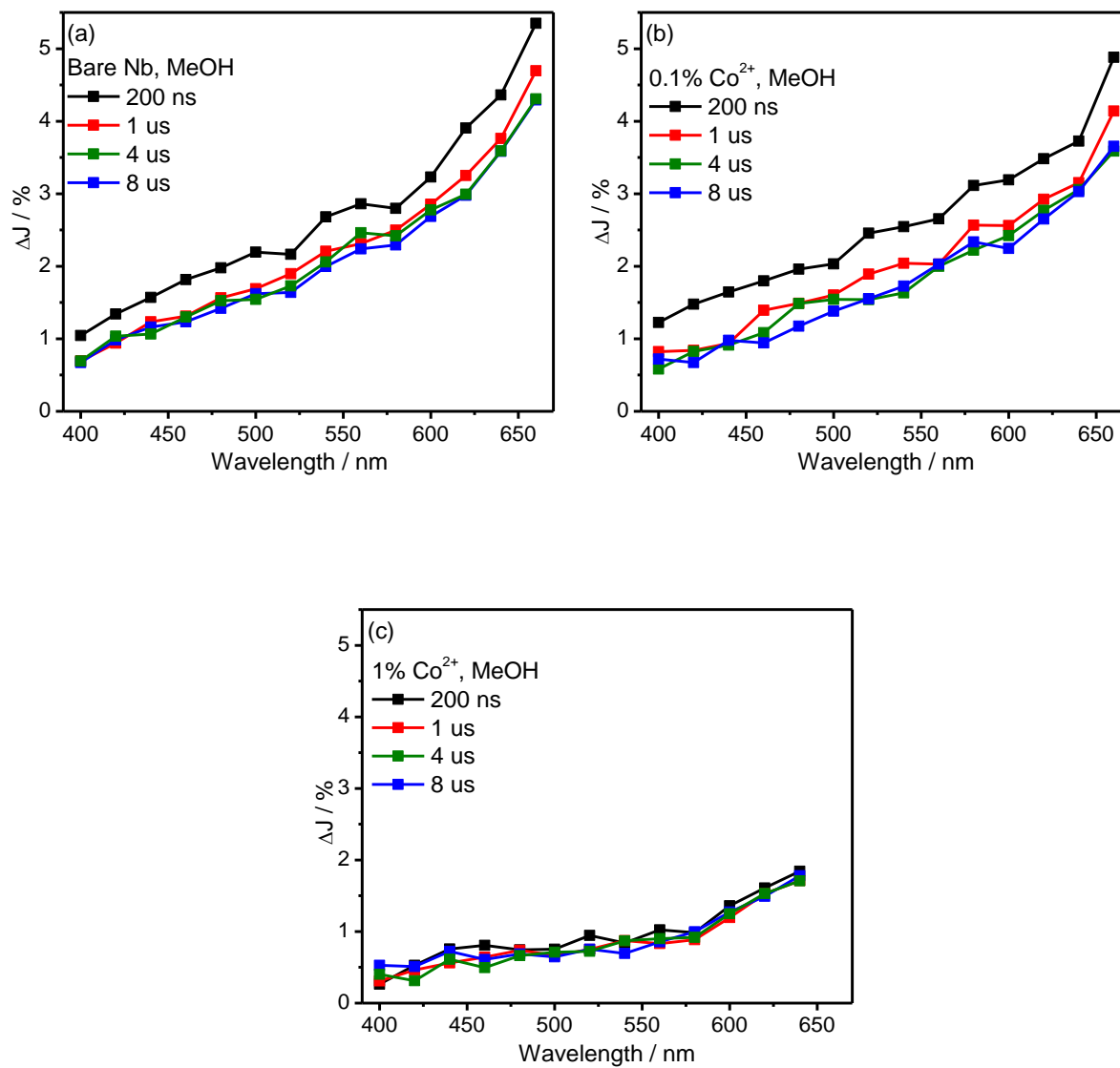


Figure B14. Transient absorption spectra of 0.1% Fe³⁺ in N₂ (a) and N₂/MeOH (b) atmospheres at different times after the laser pulse. $\lambda_{\text{exc}} = 355 \text{ nm}$ (6 mJ cm^{-2} per pulse).

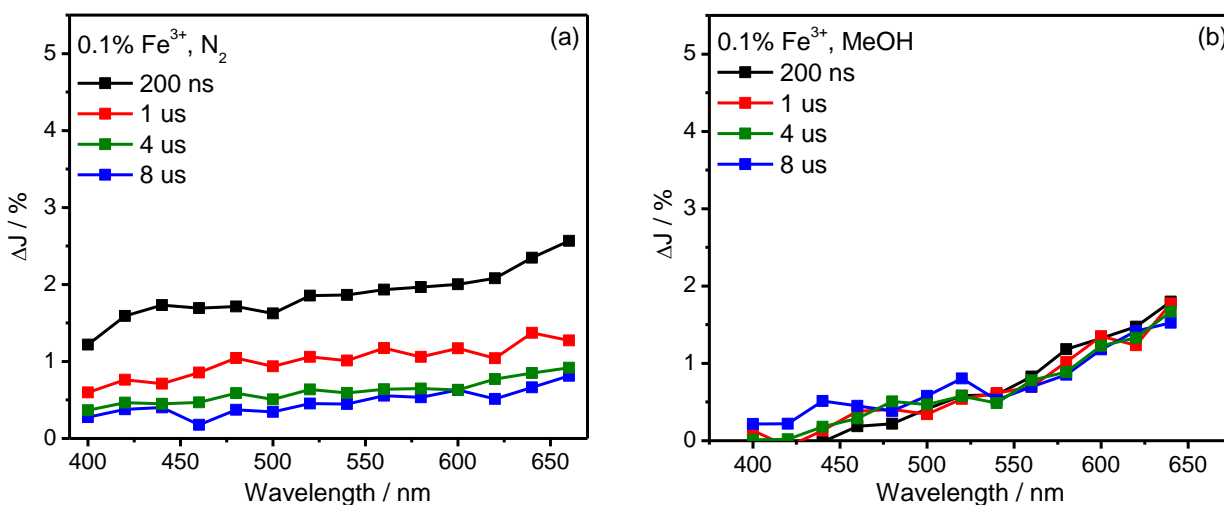


Figure B15. Transient decays at 660 nm for bare and 0.1% Co²⁺ grafted hexaniobate (a) and 640 nm for bare, 0.1% and 1% Co²⁺ grafted hexaniobate (b) after excitation with 355 nm pump pulse in N₂/MeOH mixture. The curves at 640 nm are also shown since the 660 nm decay for the 1% Co²⁺ grafted hexaniobate was not measurable due to low reduced scattering by this sample at this wavelength. $\lambda_{\text{exc}} = 355 \text{ nm}$ (6 mJ per pulse).

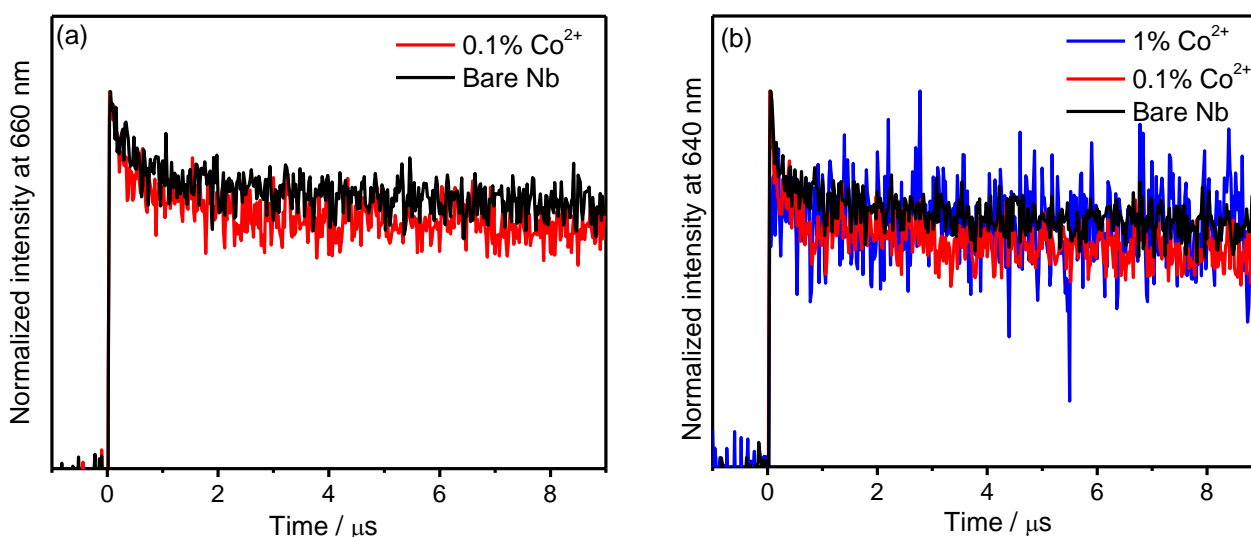
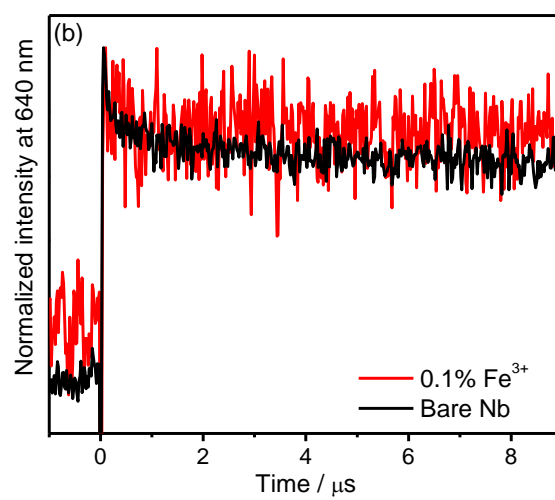
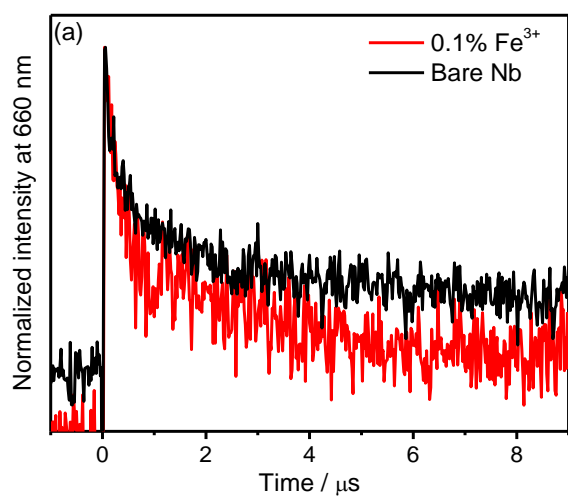


Figure B16. Transient decays at 660 nm in N₂ atmosphere (a) and 640 nm in N₂/MeOH atmosphere (b). $\lambda_{\text{exc}} = 355 \text{ nm}$ (6 mJ per pulse).



4.8. References

- (1) Nunes, B. N.; Lopes, O. F.; Patrocínio, A. O. T.; Bahnemann, D. W. Recent Advances in Niobium-Based Materials for Photocatalytic Solar Fuel Production. *Catalysts* **2020**, *10* (1), 126. <https://doi.org/10.3390/catal10010126>.
- (2) Zhou, C.; Shi, R.; Waterhouse, G. I. N.; Zhang, T. Recent Advances in Niobium-Based Semiconductors for Solar Hydrogen Production. *Coord. Chem. Rev.* **2020**, *419*, 213399. <https://doi.org/10.1016/j.ccr.2020.213399>.
- (3) Nico, C.; Monteiro, T.; Graça, M. P. F. Niobium Oxides and Niobates Physical Properties: Review and Prospects. *Prog. Mater. Sci.* **2016**, *80*, 1–37. <https://doi.org/10.1016/j.pmatsci.2016.02.001>.
- (4) Nunes, B. N. B. N.; Haisch, C.; Emeline, A. V.; Bahnemann, D. W. D. W.; Patrocínio, A. O. T. Photocatalytic Properties of Layer-by-Layer Thin Films of Hexaniobate Nanoscrolls. *Catal. Today* **2019**, *326* (June 2018), 60–67. <https://doi.org/10.1016/j.cattod.2018.06.029>.
- (5) Townsend, T. K.; Sabio, E. M.; Browning, N. D.; Osterloh, F. E. Improved Niobate Nanoscroll Photocatalysts for Partial Water Splitting. *ChemSusChem* **2011**, *4* (2), 185–190. <https://doi.org/10.1002/cssc.201000377>.
- (6) Domen, K.; Kudo, A.; Shinozaki, A.; Tanaka, A.; Maruya, K. I.; Onishi, T. Photodecomposition of Water and Hydrogen Evolution from Aqueous Methanol Solution over Novel Niobate Photocatalysts. *J. Chem. Soc. Chem. Commun.* **1986**, No. 4, 356–357. <https://doi.org/10.1039/C39860000356>.
- (7) Kudo, A.; Sayama, K.; Tanaka, A.; Asakura, K.; Domen, K.; Maruya, K.; Onishi, T. Nickel-Loaded $K_4Nb_6O_{17}$ Photocatalyst in the Decomposition of H_2O into H_2 and O_2 : Structure and Reaction Mechanism. *J. Catal.* **1989**, *120* (2), 337–352. [https://doi.org/10.1016/0021-9517\(89\)90274-1](https://doi.org/10.1016/0021-9517(89)90274-1).
- (8) Domen, K.; Kudo, A.; Tanaka, A.; Onishi, T. Overall Photodecomposition of Water on a Layered Niobate Catalyst. *Catal. Today* **1990**, *8* (1), 77–84. [https://doi.org/10.1016/0920-5861\(90\)87009-R](https://doi.org/10.1016/0920-5861(90)87009-R).
- (9) Sayama, K.; Tanaka, A.; Domen, K.; Maruya, K.; Onishi, T. Photocatalytic Decomposition of Water over Platinum-Intercalated $K_4Nb_6O_{17}$. *J. Phys. Chem.* **1991**, *95* (3), 1345–1348.
- (10) Nishioka, S.; Oshima, T.; Hirai, S.; Saito, D.; Hojo, K.; E. Mallouk, T.; Maeda, K. Excited Carrier Dynamics in a Dye-Sensitized Niobate Nanosheet

- Photocatalyst for Visible-Light Hydrogen Evolution. *ACS Catal.* **2021**, *11* (2), 659–669. <https://doi.org/10.1021/acscatal.0c04803>.
- (11) Oshima, T.; Nishioka, S.; Kikuchi, Y.; Hirai, S.; Yanagisawa, K.; Eguchi, M.; Miseki, Y.; Yokoi, T.; Yui, T.; Kimoto, K.; Sayama, K.; Ishitani, O.; E. Mallouk, T.; Maeda, K. An Artificial Z-Scheme Constructed from Dye-Sensitized Metal Oxide Nanosheets for Visible Light-Driven Overall Water Splitting. *J. Am. Chem. Soc.* **2020**, *142* (18), 8412–8420. <https://doi.org/10.1021/jacs.0c02053>.
- (12) Zhou, C.; Shi, R.; Shang, L.; Zhao, Y.; Waterhouse, G. I. N.; Wu, L. Z.; Tung, C. H.; Zhang, T. A Sustainable Strategy for the Synthesis of Pyrochlore $\text{H}_4\text{Nb}_2\text{O}_7$ Hollow Microspheres as Photocatalysts for Overall Water Splitting. *Chempluschem* **2017**, *82* (2), 181–185. <https://doi.org/10.1002/cplu.201600501>.
- (13) Domen, K.; Ebina, Y.; Ikeda, S.; Tanaka, A.; Kondo, J. N.; Maruya, K. Layered Niobium Oxides - Pillaring and Exfoliation. *Catal. Today* **1996**, *28*, 167–174. [https://doi.org/10.1016/0920-5861\(95\)00223-5](https://doi.org/10.1016/0920-5861(95)00223-5).
- (14) Lagaly, G.; Beneke, K. Cation Exchange Reactions of the Mica-like Potassium Niobate $\text{K}_4\text{Nb}_6\text{O}_{17}$. *J. Inorg. Nucl. Chem.* **1976**, *38* (8), 1513–1518. [https://doi.org/10.1016/0022-1902\(76\)90019-1](https://doi.org/10.1016/0022-1902(76)90019-1).
- (15) Jacobson, A. J.; Johnson, J. W.; Lewandowski, J. T. Intercalation of the Layered Solid Acid $\text{HCa}_2\text{Nb}_3\text{O}_{10}$ by Organic Amines. *Mater. Res. Bull.* **1987**, *22* (1), 45–51. [https://doi.org/10.1016/0025-5408\(87\)90148-6](https://doi.org/10.1016/0025-5408(87)90148-6).
- (16) Saupe, G. B.; Waraksa, C. C.; Kim, H. N.; Han, Y. J.; Kaschak, D. M.; Skinner, D. M.; Mallouk, T. E. Nanoscale Tubules Formed by Exfoliation of Potassium Hexaniobate. *Chem. Mater.* **2000**, *12* (6), 1556–1562. <https://doi.org/10.1021/cm981136n>.
- (17) Compton, O. C.; Carroll, E. C.; Kim, J. Y.; Larsen, D. S.; Osterloh, F. E. Calcium Niobate Semiconductor Nanosheets as Catalysts for Photochemical Hydrogen Evolution from Water. *J. Phys. Chem. C* **2007**, *111* (40), 14589–14592. <https://doi.org/10.1021/jp0751155>.
- (18) Sarahan, M. C.; Carroll, E. C.; Allen, M.; Larsen, D. S.; Browning, N. D.; Osterloh, F. E. $\text{K}_4\text{Nb}_6\text{O}_{17}$ -Derived Photocatalysts for Hydrogen Evolution from Water: Nanoscrolls versus Nanosheets. *J. Solid State Chem.* **2008**, *181* (7), 1678–1683. <https://doi.org/10.1016/j.jssc.2008.06.021>.
- (19) Compton, O. C.; Osterloh, F. E. Niobate Nanosheets as Catalysts for Photochemical Water Splitting into Hydrogen and Hydrogen Peroxide. *J. Phys.*

- Chem. C* **2009**, *113* (1), 479–485. <https://doi.org/10.1021/jp807839b>.
- (20) Balayeva, N. O.; Fleisch, M.; Bahnemann, D. W. Surface-Grafted WO₃/TiO₂ Photocatalysts: Enhanced Visible-Light Activity towards Indoor Air Purification. *Catal. Today* **2018**, *313*, 63–71. <https://doi.org/10.1016/j.cattod.2017.12.008>.
- (21) Liu, M.; Qiu, X.; Miyauchi, M.; Hashimoto, K. Energy-Level Matching of Fe(III) Ions Grafted at Surface and Doped in Bulk for Efficient Visible-Light Photocatalysts. *J. Am. Chem. Soc.* **2013**, *135* (27), 10064–10072. <https://doi.org/10.1021/ja401541k>.
- (22) Nakato, T.; Kuroda, K.; Kato, C. Syntheses of Intercalation Compounds of Layered Niobates with Methylviologen and Their Photochemical Behavior. *Chem. Mater.* **1992**, *4* (1), 128–132. <https://doi.org/10.1021/cm00019a027>.
- (23) Nunes, B. N.; Patrocínio, A. O. T.; Bahnemann, D. W. Influence of the Preparation Conditions on the Morphology and Photocatalytic Performance Pt-Modified Hexaniobate Composites. *J. Phys. Condens. Matter* **2019**, *31* (39), 394001. <https://doi.org/10.1088/1361-648x/ab2c5e>.
- (24) Maeda, K.; Eguchi, M.; Youngblood, W. J.; Mallouk, T. E. Niobium Oxide Nanoscrolls as Building Blocks for Dye-Sensitized Hydrogen Production from Water under Visible Light Irradiation. *Chem. Mater.* **2008**, *20* (21), 6770–6778. <https://doi.org/10.1021/cm801807b>.
- (25) Shiguihara, A. L.; Bizeto, M. A.; Constantino, V. R. L. Exfoliation of Layered Hexaniobate in Tetra(n-Butyl)Ammonium Hydroxide Aqueous Solution. *Colloids Surfaces A Physicochem. Eng. Asp.* **2007**, *295* (1–3), 123–129. <https://doi.org/10.1016/j.colsurfa.2006.08.040>.
- (26) Irie, H.; Kamiya, K.; Shibnuma, T.; Miura, S.; Tryk, D. A.; Yokoyama, T.; Hashimoto, K. Visible Light-Sensitive Cu(II)-Grafted TiO₂ Photocatalysts: Activities and X-Ray Absorption Fine Structure Analyses. *J. Phys. Chem. C* **2009**, *113* (24), 10761–10766. <https://doi.org/10.1021/jp903063z>.
- (27) Wood, D. L.; Tauc, J. Weak Absorption Tails in Amorphous Semiconductors. *Phys. Rev. B* **1972**, *5* (8), 3144–3151. <https://doi.org/10.1103/PhysRevB.5.3144>.
- (28) Patrocínio, A. O. T.; Schneider, J.; Franca, M. D.; Santos, L. M.; Caixeta, B. P.; Machado, A. E. H.; Bahnemann, D. W. Charge Carrier Dynamics and Photocatalytic Behavior of TiO₂ Nanopowders Submitted to Hydrothermal or Conventional Heat Treatment. *RSC Adv.* **2015**, *5* (86), 70536–70545. <https://doi.org/10.1039/c5ra13291f>.

- (29) Al-Madanat, O.; AlSalka, Y.; Curti, M.; Dillert, R.; Bahnemann, D. W. Mechanistic Insights into Hydrogen Evolution by Photocatalytic Reforming of Naphthalene. *ACS Catal.* **2020**, *10* (13), 7398–7412. <https://doi.org/10.1021/acscatal.0c01713>.
- (30) Nash, T. The Colorimetric Estimation of Formaldehyde by Means of the Hantzsch Reaction. *Biochem. J.* **1953**, *55* (3), 416–421. <https://doi.org/10.1042/bj0550416>.
- (31) Tan, B. J.; Klabunde, K. J.; Sherwood, P. M. A. XPS Studies of Solvated Metal Atom Dispersed Catalysts. Evidence for Layered Cobalt—Manganese Particles on Alumina and Silica. *J. Am. Chem. Soc.* **1991**, *113* (3), 855–861. <https://doi.org/10.1021/ja00003a019>.
- (32) Schenck, C. V.; Dillard, J. G.; Murray, J. W. Surface Analysis and the Adsorption of Co(II) on Goethite. *J. Colloid Interface Sci.* **1983**, *95* (2), 398–409. [https://doi.org/10.1016/0021-9797\(83\)90199-6](https://doi.org/10.1016/0021-9797(83)90199-6).
- (33) Mizoroki, T.; Nakayama, M. The Absorption Spectrum of the Cobalt(II) Ion Catalyst in the Reaction of Methanol with Carbon Monoxide and Hydrogen under a High Pressure. *Bull. Chem. Soc. Jpn.* **1965**, *38* (11), 1876–1880. <https://doi.org/10.1246/bcsj.38.1876>.
- (34) Ravi Dhas, C.; Venkatesh, R.; Jothivenkatachalam, K.; Nithya, A.; Suji Benjamin, B.; Moses Ezhil Raj, A.; Jeyadheepan, K.; Sanjeeviraja, C. Visible Light Driven Photocatalytic Degradation of Rhodamine B and Direct Red Using Cobalt Oxide Nanoparticles. *Ceram. Int.* **2015**, *41* (8), 9301–9313. <https://doi.org/https://doi.org/10.1016/j.ceramint.2015.03.238>.
- (35) Yu, H.; Irie, H.; Shimodaira, Y.; Hosogi, Y.; Kuroda, Y. An Efficient Visible-Light-Sensitive Fe(III)-Grafted TiO₂ Photocatalyst. *J. Phys. Chem. C* **2010**, *114*, 16481–16487.
- (36) Mączka, M.; Ptak, M.; Majchrowski, A.; Hanuza, J. Raman and IR Spectra of K₄Nb₆O₁₇ and K₄Nb₆O₁₇·3H₂O Single Crystals. *J. Raman Spectrosc.* **2011**, *42* (2), 209–213. <https://doi.org/10.1002/jrs.2668>.
- (37) Souza, E. C. C. Thermal Stability and Spectroscopic Assessment of Brønsted Sites in Solid Acid-Layered Niobates. *J. Phys. Chem. C* **2019**, *123* (40), 24426–24435. <https://doi.org/10.1021/acs.jpcc.9b07087>.
- (38) Tang, C.-W.; Wang, C.-B.; Chien, S.-H. Characterization of Cobalt Oxides Studied by FT-IR, Raman, TPR and TG-MS. *Thermochim. Acta* **2008**, *473* (1),

- 68–73. <https://doi.org/https://doi.org/10.1016/j.tca.2008.04.015>.
- (39) Yang, J.; Liu, H.; Martens, W. N.; Frost, R. L. Synthesis and Characterization of Cobalt Hydroxide, Cobalt Oxyhydroxide, and Cobalt Oxide Nanodiscs. *J. Phys. Chem. C* **2010**, *114* (1), 111–119. <https://doi.org/10.1021/jp908548f>.
- (40) Souza, E. C. C. Synthesis, Structure and Optical Properties of Layered $M_4Nb_6O_{17}.NH_2O$ ($M = K, Rb, Cs$) Hexaniobates. *J. Alloys Compd.* **2020**, *820*, 1–8. <https://doi.org/10.1016/j.jallcom.2019.153152>
- (41) Li, Y.; Qiu, W.; Qin, F.; Fang, H.; Hadjiev, V. G.; Litvinov, D.; Bao, J. Identification of Cobalt Oxides with Raman Scattering and Fourier Transform Infrared Spectroscopy. *J. Phys. Chem. C* **2016**, *120* (8), 4511–4516. <https://doi.org/10.1021/acs.jpcc.5b11185>.
- (42) Ristić, M.; Popović, S.; Musić, S. Sol-Gel Synthesis and Characterization of Nb_2O_5 Powders. *Mater. Lett.* **2004**, *58* (21), 2658–2663. <https://doi.org/10.1016/j.matlet.2004.03.041>.
- (43) Lyu, C.; He, D.; Chang, Y.; Zhang, Q.; Wen, F.; Wang, X. Cobalt Oxyhydroxide as an Efficient Heterogeneous Catalyst of Peroxymonosulfate Activation for Oil-Contaminated Soil Remediation. *Sci. Total Environ.* **2019**, *680*, 61–69. <https://doi.org/10.1016/j.scitotenv.2019.04.324>.
- (44) Yang, S.; Sun, L.; An, X.; Qian, X. Construction of Flexible Electrodes Based on Ternary Polypyrrole@cobalt Oxyhydroxide/Cellulose Fiber Composite for Supercapacitor. *Carbohydr. Polym.* **2020**, *229* (August 2019), 115455. <https://doi.org/10.1016/j.carbpol.2019.115455>.
- (45) Lübke, M.; Gigler, A. M.; Stark, R. W.; Moritz, W. Identification of Iron Oxide Phases in Thin Films Grown on $Al_2O_3(0001)$ by Raman Spectroscopy and X-Ray Diffraction. *Surf. Sci.* **2010**, *604* (7), 679–685. <https://doi.org/https://doi.org/10.1016/j.susc.2010.01.015>.
- (46) Busca, G.; Lorenzelli, V. Infrared Study of the Adsorption of Nitrogen Dioxide, Nitric Oxide and Nitrous Oxide on Hematite. *J. Catal.* **1981**, *72* (2), 303–313. [https://doi.org/10.1016/0021-9517\(81\)90013-0](https://doi.org/10.1016/0021-9517(81)90013-0).
- (47) Liang, S.; Zhu, S.; Chen, Y.; Wu, W.; Wang, X.; Wu, L. Rapid Template-Free Synthesis and Photocatalytic Performance of Visible Light-Activated $SnNb_2O_6$ Nanosheets. *J. Mater. Chem.* **2012**, *22* (6), 2670–2678. <https://doi.org/10.1039/c1jm14307g>.
- (48) Makino, K.; Hagiwara, T.; Murakami, A. A Mini Review: Fundamental Aspects

- of Spin Trapping with DMPO. *Int. J. Radiat. Appl. Instrumentation. Part* **1991**, *37* (5–6), 657–665. [https://doi.org/10.1016/1359-0197\(91\)90164-W](https://doi.org/10.1016/1359-0197(91)90164-W).
- (49) Koito, Y.; Rees, G. J.; Hanna, J. V.; Li, M. M. J.; Peng, Y. K.; Puchtler, T.; Taylor, R.; Wang, T.; Kobayashi, H.; Teixeira, I. F.; Khan, M. A.; Kreissl, H. T.; Tsang, S. C. E. Structure–Activity Correlations for Brønsted Acid, Lewis Acid, and Photocatalyzed Reactions of Exfoliated Crystalline Niobium Oxides. *ChemCatChem* **2017**, *9* (1), 144–154. <https://doi.org/10.1002/cctc.201601131>.
- (50) Kim, J. C.; Woo, S. I. Characterization of Cobalt Clusters Nucleated on CoNay by Ferromagnetic Resonance Spectroscopy and Carbon Monoxide Hydrogenation. *Appl. Catal.* **1988**, *39* (C), 107–121. [https://doi.org/10.1016/S0166-9834\(00\)80942-2](https://doi.org/10.1016/S0166-9834(00)80942-2).
- (51) Furukawa, S.; Shishido, T.; Teramura, K.; Tanaka, T. Reaction Mechanism of Selective Photooxidation of Hydrocarbons over Nb₂O₅. *J. Phys. Chem. C* **2011**, *115* (39), 19320–19327. <https://doi.org/10.1021/jp207316f>.
- (52) Mesa, C. A.; Kafizas, A.; Francàs, L.; Pendlebury, S. R.; Pastor, E.; Ma, Y.; Le Formal, F.; Mayer, M. T.; Grätzel, M.; Durrant, J. R. Kinetics of Photoelectrochemical Oxidation of Methanol on Hematite Photoanodes. *J. Am. Chem. Soc.* **2017**, *139* (33), 11537–11543. <https://doi.org/10.1021/jacs.7b05184>.
- (53) Haisch, C.; Schneider, J.; Fleisch, M.; Gutzmann, H.; Klassen, T.; Bahnemann, D. W. Cold Sprayed WO₃ and TiO₂ Electrodes for Photoelectrochemical Water and Methanol Oxidation in Renewable Energy Applications. *Dalt. Trans.* **2017**, *46* (38), 12811–12823. <https://doi.org/10.1039/c7dt02063e>.
- (54) Koinuma, M.; Seki, H.; Matsumoto, Y. Photoelectrochemical Properties of Layered Niobate (K₄Nb₆O₁₇) Films Prepared by Electrophoretic Deposition. *J. Electroanal. Chem.* **2002**, *531*, 81–85.
- (55) Gelderman, K.; Lee, L.; Donne, S. W. Flat-Band Potential of a Semiconductor: Using the Mott-Schottky Equation. *J. Chem. Educ.* **2007**, *84* (4), 685–688. <https://doi.org/10.1021/ed084p685>.
- (56) Milazzo, G.; Caroli, S.; Sharma, V. K. *Tables of Standard Electrode Potentials*; 1978.
- (57) Günemann, C.; Curti, M.; Schneider, J.; Bahnemann, D. W. Dynamics of Photoinduced Bulk and Surface Reactions Involving Semiconductors Characterized by Time Resolved Spectroscopy Techniques (2015-2018). *Photochemistry* **2020**, *47*, 122–158. <https://doi.org/10.1039/9781788016520->

00122.

- (58) Carroll, E. C.; Compton, O. C.; Madsen, D.; Osterloh, F. E.; Larsen, D. S. Ultrafast Carrier Dynamics in Exfoliated and Functionalized Calcium Niobate Nanosheets in Water and Methanol. *J. Phys. Chem. C* **2008**, *112* (7), 2394–2403. <https://doi.org/10.1021/jp077427d>.
- (59) Bahnemann, D.; Henglein, A.; Lilie, J.; Spanhel, L. Flash Photolysis Observation of the Absorption Spectra of Trapped Positive Holes and Electrons in Colloidal TiO₂. *J. Phys. Chem.* **1984**, *88* (4), 709–711. <https://doi.org/10.1021/j150648a018>.
- (60) Yoshihara, T.; Katoh, R.; Furube, A.; Tamaki, Y.; Murai, M.; Hara, K.; Murata, S.; Arakawa, H.; Tachiya, M. Identification of Reactive Species in Photoexcited Nanocrystalline TiO₂ Films by Wide-Wavelength-Range (400-2500 nm) Transient Absorption Spectroscopy. *J. Phys. Chem. B* **2004**, *108* (12), 3817–3823. <https://doi.org/10.1021/jp031305d>.
- (61) Faustino, L. A.; Souza, B. L.; Nunes, B. N.; Duong, A.-T.; Sieland, F.; Bahnemann, D. W.; Patrocínio, A. O. T. Photocatalytic CO₂ Reduction by Re(I) Polypyridyl Complexes Immobilized on Niobates Nanoscrolls. *ACS Sustain. Chem. Eng.* **2018**, *6* (5), 6073–6083. <https://doi.org/10.1021/acssuschemeng.7b04713>.

5. Efficient Photocatalytic H₂ Evolution by Hexaniobate Nanosheets Grafted with Copper Nanoclusters

5.1. Foreword

This chapter includes the article “Efficient Photocatalytic H₂ Evolution by Hexaniobate Nanosheets Grafted with Copper Nanoclusters” by Barbara N. Nunes, Detlef W. Bahnemann and Antonio Otavio T. Patrocínio published on ChemPhotoChem, 2022, e202100272. doi.org/10.1002/cptc.202100272. The figures and tables identified through this chapter with the letter “C” are reproduced in Appendix C. Reprinted with permission. Copyright 2022 John Wiley and Sons.

5.2. Abstract

Hexaniobate nanosheets (K_{4-x}H_xNb₆O₁₇) were combined with Cu²⁺ ions by grafting, a green one-step methodology. The resulted nanocomposite exhibits high surface area with most of Cu²⁺ ions strongly connected to the hexaniobate layers as amorphous nanoclusters. Photocatalytic experiments evidence that the Cu-grafted hexaniobate can act as an efficient photocatalyst for H₂ evolution. The best performance for the Cu-grafted hexaniobate was reached when the Cu concentration was 0.5 wt% (1.62±0.10 mmol g⁻¹ h⁻¹), whereas hexaniobate layers with 0.5 wt% photodeposited Pt exhibited a hydrogen evolution rate of 0.95±0.04 mmol h⁻¹ g⁻¹ under same experimental conditions. Grafting leads to covalently bounded Cu species onto the hexaniobate surface ensuring a strong electronic interaction. Detailed XPS and EPR studies evidence that initial Cu²⁺ species are promptly reduced to Cu¹⁺/Cu⁰ under illumination. The prominent performance of Cu-grafted samples was related to the improved charge separation efficiency as shown by ns-transient spectroscopy. Therefore, the present methodology offers a green option to produce efficient Earth-abundant-based photocatalysts for H₂ evolution.

5.3. Introduction

Application of molecular hydrogen as a fuel has a growing importance due to its high energy content per unit weight and its clean combustion yielding water as the only by-product. Indeed, it is also noteworthy that H₂ is essential for the chemical industry either as raw material or reducing agent, particularly for fertilizer production and oil refining.¹ The annual demand for pure hydrogen achieves values around 70 Mt.² In the

current scenario, fossil fuels such as natural gas and coal are the main sources for H₂ synthesis, consequently, great amounts of CO₂ are emitted, achieving 830 million tons per year only in this sector.³ Therefore, green H₂ production, in which reduction is driven by renewable energy sources, is seen as one of the long-term solutions for addressing the demand of energy and production sectors. Photocatalytic H₂ evolution is among the most investigated processes for this aim as it involves direct conversion of radiant light into clean fuels.

Since the report from Domen and coworkers,⁴ layered niobates have been investigated as photocatalyst for H₂ evolution. Ever since, within the vast diversity of niobates, one of the most studied structures for photocatalytic H₂ production is that of potassium hexaniobate (K₄Nb₆O₁₇).⁵⁻⁸ Its layered structure formed by Nb₆O₁₇⁴⁻ units provides interlayer spaces which are accessible to hydronium ions and water.⁹ Thus, their extended 2D layered arrangement offers a considerable surface area and multiple modification possibilities such as intercalation or surface modification.¹⁰ In addition, they show a conduction band energy of around -0.5 V vs. SHE and a valence band of +2.7-3.0 V vs. SHE both of which are appropriate for water splitting.¹¹ Nevertheless, this material shows also some limitations related to the high band gap energy, around 3.5 eV, and the high propensity to produce H₂O₂ and to undergo self-poisoning. Such limitations can be overcome by chemical modification of its interlayer spaces as well as by surface modification. Previously, we have reported hexaniobate nanosheets grafted with Co²⁺ and Fe³⁺ ions aiming at improving their optical and surface properties.¹² The presence of 0.1% Co²⁺ on the hexaniobate surface could support the H₂ production in water when coupled with Pt as cocatalyst, thus avoiding self-poisoning.

Metallic platinum is very well established as cocatalyst to support the photocatalytic H₂ production by metal oxide semiconductors. In general, noble metals are applied for this purpose, since they are able to form a Schottky junction with the semiconductor, so the photogenerated electrons can be transferred to the metal to finally yield H₂ gas. Thus, metallic co-catalysts act as active and electron trapping sites promoting charge separation and lowering the activation energies for proton reduction.¹³ However, Pt and other noble metals are rare and expensive, being an additional barrier for future upscaling.¹⁴ Therefore, in the perspective of lowering material costs by using Earth-abundance metals, Cu-based photocatalysts have been proposed as a potential substituent for Platinum.¹⁵ Zhu and coworkers reported improved photoactivity towards H₂ evolution by coupling K₄Nb₆O₁₇ and copper nanoparticles.¹⁶ The hexaniobate was combined with Cu

nanoparticles by chemically reducing the metal on its surface. H₂ evolution rates achieved values around 1.9 mmol h⁻¹ g⁻¹ in methanolic solution under UV-vis irradiation, which were 9 times higher than that for bare K₄Nb₆O₁₇. Other semiconductors such as TiO₂ and g-C₃N₄ has also been combined to Cu-based cocatalysts.^{15,17}

Herein, we report the improvement in the photocatalytic H₂ production of hexaniobate nanosheets previously submitted to Cu²⁺ grafting. Different from previous works, grafting was carried out under soft conditions without any additional reagent, offering therefore a sustainable and green preparation methodology. Different Cu²⁺ concentrations were evaluated and the performances of the resulting nanocomposites were compared to those for the hexaniobate containing photodeposited Pt and Cu nanoparticles. Additionally, the reaction mechanism was investigated by means of *in situ* electron paramagnetic resonance (EPR) and transient absorption (TA) spectroscopies in order to probe the behavior and the role of the Cu centers on the photocatalytic activity. As it will be show in the following, this study provides new insights regarding the surface modification of layered materials aiming at photocatalytic applications as well as reporting highly efficient nanocomposite for photoinduced H₂ evolution.

5.4. Materials and Methods

5.4.1. Hexaniobate nanosheets

Bulk K₄Nb₆O₁₇·3H₂O was prepared by a solid reaction method.^{18,19} Nb₂O₅ (optical grade, CBMM - *Companhia Brasileira de Metalurgia e Mineração*) and K₂CO₃ in a molar ratio 2:3 were macerated and thus heated at 1100 °C for two cycles of 5h. In sequence, to exchange K⁺ to H⁺ ions, 3.0 g of the as synthesized K₄Nb₆O₁₇·3H₂O were added into 150 ml of H₂SO₄ 0.2 mol L⁻¹ and stirred for 3 days.²⁰ The solid was centrifuged, washed with deionized water and dried at 70 °C. After that, in order to obtain the niobate nanosheets by exfoliation, the K_{4-x}H_xNb₆O₁₇ (0.5 g) was added into 100 ml of tert-butylammonium hydroxide (8×10⁻³ mol L⁻¹) and stirred for seven days.²¹ Once the stirring is suspended, non-exfoliated material tends to precipitate, while the exfoliated layers remain as a stable suspension. Thus, the supernatant was collected and some drops of HNO₃ were added in order to obtain the restacked hexaniobate. Finally, the white powder was centrifuged and washed several times until the supernatant achieved pH > 6. The final material was dried at 70 °C.

5.4.2. Cu²⁺ grafting

Cu²⁺ ions were added on the exfoliated hexaniobate surface by an impregnation method.^{22,23} Appropriate amounts of Cu(NO₃)₂·3H₂O corresponding to 1.0, 0.5 and 0.1 wt% relative to the hexaniobate mass were added to an aqueous hexaniobate suspension and stirred at 90 °C for 1 h. In sequence, the powder was centrifuged, washed with deionized water and dried at 70 °C.

5.4.3. Characterization

X-ray diffractometry (XRD) was run in a D8 Advance device (Bruker AXS GmbH) with Cu K α radiation ($\lambda = 1.54060 \text{ \AA}$), at 0.01° step. Raman spectra were measured in a confocal Bruker Senterra micro-Raman spectrometer equipped with an Olympus BX51 microscope with a 532 nm laser (2 mW) as excitation source. Diffuse reflectance UV–vis spectra were recorded in a spectrophotometer Varian Cary-100 Bio, Agilent technologies and BaSO₄ was applied as standard. Optical band gap energies were calculated following the Tauc method.²⁴ Transmission electron microscopy (TEM) images were obtained by a Tecnai G2 F20 TMP (FEI Company) microscope with field emission gun (FEG) at 200 kV, objective lenses TWIN and point resolution of 0.27 nm. Electron Paramagnetic Resonance (EPR) measurements were performed in a MiniScope X-band EPR spectrometer (MS400 Magnostech GmbH) operating at about 9.42–9.44 GHz field frequency as described before.²² The conditions were selected as center field at 335 mT and sweep time 60 s, with liquid N₂ to achieve the temperature of 77 K. For irradiation, a built-in optical fiber connected to a Hamamatsu LC8 light source (200 W Hg-Xe lamp) was used. X-ray photoelectron spectroscopy (XPS) was performed by a Phi5000 VersaProbeII, ULVAC-Phi Inc. spectrometer using monochromatic Al K α X-ray excitation. Survey spectra were collected with 187.5 eV pass energy with step of 0.8 eV, high-resolution spectra were collected with 23.5 eV pass energy and a 0.1 eV step. Transient absorption spectroscopy were performed in a Applied Photophysics LKS 80 Laser Flash Photolysis Spectrometer equipped with a diffuse reflectance accessory and pumped by Nd:YAG laser (Quantel, Brilliant B).²⁵ As pump pulse, the third harmonic of the laser (355 nm, 6 ns pulses) was applied with an average energy of 6 mJ·cm⁻². A Xenon lamp, Osram XBO, 150 W provided the probe pulse. The signals between 400 and 660 nm were detected by a R928 Hamamatsu PMT connected a 1GHz oscilloscope, Agilent. The powder samples were placed in a 1 mm quartz cell and then purged for 30 min with

either pure N₂ or a mixture of nitrogen and methanol vapor. Changes in the reflected light intensity (ΔJ) at each probed wavelength were calculated from the reflected light before (J_0) and after (J) the laser excitation, Equation 1.

$$\Delta J = 1 - 10^{-Abs} = \frac{J_0 - J}{J_0} \quad (2)$$

5.4.4. Photocatalytic H₂ evolution

The experiments were carried out adding 6 mg of photocatalyst in 6 mL of 10% methanol aqueous solution (0.25 mol L⁻¹) in a septum sealed borosilicate glass reactor (10 mL capacity). For the Pt-deposited sample, appropriated amount of H₂PtCl₆ was added to *in situ* Pt photodeposition. The suspension was purged with argon for 5 min and then irradiated with a solar simulator 1000 W Xe lamp (Hönle UV Technology, Sol 1200),²⁶ under constant stirring. The temperature was maintained at 25 ± 1 °C using a water bath. The amounts of H₂ were quantified using a GC-TCD chromatograph Shimadzu 8A (Shimadzu, Kyoto, Japan) equipped a 5 Å molecular sieve packed column and Ar as the carrier gas.

5.5. Results and Discussion

As described previously,^{12,27} potassium hexaniobate prepared by solid state reaction exhibits a structure corresponding to K₄Nb₆O₁₇·3H₂O (JCPDS 21-1297). Following exfoliation with tetrabutylammonium hydroxide increased the surface area, so the crystallinity is lost as the well-ordered stacked layers became randomly organized. The exfoliated layers remain in suspension and were precipitated by acidification as reported elsewhere,^{12,27} resulting in hexaniobate sheets free of ammonium ions. Exfoliated hexaniobate nanosheets (Bare Nb) and the sample modified by grafting with 1% Cu²⁺ have the same XRD profile and no additional peaks related to the Cu²⁺ species were observed (Figure C1). Similarly, in the Raman spectra for both samples (Figure C2), all bands could be assigned only to [NbO₆] octahedral units.^{28,29} No additional bands could be identified for Cu²⁺ species in the grafted sample, however, grafting does lead to an increase of laser scattering and to small blue shifts in some peaks of the hexaniobate. The peak at 655 cm⁻¹ attributed to stretching of longer Nb-O bonds is shifted to 649 cm⁻¹ and the small peak at 392 cm⁻¹ related to internal bending modes of O-Nb-O groups is shifted to 383 cm⁻¹. Besides, the peak at 100 cm⁻¹, which corresponds to the lattice vibrations, disappeared after the surface grafting. This effect can be ascribed to the translation of

Cu^{2+} species and their influence on the lattice vibration.³⁰ These observations indicate that grafting did not cause any significant internal structural change in the hexaniobate layer and may be present at sample surface or intercalated in the interlayer spaces as a result of ion exchange. Further characterization by TEM was carried out, Figure 1, and it is possible to note hexaniobate sheets and scrolls with varying length between 60 and 120 nm. Additionally, amorphous clusters could be observed on the surface of the grafted sample, as highlighted by the arrows, which are not present on the pristine hexaniobate. Such nanoclusters have been observed by our group for Co^{2+} and Fe^{3+} -grafted hexaniobates¹² and also for TiO_2 nanoparticles grafted with Cu^{2+} ions.^{31,32} Therefore, it seems most of Cu^{2+} ions remains at the surface to form amorphous clusters of around 10 nm length. The experimental data, however, does not allow to exclude the possibility of Cu^{2+} intercalation due to ion exchange with protons or K^+ ions, given the electrostatic interaction of these ions with the negatively charged $[\text{Nb}_6\text{O}_{17}]^{4-}$ layers. The presence of Cu^{2+} and its relative concentration on the hexaniobate were confirmed by ICP-OES. The found values were 0.109 (± 0.002)%, 0.512 (± 0.003)% and 1.080 (± 0.010)%, similar to the respective nominal percentages of 0.1%, 0.5% and 1%, respectively.

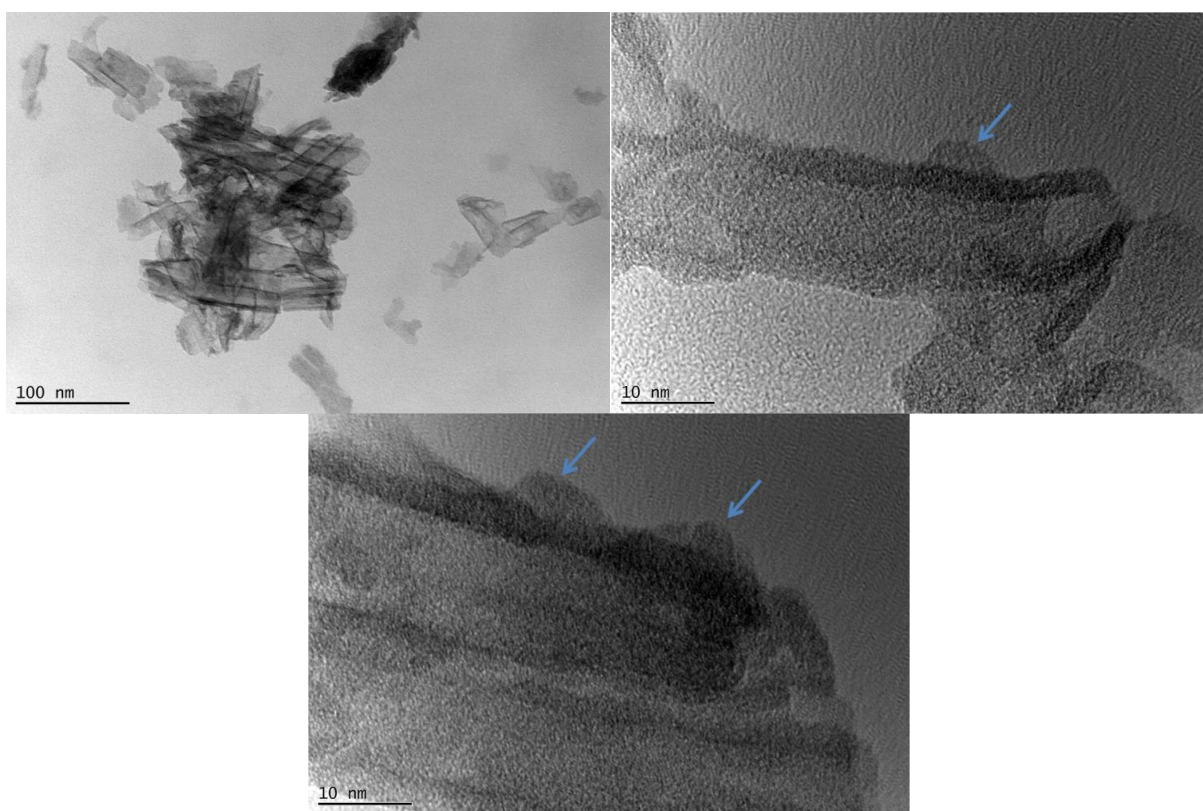


Figure 1 – TEM images for the 1% Cu^{2+} -grafted hexaniobate sample.

Samples were also characterized by UV–vis diffuse reflectance spectroscopy, Figure 2. An intense absorption between 290 and 350 nm is observed for the pristine hexaniobate and is attributed to its band gap excitation corresponding to an energy gap of 3.68 eV as determined by the Tauc method (Figure C3), in agreement with previous reports.⁸ Cu grafting leads to new absorption bands in the visible region of the spectrum. A shoulder between 400-500 nm is observed for all three Cu²⁺ grafted samples along with a broad absorption from around 550 nm to wavelengths exceeding 800 nm. The first absorption tail was also reported for other semiconductors modified with Cu²⁺ ions, such as TiO₂²³ and Nb₃O₈ nanosheets³³ and is related to an interfacial charge transfer (IFCT) transition from the semiconductor valence band to the Cu²⁺ centers. As a result, the optical band gap of the grafted samples undergoes a small red-shift in relation to the bare hexaniobated reaching 3.63 eV for the 1wt% Cu²⁺-grafted sample. The low energy absorption band is proportional to the Cu concentration and it is attributed to d-d transitions of Cu²⁺ species.^{33,34} In the inset of Figure 2, it is possible to observe the resulting bluish color for the grafted samples, particularly for the 1 wt% Cu²⁺ one.

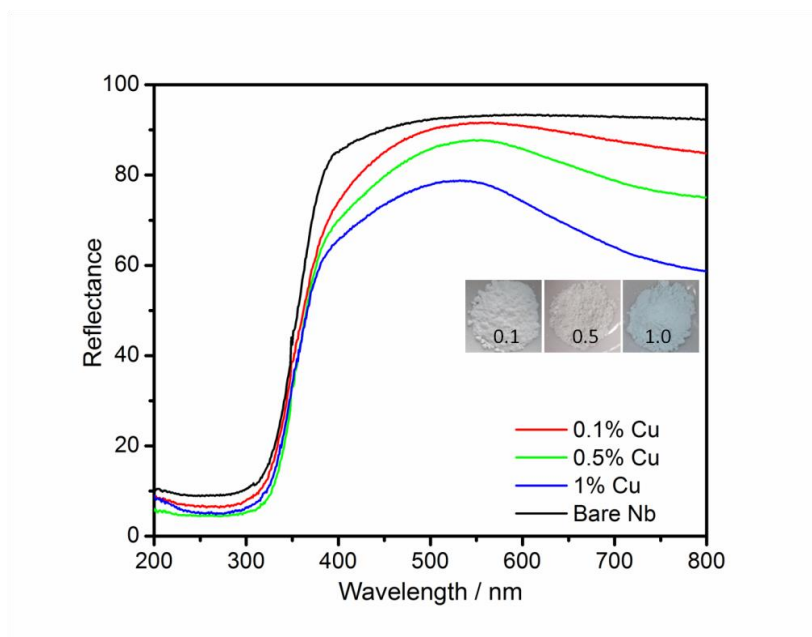


Figure 2 - Diffuse reflectance UV–vis spectra of bare and Cu²⁺ grafted hexaniobates.

Bare and 1 wt% Cu²⁺ grafted hexaniobates were further characterized by XPS. The survey spectra can be found in Figure C4 in which only the expected elements were found. The absence of the N1s peak in the spectra of both samples evidences the absence of tetrabutylammonium ions. The determined Cu atomic percentage was 1.2, which is experimentally similar to the nominal Cu concentration and reinforces the proposition

that the most of Cu ions remain at sample surface instead of intercalated between the layers. High resolution spectra in the Nb 3d, O 1s and Cu 2p regions are shown in Figure 3. For the Nb(V) 3d_{5/2} and 3d_{3/2} doublet, Figure 3(a), peak positions for the bare sample, Table 1, are in good agreement with the previously reported literature for Nb(V) oxides.³⁵ For the 1% Cu grafted sample, however, shifts and a different profile in relation the bare material can be observed. In this case, the peaks can be deconvoluted into two separate doublets. The major doublet is slightly shifted for higher binding energies in relation to that observed for the bare sample, while a second doublet clearly appears at lower binding energies. Similarly, an additional peak can be observed for O 1s spectrum, Figure 3(b). The new peaks that appear in both Nb 3d and O 1s regions indicate the existence of distinct chemical environments as Cu⁺² ions are grafted onto the surface. The shift to lower binding energies in relation to the bare hexaniobate can be correlated to an increase in the electron density of some Nb⁺⁵ and O⁻² ions on the surface due to the formation of Nb-O-Cu bonds.

Within the Cu 2p region, Figure 3c, the Cu 2p_{3/2} peak with maximum at 933.2 eV is observed. The expected shakeup satellite peak for Cu²⁺ species around 944 eV³⁶ was, however, not observed. Since the sample was not exposed to any reducing agent or long term photolysis before analysis, the absence of the Cu⁺² satellite peak was surprising. The observed binding energy for the 2p 3/2 peak, Table 1, actually corresponds to reduced Cu species, Cu⁺, Cu⁰ or both. Such species exhibit very similar binding energies and cannot be distinguished by XPS²³ The absence of the characteristic Cu²⁺ satellite peak was previously observed for TiO₂/Cu samples by Irie et. al,²³ Chen et. al,³⁷ and more recently by Schubert et al.³⁸ It is suggested that the reduction of Cu⁺² centers could be occurring during the sample preparation as an effect of the scattered light or even *in situ* during XPS analysis.

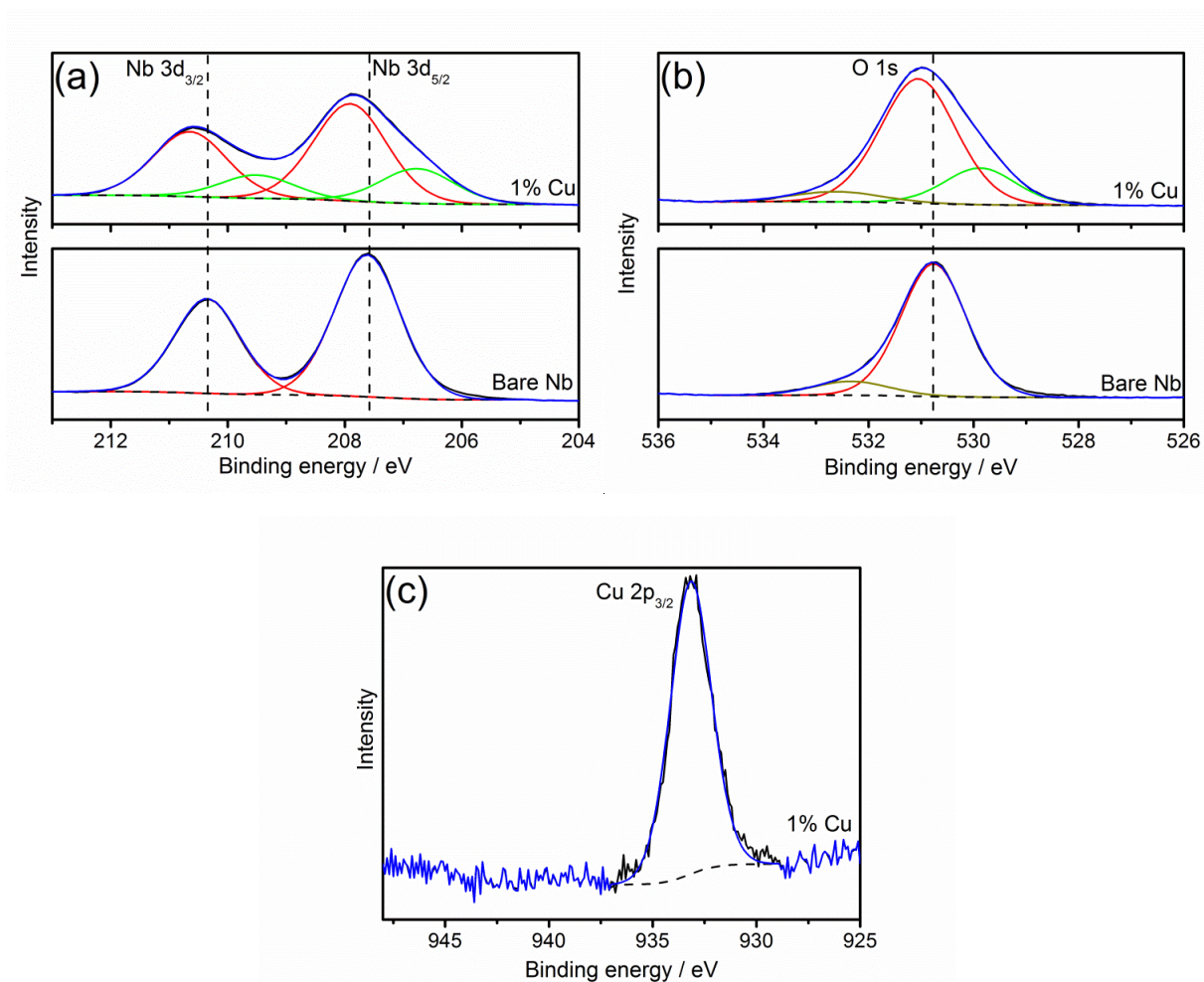


Figure 3 - High resolution XPS spectra of Bare Nb and 1% Cu²⁺-grafted hexaniobate in the (a) Nb 3d, (b) O 1s, and (c) Cu 2p regions.

Table 1 – Binding energies (eV) for the different elements on the investigated samples by high resolution XPS.

Sample	Niobium		Oxygen	Copper
	3d _{3/2}	3d _{5/2}	O 1s	2p _{3/2}
Bare Nb	210.4	207.6	530.8	-
1% Cu ²⁺	210.6	207.9	531.1	933.2
	209.5	206.8	529.9	

Our experimental observations show that Cu²⁺ ions on the hexaniobate surface remain as very active redox sites. Even in the absence of a reducing agent during the preparation process, there is a clear change in the electronic density of the Cu centers grafted onto the surface, and also in those of the Nb(V) and O²⁻ ions close to them. Taking

into account the soft conditions used to prepare the grafted samples and the high bandgap energy of bare hexaniobate (3.68 eV), the observed XPS peaks in the Cu 2p region are mostly related to Cu⁺¹ species formed by IFCT excitation during the grafting process with water as final electron donor. Moreover, considering the low Cu content (1% w/w) on the hexaniobate, the presence of Cu⁺² species cannot be fully excluded. Therefore, in order to gain further information on the electronic structure of the grafted sample, particularly on the oxidation state of the Cu ions, EPR experiments were carried out.

The powder samples were examined in the dark and following different UV irradiation times. The bare hexaniobate is EPR silent in the dark while under UV irradiation three peaks can be observed ($g = 2.03, 2.01$ and 2.00 , Figure C5) which are attributed to $\cdot\text{O}_2^-$ radicals formed by an electron transfer to adsorbed O_2 .¹² In relation to the Cu grafted samples, all three samples were submitted to EPR analysis; however, those with 0.5% and 1% Cu gave rise to too intense signals, which is expected given the sensitivity of the EPR technique. Thus, we have selected the sample with 0.1% Cu²⁺ which allowed us to properly analyze the spectra, Figure 4(a). Two main signals are observed with g values of 2.06 and 2.00. The broad and asymmetrical signal at $g = 2.06$ is assigned to Cu²⁺ ions surrounded by an inhomogeneous chemical environment, leading to an overlap of different interacting signals.^{39,40} This behavior agrees well with the formation of amorphous clusters on the hexaniobate surface, as indicated by TEM images. Interestingly, as highlighted in Figure 4(b), the signal intensity decreases when exposed to longer irradiation times, indicating the photoreduction of Cu²⁺ to form EPR silent Cu¹⁺ species. Concomitantly, it is possible to observe that the intensity of the signal at $g = 2.00$ increases when the sample is exposed to light. This signal is related to trapped holes formed in the hexaniobate valence band after the electron transfer to Cu²⁺ species on the surface.³⁹ The spectra were also monitored after turning off the light source, as shown in Figure 4(c). The signal for Cu²⁺ gradually increases and finally reaches the same intensity as before the irradiation, particularly when the sample is removed from the liquid N₂. In relation to the trapped holes, at the first moment, the signal intensity becomes higher but then turns comparable to the initial intensity when the sample is removed from the liquid N₂. In fact, the samples are photochromic and become dark blue colored under irradiation at room temperature but then turn back to white when left in the dark at ambient atmosphere.

The combination of XPS and EPR data indicate that Cu²⁺ and Cu⁺ species coexist on the surface of hexaniobate. While XPS clearly shows the presence of reduced Cu

species on the surface, EPR is highly sensitive to Cu^{2+} ions allowing their identification. Given their high redox reversibility and the amorphous character of the clusters on the surface, the $\text{Cu}^{+/+2}$ relative concentration under dark conditions will depend on the exposure to the air. When the sample is irradiated reduction of the Cu^{2+} centers is induced, yielding Cu^+ ions and probably Cu^0 after long-term photolysis. The growing EPR signal related to trapped holes as the irradiation time increases is a clear evidence that Cu centers act as electron scavenger possibly decreasing geminate electron/hole recombination in the hexaniobate sheets.

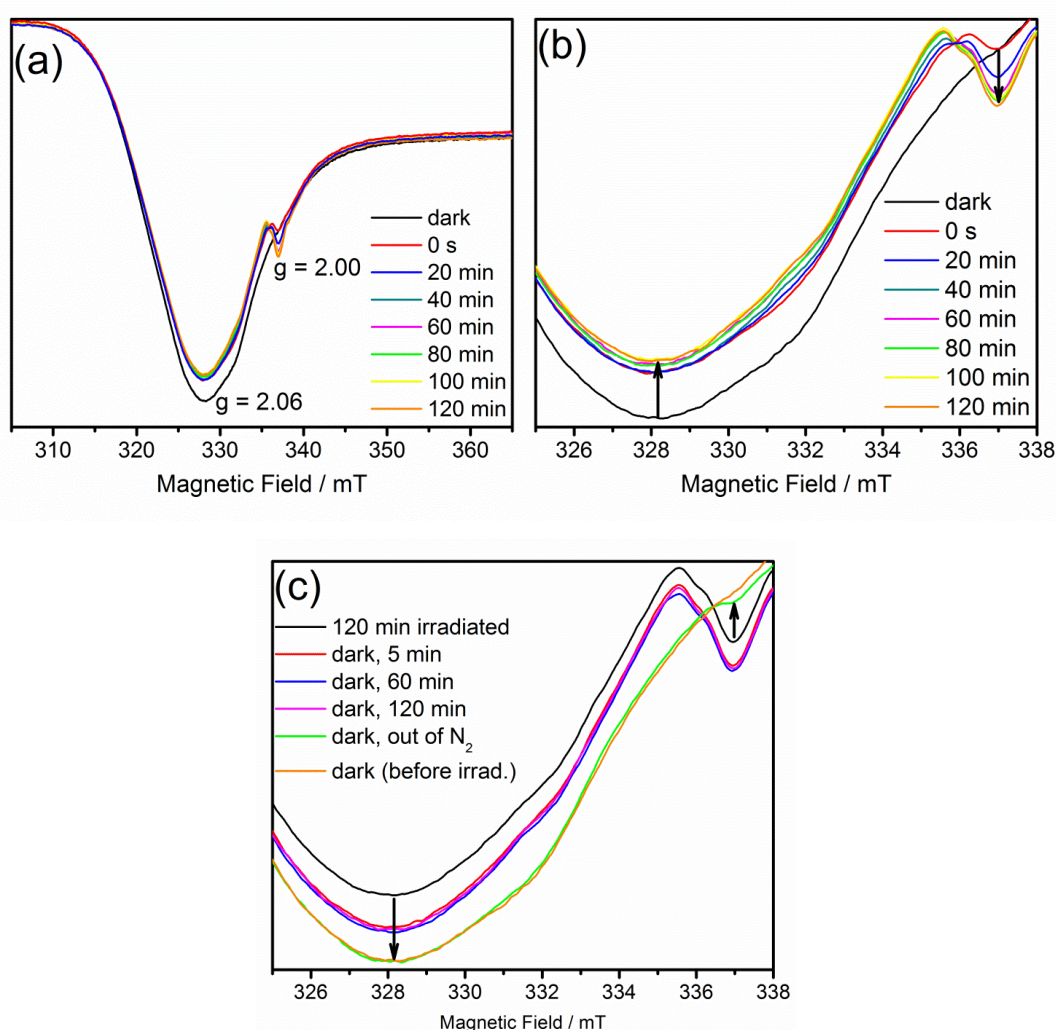


Figure 4 - EPR spectra of 0.1% Cu^{2+} grafted hexaniobate powder in liquid N_2 in the dark and upon different irradiation times of extended (a) and amplified (b, c) ranges.

To evaluate the photocatalytic H_2 evolution, the samples were exposed to full UV-vis excitation ($350 < \lambda < 800$ nm) as well as to visible light only ($\lambda > 400$ nm). No H_2 gas

formation was observed under visible light illumination only, allowing us to conclude that excitation of d-d electronic transitions is unable to promote photocatalytic H₂ evolution. Thus, we focused on UV-vis irradiation where direct band gap or IFCT transitions are promoted. The samples were tested for photocatalytic H₂ evolution, as shown in Figure 5. In comparison to the bare hexaniobate, all the Cu²⁺ grafted samples resulted in a considerable increase in the H₂ evolution rate (Table 2). The smallest Cu concentration (0.1%) on hexaniobate is already able to increase the performance of the pristine hexaniobate 13 times, which clearly evidences the role of the metallic surface on the formation of the H₂ molecule. The samples with 0.5% and 1% Cu resulted nearly in same rates, considering experimental deviations and were able to increase the H₂ evolution rate of the exfoliated hexaniobate by 18 times. Therefore, experimental data clearly indicates that the H₂ evolution rate for the Cu-modified hexaniobate reaches a maximum when the Cu loading is around 0.5%.

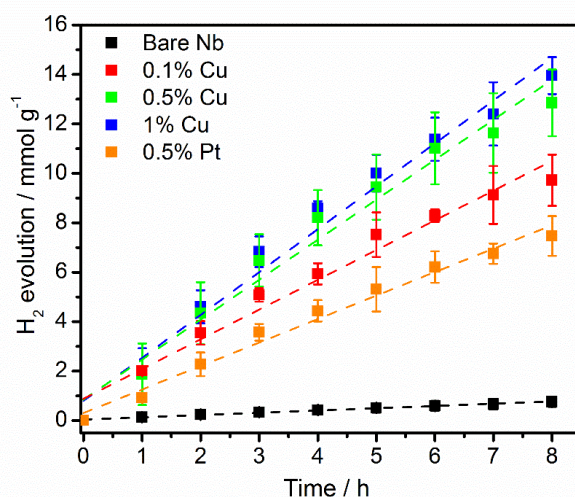


Figure 5 - H₂ evolution promoted by bare Nb, Cu²⁺-grafted hexaniobate and 0.5% Pt samples under UV-vis irradiation from 10% methanol aqueous solution.

Table 2 - H₂ evolution rates for bare and grafted hexaniobates in 10% MeOH aqueous solution under UV-vis irradiation (1000 W Xe lamp, $\lambda > 350$ nm)..

Sample	H ₂ evolution rate / mmol h ⁻¹ g ⁻¹
bare Nb	0.092 ±0.003
0.1% Cu	1.20 ±0.07
0.5% Cu	1.62 ±0.10
1% Cu	1.73 ±0.09

The H₂ evolution rate of hexaniobate containing 0.5 wt.% Pt, photodeposited from H₂PtCl₆ aqueous solution, has also been determined employing the same experimental conditions, Figure 5. The Pt-loaded hexaniobate resulted in a H₂ evolution rate of 0.95±0.04 mmol h⁻¹ g⁻¹, which was around 1.7 times lower than that for 0.5% Cu grafted hexaniobate. Thus, grafted Cu²⁺ centers apparently work as highly efficient co-catalysts on the hexaniobate surface for H₂ evolution presenting an inexpensive way to substitute Platinum as co-catalyst. In addition, we also evaluated the photocatalytic performance of the 0.5% Cu²⁺-grafted hexaniobate sample in plain water (pH = 7) and compared it with that for hexaniobate loaded with 0.5% photodeposited Pt. The observed H₂ evolution rates were 0.11 mmol h⁻¹ g⁻¹ and 0.19 mmol h⁻¹ g⁻¹, respectively, for the Cu²⁺-grafted sample and for Pt-hexaniobate (Figure C6). No oxygen evolution was observed for both samples as probed by GC and mass spectrometry. This observation is in line with the previous reports on preferential formation of peroxide following excitation of hexaniobate sheets on plain water.^{41,42} Therefore, it is possible to conclude that grafted Cu ions are also able to work as co-catalyst with hexaniobate layers towards partial water splitting with efficiencies comparable to Pt-modified samples, which in this case seems to be less affected by the possible production of oxygen reactive species ([•]OH, ⁻OOH). Nevertheless, as observed by EPR spectra (Figure 4), copper centers can favor the accumulation of holes on the grafted hexaniobate surface, hence the addition of a hole scavenger such as methanol improves the H₂ production efficiency by quickly consuming the photogenerated holes and additionally it can promote the so-called current doubling effect previously reported for TiO₂ nanoparticles and photoelectrodes.⁴³⁻⁴⁵ We also compared our result with others reports in the literature in which Cu was used as cocatalyst on the surface of other semiconductors, Table 3. Considering investigations where Cu was used in its oxidized form, previously reported H₂ evolution rates are either comparable or lower than those observed in the present study.^[34-37] When H₂ amounts were much higher, copper was applied in its metallic form and higher concentrations of the selected hole scavenger were used.^{50,51} Interestingly, the H₂ evolution rate obtained by the grafting was similar to the one obtained by Zhu et al. employing stacked K₄Nb₆O₁₇ modified with metallic Cu deposited by using hydrazine as reducing agent^[16]. The authors reported an optimal Cu concentration of 0.4 wt%, very similar to that observed by us. Thus, the grafting methodology was able to produce a high efficient photocatalyst for H₂ production without the use of any additional chemical. In this sense, H₂ evolution was also evaluated by simply adding Cu²⁺ aqueous solution in the reaction media, i.e.,

without grafting, in amounts corresponding to 0.1 wt%, 0.5 wt% and 1 wt% of Cu²⁺ in relation to the hexaniobate, Figure S7. In these conditions, Cu⁰ is photodeposited *in situ* on the surface of the hexaniobate as previously reported for other metal oxides^{49,51,52} and for other metallic co-catalysts such as Pt.⁵³ For the photodeposited samples, the increase in the H₂ evolution rates in comparison to the bare hexaniobate is not as pronounced as observed for the grafted samples. Here, the highest performance is observed for 0.5% Cu²⁺ grafted hexaniobate (0.70±0.05 mmol h⁻¹ g⁻¹), 2.3 times smaller than that for the grafted 0.5 wt% Cu sample, followed by the 0.1 wt% Cu²⁺ (0.54±0.03 mmol h⁻¹ g⁻¹) and 1 wt% Cu²⁺ (0.35±0.03 mmol h⁻¹ g⁻¹). Clearly, grafting procedure improves the electronic interaction between the hexaniobate layers and the Cu centers, and additionally, it seems to avoid aggregation since the performance of the non-grafted 1% Cu sample is smaller than that containing 0.5% Cu, which is not observed for the grafted samples.

Table 3 – Photocatalytic H₂ evolution for different materials using Cu-based cocatalyst.

Material	Preparation	H ₂ rate / mmol g ⁻¹ h ⁻¹	Conditions	Reference
TiO ₂ , Cu ₂ O (40 wt%)	Hydrothermal synthesis; 80 °C, 4h	0.50	20% MeOH, 300 W Xe lamp	46
TiO ₂ , Cu ₂ (OH) ₂ CO ₃ (1.5 mol%)	<i>In situ</i> impregnation, 5h	1.55	25% MeOH, 300 W Xenon lamp	47
ZnO, Cu-Cu ₂ O (30 wt%)	Hot-injection synthesis	1.47	Na ₂ S-Na ₂ SO ₃ solution, 300 W Xe-lamp	48
K ₄ Nb ₆ O ₁₇ , Cu (0.4 wt%)	Chemical reduction, 90 °C, 5h	1.92	20% MeOH, 500 W Hg lamp	16
HNb ₃ O ₈ , Cu _x O	Photodeposition	0.98	10% MeOH, 300 W Xe-lamp	49
TiO ₂ , Cu (2 wt%)	Grinding with commercial Cu nanopowder	9.54	30% MeOH, 300 W Xe lamp	50
TiO ₂ , Cu (1 wt%)	UV photoreduction	8.47	50% MeOH, 450 W Hg lamp	51
K _x H _(4-x) Nb ₆ O ₁₇ , Cu _x O (0.5 wt%)	Impregnation, 90 °C, 1h	1.62	10% MeOH, solar simulator, 1000 W	This work

Finally, the 0.5 wt% Cu²⁺ grafted hexaniobate sample was recycled after the first run and employed again as photocatalyst under the same irradiation conditions to check its stability. The H₂ evolution rate during the second irradiation cycle was 1.53±0.07 mmol h⁻¹ g⁻¹, which is very similar to that observed during the 1st cycle (Figure 6). Moreover, the samples exposed to long-term irradiation were investigated by XRD and XPS and no significant changes in relation to the as-prepared sample were observed with both techniques (Figure C8).

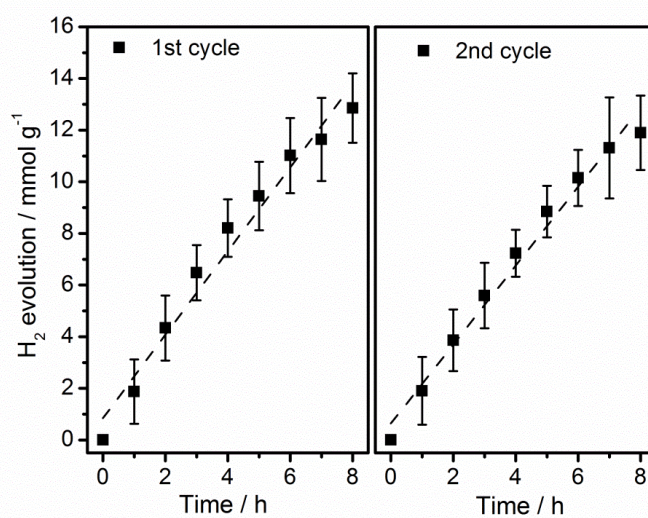


Figure 6 - H₂ evolution from 10% methanol aqueous solution under UV-vis irradiation (1000 W Xe lamp, $\lambda > 350$ nm) in the presence 0.5% Cu²⁺ grafted hexaniobate after two sequential runs.

Further investigations concerning the charge carrier kinetics on the Cu-grafted hexaniobate were obtained by TAS measurements. The transient spectra in the 400-680 nm region of the bare and 0.5% Cu²⁺ grafted hexaniobate 200 ns after laser excitation in N₂ and MeOH vapor are shown in Figure 7. The spectra of bare hexaniobate exhibit the typical behavior of that observed for wide-band gap semiconductors. Prior to laser excitation, the solid does not exhibit any absorption in this region, so the changes in the transient reflectance (ΔJ) are directly proportional to the number of photogenerated charge carriers.⁵⁴ As discussed before,¹² bare hexaniobate in N₂ atmosphere exhibits different hole trapping states which are related to the migration of charge carriers along the layers, so a broad absorption band covering the entire visible region is observed. When exposed to MeOH vapor, which acts as hole scavenger, ΔJ at higher wavelengths increases corresponding to free electrons in the hexaniobate conduction band.

For the Cu-grafted hexaniobate the interpretation of the transient spectra can be more complicated. The sample exhibits steady-state absorption on 500-800 nm region attributed to the d-d transition of Cu^{2+} ions present at the oxide surface, Figure 2. As shown by EPR measurements, UV excitation of the sample should induce an electron transfer from the hexaniobate valence band (VB) to the Cu^{+2} centers. Thus, the observed transient absorption in TAS experiments is the result of the new absorption features due to hole formation at hexaniobate VB with the bleaching of the d-d- transitions due to formation of Cu^{+0} centers. Given the spectral resolution of the transient spectra and the relative low concentration of the Cu^{+2} ions it is not really possible to identify any individual spectral feature in relation to the signals observed for the bare hexaniobate. Actually, free electron absorption (λ^n)⁵⁵ seems to dominate the signal over the entire time window (Figure C9). Interestingly though, different from what is observed for the pristine hexaniobate, the signal intensity for the grafted sample at higher wavelengths is not increased under MeOH vapor in relation to that observed under N_2 atmosphere. Apparently, excited electrons are being efficiently transferred to the Cu centers even in the absence of a hole scavenger.

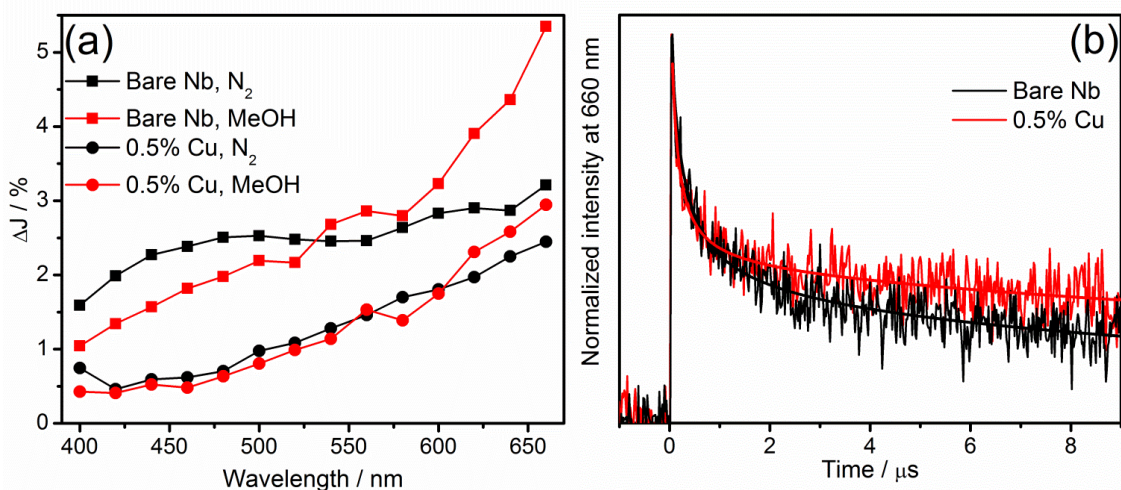


Figure 7 - Transient absorption spectra of the samples at 200 ns after the laser pulse (a) and kinetic decays at 660 nm under N_2 with their respective fittings (b). $\lambda_{\text{exc}} = 355 \text{ nm}$ (6 mJ cm^{-2} per pulse).

Kinetic traces at 660 nm for the bare and the 0.5% Cu-grafted samples under N_2 are shown in Figure 7(b). At 660 nm, one can observe that both samples follow very similar decay profiles. The data can be fitted by two second order components, Equation 1, in

which trapped electrons and holes are treated as independent equal concentration species.⁵⁶ In the formula, t is time elapsed after the laser pulse, k_1 and k_2 are the second order rate constants, ΔJ_0 is the initial amplitude of the signal at the probe wavelength directly after laser excitation and ΔJ_2 corresponds to the initial amplitude of the slower component associated with k_2 .

$$\Delta J = \frac{\Delta J_0 - \Delta J_2}{1 + \Delta J_0 k_1 t} + \frac{\Delta J_2}{1 + \Delta J_0 k_2 t} \quad (1)$$

The rate constants are expressed in a.u.⁻¹ s⁻¹ as the conversion of the observed rate constants to M⁻¹ s⁻¹ is difficult due to uncertainties concerning absorption and scattering coefficients. The fit parameters determined for the bare hexaniobate were $k_1 = (4.3 \pm 0.6) \times 10^6$ a.u.⁻¹ s⁻¹, $k_2 = (5.4 \pm 0.9) \times 10^4$ a.u.⁻¹ s⁻¹ and $\Delta J_2 = 59\%$, while for the 0.5% Cu grafted sample, $k_1 = (4.6 \pm 0.2) \times 10^6$ a.u.⁻¹ s⁻¹, $k_2 = (1.1 \pm 0.2) \times 10^4$ a.u.⁻¹ s⁻¹ and $\Delta J_2 = 60\%$. Data indicate that the presence of 0.5% Cu ions on the surface cannot fully avoid the fastest (geminate) recombination at the hexaniobate as k_1 is similar for both samples, but for the trapped charge carriers which correspond to the smaller recombination rate constant (k_2), a decrease of 80% is observed due to the presence of grafted Cu ions.

In summary, Cu²⁺ grafting onto the hexaniobate surface lead to amorphous nanoclusters but does not change the structure and bulk properties of the layered material as observed by XRD, RAMAN and TEM analysis. Nevertheless, a significant electronic interaction between the copper species and the hexaniobate was found, particularly when evaluating XPS results, in which changes in the electronic densities of the Nb(V) and O²⁻ ions were observed along with the presence of Cu⁺⁰ species. In addition, EPR and TAS studies showed that this effective contact allowed the transfer of photogenerated electrons to the Cu centers while holes are trapped on the hexaniobate. Concomitantly, an enhanced performance for photocatalytic H₂ evolution was achieved for the Cu-grafted samples. Thus, our results showed that the interaction between Cu and the hexaniobate surface is highly beneficial for photocatalysis and in our case it was achieved at mild temperatures (90 °C) and without any chemical reducing agent. Indeed, recent studies with TiO₂ and Cu showed that heat treatments at around 100-150 °C can improve TiO₂ and Cu interaction without inducing Cu diffusion into the oxide, and consequently, it enhances the photocatalytic H₂ production.³⁸ In contrast, when no heat treatment was applied, the Cu-TiO₂ linkage strength was found to be weak, since more than 60% of the Cu content leached from TiO₂ after washing, or at high temperatures, ion diffusion into the semiconductor lattice hinders the proton reduction. In both cases, the H₂ evolution

performance decreased significantly. In the case of hexaniobate, the grafting methodology promoted a strong contact of Cu^{+2} with the hexaniobate surface, although intercalation in the interlayer spaces due to ion exchange cannot be excluded. In addition, as observed by the two cycles of irradiation (Figure 6), no significant changes were observed on the photocatalytic performance after 16 hours irradiation. XPS (Figure C8(b)) and ICP-OES analyses after the photocatalytic experiments in aqueous media evidence that no significant lixiviation of Cu occurs. This improved interaction of hexaniobate and Cu species when compared to TiO_2 can be related to the more acid surface of hexaniobate, so a stronger absorption and better electronic contact is expected in this case.

5.6. Conclusion

Hexaniobate nanosheets were successfully modified with Cu^{2+} by grafting using soft conditions and no additional chemicals. The copper ions on the hexaniobate surface were found to form amorphous centers which did not change the bulk properties of the semiconductor. As demonstrated by EPR and XPS analysis, Cu^{2+} species were covalently adsorbed on the hexaniobate surface and presented high redox activity leading to formation of reduced Cu(I)/Cu(0) species. Cu-grafted hexaniobate exhibits an expressive improvement in the H_2 evolution under UV-vis irradiation from methanolic aqueous solution and promising results for partial water splitting in comparison to the pristine hexaniobate or the photodeposited Pt sample. Finally, TAS results could show that Cu nanoclusters effectively act as electron traps, improving the charge separation under excitation. Thus, these studies can contribute to the development of more efficient and accessible photocatalysts as well as co-catalysts for sustainable H_2 production.

5.7. Supporting Information

Figure C1. XRD patterns of bare and 1% Cu-grafted hexaniobate nanosheets.

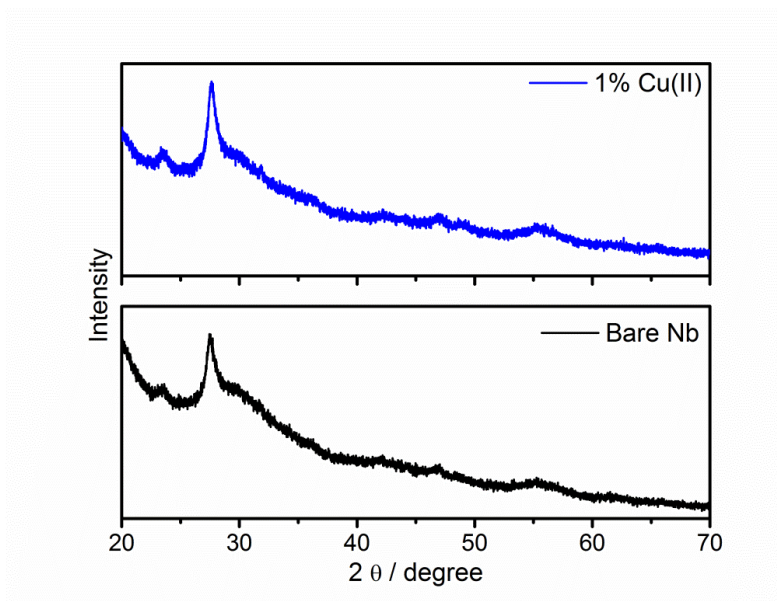


Figure C2. Raman spectra of bare and 1% Cu-grafted hexaniobate ($\lambda_{\text{exc}} = 532 \text{ nm}$).

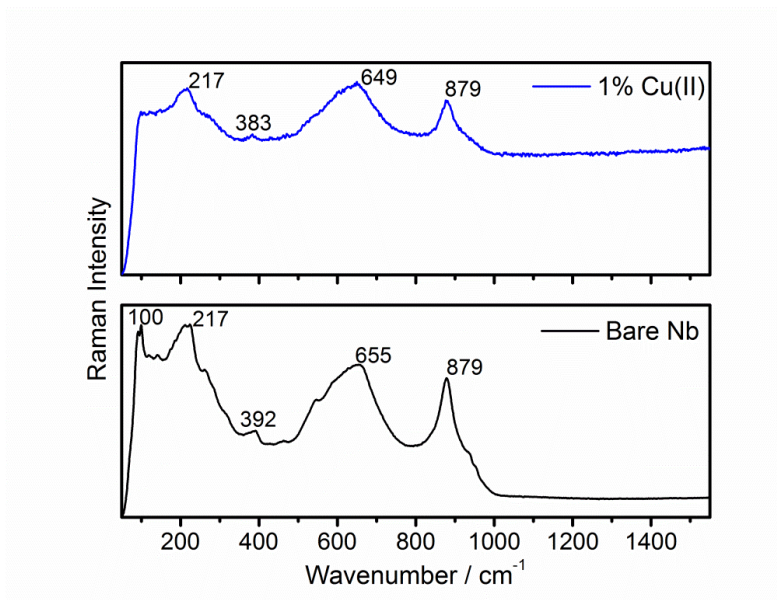


Figure C3. Bandgap calculation for the samples Bare Nb and Cu-grafted hexaniobates by using the Tauc method.

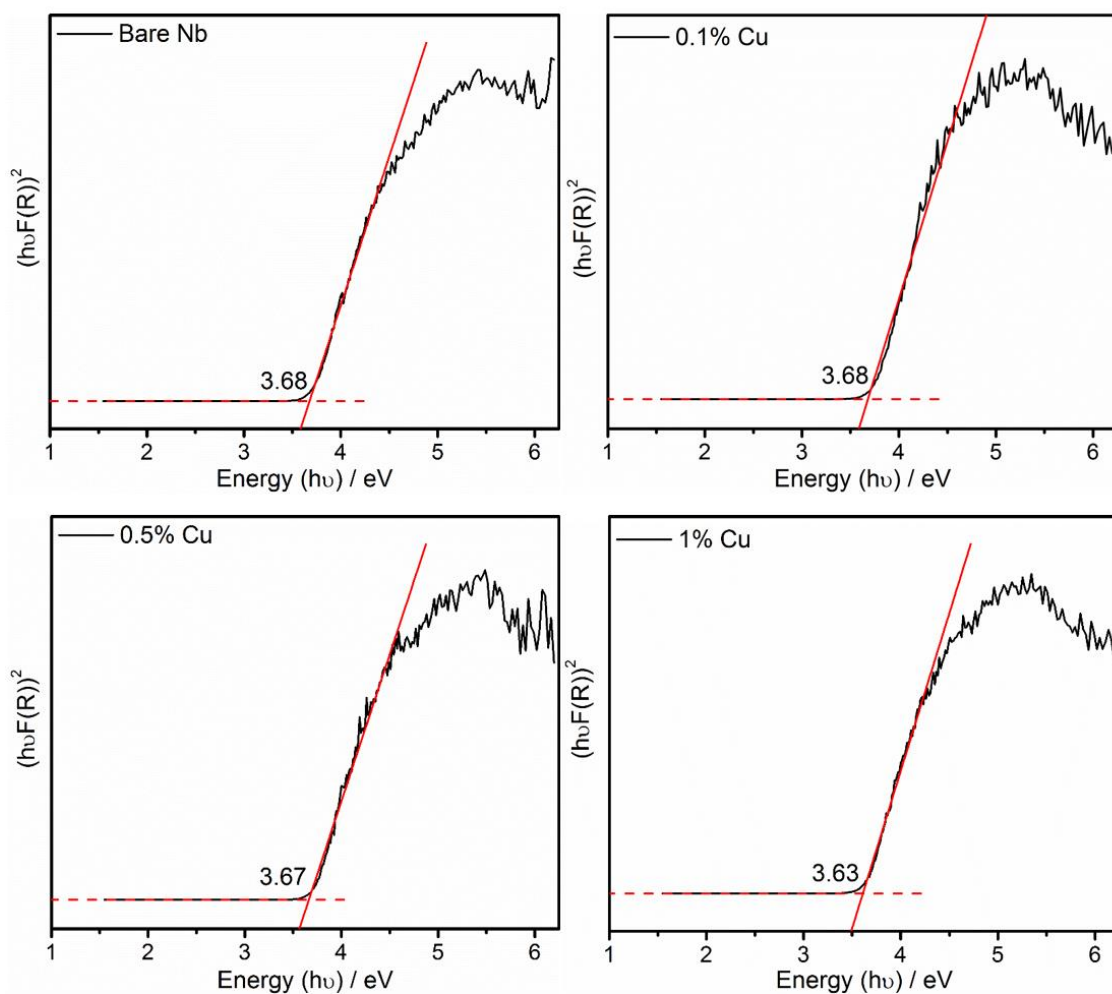


Figure C4. Survey XPS spectra for bare (a) and 1% Cu-grafted (b) hexaniobate.

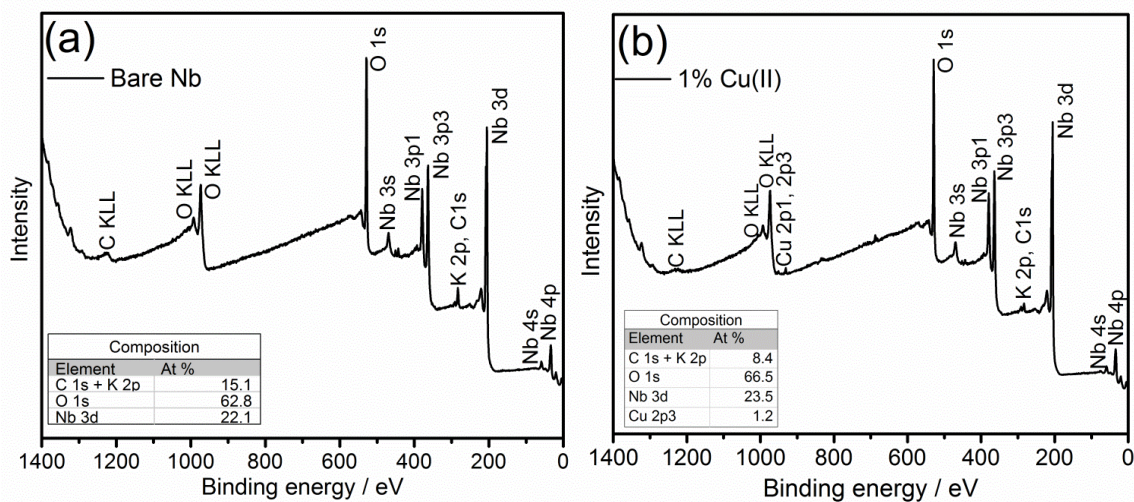


Figure C5. EPR spectra of solid bare Nb in air and in the dark or under UV irradiation

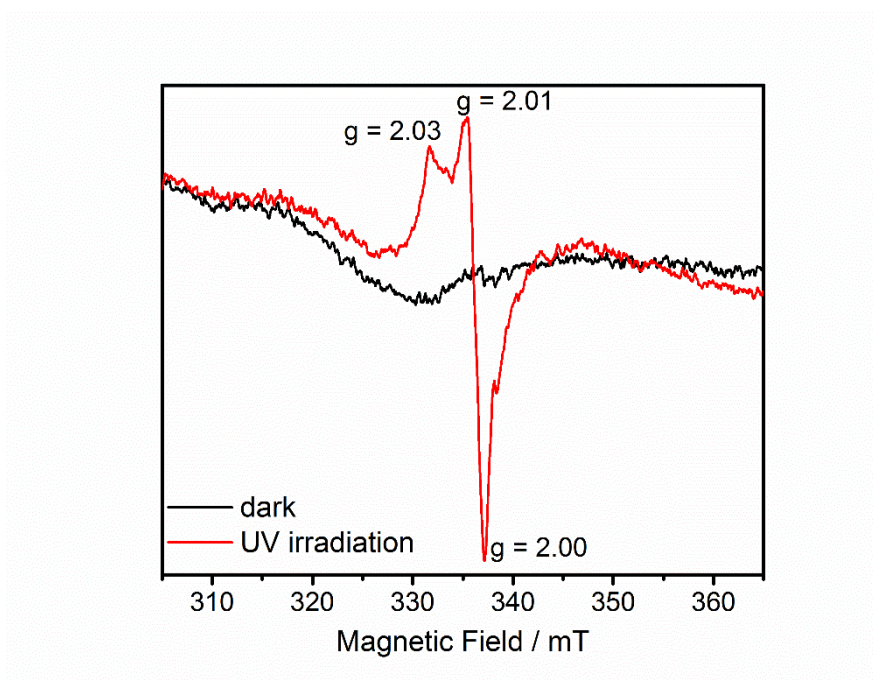


Figure C6. H₂ evolution from pure water for 0.5% Cu-grafted hexaniobate and bare hexaniobate loaded with 0.5% Pt.

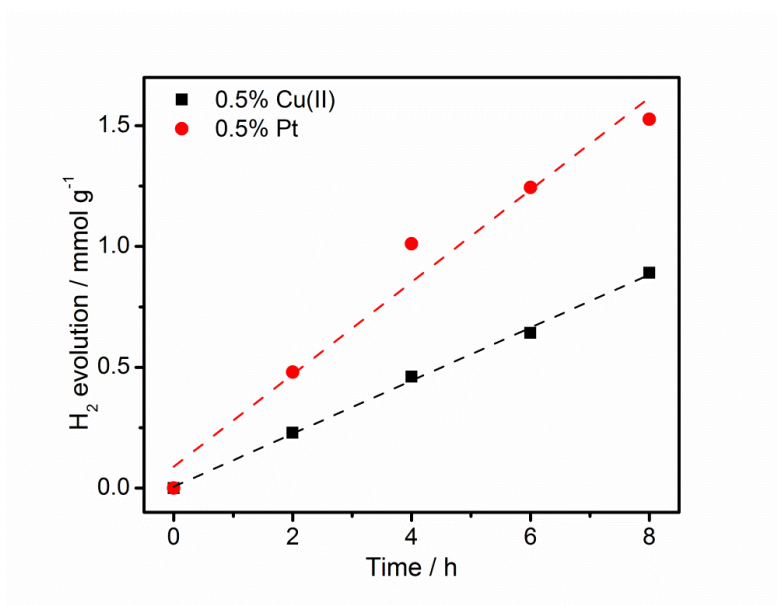


Figure C7. H₂ evolution promoted by bare Nb with and without Cu²⁺ ions in solution under UV-vis irradiation from 10% methanol aqueous solution.

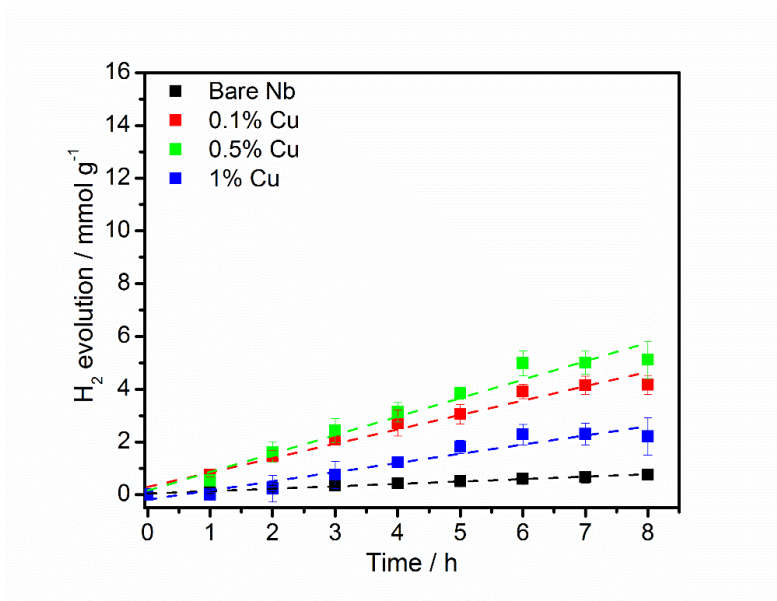


Figure C8. XRD (a) and XPS (b) analysis for 1% Cu-grafted hexaniobate after irradiation. Inset in (b) shows the high resolution spectrum at Cu 2p region.

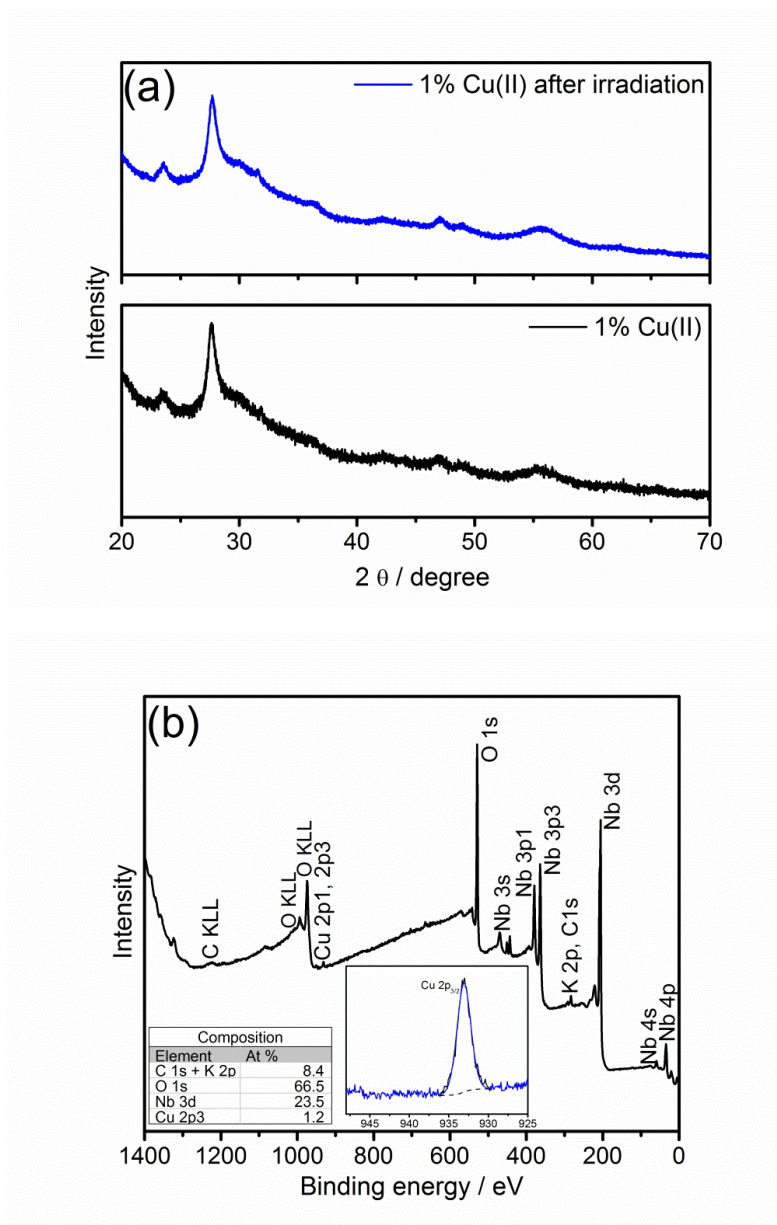
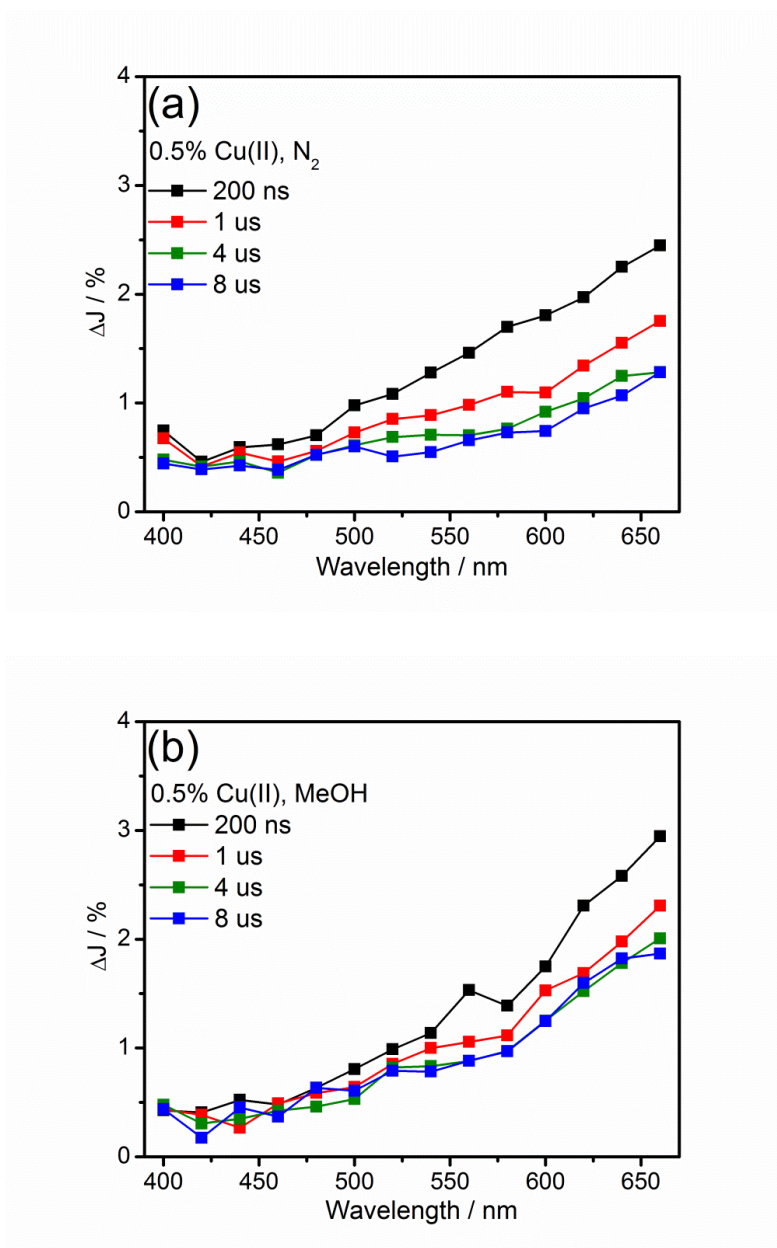


Figure C9. Transient absorption spectra of 1%Cu-grafted hexaniobate in N₂ (a) and in presence of MeOH (b) at different times after the laser pulse. $\lambda_{exc} = 355 \text{ nm}$ (6 mJ cm^{-2} per pulse).



5.8. References

- (1) Armaroli, N.; Balzani, V. The Hydrogen Issue. *ChemSusChem* **2011**, *4* (1), 21–36. <https://doi.org/10.1002/cssc.201000182>.
- (2) Jose M Bermudez; Taku Hasegawa. Hydrogen <https://www.iea.org/reports/hydrogen>.
- (3) International Energy Agency. The Future of H₂ <https://www.iea.org/reports/the-future-of-hydrogen>.
- (4) Domen, K.; Kudo, A.; Shinozaki, A.; Tanaka, A.; Maruya, K. I.; Onishi, T. Photodecomposition of Water and Hydrogen Evolution from Aqueous Methanol Solution over Novel Niobate Photocatalysts. *J. Chem. Soc. Chem. Commun.* **1986**, No. 4, 356–357. <https://doi.org/10.1039/C39860000356>.
- (5) Townsend, T. K.; Sabio, E. M.; Browning, N. D.; Osterloh, F. E. Improved Niobate Nanoscroll Photocatalysts for Partial Water Splitting. *ChemSusChem* **2011**, *4* (2), 185–190. <https://doi.org/10.1002/cssc.201000377>.
- (6) Liu, C.; Feng, Y.; Han, Z.; Sun, Y.; Wang, X.; Zhang, Q.; Zou, Z. Z-Scheme N-Doped K₄Nb₆O₁₇/g-C₃N₄ Heterojunction with Superior Visible-Light-Driven Photocatalytic Activity for Organic Pollutant Removal and Hydrogen Production. *Chinese J. Catal.* **2021**, *42* (1), 164–174. [https://doi.org/https://doi.org/10.1016/S1872-2067\(20\)63608-7](https://doi.org/https://doi.org/10.1016/S1872-2067(20)63608-7).
- (7) Kudo, A.; Tanaka, A.; Domen, K.; Maruya, K. ichi; Aika, K. ichi; Onishi, T. Photocatalytic Decomposition of Water over NiOK₄Nb₆O₁₇ Catalyst. *J. Catal.* **1988**, *111* (1), 67–76. [https://doi.org/10.1016/0021-9517\(88\)90066-8](https://doi.org/10.1016/0021-9517(88)90066-8).
- (8) Sarahan, M. C.; Carroll, E. C.; Allen, M.; Larsen, D. S.; Browning, N. D.; Osterloh, F. E. K₄Nb₆O₁₇-Derived Photocatalysts for Hydrogen Evolution from Water: Nanoscrolls versus Nanosheets. *J. Solid State Chem.* **2008**, *181* (7), 1678–1683. <https://doi.org/10.1016/j.jssc.2008.06.021>.
- (9) Osterloh, F. E. Inorganic Nanostructures for Photoelectrochemical and Photocatalytic Water Splitting. *Chem. Soc. Rev.* **2013**, *42* (6), 2294–2320. <https://doi.org/10.1039/c2cs35266d>.
- (10) Nunes, B. N.; Lopes, O. F.; Patrocínio, A. O. T.; Bahnemann, D. W. Recent Advances in Niobium-Based Materials for Photocatalytic Solar Fuel Production. *Catalysts* **2020**, *10* (1), 126. <https://doi.org/10.3390/catal10010126>.
- (11) Islam, A.; Teo, S. H.; Taufiq-Yap, Y. H.; Vo, D.-V. N.; Awual, M. R. Towards

- the Robust Hydrogen (H₂) Fuel Production with Niobium Complexes-A Review. *J. Clean. Prod.* **2021**, *318* (April), 128439.
<https://doi.org/10.1016/j.jclepro.2021.128439>.
- (12) Nunes, B. N.; Bahnemann, D. W.; Patrocinio, A. O. T. Photoinduced H₂ Evolution by Hexaniobate Sheets Grafted with Metal Ions: The Fate of Photogenerated Carriers. *ACS Appl. Energy Mater.* **2021**, *4* (4), 3681–3692.
<https://doi.org/10.1021/acsaem.1c00128>.
- (13) Wang, Z.; Li, C.; Domen, K. Recent Developments in Heterogeneous Photocatalysts for Solar-Driven Overall Water Splitting. *Chem. Soc. Rev.* **2019**, *48* (7), 2109–2125. <https://doi.org/10.1039/c8cs00542g>.
- (14) Ran, J.; Zhang, J.; Yu, J.; Jaroniec, M.; Qiao, S. Z. Earth-Abundant Cocatalysts for Semiconductor-Based Photocatalytic Water Splitting. *Chem. Soc. Rev.* **2014**, *43* (22), 7787–7812. <https://doi.org/10.1039/c3cs60425j>.
- (15) Zhu, J.; Cheng, G.; Xiong, J.; Li, W.; Dou, S. Recent Advances in Cu-Based Cocatalysts toward Solar-to-Hydrogen Evolution: Categories and Roles. *Sol. RRL* **2019**, *3* (10), 1–20. <https://doi.org/10.1002/solr.201900256>.
- (16) Zhu, K.; Kang, S. Z.; Qin, L.; Han, S.; Li, G.; Li, X. Novel and Highly Active Potassium Niobate-Based Photocatalyst for Dramatically Enhanced Hydrogen Production. *ACS Sustain. Chem. Eng.* **2018**, *6* (7), 8591–8598.
<https://doi.org/10.1021/acssuschemeng.8b00908>.
- (17) Christoforidis, K. C.; Fornasiero, P. Photocatalysis for Hydrogen Production and CO₂ Reduction: The Case of Copper-Catalysts. *ChemCatChem* **2019**, *11* (1), 368–382. <https://doi.org/10.1002/cctc.201801198>.
- (18) Nakato, T.; Kuroda, K.; Kato, C. Syntheses of Intercalation Compounds of Layered Niobates with Methylviologen and Their Photochemical Behavior. *Chem. Mater.* **1992**, *4* (1), 128–132. <https://doi.org/10.1021/cm00019a027>.
- (19) Bizeto, M. A.; Constantino, V. R. L. Structural Aspects and Thermal Behavior of the Proton-Exchanged Layered Niobate K₄Nb₆O₁₇. *Mater. Res. Bull.* **2004**, *39* (11), 1729–1736. <https://doi.org/10.1016/j.materresbull.2004.05.001>.
- (20) Maeda, K.; Eguchi, M.; Youngblood, W. J.; Mallouk, T. E. Niobium Oxide Nanoscrolls as Building Blocks for Dye-Sensitized Hydrogen Production from Water under Visible Light Irradiation. *Chem. Mater.* **2008**, *20* (21), 6770–6778.
<https://doi.org/10.1021/cm801807b>.
- (21) Shiguihara, A. L.; Bizeto, M. A.; Constantino, V. R. L. Exfoliation of Layered

- Hexaniobate in Tetra(n-Butyl)Ammonium Hydroxide Aqueous Solution. *Colloids Surfaces A Physicochem. Eng. Asp.* **2007**, 295 (1–3), 123–129. <https://doi.org/10.1016/j.colsurfa.2006.08.040>.
- (22) Balayeva, N. O.; Fleisch, M.; Bahnemann, D. W. Surface-Grafted WO₃/TiO₂ Photocatalysts: Enhanced Visible-Light Activity towards Indoor Air Purification. *Catal. Today* **2018**, 313, 63–71. <https://doi.org/10.1016/j.cattod.2017.12.008>.
- (23) Irie, H.; Kamiya, K.; Shibamura, T.; Miura, S.; Tryk, D. A.; Yokoyama, T.; Hashimoto, K. Visible Light-Sensitive Cu(II)-Grafted TiO₂ Photocatalysts: Activities and X-Ray Absorption Fine Structure Analyses. *J. Phys. Chem. C* **2009**, 113 (24), 10761–10766. <https://doi.org/10.1021/jp903063z>.
- (24) Wood, D. L.; Tauc, J. Weak Absorption Tails in Amorphous Semiconductors. *Phys. Rev. B* **1972**, 5 (8), 3144–3151. <https://doi.org/10.1103/PhysRevB.5.3144>.
- (25) Arimi, A.; Günemann, C.; Curti, M.; Bahnemann, D. W. Regarding the Nature of Charge Carriers Formed by UV or Visible Light Excitation of Carbon-Modified Titanium Dioxide. *Catalysts* **2019**, 9 (8), 697. <https://doi.org/10.3390/catal9080697>.
- (26) Al-Madanat, O.; AlSalka, Y.; Curti, M.; Dillert, R.; Bahnemann, D. W. Mechanistic Insights into Hydrogen Evolution by Photocatalytic Reforming of Naphthalene. *ACS Catal.* **2020**, 10 (13), 7398–7412. <https://doi.org/10.1021/acscatal.0c01713>.
- (27) Nunes, B. N.; Patrocinio, A. O. T.; Bahnemann, D. W. Influence of the Preparation Conditions on the Morphology and Photocatalytic Performance Pt-Modified Hexaniobate Composites. *J. Phys. Condens. Matter* **2019**, 31 (39), 394001. <https://doi.org/10.1088/1361-648x/ab2c5e>.
- (28) Mączka, M.; Ptak, M.; Majchrowski, A.; Hanuza, J. Raman and IR Spectra of K₄Nb₆O₁₇ and K₄Nb₆O₁₇·3H₂O Single Crystals. *J. Raman Spectrosc.* **2011**, 42 (2), 209–213. <https://doi.org/10.1002/jrs.2668>.
- (29) Souza, E. C. C. Thermal Stability and Spectroscopic Assessment of Brønsted Sites in Solid Acid-Layered Niobates. *J. Phys. Chem. C* **2019**, 123 (40), 24426–24435. <https://doi.org/10.1021/acs.jpcc.9b07087>.
- (30) Souza, E. C. C. Synthesis, Structure and Optical Properties of Layered M₄Nb₆O₁₇·NH₂O (M=K, Rb, Cs) Hexaniobates. *J. Alloys Compd.* **2020**, 820, 1–8.
- (31) Miyauchi, M.; Irie, H.; Liu, M.; Qiu, X.; Yu, H.; Sunada, K.; Hashimoto, K. Visible-Light-Sensitive Photocatalysts: Nanocluster-Grafted Titanium Dioxide

- for Indoor Environmental Remediation. *J. Phys. Chem. Lett.* **2016**, *7* (1), 75–84. <https://doi.org/10.1021/acs.jpcclett.5b02041>.
- (32) Liu, M.; Inde, R.; Nishikawa, M.; Qiu, X.; Atarashi, D.; Sakai, E.; Nosaka, Y.; Hashimoto, K.; Miyauchi, M. Enhanced Photoactivity with Nanocluster-Grafted Titanium Dioxide Photocatalysts. *ACS Nano* **2014**, *8* (7), 7229–7238. <https://doi.org/10.1021/nn502247x>.
- (33) Yin, G.; Nishikawa, M.; Nosaka, Y.; Srinivasan, N.; Atarashi, D.; Sakai, E.; Miyauchi, M. Photocatalytic Carbon Dioxide Reduction by Copper Oxide Nanocluster-Grafted Niobate Nanosheets. *ACS Nano* **2015**, *9* (2), 2111–2119. <https://doi.org/10.1021/nn507429e>.
- (34) Filho, N. L. D.; Fisica, D. De; Paulista, U. E.; Brasil, A.; Solteira-sp, I. Adsorption of Cu(II) and Co(II) Complexes on a Silica Gel Surface Chemically Modified with 2-Mercaptoimidazole Characteristics of the Material. *Mikrochim. Acta* **1999**, *240*, 233–240.
- (35) Atuchin, V. V.; Kalabin, I. E.; Kesler, V. G.; Pervukhina, N. V. Nb 3d and O 1s Core Levels and Chemical Bonding in Niobates. *J. Electron Spectros. Relat. Phenomena* **2005**, *142*(2), 129–134. <https://doi.org/10.1016/j.elspec.2004.10.003>.
- (36) Tian, H.; Zhang, X. L.; Scott, J.; Ng, C.; Amal, R. TiO₂-Supported Copper Nanoparticles Prepared via Ion Exchange for Photocatalytic Hydrogen Production. *J. Mater. Chem. A* **2014**, *2* (18), 6432–6438. <https://doi.org/10.1039/C3TA15254E>.
- (37) Chen, M.; Wang, H.; Chen, X.; Wang, F.; Qin, X.; Zhang, C.; He, H. High-Performance of Cu-TiO₂ for Photocatalytic Oxidation of Formaldehyde under Visible Light and the Mechanism Study. *Chem. Eng. J.* **2020**, *390*, 124481. <https://doi.org/10.1016/j.cej.2020.124481>.
- (38) Schubert, J. S.; Kalantari, L.; Lechner, A.; Giesriegl, A.; Nandan, S. P.; Ayala, P.; Kashiwaya, S.; Sauer, M.; Foelske, A.; Rosen, J.; Blaha, P.; Cherevan, A. S.; Eder, D. Elucidating the Formation and Active State of Cu Co-Catalysts for Photocatalytic Hydrogen Evolution. *J. Mater. Chem. A* **2021**. <https://doi.org/10.1039/d1ta05561e>.
- (39) Nosaka, Y.; Takahashi, S.; Sakamoto, H.; Nosaka, A. Y. Reaction Mechanism of Cu(II)-Grafted Visible-Light Responsive TiO₂ and WO₃ Photocatalysts Studied by Means of ESR Spectroscopy and Chemiluminescence Photometry. *J. Phys. Chem. C* **2011**, *115* (43), 21283–21290. <https://doi.org/10.1021/jp2070634>.

- (40) Dozzi, M. V.; Chiarello, G. L.; Pedroni, M.; Livraghi, S.; Giamello, E.; Selli, E. High Photocatalytic Hydrogen Production on Cu(II) Pre-Grafted Pt/TiO₂. *Applied Catal. B, Environ.* **2017**, *209*, 417–428.
<https://doi.org/10.1016/j.apcatb.2017.04.029>.
- (41) Compton, O. C.; Osterloh, F. E. Niobate Nanosheets as Catalysts for Photochemical Water Splitting into Hydrogen and Hydrogen Peroxide. *J. Phys. Chem. C* **2009**, *113* (1), 479–485. <https://doi.org/10.1021/jp807839b>.
- (42) Nunes, B. N. B. N.; Haisch, C.; Emeline, A. V.; Bahnemann, D. W. D. W.; Patrocínio, A. O. T. Photocatalytic Properties of Layer-by-Layer Thin Films of Hexaniobate Nanoscrolls. *Catal. Today* **2019**, *326* (June 2018), 60–67.
<https://doi.org/10.1016/j.cattod.2018.06.029>.
- (43) Hykaway, N.; Sears, W. M.; Morisaki, H.; Morrison, S. R. Current-Doubling Reactions on Titanium Dioxide Photoanodes. *J. Phys. Chem.* **1986**, *90* (25), 6663–6667. <https://doi.org/10.1021/j100283a014>.
- (44) Ahmed, A. Y.; Kandiel, T. A.; Ivanova, I.; Bahnemann, D. Photocatalytic and Photoelectrochemical Oxidation Mechanisms of Methanol on TiO₂ in Aqueous Solution. *Appl. Surf. Sci.* **2014**, *319*, 44–49.
<https://doi.org/10.1016/j.apsusc.2014.07.134>.
- (45) Mandelbaum, P. A.; Regazzoni, A. E.; Blesa, M. A.; Bilmes, S. A. Photo-Electro-Oxidation of Alcohols on Titanium Dioxide Thin Film Electrodes. *J. Phys. Chem. B* **1999**, *103* (26), 5505–5511. <https://doi.org/10.1021/jp984812h>.
- (46) Zhang, Y. H.; Li, Y. L.; Jiu, B. B.; Gong, F. L.; Chen, J. L.; Fang, S. M.; Zhang, H. L. Highly Enhanced Photocatalytic H₂ Evolution of Cu₂O Microcube by Coupling with TiO₂ Nanoparticles. *Nanotechnology* **2019**, *30* (14).
<https://doi.org/10.1088/1361-6528/aafccb>.
- (47) Xu, H.; Dai, D.; Li, S.; Ge, L.; Gao, Y. In Situ Synthesis of Novel Cu₂CO₃(OH)₂ Decorated 2D TiO₂ Nanosheets with Efficient Photocatalytic H₂ Evolution Activity. *Dalt. Trans.* **2018**, *47* (2), 348–356. <https://doi.org/10.1039/c7dt04096b>.
- (48) Lou, Y.; Zhang, Y.; Cheng, L.; Chen, J.; Zhao, Y. A Stable Plasmonic Cu@Cu₂O/ZnO Heterojunction for Enhanced Photocatalytic Hydrogen Generation. *ChemSusChem* **2018**, *11* (9), 1505–1511.
<https://doi.org/10.1002/cssc.201800249>.
- (49) Xiong, J.; Liu, Y.; Liang, S.; Zhang, S.; Li, Y.; Wu, L. Insights into the Role of Cu in Promoting Photocatalytic Hydrogen Production over Ultrathin HNb₃O₈

- Nanosheets. *J. Catal.* **2016**, *342*, 98–104.
<https://doi.org/10.1016/j.jcat.2016.07.016>.
- (50) Ni, D.; Shen, H.; Li, H.; Ma, Y.; Zhai, T. Synthesis of High Efficient Cu/TiO₂ Photocatalysts by Grinding and Their Size-Dependent Photocatalytic Hydrogen Production. *Appl. Surf. Sci.* **2017**, *409*, 241–249.
<https://doi.org/10.1016/j.apsusc.2017.03.046>.
- (51) Montoya, A. T.; Gillan, E. G. Enhanced Photocatalytic Hydrogen Evolution from Transition-Metal Surface-Modified TiO₂. *ACS Omega* **2018**, *3* (3), 2947–2955.
<https://doi.org/10.1021/acsomega.7b02021>.
- (52) Nie, J.; Schneider, J.; Sieland, F.; Zhou, L.; Xia, S.; Bahnemann, D. W. New Insights into the Surface Plasmon Resonance (SPR) Driven Photocatalytic H₂ Production of Au-TiO₂. *RSC Adv.* **2018**, *8* (46), 25881–25887.
<https://doi.org/10.1039/c8ra05450a>.
- (53) Wenderich, K.; Mul, G. Methods, Mechanism, and Applications of Photodeposition in Photocatalysis: A Review. *Chem. Rev.* **2016**, *116* (23), 14587–14619. <https://doi.org/10.1021/acs.chemrev.6b00327>.
- (54) Günnemann, C.; Curti, M.; Schneider, J.; Bahnemann, D. W. Dynamics of Photoinduced Bulk and Surface Reactions Involving Semiconductors Characterized by Time Resolved Spectroscopy Techniques (2015-2018). *Photochemistry* **2020**, *47*, 122–158. <https://doi.org/10.1039/9781788016520-00122>.
- (55) Yoshihara, T.; Katoh, R.; Furube, A.; Tamaki, Y.; Murai, M.; Hara, K.; Murata, S.; Arakawa, H.; Tachiya, M. Identification of Reactive Species in Photoexcited Nanocrystalline TiO₂ Films by Wide-Wavelength-Range (400-2500 nm) Transient Absorption Spectroscopy. *J. Phys. Chem. B* **2004**, *108* (12), 3817–3823. <https://doi.org/10.1021/jp031305d>.
- (56) Faustino, L. A.; Souza, B. L.; Nunes, B. N.; Duong, A.-T.; Sieland, F.; Bahnemann, D. W.; Patrocínio, A. O. T. Photocatalytic CO₂ Reduction by Re(I) Polypyridyl Complexes Immobilized on Niobates Nanoscrolls. *ACS Sustain. Chem. Eng.* **2018**, *6* (5), 6073–6083.
<https://doi.org/10.1021/acssuschemeng.7b04713>.

6. Summarizing Discussion and Conclusions

In this thesis, the properties of modified hexaniobates as heterogeneous photocatalysts have been explored with the main focus lying on the electronic and interfacial processes towards H₂ evolution. Besides a fair to good photocatalytic efficiency of these materials, as pointed out in the Chapter 2, detailed investigations concerning the dynamics of the photocatalytic processes were not carried out before and, hopefully, the present work has contributed to fill this gap. The knowledge about the mechanisms of the electronic and photochemical processes occurring in layered niobates has so far been rather superficial and the influence of different modifying species on the photocatalytic activity had not been studied before. Since heterogeneous photocatalysis is a light-induced process the redox reactivity of which is initiated by the photocatalyst, its properties are essential for the effectiveness of the desired reactions. The efficiency of a photocatalytic process will depend directly on the competition between electron transfer and recombination processes involving photogenerated electron/hole pairs. Charge carriers can recombine by dissipating energy as heat, be trapped in metastable states or react with donor or acceptor molecules in the surrounding medium. In the latter purpose, a long lifetime for the charge carriers and high interfacial electron transfer rates are necessary. These phenomena are directly related to the characteristics of the photocatalyst such as its structure, surface area, crystalline phase, surface defects, presence of dopants and/or impurities, particle size, among others. To enable the photocatalytic H₂ production from water, suitable energy band levels are necessary to proton reduction and H₂O oxidation. Furthermore, the photocatalyst needs to be stable in relation to its chemical and structural characteristics even after long exposition to light and offer sufficient surface area and porosity to enable the molecules to reach the active sites.

Thus, the review in Chapter 2 shows that a large variety of Nb⁵⁺-based materials exhibits suitable electronic/morphological properties for the initiation of light-driven reactions in particularly for the H₂ evolution. Among these materials, it became clear that the niobates offer untold possibilities of structure, morphologies, and electronic configuration, which can supply desired properties for photocatalytic reactions. For instance, it has been reported that an improved contact between the components of the photocatalyst and a high dispersion of cocatalysts on the niobate surface has a high impact on the material's photocatalytic performances. These advantages are mostly

related to the two-dimensional (2D) structure offered by the niobates. 2D materials may provide electronic and structural advantages related to their high surface area, superior electron mobility, facile and more effective chemical modification, etc ^{1,2}. Some of these advantages can be explained by the higher number of active sites offered by the large specific surface area; a fast charge transfer from the bulk to the surface due to the nanometer-scale thickness of each layer; and an excellent integration with cocatalysts or other semiconductors³. Therefore, more effective charge separation and novel electronic processes on the photocatalyst surface can be induced by coupling different materials, in which an efficient charge transfer can occur at the interface. Thus, taking into account the highly exposed active sites of the 2D structure, such a coupling with other materials can be easily achieved. As pointed out by Kim and coauthors⁴, there are many advantages of using exfoliated 2D nanosheets for the preparation of the nanocomposites. Thus, as proposed by the title of this work “Photocatalytic Applications of Layered Niobates and their Composites”, exfoliated hexaniobate can offer great possibilities for photocatalytic reactions when combined to other materials. The surface and the charged layers of exfoliated hexaniobate nanosheets offer the possibility to combine different species, functional groups, or nanostructured materials, and may even form stable colloidal suspensions in polar solvents⁴.

Potassium hexaniobate ($K_4Nb_6O_{17}$) is a very attractive material in this context, besides its suitable band structure, the negatively charged layers formed by $Nb_6O_{17}^{4-}$ units with interlayers accessible to other molecules such as water and methanol offer vast possibilities for photocatalytic H_2 evolution. Moreover, in contrast to some nanostructured materials in which their synthesis commonly depends strongly on crystal growth mechanisms, the 2D nanostructures obtained from the hexaniobate exfoliation under soft conditions do not cause any changes in the chemical composition and structure of its single layers. This exfoliation process of the potassium hexaniobate is illustrated in Figure 1. Thus, the hexaniobate layers allow the diffusion of photogenerated charge carriers along its structure favoring their mobility and migration to the active sites⁵. Another interesting characteristic of this material is that, after an ion exchange followed by the exfoliation using TBAOH, both nanosheets and nanoscrolls are formed. Depending on the ionic strength of the medium, the hexaniobate sheets can curl into nanotubes⁶. Besides that, the tubular nanoscrolls formed after exfoliation seem to maintain the intercalation properties of pristine hexaniobate ^{7,8}.

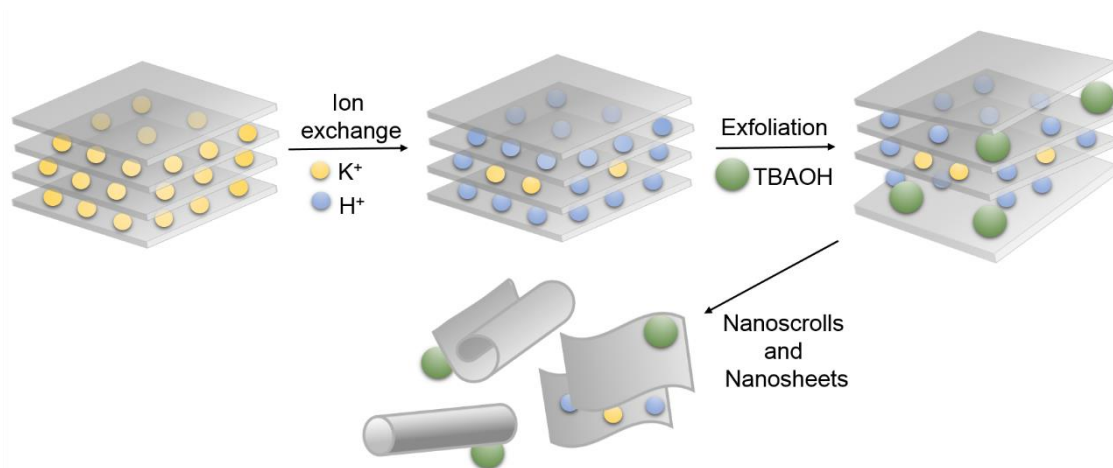


Figure 1 – Schematic representation of nanosheets and nanoscrolls formation from the exfoliation of potassium hexaniobate

As detailed in Chapter 3, hexaniobate forms a stable suspension of layers in TBAOH solution, in which nanofilms can be assembled based on the electrostatic attraction between their components. The electronic interaction between the negatively charged layers of exfoliated hexaniobate in TBAOH and the positively charged polyelectrolyte poly(allylamine hydrochloride) in aqueous solution promotes the growth of the films, which varies uniformly with the number of layers. Moreover, not only pristine hexaniobate nanosheets can be used, but also those previously modified with co-catalyst precursors such as $[\text{Pt}(\text{NH}_3)_4]^{2+}$. As experimentally shown in Chapter 3, this precursor enables the formation of metallic platinum nanoclusters into the hexaniobate nanoscrolls. Although both nanosheets and nanoscrolls of exfoliated hexaniobate in suspension would be expected, the scrolled morphology was favored in relation to the open sheets in the films, as observed by the respective electron microscopy images. This composition of fuzzy assembled hexaniobate nanoscrolls with small and very well distributed metallic Pt nanoclusters enables the diffusion of water and methanol through all deposited layers, unlike a film formed by nanosheets, as represented in Figure 2.

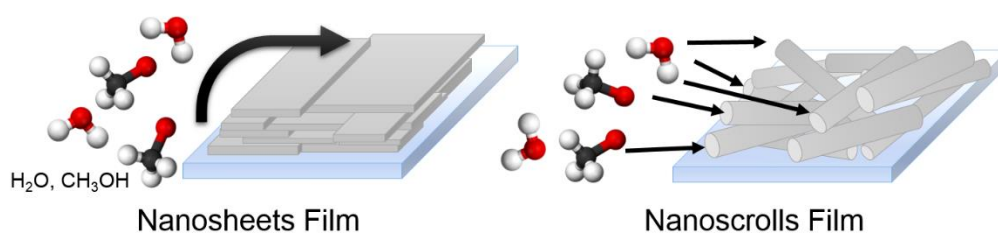
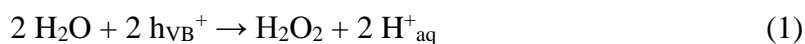


Figure 2 - Schematic representation of the favoured diffusion in a film formed by nanoscrolls in comparison to those formed by nanosheets.

Consequently, highly efficient H₂ production was achieved even with thicker films, particularly in the presence of methanol as sacrificial electron donor. Photoelectrochemical investigations indicated that in plain aqueous electrolytes and in the presence of methanol, the prepared LbL films exhibit good electron transport properties between the layers, which are mainly controlled by the intrinsic properties of the hexaniobate. Nevertheless, as discussed in Chapter 1, in the absence of an electron donor such as methanol, water photooxidation at the hexaniobate surface leads to the formation of H₂O₂ (Equation 1), which has a high affinity for the Nb⁵⁺ centers. H₂O₂ molecules remain strongly adsorbed to the hexaniobate surface, limiting its photocatalytic activity towards water splitting.



In order to overcome this limitation, other species were combined with the exfoliated hexaniobate nanosheets. Moreover, better light-harvesting properties towards the visible range are also desirable. Thus, chemical modifications able to influence the oxidative pathways on the hexaniobate surface were applied aiming at the same time not to affect the structure of the photocatalyst. Furthermore, our studies with Pt-modified hexaniobate showed that thermal treatment at high temperatures is deleterious for the photocatalytic activity due to a restacking of the hexaniobate layers⁹. So far, for the first time, exfoliated hexaniobate (H_xK_{4-x}Nb₆O₁₇) layers were modified by the surface grafting methodology and investigated towards their photocatalytic properties. In this case, the grafting method could promote the surface modification, inducing novel electronic processes without changing the bulk properties. As shown in Chapter 4, the surface of exfoliated hexaniobate layers was modified by grafting with the Co²⁺ and Fe³⁺ metal ions. It has been reported in the literature that some transition metal oxides, such as those of cobalt and iron, which are also inexpensive and abundant, can be employed to support the photo(electro)catalytic water oxidation¹⁰⁻¹². For instance, Maeda and co-authors reported that Co₃O₄ nanoparticles on the TiO₂ surface can catalyze the evolution of O₂ by water photo-oxidation under visible light and in aqueous AgNO₃ solution¹³. The best performance was achieved by loading TiO₂ with 2 wt% of cobalt by impregnation and treating the samples at 423 K. Jang and coauthors achieved a better performance for photocatalytic water oxidation by modifying the layered HTiNb(Ta)O₅ with nanoparticles of iron oxide¹⁴. Interestingly, stoichiometric amounts of H₂ and O₂ were achieved under UV irradiation, and it was possible to produce O₂

from AgNO₃ aqueous solutions upon visible light illumination. Many other examples can be found in the literature, which relate different photo-oxidation reactions under visible light coupling a semiconductor with cobalt oxides¹⁵⁻¹⁷ or iron oxides¹⁸⁻²⁰.

In this work, as a result of the grafting method, amorphous oxo-clusters were formed on the hexaniobate surface, being attached to terminal Nb–O groups. XPS analysis of the sample containing 1% of Co²⁺ confirmed that the Co²⁺ centers were located on the hexaniobate surface. When the samples were tested for the water splitting reaction, no gases were produced without simultaneously using a further cocatalyst, particularly due to the expected inability of Co and Fe species to act as active sites to promote the proton reduction forming H₂. The grafted samples were also tested using an aqueous AgNO₃ solution under UV-vis irradiation; however, no photocatalytic activity was observed. When the grafted samples were further modified with metallic Pt, photoinduced H₂ evolution was achieved in plain water at higher rates than those observed for the bare hexaniobate, when 0.1 wt.% grafting metal was employed.

The amount of 0.1 wt.% grafting metal on the hexaniobate surface improved the photocatalytic performances both in plain water and methanolic aqueous solutions. However, higher amounts of these species, that is, 0.5% and 1% led to a lower photocatalytic performance in comparison to the bare hexaniobate. In this case, the recombination of photogenerated charge carriers was favored and can be related to the presence of more surface defects acting as recombination centers based on transient absorption data. The general lower efficiency of Fe³⁺ centers to improve the photocatalytic activity of hexaniobate can be related to their redox potential in comparison to the Co²⁺ species. Taking into consideration the potential of –0.7 eV for the conduction band of hexaniobate, the redox potentials (versus SHE) of Co²⁺ or Co(OH)₂ should allow a more effective electronic transfer when compared to those of Fe³⁺ or FeOOH species (equations 2-5)²¹. The much more positive reduction potential of Fe^{3+/2+} probably moves the electron transfer from the hexaniobate into the Marcus inverted region, thus favoring the charge recombination. Therefore, the cobalt centers can act more effectively on the charge separation, avoiding the charge recombination and thus supporting the methanol photo-oxidation. This was also supported by transient absorption spectroscopy, in which 0.1% of Fe³⁺ did not decrease the observed rate constant (k₂) as in comparison to the bare hexaniobate. In addition, the positive redox potential of the Fe³⁺ species also justifies the inability of Fe³⁺-grafted hexaniobates to reduce O₂ molecules and to form superoxide radicals, which can also oxidize methanol.



In relation to the analysis towards water splitting, higher amounts of Co^{2+} on the hexaniobate surface also seems to compete with the Pt centers for the photoexcited electrons so the photoactivity expressively decreases for the Co^{2+} concentrations of 0.5% and 1%. An amount of 2 wt.% of Pt was then employed to avoid such competition. In this case, EPR studies for the 0.1% Co^{2+} sample with 2% Pt evidenced that small amounts of Co^{2+} on the hexaniobate surface change the oxidative pathway and favor the formation OH^{\bullet} radicals from water. Thus, Co^{2+} ions on the surface act as hole acceptors forming Co^{3+} centers ($\text{Co}^{3+}/\text{Co}^{2+}$ 1.9 V versus SHE) changing the fate of holes on the hexaniobate surface, as evidenced by the scheme in Figure 3. In case of Fe^{3+} modified samples, the same phenomenon is not feasible.

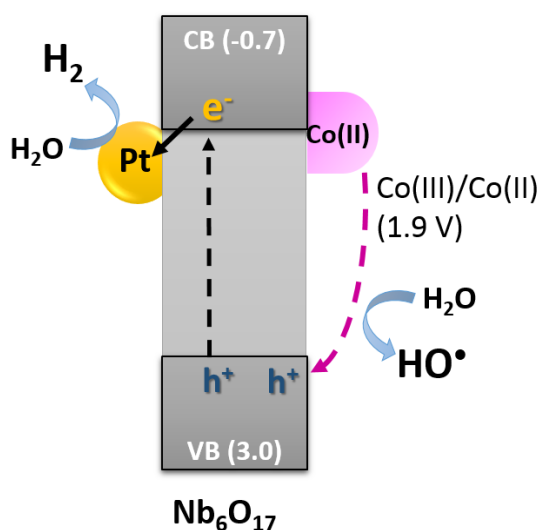


Figure 3 – Scheme of the charge transfers steps for H_2 evolution from plain water after UV excitation of the sample 0.1% Co^{2+} with 2% of photodeposited Pt.

Interestingly, when Pt and CH_3OH were applied for the photocatalytic H_2 evolution, the tested samples of bare, 0.1% Fe^{3+} , and 0.1% Co^{2+} exhibit very similar activities, showing that under these conditions, the grafted ions do not play an effective role within the oxidation mechanism. In this case, kinetic factors need to be taken into account as well. Some investigations on TiO_2 -based photocatalysts showed that, after

excitation, it is necessary to obtain longer lifetimes of the photogenerated charge carriers to efficiently promote chemical transformations on their surface²². As illustrated in Figure 4, firstly, the charge carriers are photogenerated at picosecond timescale and then, they will be separated and transferred to the active sites on the photocatalyst surface at nano seconds.

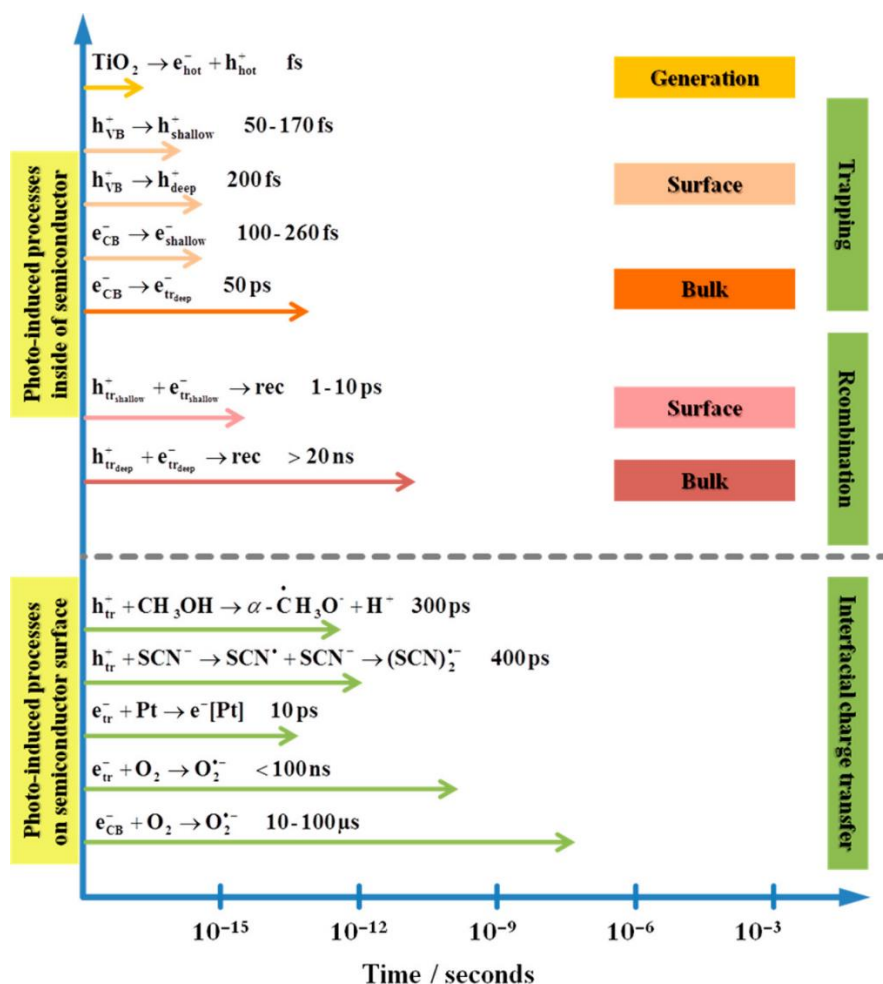
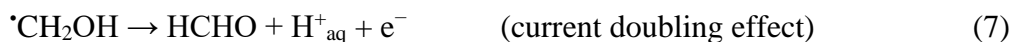


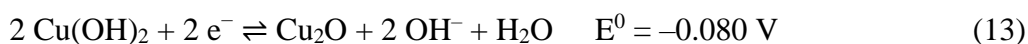
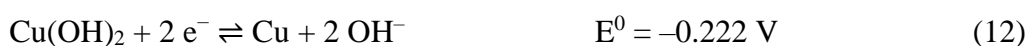
Figure 4 - Time scales of photoinduced reactions in TiO_2 photocatalysis. Reproduced with permission from reference [24].

In sequence, the oxidation and reduction processes occur and their rates would depend on the semiconductor, the reaction medium and the compound of interest. One electron methanol oxidation, for example occur within fs or ps time scale whereas the water oxidation only occurs within ms^{23,24}. Moreover, methanol photo-oxidation in the absence of O_2 can promote the so-called current doubling effect (equations 6 and 7). Firstly, the hydroxymethyl radical ($\dot{\text{C}}\text{H}_2\text{OH}$) is formed following the one-electron oxidation of CH_3OH . Then, it can inject an additional electron into the photocatalyst conduction band forming formaldehyde as stable product^{24,25}. Thus, all these factors

contribute for the distinct performance of the grafted hexaniobate samples and can be further explored to help on the development of more efficient photocatalysts.



In Chapter 5, in order to replace metallic platinum, copper ions were applied as Earth-abundant co-catalysts for the efficient photocatalytic H₂ evolution. Differently from the previous analysis where the discussion was based on the oxidative pathways, in this case, the reductive reactions on the hexaniobate was studied in a way to support the H₂ production in the absence of rare and precious metals. The same grafting methodology was employed for the deposition of copper species, allowing for a strong interaction with the hexaniobate nanosheets. As observed for the other composites, amorphous nanoclusters of copper oxides were initially formed on the hexaniobate surface without changing its bulk properties. Interestingly, the method favored the interaction between the copper centers and the hexaniobate surface in a way that the Cu²⁺ ions remain as very active redox sites. As a result, all the copper species such as Cu⁰, Cu¹⁺, and Cu²⁺ were found to exist simultaneously on the photocatalyst surface. The redox reactions and respective potentials for Cu²⁺ species are summarized in equations 8 to 13²¹. Given the initial Cu²⁺ precursor, amorphous CuO or Cu(OH)₂ are expected to be formed on the hexaniobate surface. These species have redox potentials slightly less negative than that for the conduction band of the hexaniobate, favoring the proper electronic transfer.



As a result of this strong electronic interaction, the copper centers improved the charge separation after the hexaniobate photoexcitation, favouring the accumulation of holes on the grafted hexaniobate surface. The addition of a hole scavenger such as

methanol improves the H₂ production efficiency by quickly consuming the photogenerated holes and additionally it promotes the current doubling effect. The higher efficiency for H₂ evolution in methanolic solutions in comparison to the sample containing photodeposited Pt can be also related to the additional light absorption by the IFTC (interfacial charge transfer) transition. The mechanism of H₂ evolution from methanolic aqueous solution for the Cu-grafted sample is illustrated in Figure 5. Besides, by means of transient absorption studies, it was possible to conclude that excited electrons are being efficiently transferred to the Cu centers, even in the absence of methanol. In pure water, however, Pt-modified samples exhibited better performances than Cu-based ones, which is probably associated with water oxidation kinetics. Nevertheless, these studies contribute to the development of more efficient and accessible photocatalysts as well as of co-catalysts for the sustainable H₂ production.

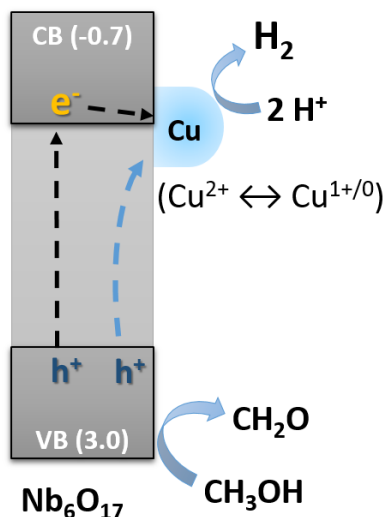


Figure 5 – Scheme of the H₂ evolution mechanism from methanolic aqueous solution after UV-vis excitation of the Cu²⁺-grafted hexaniobate.

Therefore, the results presented in this thesis can contribute significantly to the understanding of the fundamental processes in heterogeneous photocatalysis. Two-dimensional materials can offer an ideal platform to understand photocatalytic processes²⁶. This configuration is advantageous for investigations in relation to the three main steps of a photocatalytic reaction: the formation of charge carriers by light absorption, their separation and transport, and finally the redox reactions on the photocatalyst surface. Once the surface atoms of 2D nanomaterials are dominant in relation to those in the bulk counterparts, surface modification causes significant effects on the whole material. Thus, intrinsic properties of 2D nanomaterials can be more easily

tailored via surface chemical modifications. Interestingly, this work shows that the properties of 2D structures of exfoliated hexaniobate layers is maintained even when this material is deposited on a substrate to form photocatalytic thin films. Electrostatic attraction between the film components induced the formation of nanoscrolls of hexaniobate on the substrate. Thus, differently from the stacking of nanosheets, which is expected to decrease the access of those molecules by joining the layers, the nanoscrolls maintained the diffusion properties of the photocatalyst, showing photocatalytic performances linearly proportional to the amount of deposited hexaniobate. In addition, better photocatalytic performances were achieved by Pt nanoclusters, which were localized inside the nanoscrolls with sizes less than 1–2 nm. These results have shown that thin film deposition is feasible using exfoliated hexaniobate layers and it can be a promisor possibility of a future large-scale utilization.

Furthermore, the exfoliated hexaniobate surface was modified by the grafting method. For the different tested ions, amorphous clusters were formed on the surface. Even though a visible-light induced activity was not achieved, these centers could generate additional absorption features in the UV-A (Co and Fe) or visible light (Cu) regions, which are attributed to an IFCT transition from the hexaniobate valence band to the metal ion centers. These new centers on the hexaniobate surface also induce modifications on the photogenerated charge carrier separation and transportation processes. TAS studies showed that in the hexaniobate sheets, electrons and holes can either undergo geminate recombination or migrate along the hexaniobate layer and be trapped in surface sites with different energies. In general, in the presence of Fe, Co or Cu on the surface, the transient spectra resemble those expected for free electrons in a semiconductor. However, each one of these ions affected the photocatalytic activity in different ways. The least effective modification of the hexaniobate surface for photocatalytic reactions was that of iron. In contrast, the cobalt one could act as a redox shuttle, being active in both reductive and oxidative pathways, depending on the medium conditions. In the case where Cu was employed as modifier, high redox activity of the ions was observed on the hexaniobate surface, acting particularly on the reductive pathways of the hexaniobate. Therefore, grafted ions can effectively contribute to more efficient charge separation and higher photocatalytic performances.

In conclusion, the modifications of the hexaniobate investigated in this work could improve the photocatalytic performances of this material. These studies allowed a deeper comprehension of the photocatalytic surface processes that take place on

hexaniobate-based composites and hence can support further developments in more efficient niobate-based photocatalysts. Thus, for future research, many opportunities of new investigations for these systems can be considered. For instance, as the next step, it would be interesting to couple Co^{2+} and Cu^{2+} metal grafting in a way to get H_2 in absence of both, a sacrificial reagent and a rare metal. Besides, another possibility is the preparation of thin films by the Layer-by-Layer technique, separating the active sites for water oxidation and reduction. For this purpose, Co^{2+} and Cu^{2+} centers could be separately localized either in the nanoscrolls or on its surface. In another perspective, these materials could also be evaluated for other photocatalytic applications such as CO_2 reduction, water treatment, and coupling the H_2 evolution with the conversion of other organic compounds.

References

- (1) Low, J.; Cao, S.; Yu, J.; Wageh, S. Two-Dimensional Layered Composite Photocatalysts. *Chem. Commun.* **2014**, 50 (74), 10768. <https://doi.org/10.1039/C4CC02553A>.
- (2) Chia, X.; Pumera, M. Characteristics and Performance of Two-Dimensional Materials for Electrocatalysis. *Nat. Catal.* **2018**, 1 (12), 909–921. <https://doi.org/10.1038/s41929-018-0181-7>.
- (3) Su, Q.; Li, Y.; Hu, R.; Song, F.; Liu, S.; Guo, C.; Zhu, S.; Liu, W.; Pan, J. Heterojunction Photocatalysts Based on 2D Materials: The Role of Configuration. *Adv. Sustain. Syst.* **2020**, 4 (9), 2000130. <https://doi.org/10.1002/adsu.202000130>.
- (4) Kim, I. Y.; Jo, Y. K.; Lee, J. M.; Wang, L.; Hwang, S. J. Unique Advantages of Exfoliated 2D Nanosheets for Tailoring the Functionalities of Nanocomposites. *J. Phys. Chem. Lett.* **2014**, 5 (23), 4149–4161. <https://doi.org/10.1021/jz502038g>.
- (5) Di, J.; Xiong, J.; Li, H.; Liu, Z. Ultrathin 2D Photocatalysts: Electronic-Structure Tailoring, Hybridization, and Applications. *Adv. Mater.* **2018**, 30 (1), 1704548. <https://doi.org/10.1002/adma.201704548>.
- (6) Saupe, G. B.; Waraksa, C. C.; Kim, H. N.; Han, Y. J.; Kaschak, D. M.; Skinner, D. M.; Mallouk, T. E. Nanoscale Tubules Formed by Exfoliation of Potassium Hexaniobate. *Chem. Mater.* **2000**, 12 (6), 1556–1562. <https://doi.org/10.1021/cm981136n>.
- (7) Shiguihara, A. L.; Bizeto, M. A.; Constantino, V. R. L. Exfoliation of Layered Hexaniobate in Tetra(n-Butyl)Ammonium Hydroxide Aqueous Solution. *Colloids Surfaces A Physicochem. Eng. Asp.* **2007**, 295 (1–3), 123–129. <https://doi.org/10.1016/j.colsurfa.2006.08.040>.
- (8) Bizeto, M. A.; Constantino, V. R. L. Porphyrin Inclusion into Hexaniobate Nanoscrolls. *Microporous Mesoporous Mater.* **2005**, 83 (1–3), 212–218. <https://doi.org/10.1016/j.micromeso.2005.04.013>.
- (9) Nunes, B. N.; Patrocínio, A. O. T.; Bahnemann, D. W. Influence of the

- Preparation Conditions on the Morphology and Photocatalytic Performance Pt-Modified Hexaniobate Composites. *J. Phys. Condens. Matter* **2019**, *31* (39), 394001. <https://doi.org/10.1088/1361-648x/ab2c5e>.
- (10) Deng, X.; Tüysüz, H. Cobalt-Oxide-Based Materials as Water Oxidation Catalyst: Recent Progress and Challenges. *ACS Catal.* **2014**, *4* (10), 3701–3714. <https://doi.org/10.1021/cs500713d>.
- (11) Deng, J.; Zhuo, Q.; Lv, X. Hierarchical TiO₂/Fe₂O₃ Heterojunction Photoanode for Improved Photoelectrochemical Water Oxidation. *J. Electroanal. Chem.* **2019**, *835*, 287–292. <https://doi.org/10.1016/j.jelechem.2019.01.056>.
- (12) Zhang, P.; Yu, L.; Lou, X. W. (David). Construction of Heterostructured Fe₂O₃ - TiO₂ Microdumbbells for Photoelectrochemical Water Oxidation. *Angew. Chemie Int. Ed.* **2018**, *57* (46), 15076–15080. <https://doi.org/10.1002/anie.201808104>.
- (13) Maeda, K.; Ishimaki, K.; Okazaki, M.; Kanazawa, T.; Lu, D.; Nozawa, S.; Kato, H.; Kakihana, M. Cobalt Oxide Nanoclusters on Rutile Titania as Bifunctional Units for Water Oxidation Catalysis and Visible Light Absorption: Understanding the Structure-Activity Relationship. *ACS Appl. Mater. Interfaces* **2017**, *9* (7), 6114–6122. <https://doi.org/10.1021/acsami.6b15804>.
- (14) Jang, J.; Kim, H.; Reddy, V.; Bae, S.; Ji, S.; Lee, J. Photocatalytic Water Splitting over Iron Oxide Nanoparticles Intercalated in HTiNb(Ta)O Layered Compounds. *J. Catal.* **2005**, *231* (1), 213–222. <https://doi.org/10.1016/j.jcat.2005.01.026>.
- (15) Jo, W.-K.; Kumar, S.; Isaacs, M. A.; Lee, A. F.; Karthikeyan, S. Cobalt Promoted TiO₂/GO for the Photocatalytic Degradation of Oxytetracycline and Congo Red. *Appl. Catal. B Environ.* **2017**, *201*, 159–168. <https://doi.org/10.1016/j.apcatb.2016.08.022>.
- (16) Kanakillam, S. S.; Shaji, S.; Krishnan, B.; Vazquez-Rodriguez, S.; Martinez, J. A. A.; Palma, M. I. M.; Avellaneda, D. A. Nanoflakes of Zinc Oxide:Cobalt Oxide Composites by Pulsed Laser Fragmentation for Visible Light Photocatalysis. *Appl. Surf. Sci.* **2020**, *501*, 144223. <https://doi.org/10.1016/j.apsusc.2019.144223>.

- (17) Sun, J.; Shen, C.-H.; Guo, J.; Guo, H.; Yin, Y.-F.; Xu, X.-J.; Fei, Z.-H.; Liu, Z.-T.; Wen, X.-J. Highly Efficient Activation of Peroxymonosulfate by $\text{Co}_3\text{O}_4/\text{Bi}_2\text{WO}_6$ p-n Heterojunction Composites for the Degradation of Ciprofloxacin under Visible Light Irradiation. *J. Colloid Interface Sci.* **2021**, *588*, 19–30. <https://doi.org/10.1016/j.jcis.2020.12.043>.
- (18) Ma, C.; Lee, J.; Kim, Y.; Cheol Seo, W.; Jung, H.; Yang, W. Rational Design of $\alpha\text{-Fe}_2\text{O}_3$ Nanocubes Supported BiVO_4 Z-Scheme Photocatalyst for Photocatalytic Degradation of Antibiotic under Visible Light. *J. Colloid Interface Sci.* **2021**, *581*, 514–522. <https://doi.org/10.1016/j.jcis.2020.07.127>.
- (19) Wang, F.; Yu, X.; Ge, M.; Wu, S. One-Step Synthesis of $\text{TiO}_2/\gamma\text{-Fe}_2\text{O}_3/\text{GO}$ Nanocomposites for Visible Light-Driven Degradation of Ciprofloxacin. *Chem. Eng. J.* **2020**, *384*, 123381. <https://doi.org/10.1016/j.cej.2019.123381>.
- (20) Frindy, S.; Sillanpää, M. Synthesis and Application of Novel $\alpha\text{-Fe}_2\text{O}_3/\text{Graphene}$ for Visible-Light Enhanced Photocatalytic Degradation of RhB. *Mater. Des.* **2020**, *188*, 108461. <https://doi.org/10.1016/j.matdes.2019.108461>.
- (21) Milazzo, G.; Caroli, S.; Sharma, V. K. *Tables of Standard Electrode Potentials*; 1978.
- (22) Kong, D.; Zheng, Y.; Kobielski, M.; Wang, Y.; Bai, Z. Recent Advances in Visible Light-Driven Water Oxidation and Reduction in Suspension Systems. *Mater. Today* **2018**, *21* (8), 897–924. <https://doi.org/10.1016/j.mattod.2018.04.009>.
- (23) Yamakata, A.; Ishibashi, T.; Onishi, H. Water- and Oxygen-Induced Decay Kinetics of Photogenerated Electrons in TiO_2 and Pt/TiO_2 : A Time-Resolved Infrared Absorption Study. *J. Phys. Chem. B* **2001**, *105* (30), 7258–7262. <https://doi.org/10.1021/jp010802w>.
- (24) Schneider, J.; Matsuoka, M.; Takeuchi, M.; Zhang, J.; Horiuchi, Y.; Anpo, M.; Bahnemann, D. W. Understanding TiO_2 Photocatalysis: Mechanisms and Materials. *Chem. Rev.* **2014**, *114* (19), 9919–9986. <https://doi.org/10.1021/cr5001892>.
- (25) Hykaway, N.; Sears, W. M.; Morisaki, H.; Morrison, S. R. Current-Doubling Reactions on Titanium Dioxide Photoanodes. *J. Phys. Chem.* **1986**, *90* (25),

6663–6667. <https://doi.org/10.1021/j100283a014>.

- (26) Bi, W.; Wu, C. Two-Dimensional Nanomaterials—An Ideal Platform to Understand Photocatalysis. In *Inorganic Two-dimensional Nanomaterials: Fundamental Understanding, Characterizations and Energy Applications*; The Royal Society of Chemistry, 2017; pp 334–368.
<https://doi.org/10.1039/9781788010306-00334>.

Curriculum Vitae

Personal data

Name: Barbara Nascimento Nunes
Adress: Schaufelder Straße, 27. 30167 Hannover, Germany
Date of birth: May 18th, 1993
Place of birth: Uberlandia, Brazil

Education

04/2018 – 04/2022: Cocutelle Ph.D. Student at Institute of Technical Chemistry, Leibniz University of Hannover, Hannover, Germany
and at Institute of Chemistry, Federal University of Uberlandia, Uberlandia, Brazil
Ph.D. Thesis: “Photocatalytic Application of Layered Niobates and their Composites”

08/2015 – 09/2017: Master of Science in Chemistry at Institute of Chemistry, Federal University of Uberlandia, Uberlandia, Brazil
Master Thesis: “*Preparação e avaliação fotocatalítica de hexaniobatos lamelares e seus filmes finos obtidos por Layer-by-Layer*”.

02/2011 – 07/2015: Bachelor’s degree in Industrial Chemistry at Federal University of Uberlandia, Uberlandia, Brazil
Bachelor Thesis: “*Preparação de Hidróxidos Duplos Lamelares [Co-Al-Cl] e seus compósitos de Polipirrol para aplicação como adsorventes de 2,4-D*”

02/2008 – 12/2010: High School at Escola Estadual Messias Pedreiro, Uberlandia, Brazil

Work Experience:

07/2018 – 10/2021: Teaching Assistant
Institute of Technical Chemistry, Leibniz University of Hannover

12/2014 – 04/2015: Intern
Suavetex Ltda Industry, Uberlandia, Brazil

Publications List

Journal Publications

Nunes, B. N.; Bahnemann, D. W.; Patrocínio, A. O. T. Efficient photocatalytic H₂ evolution by hexaniobate nanosheets grafted with copper nanoclusters. ChemPhotoChem, e202100272, 2022. <https://doi.org/10.1002/cptc.202100272>.

Contribution: investigation, validation, and writing

Silva, M. A. R.; Silva, I. F.; Xue, Q.; Lo, B. T. W.; Tarakina, N. V.; Nunes, B. N.; Adler, P.; Sahoo, S. K.; Bahnemann, D. W.; López-Salas, N.; Savateev, A.; Ribeiro, C.; Kühne, T. D.; Antonietti, M.; Teixeira, I. F. Sustainable oxidation catalysis supported by light: Fe-poly (heptazine imide) as a heterogeneous single-atom photocatalyst. Applied Catalysis B: Environmental, v. 304, 120965, p. 1-11, 2022. <https://doi.org/10.1016/j.apcatb.2021.120965>

Contribution: investigation, review, and editing

Al-Madanat, O.; Nunes, B. N.; AlSalka, Y.; Hakki, A.; Curti, M.; Patrocínio, A. O. T.; Bahnemann, D. W. Application of EPR Spectroscopy in TiO₂ and Nb₂O₅ Photocatalysis. Catalysts, 11(12), 1514, p. 1-37. <https://doi.org/10.3390/catal11121514>

Contribution: writing, review, and editing

Nunes, B. N.; Bahnemann, D. W.; Patrocínio, A. O. T. Photoinduced H₂ Evolution by Hexaniobate Sheets Grafted with Metal Ions: The Fate of Photogenerated Carriers. ACS Applied Energy Materials, v. 4, p. 3681-3692, 2021. <https://doi.org/10.1021/acsaem.1c00128>

Contribution: investigation, validation, and writing

Ismail, A. A. Al-Hajji, L. A., Alsaidi, M., Nunes, B. N., Bahnemann, D. W. Pyrolysis conversion of metal organic frameworks to form uniform codoped C/N-Titania photocatalyst for H₂ production through simulated solar light. Journal of Photochemistry and Photobiology A: Chemistry, v. 407, 113037, p. 1-8, 2021. <https://doi.org/10.1016/j.jphotochem.2020.113037>

Contribution: investigation, review, and editing

Nunes, B. N.; Lopes, O. F.; Patrocinio, A. O. T.; Bahnemann, D. W. Recent Advances in Niobium-Based Materials for Photocatalytic Solar Fuel Production. *Catalysts*, v. 10, p. 1-21, 2020. <https://doi.org/10.3390/catal10010126>

Contribution: investigation, validation, and writing

Nunes, B. N.; Haisch, C.; Emeline, A. V.; Bahnemann, D. W.; Patrocinio, A. O. T. Photocatalytic properties of layer-by-layer thin films of hexaniobate nanoscrolls. *Catalysis Today*, v. 326, p. 60-67, 2019. <https://doi.org/10.1016/j.cattod.2018.06.029>

Contribution: investigation, validation, and writing

Nunes, B. N.; Patrocinio, A. O. T.; Bahnemann, D. W. Influence of the preparation conditions on the morphology and photocatalytic performance Pt-modified hexaniobate composites. *Journal of Physics: Condensed Matter*, v. 31, p. 394001, 2019. <https://doi.org/10.1088/1361-648X/ab2c5e>

Contribution: investigation, validation, and writing

Faustino, L. A.; Souza, B. L.; Nunes, B. N.; Duong, A.-T.; Sieland, F.; Bahnemann, D. W.; Patrocinio, A. O. T. Photocatalytic CO₂ reduction by Re(I) polypyridyl complexes immobilized on niobates nanoscrolls. *ACS Sustainable Chemistry & Engineering*, v. 6, p. 6073-6083, 2018. <https://doi.org/10.1021/acssuschemeng.7b04713>

Contribution: investigation, review, and editing

Haisch, C.; Nunes, B. N.; Schneider, J.; Bahnemann, D.; Patrocinio, A. O. T. Transient Absorption Studies on Nanostructured Materials and Composites: Towards the Development of New Photocatalytic Systems. *Zeitschrift für Physikalische Chemie-International Journal of Research in Physical Chemistry & Chemical Physics*, v. 1, p. 1-25, 2018. <https://doi.org/10.1515/zpch-2018-1137>

Contribution: writing, review, and editing

Nunes, B. N.; Paula, L. F.; Costa, Í. A.; Machado, A. E. H.; Paterno, L. G.; Patrocinio, A. O. T. Layer-by-layer assembled photocatalysts for environmental remediation and solar energy conversion. *Journal of Photochemistry and Photobiology C-Photochemistry Reviews*, v. 32, p. 1-20, 2017. <https://doi.org/10.1016/j.jphotochemrev.2017.05.002>

Contribution: writing, review, and editing

Book Chapters

Nunes, B. N.; Faustino, L. A.; Muller, A. V.; Polo, A. S.; Patrocínio, A. O. T. Nb₂O₅ dye-sensitized solar cells. In: Nanomaterials for Solar Cell Applications. 1 ed.: Elsevier, 2019, p. 287-322.

Contribution: writing, review, and editing

Nunes, B. N.; Barros, C. L.; Bahnemann, D. W.; Patrocínio, A. O. T. Historical Development of Inorganic Photochemistry. In: Springer Handbook of Inorganic Photochemistry. 1 ed.: Springer, 2022, *in press*.

Contribution: writing, review, and editing

Presentations

Nunes, B. N.; Bahnemann, D. W.; Patrocínio, A. O. T. Photocatalytic properties of layered niobates. Oral Presentation, 6th Russian-German School-Seminar, Leibniz University of Hannover, 2018, Hannover, Germany.

Nunes, B. N.; Bahnemann, D. W.; Patrocínio, A. O. T. Photocatalytic activity of Pt-modified hexaniobate layers and their preparation conditions. Poster, Microscale Motion and Light Workshop, 2019, Max Planck Institute of Physics of Complex Systems, Dresden, Germany.

Nunes, B. N.; Bahnemann, D. W.; Patrocínio, A. O. T. Photocatalytic activity of modified hexaniobate. Oral Presentation, 7th Russian-German School-Seminar, Saint Petersburg University, 2019, Saint Petersburg, Russia.

Nunes, B. N.; Bahnemann, D. W.; Patrocínio, A. O. T. Co²⁺-grafted hexaniobate for photocatalytic H₂ evolution. Poster, 2nd Symposium on Chemical Bond Activation in Oldenburg, Carl von Ossietzky University Oldenburg, 2020, Oldenburg, Germany.

Nunes, B. N.; Bahnemann, D. W.; Patrocínio, A. O. T. Insights on the mechanism of surface grafted hexaniobate for H₂ evolution. Poster, 1. Catalight Young Scientist Symposium: Light Driven Catalysis, 2020, SFB/TRR 234 CataLight Germany, online conference.